UNIVERSITÀ
DI TORINO

Università degli Studi di Torino

Scuola di Dottorato

Synergies between Effective-One-Body Models and Numerical Relativity Simulations for Noncircularized Black Hole Binaries

---

Candidato:
Simone Albanesi

Tutor:
Alessandro Nagar
Mariaelena Boglione

To my beloved cat, Tilly, who
continuously bothered me
during the writing of this thesis.

Preface

This thesis, "Synergies between Effective-One-Body Models and Numerical Relativity Simulations for Noncircularized Black Hole Binaries", is based on results concerning the modelization of noncircularized black hole binaries with the effective-one-body (EOB) approach completed and improved with numerical methods. The first two chapters of this manuscript are an introduction to the original results, which will be presented starting from the third chapter. Since this work is a collection of published results, many discussions are taken, mutatis mutandis, from the original references [1–7]. The papers on which this thesis is based are listed below in chronological order. The original results here presented were achieved in collaboration with other researchers. More specifically, the analytical results were achieved mainly in collaboration with my supervisor, Dr. Alessandro Nagar, and another researcher, Dr. Andrea Placidi, who was a Ph.D. student at the University of Perugia when we authored the articles on the 2PN noncircular corrections [3–5]. The numerical results stem from a collaboration with the research group of Prof. Sebastiano Bernuzzi, from the University of Jena. During my Ph.D. I have also contributed to other projects [8–14], but these results will not be discussed in detail in this thesis.

---

1. *Effective one-body model for extreme-mass-ratio spinning binaries on eccentric equatorial orbits: Testing radiation reaction and waveform*

   Simone Albanesi, Alessandro Nagar, and Sebastiano Bernuzzi

   Journal: Phys. Rev. D, volume 104, 024067 (2021)

   DOI: 10.1103/PhysRevD.104.024067

   Preprint: arXiv:2104.10559

---

2. *GW190521 as a dynamical capture of two nonspinning black holes*

   Rossella Gamba, Matteo Breschi, Gregorio Carullo, Simone Albanesi, Piero Rettegno, Sebastiano Bernuzzi, Alessandro Nagar

   Journal: Nature Astron., volume 7, 11-17 (2023)

   DOI: 10.1038/s41550-022-01813-w

   Preprint: arXiv:2106.05575

---

3. *Exploiting Newton-factorized, 2PN-accurate waveform multipoles in effective-one-body models for spin-aligned noncircularized binaries*

   Andrea Placidi, Simone Albanesi, Alessandro Nagar, Marta Orselli, Sebastiano Bernuzzi, and Gianluca Grignani

   Journal: Phys. Rev. D, volume 105, 104030 (2022)

   DOI: 10.1103/PhysRevD.105.104030

   Preprint: arXiv:2112.05448

---

4. *Assessment of effective-one-body radiation reactions for generic planar orbits*

   Simone Albanesi, Alessandro Nagar, Sebastiano Bernuzzi, Andrea Placidi, and Marta Orselli

   Journal: Phys. Rev. D, volume 105, 104031 (2022)

   DOI: 10.1103/PhysRevD.105.104031

   Preprint: arXiv:2202.10063

---

5. *New avenue for accurate analytical waveforms and fluxes for eccentric compact binaries*

   Simone Albanesi, Andre Placidi, Alessandro Nagar, Marta Orselli, and Sebastiano Bernuzzi

   Journal: Phys. Rev. D, volume 105, L121503 (2022)

   DOI: 10.1103/PhysRevD.105.L121503

   Preprint: arXiv:2203.16286

---

6. *Faithful effective-one-body waveform of small-mass-ratio coalescing black hole binaries: The eccentric, nonspinning case*

   Simone Albanesi, Sebastiano Bernuzzi, Thibault Damour, Alessandro Nagar, Andrea Placidi

   Journal: Phys. Rev. D, volume 108, 084037 (2023)

   DOI: 10.1103/PhysRevD.108.084037

   Preprint: arXiv:2305.19336

---

7. *Towards numerical-relativity informed effective-one-body waveforms for dynamical capture black hole binaries*

   Tomas Andrade, Juan Trenado, Simone Albanesi, Rossella Gamba, Sebastiano Bernuzzi, Alessandro Nagar, Juan Calderon Bustillo, Nicolas Sanchis-Gual, José A. Font, William Cook, Boris Daszuta, Francesco Zappa, and David Radice

   Preprint: arXiv:2307.08697

Contents

Introduction

Following the landmark discovery of the gravitational wave (GW) event GW190514 [15], subsequent years have witnessed the detection of numerous gravitational signals generated by the coalescence of compact binary objects [16–18], bringing gravitational wave astronomy into its mature phase. While most detected events have been generated by the coalescence of binary black holes, events resulting from binaries with neutron stars can also produce an electromagnetic counterpart. A notable example is GW170817 [19], which represents the first detected signal originating from a binary neutron star merger. The kilonova generated by this coalescence has been observed by numerous observatories [20, 21], marking the beginning of the multi-messenger astronomy era. Since the sensitivity band of the interferometers is between 10 Hz and a few kHz, we are currently able to detect signals generated by the last few orbits before merger, when the distance between the compact objects is at most a few Schwarzschild radii. This means that the gravitational waves that we observed were generated in extreme gravitational fields; therefore, these events are of primary importance for studying the validity of general relativity (GR) in the strong-field regime.

The data that have been collected in recent years by the LIGO-Virgo-KAGRA (LVK) collaboration have opened a new window of investigation on the Universe, and more interferometers will be built in the forthcoming years, allowing us to better understand the weakest of the fundamental forces. In particular, many ground-based interferometers are going to be built across the globe: LIGO-India [22, 23] in this decade, Einstein Telescope [24, 25] and Cosmic Explorer [26] in the next decade. Future plans also include space-based detectors, that will allow us to study GWs in sensitivity bands that are not accessible from the Earth's surface: the Laser Interferometer Space Antenna [27] and TianQuin [28] will work in the $[100\mu\text{Hz}, 100\text{mHz}]$ band, while DECIGO [29] will be sensitive from 0.1 to 10 Hz. Finally, nano-Hertz wavelengths can be studied with pulsar timing arrays [30–36].

To fully exploit the opportunities provided by current and future detectors, accurate waveform models for gravitational wave sources, compact binary coalescences in particular, are essential. The description of strong-gravitating systems requires the solution of the Einstein Field Equations (EFE). However, the non-linearity and complex structure of these equations rule out the possibility of exact analytical solutions for binaries, even in the vacuum case. Consequently, the waveform models rely on analytical approximations or numerical simulations. Both approaches are highly non-trivial and involve numerous subtleties and difficulties, making them active areas of research. The synergy between numerical and approximate analytical solutions is fundamental in constructing state-of-the-art waveform models. Among the various analytical and semi-analytical approaches used to study two-body problems, notable methods include the post-Newtonian (PN) [37–41] and post-Minkowskian (PM) [42–46] expansions, whose synergies [47–50] are essential to obtain effective-one-body (EOB) models [11, 51–60]. Other approaches include phe-

nomenological models [61–68], and the gravitational self-force (GSF) approach [69–75]. On the numerical side, several research groups are currently able to generate waveform catalogs by solving on supercomputers the EFE formulated in the 3+1 formalism [76–88]. We will delve into further detail about these methods in Chapter 2, focusing in particular on EOB models and numerical relativity (NR) simulations.

The primary focus of the gravitational wave community has been on investigating binaries in which two compact objects revolve around each other following quasi-circular orbits. The adoption of the (quasi)-circular approximation is grounded in two principal rationales. First, studying binaries with quasi-circular orbits is easier than studying generic orbits, both from analytical and numerical points of view. Second, the orbits of the systems that we are currently able to detect are thought to become quasi-circular by the time they enter the sensitivity band of our detectors. Indeed, over the course of millions or even billions of years, these binaries, influenced by the emission of gravitational waves, naturally tend to circularize their orbits. However, although less common, eccentric and even hyperbolic orbits can occur in dense clusters [89–94] or due to the perturbation caused by a third body [95]. Modeling these non-circularized systems has garnered significant attention in recent years. In particular, the signal GW190521 [96] might have been generated by this kind of systems, as shown by recent analysis [2, 97, 98], even if its origin is still debated [99–101]. The description of eccentric and hyperbolic black hole binaries also constitutes the main focus of this thesis. Specifically, we begin our study by examining eccentric binaries in the test particle limit using numerical black hole perturbation techniques and EOB models. We then argue that the EOB approach can be used to describe comparable mass binaries with eccentric and hyperbolic orbits.

The thesis is structured as follows. In the first two chapters, we introduce well-known methods and models used in the field of gravitational wave physics. In particular, in Chapter 1 we begin by discussing gravitational waves in linearized theory and the motion of massive particles in Kerr geometry, while in Chapter 2, we introduce the most used analytical and numerical methods employed for the description of binary black holes. We consider the EOB approach in Secs. 2.2 and 2.3, and briefly introduce numerical relativity simulations in Sec. 2.4. From Chapter 3 we present original results. In particular, we discuss the gravitational waves generated by the motion of a test particle along eccentric orbits in the Kerr equatorial plane, discussing both geodesic and non-conservative dynamics. We also discuss the analytical Newtonian noncircular prescription to be introduced in the EOB radiation sector in order to faithfully reproduce the numerical results obtained in linear perturbation theory. In Chapter 4, we extend these noncircular corrections of the EOB radiation to the 2PN order and test their relevance, both in the test particle limit and in the comparable mass case. In Chapter 5 we discuss in detail the transition from the inspiral to plunge, merger, and ringdown of a test particle in Schwarzschild spacetime. We conclude this thesis by discussing hyperbolic orbits in Chapter 6, focusing in particular on the comparable mass case and presenting NR simulations of dynamical captures and hyperbolic scatterings performed with the code `GR-Athena++`.

Chapter 1

Gravitational perturbations and test masses

When studying physical systems, it is always instructive to start from the simplest case that one can think of. For this reason, before diving into the study of BBHs with comparable masses, we will focus on test masses orbiting around, and thus perturbing, central black holes. These systems are proxies of extreme mass ratio inspirals (EMRIs) [102], astrophysical binaries in which a stellar black hole orbits around a (super)massive black hole. In this chapter, we discuss only linear-order perturbations, even if second-order terms are thought to be essential for accurately describing these astrophysical systems [103]. Therefore, the goal of this chapter is to discuss the linearization of the GR equations on a stationary background.

We begin by recalling that the Einstein Field Equations (EFE) read

$$R_{\mu\nu} - \frac{1}{2}Rg_{\mu\nu} = \frac{8\pi G}{c^4}T_{\mu\nu}, \tag{1.1}$$

where $g_{\mu\nu}$ is the spacetime metric, $R_{\mu\nu}$ is the Ricci tensor, R is the scalar curvature, and $T_{\mu\nu}$ is the stress-energy tensor. The term on the left-hand side (lhs) is also called Einstein tensor and is denoted as $G_{\mu\nu} \equiv R_{\mu\nu} - \frac{1}{2}Rg_{\mu\nu}$. In other words, on the lhs there is the spacetime geometry, encoded in the metric tensor, while on the right-hand side (rhs) there is the matter-energy distribution. In Eq. (1.1) we have written the speed of light in vacuum c and the gravitational constant G explicitly, but in the following, we will always use geometrized units ($G = c = 1$), if not specified otherwise. The Ricci tensor and scalar are defined as $R_{\mu\nu} = R^{\alpha}_{\ \mu\alpha\nu}$ and $R = R^{\alpha}_{\ \alpha}$, where $R^{\lambda}_{\ \mu\nu\sigma}$ is the Riemann tensor and can be written in terms of Christoffel symbols $\Gamma^{\lambda}_{\mu\nu}$

$$R^{\lambda}_{\ \mu\nu\sigma} = \partial_\nu\Gamma^{\lambda}_{\mu\sigma} - \partial_\sigma\Gamma^{\lambda}_{\mu\nu} + \Gamma^{\lambda}_{\alpha\nu}\Gamma^{\alpha}_{\mu\sigma} - \Gamma^{\lambda}_{\alpha\sigma}\Gamma^{\alpha}_{\mu\nu}, \tag{1.2}$$

$$\Gamma^{\lambda}_{\mu\nu} = \frac{1}{2}g^{\lambda\alpha}\left(\partial_\mu g_{\alpha\nu} + \partial_\nu g_{\mu\alpha} - \partial_\alpha g_{\mu\nu}\right). \tag{1.3}$$

We also recall that GR is invariant under the group of all possible coordinate transformation. Under a generic diffeomorphism $x^\mu \to x'^\mu(x)$, a generic tensor $T^{\mu_1,\ldots,\mu_p}_{\nu_1,\ldots,\nu_q}(x)$ transforms as

$$T'^{\mu_1,\ldots,\mu_p}_{\nu_1,\ldots,\nu_q}(x') = \frac{\partial x'^{\mu_1}}{\partial x^{\alpha_1}}\cdots\frac{\partial x'^{\mu_p}}{\partial x^{\alpha_p}}\frac{\partial x^{\beta_1}}{\partial x'^{\nu_1}}\cdots\frac{\partial x^{\beta_p}}{\partial x'^{\nu_p}}T^{\alpha_1,\ldots,\alpha_p}_{\beta_1,\ldots,\beta_q}(x). \tag{1.4}$$

and therefore the metric, which is a 2-rank tensor, transforms as

$$g_{\mu\nu}(x) \to g'_{\mu\nu}(x') = \frac{\partial x^\alpha}{\partial x'^\mu}\frac{\partial x^\beta}{\partial x'^\nu}g_{\alpha\beta}(x). \tag{1.5}$$

The linearization problem is already non-trivial since the aforementioned coordinate freedom of GR does not allow us to distinguish between physical perturbations and perturbations produced by infinitesimal coordinate changes. To overcome this issue, one can either fix the gauge or formulate the linear perturbation problem in a gauge-invariant manner. To follow the latter approach, one has to find a way to define linear perturbations of a background metric such that infinitesimal coordinate transformations $x^\mu \to x^\mu + \xi^\mu$ with $|\xi^\mu| \ll 1$ leave unchanged the perturbations. More precisely, given a tensor $\boldsymbol{X}$ defined on a background metric $\bar{\boldsymbol{g}}$, its perturbation $\delta\boldsymbol{X}$ transforms as $\delta\boldsymbol{X} \to \delta\boldsymbol{X}' = \delta\boldsymbol{X} + \mathcal{L}_\xi \boldsymbol{X}$, where $\mathcal{L}_\xi$ is the Lie derivative along ξ in the metric $\bar{\boldsymbol{g}}$. Then $\delta\boldsymbol{X}$ is gauge invariant if and only if $\mathcal{L}_\xi \boldsymbol{X} = 0$ (see also Lemma (2.1) and (2.2) of Ref. [104]). This means that the construction of gauge invariant linear perturbation relies on background symmetries. When discussing linear perturbation in Minkowski, we will see that if one does not exploit background symmetries, then a gauge fixing is needed to isolate the gravitational wave content. On the contrary, we will briefly see how to construct gauge invariant perturbations when we consider Schwarzschild. Finally, for Kerr spacetime, it is convenient to consider perturbations in the curvature rather than in the metric.

1.1 Linear perturbations on a Minkowskian background

We begin by considering linear perturbations in Minkowski spacetime, mainly following Ref. [105]. Denoting the Minkowskian metric as $\boldsymbol{\eta}$, we can write the total metric as

$$g_{\mu\nu} = \eta_{\mu\nu} + h_{\mu\nu}, \tag{1.6}$$

where the symmetric tensor $h_{\mu\nu}$ is the coordinate-dependent perturbation, and $|h_{\mu\nu}| \ll 1$ in a certain reference frame for a sufficiently large region. Since the metric transforms according to Eq. (1.5), we have that under the usual infinitesimal coordinate transformation $x^\mu \to x'^\mu = x^\mu + \xi^\mu$, the metric perturbation transforms at linear order as

$$h_{\mu\nu} \to h'_{\mu\nu} = h_{\mu\nu} - \left(\partial_\mu \xi_\nu + \partial_\nu \xi_\mu\right). \tag{1.7}$$

Linearizing the Riemann tensor, we obtain the expression

$$R_{\mu\nu\rho\sigma} = \frac{1}{2}\left(\partial_\nu\partial_\rho h_{\mu\sigma} + \partial_\mu\partial_\sigma h_{\nu\rho} - \partial_\mu\partial_\rho h_{\nu\sigma} - \partial_\nu\partial_\sigma h_{\mu\rho}\right), \tag{1.8}$$

that is *invariant* under the transformation of Eq. (1.7). The linearized EFE can then be written as

$$\Box\bar{h}_{\mu\nu} + \eta_{\mu\nu}\partial^\rho\partial^\sigma\bar{h}_{\rho\sigma} - \partial^\rho\partial_\nu\bar{h}_{\mu\rho} - \partial^\rho\partial_\mu\bar{h}_{\nu\rho} = -16\pi T_{\mu\nu}, \tag{1.9}$$

where we have introduced, for convenience, $\bar{h}_{\mu\nu} = h_{\mu\nu} - \frac{1}{2}h\eta_{\mu\nu}$, being $h = h^\mu_{\ \mu}$ the trace of the perturbation. The transformation laws for $\bar{h}_{\mu\nu}$ and its derivative are

$$\bar{h}_{\mu\nu} \to \bar{h}'_{\mu\nu} = \bar{h}_{\mu\nu} - \xi_{\mu\nu}, \tag{1.10}$$

$$\partial^\nu\bar{h}_{\mu\nu} \to \left(\partial^\nu\bar{h}_{\mu\nu}\right)' = \partial^\nu\bar{h}_{\mu\nu} - \Box\xi_\mu, \tag{1.11}$$

where $\xi_{\mu\nu} \equiv \left(\partial_\mu\xi_\nu + \partial_\nu\xi_\mu - \eta_{\mu\nu}\partial_\rho\xi^\rho\right)$ and $\Box = \partial^\mu\partial_\mu$ is the (always invertible) d'Alembertian operator in Minkowski spacetime. From these transformations, it follows that we can always impose the harmonic gauge condition

$$\partial^\mu\bar{h}_{\mu\nu} = 0. \tag{1.12}$$

Indeed, if we have $\partial^\mu \bar{h}_{\mu\nu} = f_\nu(x)$ in a certain reference frame, we can always perform an infinitesimal transformation that satisfies $\Box\xi_\mu = f_\mu(x)$ in order to get $\partial^\mu \bar{h}'_{\mu\nu} = 0$. Thus, we can exploit this property to remove four degrees of freedom and reduce the linearized EFE to the simpler form

$$\Box \bar{h}_{\mu\nu} = -16\pi T_{\mu\nu}. \tag{1.13}$$

We have so far kept the stress-energy tensor, to highlight in the harmonic gauge it is not necessary to consider a vanishing $T_{\mu\nu}$. However, we will now restrict ourselves to the vacuum case $T_{\mu\nu} = 0$. We can thus perform another coordinate transformation $x'^\mu = x^\mu + \bar{\xi}^\mu(x)$ with $\Box\bar{\xi}^\mu = 0$. This transformation does not spoil the harmonic gauge condition, nor the wave equation $\Box\bar{h}_{\mu\nu} = 0$, since $\Box\bar{\xi}_{\mu\nu} = 0$. We can thus choose $\bar{\xi}^\mu$ such that

$$h^{0\mu} = h^i{}_i = \partial^j h_{ij} = 0. \tag{1.14}$$

This is known as the transverse-traceless (TT) gauge and shows that the propagative GW has only two degrees of freedom. In this gauge $\bar{h}_{\mu\nu} = h_{\mu\nu}$, so that the vacuum-propagating perturbation satisfies the typical d'Alembertian equation $\Box h_{\mu\nu} = 0$. The simplest non-trivial solution is thus a plane wave $h_{\mu\nu} = e_{\mu\nu}e^{ik\cdot x}$, where $e_{\mu\nu}$ is the polarization tensor and $k^\mu = \left(\frac{\omega}{c}, \mathbf{k}\right)$. If we choose the z-axis as the propagation direction, we can write the solution as

$$h^{\mathrm{TT}}_{\mu\nu}(t,z) = \begin{pmatrix} 0 & 0 & 0 & 0 \\ 0 & h_+ & h_\times & 0 \\ 0 & h_\times & -h_+ & 0 \\ 0 & 0 & 0 & 0 \end{pmatrix}_{\mu\nu} e^{i(\omega t - kz)}. \tag{1.15}$$

If we consider a waveform $h_{\mu\nu}$ in the harmonic gauge propagating in vacuum along the direction $\hat{\boldsymbol{n}} = \boldsymbol{k}/|\boldsymbol{k}|$, we can always define the symmetric transverse projector

$$P_{ij}(\hat{\boldsymbol{n}}) = \delta_{ij} - n_i n_j, \tag{1.16}$$

and define the Lambda tensor as

$$\Lambda_{ij,kl}(\hat{\boldsymbol{n}}) = P_{ik}P_{jl} - \frac{1}{2}P_{ij}P_{kl}. \tag{1.17}$$

This object is a projector since[1] $\Lambda_{ij,kl}\Lambda_{kl,mn} = \Lambda_{ij,mn}$, it is transverse in all indices, e.g. $n^i\Lambda_{ij,kl} = 0$, it is traceless with respect to the pair-indices since $\Lambda_{ii,kl} = \Lambda_{ij,kk} = 0$, and it is symmetric for $(i,j) \leftrightarrow (k,l)$ exchanges. Given the waveform in the Lorentz gauge, we can obtain the spatial components of the perturbation in the TT-gauge as

$$h^{\mathrm{TT}}_{ij} = \Lambda_{ij,kl}h_{kl}. \tag{1.18}$$

The components h_+ and $h_\times$ are the amplitudes of the plus and cross polarizations. One can easily verify that under a global rotation with angle θ, these components transform as

$$h_+ \to h'_+ = h_+\cos 2\theta - h_\times \sin 2\theta, \tag{1.19}$$

$$h_\times \to h'_\times = h_+\sin 2\theta + h_\times \cos 2\theta. \tag{1.20}$$

[1]Note that since we are in Minkowski and we have chosen the signature $(-,+,+,+)$, we can raise and lower spatial indices as we like. Therefore, in expressions like $\Lambda_{ij,kl}\Lambda_{kl,mn} = \Lambda_{ij,mn}$, the equal indices are contracted even if they are both lower indices.

We can also consider the complex combination $h_\times \pm i h_+$, which transforms according to

$$(h_\times \pm i h_+) \to e^{\mp 2i\psi}(h_\times \pm i h_+). \tag{1.21}$$

The scalar $h_\times - i h_+$ is the quantity that is usually decomposed in spherical tensor harmonics with spin-weight -2. We will discuss this topic in more detail in the next section.

To conclude our brief discussion on linearized EFE in Minkowski, we observe that if we consider two test masses initially at rest in the TT reference frame, then these two masses remain at rest even after the passage of the GW. This can be seen considering the geodesic equation

$$\frac{d^2x^\sigma}{d\lambda^2} + \Gamma^\sigma_{\mu\nu}\frac{dx^\mu}{d\lambda}\frac{dx^\nu}{d\lambda} = 0, \tag{1.22}$$

where λ is an affine parameter along the geodesic. If we parametrize the geodesic with the proper time τ and specify the TT gauge, we have

$$\frac{d^2x^i}{d\tau^2}\Big|_{\tau=0} = -\left[\Gamma^i_{\mu\nu}\frac{dx^\mu}{d\tau}\frac{dx^\nu}{d\tau}\right]_{\tau=0} = -\left[\Gamma^i_{00}\left(\frac{dx^0}{d\tau}\right)^2\right]_{\tau=0}, \tag{1.23}$$

where we have used the fact that $dx^i/d\tau = 0$, by hypothesis. We can then linearize the affine connection and get

$$\Gamma^\rho_{\mu\nu} = \frac{1}{2}\eta^{\rho\sigma}\left(\partial_\mu h_{\nu\sigma} + \partial_\nu h_{\mu\sigma} - \partial_\sigma h_{\mu\nu}\right), \tag{1.24}$$

but since we are in TT gauge, we have $h_{00} = 0$ and $h_{0i} = 0$. Therefore, from Eq. (1.23) we have that the acceleration of the test masses is zero, so that they remain at rest even after the arrival of the GW. This result does not mean that the passage of a GW does not have physical effects, but is instead a consequence of our coordinate choice. Indeed, if we compute the proper distance of two particles with initial separation $\boldsymbol{L}$, we get $s = \sqrt{L^2 + h_{ij}(t)L_iL_j} \simeq L + \frac{L_iL_j}{2L}h_{ij}(t)$, and thus the proper separation changes over time due to GW passage.

1.2 Gravitational wave multipoles and radiation

To discuss GW multipoles, we continue to mostly follow Ref. [105]. When specifying the TT gauge, we considered the vacuum linearized EFE, so we restricted our discussion to the propagation of the perturbation. We now want to study the generation of GWs by matter sources. We start with the linearized EFE in the harmonic gauge, as written in Eq. (1.13). To solve this wave equation, it is possible to use Green's functions. Since we are dealing with a wave equation, the corresponding solution is the usual retarded Green function. The solution to Eq. (1.13) is thus

$$\bar{h}_{\mu\nu}(x) = -16\pi\int d^4x' G(x-x')T_{\mu\nu}(x') \tag{1.25}$$

with

$$G\left(x-x'\right) = -\frac{1}{4\pi|\boldsymbol{x}-\boldsymbol{x}'|}\delta(t_{\rm ret}-t'), \tag{1.26}$$

where $t_{\rm ret}$ is the retarded time $t = t - |\boldsymbol{x} - \boldsymbol{x}'|$. Assuming small velocities for motion inside the source, a waveform propagating in the $\hat{\boldsymbol{n}}$ direction observed at a large distance r is given by

$$h_{ij}^{\rm TT}(t, \boldsymbol{x}) = \frac{4G}{rc^4}\Lambda_{ij,kl}(\hat{\boldsymbol{n}})\left(S^{kl} + \frac{1}{c}n_m\dot{S}^{kl,m} + \frac{1}{2c^2}n_m n_p\ddot{S}^{kl,mp} + ...\right)_{\rm ret}, \tag{1.27}$$

where we have kept G and c explicit for clarity. The momenta in parenthesis are defined in terms of the spatial stress-energy tensor T^{ij} as

$$S^{ij}(t) = \int d^3x T^{ij}(t, \boldsymbol{x}), \tag{1.28}$$

$$S^{ij,k}(t) = \int d^3x T^{ij}(t, \boldsymbol{x})x^k, \tag{1.29}$$

$$S^{ij,kl}(t) = \int d^3x T^{ij}(t, \boldsymbol{x})x^k x^l, \tag{1.30}$$

$$\dots$$

Similarly, one can define the momenta M, M^i, M^{ij}, etc. using T^{00}/c^2, and P^i, $P^{i,j}$, $P^{i,jk}$, etc. using T^{0i}/c. From the conservation law $\partial_\mu T^{\mu 0} = 0$ and integrating over a large volume V, one can write explicitly

$$\dot{M} = \frac{1}{c}\int_V d^3x \partial_0 T^{00} = -\frac{1}{c}\int_V d^3x \partial_i T^{0i} = -\frac{1}{c}\int_{\partial V} dS^i T^{0i} = 0, \tag{1.31}$$

where $\dot{M} = \partial_t M = c\partial_0 M$, and we have used the fact that T^{0i} is zero on the boundary of V. Following a similar procedure, we can find

$$\dot{M}^i = \frac{1}{c}\int_V d^3x \partial_0 T^{00}x^i = -\frac{1}{c}\int_V d^3x \left(\partial_j T^{0j}\right)x^i \tag{1.32}$$

$$= \frac{1}{c}\int_V d^3x \left(\partial_j x^i\right)T^{0j} = P^i, \tag{1.33}$$

and also $\dot{M} = P^{i,j} + P^{j,i}$, $\dot{M}^{ijk} = P^{i,jk} + P^{j,ki} + P^{k,ij}$, etc. Similarly, we can find the conservation of linear momentum $\dot{P}^i = 0$, and then the relations $\dot{P}^{i,j} = S^{ij}$, $\dot{P}^{i,jk} = S^{ij,k} + S^{ik,j}$, etc. In addition, the angular momentum of the source is conserved because $\dot{P}^{i,j} - \dot{P}^{j,i} = S^{ij} - S^{ji} = 0$. The conservation of mass and linear and angular momentum is a consequence of the fact that we are in linearized theory; thus, the back-reaction on the source due to GW emission is neglected. Using the relations found, we can easily obtain higher-order time-derivatives of the S-momenta, obtaining in particular

$$S^{ij} = \frac{1}{2}\ddot{M}^{ij}, \tag{1.34}$$

$$\dot{S}^{ij,k} = \frac{1}{6}\dddot{M}^{ijk} + \frac{1}{3}\left(\ddot{P}^{i,jk} + \ddot{P}^{j,ik} - 2\ddot{P}^{k,ij}\right). \tag{1.35}$$

Looking at Eq. (1.27), the lowest order contribution to GWs is proportional to $\ddot{M}^{ij}$. We further notice that because on the rhs of Eq. (1.27) we have the Lambda tensor, only the traceless part of $\ddot{M}^{ij}$ contributes to the perturbation. Thus, we can define

$$Q^{ij} \equiv M^{ij} - \frac{1}{3}\delta^{ij}M_{kk}, \tag{1.36}$$

and we can write the lowest-order contribution to the GW as

$$\left[h_{ij}^{\rm TT}(t,\boldsymbol{x}\right]_{\rm quad} = \frac{1}{r}\frac{2G}{c^4}\Lambda_{ij,kl}(\hat{\boldsymbol{n}})\ddot{Q}_{kl}\left(t-r/c\right). \tag{1.37}$$

This is the famous quadrupole formula and states that the lowest order contribution to GWs is given by the mass quadrupole $\ddot{Q}^{ij}$, which is strictly related to the lowest-order of the $1/|\boldsymbol{x}-\boldsymbol{x}'|$ expansions in Eq. (1.26).

With the same procedure discussed above, one can easily find higher-order contributions, such as the mass octupole and the current quadrupole. However, given that we have an infinity of higher terms, it is convenient to perform the multipole expansion in a more generic way [106]. This can be achieved by starting from the expansion

$$\frac{1}{|\mathbf{x}-\mathbf{x}'|} = \sum_{\ell=0}^{\infty}\frac{(-1)^\ell}{\ell!}x'^{i_1}\dots x'^{i_\ell}\partial_{i_1}\dots\partial_{i_\ell}\frac{1}{|\mathbf{x}|}, \tag{1.38}$$

and then writing $h_{ij}^{\rm TT}$ in terms of the symmetric-trace-free (SFT) mass-type moments $\mathcal{U}_{ijk}$ and of the STF current-type moments $\mathcal{V}_{ijk}$, both explicit expressions can be found, e.g., in Refs. [106, 107]. Finally, using an orthonormal triad and the spin-weighted spherical harmonics, we can write the strain as [106]

$$h_+ - ih_\times = D_L^{-1}\sum_{\ell=2}^{\infty}\sum_{m=-\ell}^{\ell} h_{\ell m}\ {}_{-2}Y_{\ell m}(\Theta,\Phi), \tag{1.39}$$

where D_L is the luminosity distance of the source with respect to the observer, and the $h_{\ell m}$ multipoles are functions of the retarded time. The explicit expressions of the spherical harmonics are [107]

$${}_{-s}Y^{\ell m}(\Theta,\Phi) = (-1)^s\sqrt{\frac{2\ell+1}{4\pi}}d^\ell_{ms}(\Theta)e^{im\Phi}, \tag{1.40}$$

where the Wigner functions d^ℓ_{ms} are defined as

$$\begin{aligned} d^\ell_{ms}(\Theta) =& \sqrt{(\ell+m)!(\ell-m)!(\ell+s)!(\ell-s)!} \\ &\times\sum_{k=k_i}^{k_f}\frac{(-1)^k(\sin\frac{\Theta}{2})^{2k+s-m}(\cos\frac{\Theta}{2})^{2\ell+m-s2k}}{k!(\ell+m-k)!(\ell-s-k)!(s-m+k)!} \end{aligned} \tag{1.41}$$

and $k_i = \max(0, m-s)$, $k_f = \min(\ell+m, \ell-s)$. Note that this multipole decomposition is the standard one used when dealing with GWs generated by compact binaries.

Other crucial quantities in GW physics are the energy and angular momentum carried by the GWs. To give a proper definition, we can start by applying Noether's theorem to the linearized Lagrangian of GR and find the stress-energy tensor of the gravitational radiation, $t_{\mu\nu}$, that in asymptotically flat spacetimes satisfies the conservation law $\partial^\mu t_{\mu\nu} = 0$. We can thus define the energy, strictly related to t_{00}, and the angular momentum, associated with the invariance of the Lagrangian under spatial rotations. We can then compute the corresponding fluxes, $\dot{E}$ and $\dot{J}$, that in the multipole expansion that we have just discussed are given by

$$\dot{E} = \frac{1}{16\pi}\sum_{\ell=2}^{\infty}\sum_{m=-\ell}^{\ell}|\dot{h}_{\ell m}|^2, \tag{1.42a}$$

$$\dot{J} = -\frac{1}{16\pi}\sum_{\ell=2}^{\infty}\sum_{m=-\ell}^{\ell} m\Im\left(\dot{h}_{\ell m}h^*_{\ell m}\right), \tag{1.42b}$$

where the asterisk denotes the complex conjugation and $\Im$ the imaginary part. For most practical applications, one can stop the summation at $\ell = 8$. However, depending on the accuracy required, one could consider even more multipoles. These are, for example, needed for long inspirals in the high mass ratio regime, see e.g. Ref. [108], where multipoles up to $\ell = 10$ were included in the radiation reaction.

1.3 Linear perturbations of Schwarzschild spacetime

In this section we discuss linear perturbations of the Schwarzschild solution $\bar{g}$, whose line element $ds^2 = \bar{g}_{\mu\nu}dx^\mu dx^\nu$ can be written in Schwarzschild coordinates as

$$ds^2 = -\left(1-\frac{2M}{r}\right)dt^2 + \left(1-\frac{2M}{r}\right)^{-1}dr^2 + r^2(d\theta^2 + \sin^2\theta d^2). \tag{1.43}$$

In the above metric, there are two manifest singularities, one at $r = 2M$, and the other at $r = 0$. The former is just due to the coordinate choice, and it is therefore said to be a coordinate singularity. The singularity at $r = 0$ is instead fundamental, and cannot be removed with a suitable coordinate transformation. The Riemann tensor is indeed singular in this case, while it was not for $r = 2M$. Still, the $r = 2M$ radius plays an important role in the physical interpretation of this metric, since it is the radius of the event horizon, i.e. the region of spacetime causally disconnected from the outside region. Note that, from Birkhoff's theorem, the Schwarzschild solution is the most general spherically symmetric vacuum solution.

Linear perturbations of the Schwarzschild solution have been first studied by Regge and Wheeler for the axial-parity case [109], and by Zerilli for the polar one [110]. In both cases, the master equations for the perturbation have been found by a suitable gauge-fixing. We will instead briefly discuss a gauge-invariant approach proposed by Moncrief [111]. We start by considering a metric perturbation $h_{\mu\nu}$ such that the total metric is

$$g_{\mu\nu} = \bar{g}_{\mu\nu} + h_{\mu\nu}, \tag{1.44}$$

where $|h_{\mu\nu}| \ll |\bar{g}_{\mu\nu}|$. The key point to obtain the master equation for the perturbations without any coordinate choice [112–114] is to note that the Schwarzschild manifold can be written as the product $\mathcal{M} = M^2 \otimes S^2$, where M^2 is a Lorentzian 2-manifold with coordinates (t, r), and S^2 is the 2-sphere with angle coordinates (θ, ϕ). The waveform can be decomposed into odd-parity (axial) and even-parity (polar) multipoles. The odd modes transform as $h^{(o)} \to (-1)^{\ell+1}h^{(o)}$ under a parity transformation $(\theta, \phi) \to (\pi - \theta, \pi + \phi)$, while the even ones as $h^{(e)} \to (-1)^\ell h^{(e)}$. The metric perturbation can be written as

$$h_{\mu\nu} = \sum_{\ell=2}^{\infty}\sum_{m=-\ell}^{\ell}\left[\left(h^{\ell m}_{\mu\nu}\right)^{(o)} + \left(h^{\ell m}_{\mu\nu}\right)^{(e)}\right]. \tag{1.45}$$

Similarly, one can proceed to decompose in odd and even parity perturbations the stress-energy tensor that generates the perturbation,

$$t_{\mu\nu} = \sum_{\ell=2}^{\infty}\sum_{m=-\ell}^{\ell}\left[\left(t^{\ell m}_{\mu\nu}\right)^{(o)} + \left(t^{\ell m}_{\mu\nu}\right)^{(e)}\right]. \tag{1.46}$$

The components of these objects can be written using terms that live on M^2, scalar spherical harmonics $Y^{\ell m}$, and their covariant derivatives (with respect to the 2-sphere metric). For example, the odd-parity term for the wave perturbation can be written as [114]

$$\left(h^{\ell m}_{\mu\nu}\right)^{(o)} = \begin{pmatrix} 0 & h^{\ell m,(o)}_{A} S^{\ell m}_{c} \\ h^{\ell m,(o)}_{A} S^{\ell m}_{c} & h^{\ell m} \nabla_{(d} S^{\ell m}_{c)} \end{pmatrix}. \tag{1.47}$$

In the above expression, $A = 0, 1$ is an index on M^2, $c, d = 2, 3$ are indices on S^2, and the parentheses indicate symmetrized indices. The definitions of the functions in Eq. (1.47) can be found in Ref. [114], but the crucial aspect is that $h^{\ell m,(o)}_{A}$ and $h^{\ell m}$ are functions of (t, r), while the covariant derivative ∇_c and $S^{\ell m}_{c}$ live on the 2-sphere. Once all the terms are properly decomposed, we can write the linearized EFE

$$\bar{R}_{\mu\nu} + R_{\mu\nu} - \frac{1}{2}\bar{g}_{\mu\nu} R = 8\pi t_{\mu\nu}, \tag{1.48}$$

where the Ricci tensor $R_{\mu\nu}$ is the one related to the metric perturbation $h_{\mu\nu}$. Note that $\bar{R}_{\mu\nu} = 0$ because Schwarzschild is a vacuum solution, so the equations reduce to

$$R_{\mu\nu} - \frac{1}{2}\bar{g}_{\mu\nu} R = 8\pi t_{\mu\nu}, \tag{1.49}$$

where the Ricci components are given by

$$R_{\mu\nu} = \nabla_\rho \Gamma^\rho_{\mu\nu} - \nabla_\nu \Gamma^\rho_{\mu\rho}, \tag{1.50}$$

and the Christoffel symbols are analogous to Eq. (1.24), but with the Schwarzschild inverse metric $\bar{g}^{\rho\sigma}$ instead of the Minkowskian inverse metric $\eta^{\rho\sigma}$.

By defining various gauge-invariant combinations of multipoles, Eqs. (1.49) can be rewritten in a compact form. For the odd-parity perturbation, one can define [114] (we drop the (ℓ, m) indices for notation simplicity)

$$k_A \equiv h_A - \nabla_A h + 2h\frac{\nabla_A r}{r}, \tag{1.51}$$

where ∇ is the covariant derivative on the M^2 manifold. One can then choose the gauge-invariant master function

$$\Psi^{(o)}(t, r) = \frac{r^3}{\Lambda - 2}\epsilon^{AB}\nabla_B\left(\frac{k_A}{r^2}\right) = \frac{r}{\Lambda - 2}\left[\partial_t h^{(o)}_1 - r^2\partial_r\left(\frac{h^{(o)}_0}{r^2}\right)\right], \tag{1.52}$$

where $\Lambda = \ell(\ell + 1)$, and ϵ_{AB} is the antisymmetric volume form on M^2, so that $\epsilon^{00} = 0$, $\epsilon^{01} = -\epsilon^{10} = -1$. Inserting Eq. (1.52) in Eq. (1.49) leads to the non-homogeneous Regge-Wheeler equation

$$\partial_t^2\Psi^{(o)} - \partial_{r_*}^2\Psi^{(o)} + V^{(o)}_\ell \Psi^{(o)} = S^{(o)}, \tag{1.53}$$

where we have used the tortoise coordinate

$$r_* = r + 2M\ln\left(\frac{r}{2M} - 1\right), \tag{1.54}$$

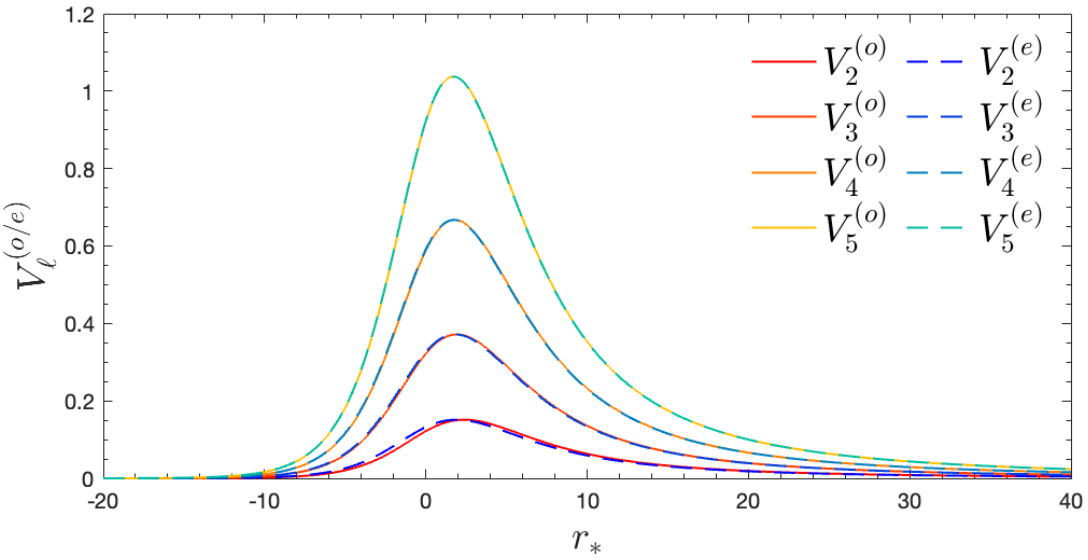

Figure 1.1: Regge-Wheeler and Zerilli potentials up to $\ell = 5$.

and $V_\ell^{(o)}$ is the Regge-Wheeler potential, which reads

$$V_\ell^{(o)} \equiv \left(1 - \frac{2M}{r}\right)\left(\frac{\Lambda}{r^2} - \frac{6M}{r^3}\right). \tag{1.55}$$

The explicit form of the source term $S^{(o)}$ can be found in Eq. (24) of Ref. [114].

For even-parity perturbations it is possible to find an equation analogous to Eq. (1.53), but with potential

$$V_\ell^{(e)} = \left(1 - \frac{2M}{r}\right)\frac{\Lambda(\Lambda-2)^2 r^3 + 6(\Lambda-2)^2 M r^2 + 36(\Lambda-2)M^2 r + 72M^3}{r^3\left[(\Lambda-2)r + 6M\right]^2} \tag{1.56}$$

and generic source term given by Eq. (34) of Ref. [114]. Therefore, it is possible to write the Regge-Wheeler and Zerilli (RWZ) equations in just one line as

$$\partial_t^2 \Psi^{(\mathrm{o/e})} - \partial_{r_*}^2 \Psi^{(\mathrm{o/e})} + V_\ell^{(\mathrm{o/e})}\Psi^{(\mathrm{o/e})} = S^{(\mathrm{o/e})}, \tag{1.57}$$

where the only differences are the potentials $V_\ell^{(\mathrm{o/e})}$ written in Eq. (1.55) and Eq. (1.56), and the source terms $S^{(\mathrm{o/e})}$. The RWZ master functions are strictly linked to the waveform strain of Eq. (1.39) by the asymptotic relation [114]

$$h_+ - ih_\times = D_L^{-1}\sum_{\ell,m}\sqrt{\frac{(\ell+2)!}{(\ell-2)!}}\left(\Psi_{\ell m}^{(e)} + i\Psi_{\ell m}^{(o)}\right){}_{-s}Y_{\ell m}(\Theta,\Phi) + \mathcal{O}\left(\frac{1}{r^2}\right). \tag{1.58}$$

It is also interesting to note that while the analytic expressions of $V^{(o)}$ and V^ℓ are quite different, both potentials have the same asymptotic expansions, both at infinity, where

$$V_\ell^{(\mathrm{o/e})} \simeq \frac{\ell(\ell+1)}{r^2}, \quad r \to \infty, \tag{1.59}$$

and near the event horizon ($r_* \to -\infty$), where they decay exponentially in the tortoise coordinate r_*. Moreover, the two potentials are also quite similar from the numerical point of view for any r_*, especially for large ℓ, as shown in Fig. 1.1.

The RWZ equations can be also written in the frequency domain as

$$\frac{d^2}{dr_*{}^2}\tilde{\Psi}^{(\mathrm{o/e})} + \left(\omega^2 - V_\ell^{(\mathrm{o/e})}\right)\tilde{\Psi}^{(\mathrm{o/e})} = \tilde{S}^{(\mathrm{o/e})}, \tag{1.60}$$

where we have used the Fourier Transform of the master function

$$\tilde{\Psi}^{(\mathrm{o/e})}(\omega, r) = \int_{-\infty}^{+\infty} dt \Psi(t, r) e^{i\omega t}, \tag{1.61}$$

and similarly for the source term. It is interesting to note that Eq. (1.60) is a Schrödinger equation in the presence of a potential barrier. In this formulation, we can impose boundary conditions requiring that there are no ingoing perturbations from infinity and that there are no outgoing perturbations from the event horizon, so that

$$\Psi \sim \int_{-\infty}^{\infty} d\omega A^{\mathrm{out}}_{\ell m}(\omega) e^{-i\omega(t-r_*)}, \quad r_* \to +\infty, \tag{1.62a}$$

$$\Psi \sim \int_{-\infty}^{\infty} d\omega A^{\mathrm{in}}_{\ell m}(\omega) e^{-i\omega(t+r_*)}, \quad r_* \to -\infty, \tag{1.62b}$$

where $A^{\mathrm{in/out}}_{\ell m}(\omega)$ are determined by the initial conditions. Note that we cannot impose $A^{\mathrm{in}}_{\ell m}(\omega) = A^{\mathrm{out}}_{\ell m}(\omega) = 0$, because this would be equivalent to searching for bound states that cannot exist since the Regge-Wheeler and Zerilli potentials are positive everywhere.

Now let us suppose to have a disturbance at $t = 0$ localized at x', and an observer at x. Then the homogeneous RWZ equations lead to a signal that has three clearly separated contributions: a precursor related to the initial localized disturbance that arrives at the observer at $t \simeq x - x'$, a superposition of dumped sinusoids with discrete complex frequencies, called quasi-normal modes (QNMs), that arrives at the observed at $t \simeq x + x'$, and a power-law tail that becomes observable when the QNM signal has exponentially decayed. While we have not discussed the procedure that leads to this solution, the fact that the QNM frequencies are complex can be understood considering that black holes are dissipative systems, since they emit GWs and have horizon absorption. In general, the QNM signal for a certain (ℓ, m) mode can be written as

$$\Psi^{\mathrm{QNM,Schw}}_{\ell m} = \sum_{n=1}^{\infty} \left(C_{\ell m n} e^{-\sigma^{+}_{\ell n}\tau} + C_{\ell -m n} e^{-\sigma^{-}_{\ell n}\tau} \right), \tag{1.63}$$

where $C_{\ell m n}$ are complex constants, τ is the retarded time rescale with the beginning time of the QNM ringing, i.e. $\tau = t - t_0^{\mathrm{QNM}}$, and $\sigma^{\pm}_{\ell n} = \alpha_{\ell n} \pm i\omega_{\ell n}$ are the QNM frequencies. While the constant amplitudes depend on the nature of the perturbation, the QNM frequencies depend only on the background metric (that is, on the mass parameter M). Note that due to the spherical symmetry of the background, we have that the QNM frequencies do not depend on the number m, and therefore the frequencies of co-rotating modes ($\sigma^{+}_{\ell n}$) and counter-rotating modes ($\sigma^{-}_{\ell n}$) differ only by a complex conjugation. Some QNM frequencies, both for nonspinning ($\hat{a} = 0$)and spinning ($\hat{a} \neq 0$) black holes (that we discuss in the next section), are shown in Fig. 1.2. The fundamental mode ($n = 1$) is the one with lowest damping coefficient $\alpha_{\ell 1}$ and highest oscillating frequency $\omega_{\ell 1}$. The overtones have smaller oscillation frequencies and are damped faster.

1.4 Linear perturbations of Kerr spacetime

In order to describe the spacetime around a rotating black hole, we need to consider the axis-symmetric Kerr metric [115]. The line element in Boyer-Lindquist coordinates reads

$$ds^2 = -\left(1 - \frac{2Mr}{\Sigma}\right) dt^2 + \frac{\Sigma}{\Delta} dr^2 + \Sigma d\theta^2 + \left(r^2 + a^2 + \frac{2Mra^2 \sin^2\theta}{\Sigma}\right) \sin^2\theta d\varphi^2 - a \sin^2\theta \frac{4Mr}{\Sigma} dt d\varphi, \tag{1.64}$$

where a is the Kerr parameter, and

$$\Sigma = r^2 + a^2 \cos^2\theta, \tag{1.65}$$

$$\Delta = r^2 + a^2 - 2Mr. \tag{1.66}$$

The polar angle $\theta \in [0, \pi]$ is zero at the north pole and $\pi/2$ in the equatorial plane. As can be seen from Eq. (1.64), the Kerr metric depends on only two parameters: the mass of the black hole M , and the spin a, which has the dimension of a length. The angular momentum of the black hole is thus given by $J = aM$. We will often use the dimensionless spin parameter, which is simply defined by $\hat{a} = a/M$. Not all the values of $\hat{a}$ are allowed; in fact the spin parameter is constrained to be in the range $\hat{a} \in [0, 1]$ to avoid naked singularities. A black hole with $\hat{a} = 1$ is said to be extremal, but in this work we will always consider sub-extremal black holes, i.e. $\hat{a} < 1$. Moreover, we will often consider particles orbiting in the equatorial plane of a spinning black hole; in this case, we assign negative values to the Kerr spin when it is anti-aligned with the orbital angular momentum, so that we can have $\hat{a} \in (-1, 1)$.

We now turn our attention to the singularities of this metric. By looking at Eq. (1.64), it is evident that the equation $\Delta = 0$ leads to two singularities for the coordinate radii

$$r_{H_\pm} = M \pm \sqrt{M^2 - a^2}. \tag{1.67}$$

However, the Riemann tensor is not singular at $r = r_{H_\pm}$, so these are just two coordinate singularities and identify the inner and outer horizons. Eq. (1.67) justifies the above discussion on the constraints on the Kerr spin, since $a > M$ would give complex values for $r_{H_\pm}$. Note that the condition $r = r_{H_\pm}$ does not imply spherical horizons, since the surface induced by fixing $t = const.$ and $r = r_{H_\pm}$ is not a 2-sphere. The only fundamental singularity occurs when $\Sigma = 0$, or in other words, on the ring identified by $(r, \theta) = (0, \pi/2)$. Another interesting feature of the Kerr metric is the frame-dragging, that is strictly linked to the non-vanishing component $g_{t\varphi}$.

We now discuss linear perturbations of Kerr spacetime. When we studied in Sec. 1.3 the linear perturbations in the Schwarzschild case, the key observation was the possibility to write the spacetime as the product of a Lorentzian 1+1 manifold and a 2-sphere. This symmetry no longer exists in axis-symmetric Kerr spacetime, and therefore we cannot follow the same path. The master equation for perturbations in Kerr spacetime found by S. Teukolsky [116] is indeed based on the Newman-Penrose formalism and is, in a sense that we will clarify later, a perturbation of the curvature rather than of the metric. We start by recalling that in the Newman-Penrose formalism, one has to consider a tetrad, which is a set of four linearly independent 4-vectors $z^\mu_a \equiv (l^\mu, n^\mu, m^\mu, \bar{m}^\mu)$, where l^μ and

n^μ are real and $\bar{m}^\mu$ is the complex conjugate of m^μ. It is useful to choose them to be null-vectors ($g_{\mu\nu} z_a^\mu z_a^\nu = 0$), and to require that

$$g_{\mu\nu} m^\mu \bar{m}^\nu = 1, \quad g_{\mu\nu} l^\mu n^\nu = -1, \tag{1.68}$$

while all the other scalar products vanish. The inverse metric can be rewritten as

$$g^{\mu\nu} = m^\mu \bar{m}^\nu + m^\nu \bar{m}^\mu - l^\mu n^\nu - l^\nu n^\mu. \tag{1.69}$$

The validity of the last equation can be verified by multiplying both sides by the elements of the tetrad. A widely used tetrad is the Kinnerslay one, which written in Boyer-Lindquist reads

$$l^\mu = \frac{1}{\Delta}(r^2 + a^2, \Delta, 0, a), \tag{1.70a}$$

$$n^\nu = \frac{1}{2\Sigma^2}(r^2 + a^2, -\Delta, 0, a), \tag{1.70b}$$

$$m^\mu = \frac{1}{\sqrt{2}} \frac{1}{r + ia\cos\theta} \left(ia\sin\theta, 0, 1, \frac{i}{\sin\theta} \right). \tag{1.70c}$$

We can then project any tensor on a tetrad. We can proceed to project the Weyl tensor $C_{\mu\nu\rho\sigma}$, that is the traceless component of the Riemann tensor of Eq. (1.2) and reads

$$\begin{aligned} C_{\mu\nu\rho\sigma} = R_{\mu\nu\rho\sigma} &- \frac{1}{2}\left(g_{\mu\rho} R_{\nu\sigma} - g_{\mu\sigma} R_{\nu\rho} - g_{\nu\rho} R_{\mu\sigma} + g_{\nu\sigma} R_{\nu\rho} \right) \\ &+ \frac{1}{6} R \left(g_{\mu\rho} g_{\nu\sigma} - g_{\mu\sigma} g_{\nu\rho} \right). \end{aligned} \tag{1.71}$$

It is interesting to note that the Weyl tensor is completely determined by the Ricci tensor in dimensions $d \leq 3$, so it is non-vanishing in vacuum only for 4 or higher-dimensional spacetimes. Then we can define the Weyl scalars by projecting the Weyl tensor on a null-tetrad. We are particularly interested in

$$\Psi_0 = C_{\mu\nu\rho\sigma} l^\mu m^\nu l^\rho m^\sigma, \tag{1.72a}$$

$$\Psi_4 = C_{\mu\nu\rho\sigma} n^\mu \bar{m}^\nu n^\rho \bar{m}^\sigma, \tag{1.72b}$$

since these two scalars can be linked to the perturbation in the TT-gauge as measured at infinity, thanks to the fact that the Kerr metric is asymptotically flat. Quantitatively we have

$$R_{0i0j} = -\frac{1}{2} \ddot{h}_{ij}^{TT}, \tag{1.73a}$$

$$\Psi_0 = -\frac{1}{2} \left(\ddot{h}_+ + i\ddot{h}_\times \right), \tag{1.73b}$$

$$\Psi_4 = -\frac{1}{8} \left(\ddot{h}_+ - i\ddot{h}_\times \right), \tag{1.73c}$$

while $\Psi_1 = \Psi_2 = \Psi_3 = 0$. We can thus recover the strain of Eq. (1.39) from a double time-integration of Ψ_4.

As anticipated, the Newman-Penrose formalism is at the base of the computation performed by S. Teukolsky to find the master equation for linear perturbations in Kerr spacetime [116]. More precisely, the perturbation is introduced in the elements of the

tetrad as $\boldsymbol{z}_a = \boldsymbol{z}_a^A + \boldsymbol{z}_a^B$, where the index A denotes the Kerr unperturbed quantities and B the perturbed ones; then all the Newman-Penrose quantities can be written as $\Psi_2 = \Psi_2^A + \Psi_2^B$, etc. Note that with the Kinnerslay tetrad of Eq. (1.70), we have $\Psi_0^A = \Psi_1^A = \Psi_3^A = \Psi_4^A = 0$. The master equation for the test field Ψ in Boyer-Lindquist coordinates reads

$$\begin{aligned}
&\left[\frac{\left(r^2+a^2\right)^2}{\Delta} - a^2\sin^2\theta\right]\partial_t^2\psi + \frac{4Mar}{\Delta}\partial_t\partial_\varphi\psi + \left[\frac{a^2}{\Delta} - \frac{1}{\sin^2\theta}\right]\partial_\varphi^2\psi \\
&- \Delta^{-s}\partial_r\left(\Delta^{s+1}\partial_r\psi\right) - \frac{1}{\sin\theta}\partial_\theta\left(\sin\theta\partial_\theta\psi\right) - 2s\left[\frac{a\left(r-M\right)}{\Delta} + i\frac{\cos\theta}{\sin^2\theta}\right]\partial_\varphi\psi \\
&- 2s\left[\frac{M\left(r^2-a^2\right)}{\Delta} - r - ia\cos\theta\right]\partial_t\psi + \left(s^2\cot^2\theta - s\right)\psi = 4\pi\Sigma T,
\end{aligned} \tag{1.74}$$

where s is the spin-weight of the test field and T is the source term, which also depends on s. The value of s is linked to different fields: $s = 0$ for scalar perturbations, $s \pm 1/2$ for neutrino fields, $s = \pm 1$ for electromagnetic perturbations, and $s = \pm 2$ for the gravitational case. In this work, we are interested in the $s = -2$ case, so that $\psi = (r - ia\cos\theta)^4\Psi_4$, and T is given by Eq. (2.15) of Ref. [116]. Note that it is not possible to exploit spherical harmonics to decompose Eq. (1.74), as we are dealing with an axisymmetric spacetime rather than a spherical one. However, despite its complicated look, it is possible to separate Eq. (1.74) by writing the test field as

$$\psi^{(s)} = \int_{-\infty}^{\infty} d\omega \sum_{\ell=2}^{\infty}\sum_{m=-\ell}^{\ell} R_{\ell m}^{(s)}(r,\omega)S_{\ell m}^{(s)}(\theta,\omega)e^{im\varphi}e^{-i\omega t}. \tag{1.75}$$

Then in the vacuum case we can write two separate equations. For the angular part, $S_{\ell m}^{(s)}$, we find

$$\begin{aligned}
&\frac{1}{\sin\theta}\partial_\theta\left(\sin\theta\partial_\theta S_{\ell m}^{(s)}(\theta,\omega)\right) + \left[a^2\omega^2\cos^2\theta - \frac{m^2}{\sin^2\theta} - 2sa\omega\cos\theta\right. \\
&\left. -2sm\frac{\cos\theta}{\sin^2\theta} - s^2\cot^2\theta + s + A_{\ell m}^{(s)}\right]S_{\ell m}^{(s)}(\theta,\omega) = 0,
\end{aligned} \tag{1.76}$$

where $A_{\ell m}^{(s)} = A_{\ell m}^{(s)}(\omega)$ is the separation constant and is ω-dependent. Due to this dependency, the separation in radial and angular parts can be performed only in the frequency domain. The $S_{\ell m}^{(s)}$ functions are denoted as spin-weighted *spheroidal* harmonics, and are the natural angular basis for the perturbation in Kerr spacetime. While for $\omega = 0$ they reduce to the spin-weighted *spherical* harmonics, in the sense that ${}_sY_{\ell m}(\theta,\varphi) = S_{\ell m}^{(s)}(\theta)e^{im\varphi}$, in the general case the two bases differ. This fact gives rise to the mode-mixing between modes with the same m but different ℓ [117]. This effect is particularly evident in the ringdown signal generated by the infalling of a particle in a spinning black hole with $\hat{a} < 0$, as discussed in Ref. [118]. Instead, for the radial part $R_{\ell m}^{(s)}$ we have the equation

$$\begin{aligned}
&\Delta^{-s}\partial_r\left(\Delta^{s+1}\partial_r\right)R_{\ell m}^{(s)}(r,\omega) + \\
&\left[\frac{K^2}{\Delta} - \frac{is}{\Delta}\left(2r - R_S\right)K + 4is\omega r - \lambda_{\ell m}^{(s)}\right]R_{\ell m}^{(s)}(r,\omega) = 0,
\end{aligned} \tag{1.77}$$

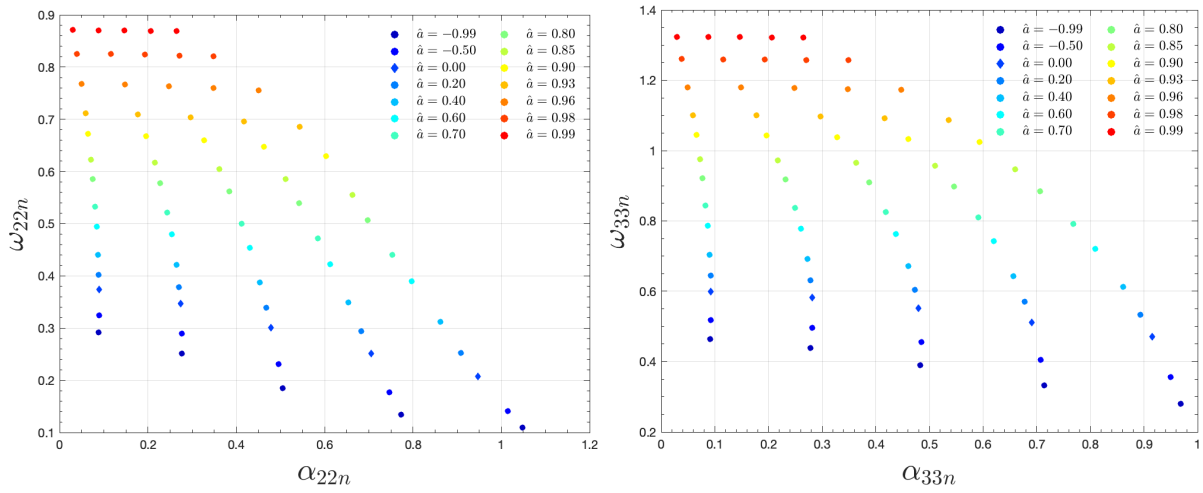

Figure 1.2: QNM frequencies $\sigma_{\ell mn} = \alpha_{\ell mn} + i\omega_{\ell mn}$ for the multipoles $(\ell, m) = (2, 2), (3, 3)$. We show the fundamental mode (leftmost points) and the first four overtones for different values of Kerr spin $\hat{a}$. QNMs frequencies for negative values of $\hat{a}$ are computed as $\sigma_{\ell mn}(-\hat{a}) = \sigma_{\ell -mn}(\hat{a})$. Schwarzschild frequencies are highlighted with diamond markers.

where $K = \left(r^2 + a^2\right)\omega - am$, and $\lambda^{(s)}_{\ell m} = A^{(s)}_{\ell m} + a^2\omega^2 - 2am\omega$. Solving this radial equation, one can find the values of the QNM frequencies for Kerr black holes [119, 120]. However, since we are no longer in spherical symmetry, the pure QNM solution is more complicated than the Schwarzschild one shown in Eq. (1.63), and reads

$$\Psi^{\rm QNM,Kerr}_{\ell m} = \sum_{n=1}^{\infty} \left(C_{\ell mn} e^{-\sigma_{\ell mn}\tau} + C_{\ell -mn} e^{-\sigma^*_{\ell -mn}\tau} \right), \tag{1.78}$$

where the QNM frequencies $\sigma_{\ell mn} = \alpha_{\ell mn} + i\omega_{\ell mn}$ also depend on the azimuthal number m, and the co-rotating and counter-rotating QNM frequencies are related by $\sigma_{\ell -mn}(\hat{a}) = \sigma_{\ell mn}(-\hat{a})$. This dependence on the azimuthal number m leads to more complex waveform phenomenologies, as shown, for example, in Ref. [118]. Some QNM frequencies are shown in Fig. 1.2 for different values of the dimensionless spin parameter $\hat{a}$. Also in the spinning case, the fundamental harmonic is the less damped one and is also the one with the higher oscillation frequency. However, when the spin increases, the overtones tend to live longer with respect to slower rotating cases, and their oscillation frequencies get closer to the fundamental harmonics. We conclude our discussion by recalling that a power-law tail overcomes the QNM signal at late times also in the spinning case, see e.g. Ref. [121].

1.5 Numerical solutions in the time-domain

In the previous sections, we have discussed the RWZ equations, which describe linear perturbations in Schwarzschild, and the Teukolsky equation, which describes linear perturbation in Kerr. We have also briefly discussed their solution in the homogeneous case, i.e. without source term. We are now interested in their solution in the inhomogeneous case, where the source term is the one of a particle orbiting around the black hole. To this end, we will use the numerical time-domain codes `RWZHyp` [122–125] and `Teukode` [126], which were coded years ago, before the beginning of this thesis. Despite their longevity, these two codes are still very useful tools to understand the physics of

gravitational waves. Note that in this section we assume that the dynamics of the particle has been already computed. We will discuss in detail later how these dynamics are obtained, but we anticipate that they can be obtained by time-integrating numerically some Hamilton equations using standard numerical techniques for ODEs, such as a 4th-order Runge-Kutta algorithm with adaptive step-size.

1.5.1 `RWZHyp`: Regge-Wheeler and Zerilli equations

We now discuss in some detail the code `RWZHyp` [122–125], which we will use to solve the RWZ equations (1.57) in the presence of a source-particle term. The functional form of the latter is [127–129]

$$S_{\ell m}^{(\mathrm{o/e})} = G_{\ell m}^{(\mathrm{o/e})}(r,t)\delta\left(r_* - r_*(t)\right) + F_{\ell m}^{(\mathrm{o/e})}(r,t)\partial_{r_*}\delta\left(r_* - r_*(t)\right), \tag{1.79}$$

where $r_*(t)$ is the tortoise coordinate of the particle and δ is the Dirac delta. Therefore, we have that the source terms are discontinuous at the particle location. While this could seem problematic, it has been shown that approximating the Dirac delta with a narrow Gaussian function ($\sigma \ll M$) produces reliable results, allowing the computation of the source term along any particle dynamics.

Another complication is that the tortoise radial coordinate is not compact, since $r_* \in (-\infty, \infty)$, while we would like to have the whole causally-connected spacetime in the computational domain. Moreover, from Eq. (1.58) it is clear that in order to have an accurate strain, we need to extract $\Psi_{\ell m}^{(\mathrm{o/e})}$ at a distance as large as possible. For this reason, a hyperboloidal layer approach [130] is employed in order to include future null infinity in the computational domain, and thus extract the waveform multipoles $\Psi_{\ell m}^{(\mathrm{o/e})}$ at infinity [123]. The coordinates used are thus $(\tau, \rho) \in \mathbb{R}^+ \times [R_*^-, S^+]_{R_*^+}$, and they coincide with (t, r_*) in the compact region $[R_*^-, R_*^+]$. This latter domain has to be chosen in order to include all the motion of the particle; a typical choice for quasi-circular inspirals is $R_*^\pm = \pm 50$. At $\rho = r_* = R_*^+$ we have the interface between the grid that contains the motion of the particle and the outer hyperboloidal layer. Here the compactification variable $\rho(r_*)$ maps $[R_*^+, \infty)$ in $[R_*^+, S]$. The time Killing vector (that is the vector associated with the stationarity of the spacetime) is left invariant in the two coordinate systems, so that the condition $\partial_t = \partial_\tau$ holds. As a consequence, the new time coordinate can be rescaled by a height function that depends only on the radial coordinate, i.e. $\tau = t - h(r_*)$. In order to leave the representation of the outgoing null ray invariant, one also asks for $t - r_* = \tau - \rho$. This latter condition determines a future hyperboloidal foliation, provided that the choice of compactification is sufficiently smooth. The surface $\rho = S$ corresponds to future null infinity and is where we extract $\Psi_{\ell m}^{(\mathrm{o/e})}$. For a quasi-circular configuration, a typical choice is $S^+ = 70$. As outlined in Ref. [124], the method of the hyperboloidal later could also used to include the horizon in the computational domain, but we do not use this method in this thesis.

To conclude, we mention that the code solves the RWZ equation as a first-order-in-time second-order-in-space system with the method of lines and a Runge-Kutta 4th order scheme. The discretization of the source term on $[R_*^-, S]_{R_*^+}$ is performed with a 4th order finite-difference scheme with central stencils (sided on the boundary). At future null infinity there are no boundary prescriptions, while maximally dissipative outgoing conditions are used at the inner boundary [131].

1.5.2 `Teukode` : Teukolsky equation

For the more general case of linear perturbations of a spinning black hole, we have to numerically solve the Teukolsky equation. However, the expression reported in Eq. (1.74) is written in Boyer-Lindquist coordinates, while in numerical computations other coordinates are more suitable. In particular, as we have discussed in the RWZ case, it is useful to compactify the spacetime, so that future null infinity is included in the computational domain, and the Weyl scalar ψ_4 can be extracted at infinity. Moreover, it is useful to have coordinates that extend up to (and even beyond) the event horizon. All these features are available in the time-domain code `Teukode` [126], that we have used in many papers that are at the base of this thesis [1, 3–5]. The Teukolsky equation can be then rewritten, in general, as [132]

$$\begin{aligned} &C_{\tau\tau}\partial_{\tau\tau}\Psi_m + C_{\tau\rho}\partial_\rho\partial_\tau\Psi_m + C_{\rho\rho}\partial_{\rho\rho}\Psi_m + C_{\theta\theta}\partial_{\theta\theta}\Psi_m + \\ &C_\tau\partial_\tau\Psi_m + C_\rho\partial_\rho\Psi_m + C_\theta\partial_\theta\Psi_m + C_0\Psi_m = S_s \end{aligned} \tag{1.80}$$

where $C(\rho, \theta, m, s)$ are coefficients that depend on the coordinates chosen, on the spin weight s and on the azimuthal number m, Ψ_m is the m-Fourier mode of the Weyl scalar (Ψ_4 if we choose $s = -2$), and S_s is the source term. Note that also in this case, the particle-source term contains a Dirac delta. This term is treated with a narrow Gaussian function, as discussed in the RWZ case. As we will show when discussing the inspiral, plunge, and merger of test particles, the waveform integrated from the Weyl scalar extracted from `Teukode` simulations is in agreement with the one computed using `RWZHyp`. We will use the Hawking-Hartle tetrad and hyperboloidal-horizon penetrating coordinates with scri-fixing at $S = 10$. Note that with the latter coordinate choice, future null infinity and the event horizon are in the computational domain. Therefore, we do not need a coordinate transformation to include future null infinity in the computational domain, as opposed to the case of `RWZHyp` where we need to perform a suitable coordinate transformation at R^+_* (see discussion in Sec. 1.5.1).

1.6 Time-like geodesics in black hole geometries

We conclude this chapter by briefly discussing the motion of test mass particles around spinning black holes, ignoring for the moment the back-reaction on the dynamics due to GW emission. In other words, we briefly discuss time-like geodesics in Kerr. This section is intended to be preparatory to Sec. 3.1, where we will discuss planar eccentric geodesic in Kerr, and also non-conservative (and thus more realistic) test mass dynamics.

1.6.1 Integrals of motion in Kerr spacetime

We have already seen the geodesic equation (1.22), but here we follow a different approach to study geodesics in Kerr spacetime. We start by defining the Lagrangian

$$\mathcal{L} = \frac{1}{2} g_{\mu\nu} \frac{dx^\mu}{d\lambda} \frac{dx^\nu}{d\lambda}, \tag{1.81}$$

where λ is a generic affine parameter. We can now choose an affine parameter τ such that $2\mathcal{L} = \mu^2$, where $\mu^2 = 0$ for null geodesics and $\mu^2 = 1$ for time-like geodesics. Note that this choice means that we are considering μ-normalized momenta. We also denote

the derivatives with respect to this parameter with a dot. Straightforward calculations show that the associated Euler-Lagrange equations

$$\frac{d}{d\tau}\left(\frac{\partial \mathcal{L}}{\partial \dot{x}^\mu}\right) - \frac{\partial \mathcal{L}}{\partial x^\mu} = 0 \tag{1.82}$$

are equivalent to Eq. (1.22). This formulation allows us to compute the canonical momenta $p_\mu \equiv \partial\mathcal{L}/\partial\dot{x}^\mu$, and thus to identify two constants of motion, namely the energy $\hat{E} \equiv -p_t = -\frac{\partial \mathcal{L}}{\partial t}$, and the angular momentum $\hat{L} \equiv p_\varphi = \frac{\partial \mathcal{L}}{\partial \dot{\varphi}}$. The hat indicates that the energy and the angular momentum are μ normalized, as a consequence of the choice $\mu^2 = 1$. The two quantities, together with μ^2, are the first three constants of motion. A fourth constant of motion, the Carter constant $\mathcal{C}$, appears quite naturally if one writes explicitly the Hamilton-Jacobi equation [133]. To show this, we start by recalling that the Hamiltonian $\mathcal{H}$ can be obtained from the Lagrangian $\mathcal{L}$ via a Legendre transformation

$$\mathcal{H}(\boldsymbol{x}, \boldsymbol{p}) = p_\mu \dot{x}^\mu - \mathcal{L}(\boldsymbol{x}, \dot{\boldsymbol{x}}). \tag{1.83}$$

From the definition of the Lagrangian in Eq. (1.81), and from the definition of canonical momenta, it follows that $\dot{x}^\mu = g^{\mu\nu} p_\nu$, and thus Eq. (1.83) becomes

$$\mathcal{H} = \frac{1}{2} g^{\mu\nu} p_\mu p_\nu. \tag{1.84}$$

We now want to construct a generating function of a canonical transformation $(\boldsymbol{x}, \boldsymbol{p}) \leftrightarrow (\boldsymbol{X}, \boldsymbol{P})$ that makes the new Hamiltonian $\tilde{\mathcal{H}}(\boldsymbol{X}, \boldsymbol{P})$ identically vanish, so that the new canonical coordinates and momenta are constant

$$\dot{X}^\mu = \frac{\partial \tilde{\mathcal{H}}}{\partial P_\mu} = 0, \quad \dot{P}_\mu = \frac{\partial \tilde{\mathcal{H}}}{\partial X^\mu} = 0. \tag{1.85}$$

Then we define the generating function $S = S(\tau, \boldsymbol{x}, \boldsymbol{P})$ of the canonical transformation such that $\boldsymbol{p}$ and $\boldsymbol{X}$ are given by

$$p_\mu = \frac{\partial S}{\partial x^\mu}, \quad X^\mu = \frac{\partial S}{\partial P^\mu}. \tag{1.86}$$

Then the generating function satisfies the Hamilton-Jacobi equation

$$\frac{\partial S}{\partial \tau} + \mathcal{H}(x^\mu, \frac{\partial S}{\partial x^\mu}) = 0 \tag{1.87}$$

If we now consider that we have already found three (manifest) integrals of motion, we can provide an ansatz for S,

$$S = -\frac{1}{2}\mu^2 \tau - \hat{E} t + \hat{L}\varphi + f(r) + g(\theta), \tag{1.88}$$

where $f(r)$ and $g(\theta)$ are unknown functions; note that the conditions $\partial S/\partial x^\mu = p_\mu$ for t and φ are automatically satisfied. If we now insert the ansatz (1.88) and the Hamiltonian written in terms of the inverse Kerr metric (as in Eq. (1.84)) in the Hamilton-Jacobi equation (1.87), we can find an equation of the type $h(r) + h(\theta) = 0$. As a consequence, both $h(r)$ and $h(\theta)$ must be separately constant. We can thus define the Carter constant as $\mathcal{C} \equiv h(\theta) = -h(r)$. The generating function reads

$$S = -\frac{1}{2}\mu^2 \tau - \hat{E} t + \hat{L}\varphi + \int \frac{\sqrt{R}}{\Delta} dt + \int \sqrt{\Theta} d\theta, \tag{1.89}$$

where we have defined

$$\Theta(\theta) = \mathcal{C} + \cos^2\theta \left[a^2 \left(\mu^2 + \hat{E}^2 \right) - \frac{1}{\sin^2\theta} \hat{L}^2 \right], \tag{1.90}$$

$$R(r) = \Delta \left[-\mathcal{C} + \mu^2 r^2 - \left(\hat{L} - a\hat{E} \right)^2 \right] + \left[\hat{E} \left(r^2 + a^2 \right) - \hat{L}a \right]^2. \tag{1.91}$$

We have thus found that any geodesic is identified by four integrals of motion: $(\mu, \hat{E}, \hat{L}, \mathcal{C})$. Note that μ is just a mass-normalization, so that each generic orbit in Kerr is practically specified by $(\hat{E}, \hat{L}, \mathcal{C})$. In the specific case of equatorial orbits, we have that the motion is planar, and therefore each equatorial orbit can be specified by just two constants of motion: $\hat{E}$ and $\hat{L}$.

1.6.2 Hamiltonian of a test mass

If we now write explicitly Eq. (1.84) for time-like geodesics in Schwarzschild, we find

$$\mathcal{H} = \frac{1}{2} \left(-\frac{\hat{E}^2}{A_0} + \frac{p_r^2}{B_0} + \frac{p_\varphi^2}{r^2} \right) = \frac{1}{2}, \tag{1.92}$$

where $A_0 = 1 - 2M/r$, $B_0 = A_0^{-1}$, and the last equality is a consequence of the Hamilton-Jacobi equation (1.87). We can thus re-arrange the terms and write

$$\hat{E}_{\rm Schw} = \sqrt{A_0 \left(1 + \frac{p_\varphi^2}{r^2} + \frac{p_r^2}{B_0} \right)}, \tag{1.93}$$

This is the equation for the μ-normalized energy of a test mass orbiting in Schwarzschild spacetime; note that also the momenta are μ-normalized. To further simplify the notation, we can rescale the coordinates and the angular momentum by M, so that the new coordinates and momenta are dimensionless. For clarity, if T, R, P_R and P_φ are the physical phase space variables, the rescaled ones, that we will use from now on, are $t = T/M$, $r = R/M$, $p_r = P_R/\mu$, and $p_\varphi = P_\varphi/(\mu M)$. With this notation, the Schwarzschild metric potential reads $A_0 = 1 - 2u$, where we have also introduced $u = 1/r$. We also define the conjugate momentum of the tortoise coordinate as $p_{r_*}^2 = \frac{A_0}{B_0} p_r^2$, which is regular at the event horizon, as opposed to p_r. Note that this definition is consistent with the one given in Eq. (1.54). While the notation A_0/B_0 might seem too pedantic in the Schwarzschild case, since $B_0 = A_0^{-1}$, it will be clear soon why we use this notation. Now, using this new notation and Eq. (1.93), we can write the μ-normalized Hamiltonian of a test particle in Schwarzschild as

$$\hat{H} = \sqrt{A_0 \left(1 + p_\varphi^2 u^2 \right) + p_{r_*}^2}. \tag{1.94}$$

Note that while the definition in Eq. (1.83) was true for any spacetime metric, the Hamiltonian defined in Eq. (1.94) has been found specifically for time-like geodesics in Schwarzschild, and we have explicitly used the fact that the time-variable t is cyclic in the Schwarzschild metric. Indeed, since we started from p_t, we are parametrizing the geodesics using the time-variable of the metric.

We now turn our attention to the Kerr case. As one can easily imagine, the generic Hamiltonian for a test particle in Kerr has a more involved structure with respect to the

Schwarzschild one, as can be seen from Eq. (2) of Ref. [134]. However, following Ref. [134] we can write the μ-normalized Hamiltonian for test particles along equatorial orbits in Kerr as

$$\hat{H}^{\rm eq}_{\rm Kerr} = \hat{H}^{\rm eq,orb}_{\rm Kerr} + \hat{H}^{\rm eq,SO}_{\rm Kerr} = \sqrt{A\left(1+\frac{p_\varphi^2}{r_c^2}\right)+p_{r_*}^2} + \frac{2\hat{a}p_\varphi}{r r_c^2}, \tag{1.95}$$

where the conjugate momenta of the tortoise coordinate is formally defined as in the Schwarzschild case,

$$p_{r_*}^2 = \frac{A}{B}p_r^2, \tag{1.96}$$

but now the metric potentials A and B read

$$A = \frac{1+2u_c}{1+2u}\left(1-2u_c\right) \ , \tag{1.97a}$$

$$B = \frac{1}{1-2u+\hat{a}^2u^2} \ . \tag{1.97b}$$

In the above definition we have used the centrifugal radius r_c, defined as

$$r_c^2 = r^2 + \hat{a}^2 + 2\frac{\hat{a}^2}{r}, \tag{1.98}$$

and its inverse $u_c = 1/r_c$. Notably, the orbital part of the Hamiltonian in Eq. (1.95), $\hat{H}^{\rm eq,orb}_{\rm Kerr}$, has the same structure as $\hat{H}_{\rm Schw}$ from Eq. (1.94), while the spin-orbit coupling $\hat{H}^{\rm eq,SO}_{\rm Kerr}$ is a new term that clearly vanishes in the absence of spin. We can now write the Hamilton equations associated with $\hat{H}^{\rm eq}_{\rm Kerr}$, that read

$$\dot{r} = \left(\frac{A}{B}\right)^{1/2}\frac{\partial \hat{H}^{\rm eq}_{\rm Kerr}}{\partial p_{r_*}}, \tag{1.99a}$$

$$\dot{\varphi} = \frac{\partial \hat{H}^{\rm eq}_{\rm Kerr}}{\partial p_\varphi} \equiv \Omega, \tag{1.99b}$$

$$\dot{p}_{r_*} = -\left(\frac{A}{B}\right)^{1/2}\frac{\partial \hat{H}^{\rm eq}_{\rm Kerr}}{\partial r}, \tag{1.99c}$$

$$\dot{p}_\varphi = 0, \tag{1.99d}$$

where we have also defined the orbital frequency as $\Omega \equiv \dot{\varphi}$. The solution of the above ODE system gives equatorial time-like geodesics in Kerr spacetime and can be easily obtained with a standard numerical solver. Being planar, these orbits are fully determined by two constants of motion. We will further discuss these orbits in Sec. 3.1.

Chapter 2

Coalescence of binary black holes

As anticipated, the coalescence of compact binaries, and in particular of binary black holes, is of primary interest to the gravitational wave physics community, since these systems generate the signals that we can detect with the interferometers of the LVK collaboration. More precisely, for binary black holes we are able to detect the last few orbits before the merger and the subsequent ringdown, while for binary neutron stars we can observe the late inspiral and the plunge, but not the signal from the after-merger, that is at frequencies beyond the current sensitivity band. In this chapter we focus, in particular, on the methods used to describe binary black holes, discussing in particular the EOB approach and numerical relativity simulations. However, note that both EOB models and NR simulations can be used to describe binary neutron stars, or even BH-NS mixed systems.

2.1 Approaches to the relativistic two-body problem

Due to the intricated structure of the EFE (1.1), it is not possible to find an exact analytical solution for the coalescence of binary black holes, so we have to rely on numerical simulations or analytical approximations.

The numerical approach is known as numerical relativity (NR), and exploits supercomputers to solve the EFE written in a 3+1 decomposition. Due to technical and computational difficulties, the first numerical evolutions of binary black holes up to the merger were achieved only in 2005 [76, 77]. Today many groups can produce numerical evolutions of binary black holes, both for quasi-circular and more complicated dynamics [78–88]. It is also possible to produce simulations of binary neutron star mergers, even including magnetic fields, see e.g. Refs. [14, 135, 136], but we will not discuss these systems in this thesis. Since the numerical evolution of binary black hole spacetimes is performed considering the full-EFE without introducing any approximation, this approach produces the most reliable and accurate waveforms, granted that enough resolution is used and that the numerical errors are under control. These simulations are very expensive in computational terms and it is difficult to simulate high-mass ratio systems, even if progress in this direction has been made recently [137]. The NR waveforms play a crucial role in gravitational wave physics since they are fundamental to calibrate, complete, and validate the (semi)-analytical models, that we discuss below. We will discuss NR simulations in more detail in Sec. 2.4.

From a chronological point of view, the first analytical approach to the two-body problem to be developed was the post-Newtonian (PN) expansion [37–41], which uses as

a small parameter the velocity of the source. This method provides corrections to the Newtonian (0PN) solution as an expansion in $\left(\frac{v}{c}\right)$, and thus becomes unreliable in the strong field regimes and when the velocities of the two black holes approach the speed of light. An approach complementary to the previous one is the post-Minkowskian (PM) approach [42–46], which is a weak-field expansion, formally in powers of G or, equivalently, in the inverse of the angular momentum. This approach is particularly useful for unbound orbits and has seen a rapid growth in recent years. Since this is a weak-field expansion, this approach is not reliable in the strong-field regime. Moreover, the PM approach is also complementary to the PN expansion, since the latter is valid in the near region of the GW source but breaks in the far region, where we want to compute waveforms. The multipolar PM expansion is thus matched to the PN solution in an intermediate region in order to compute the GW at a large distance from a source whose dynamics is described using PN equations of motion [47–50].

The two methods just discussed are at the base of the effective-one-body (EOB) approach [51–53], which consists of creating a map between the two-body problem and the motion of a particle in a ν-deformed black hole metric, where ν is the symmetric mass ratio. These models naturally include the geodesic limit, that can be obtained by setting $\nu = 0$. To improve the reliability of the model in strong-field regimes, proper resummations are adopted both for the PN expressions used in the dynamics [134, 138, 139] and in the waveform [140]. While pure EOB models can be used only to accurately describe the inspiral, with NR-calibrated corrections it is possible to improve the description of the late inspiral and plunge. NR-calibrated model can be completed with a ringdown waveform, so that these EOBNR model can be used to describe the whole evolution of compact binaries [11, 54–60]. EOB models can be used also to portray systems with precessing [141–144] and noncircularized [1, 3, 5, 6, 145–151] dynamics. As can be seen from the references cited, there are currently two main families of state-of-the-art EOB models: `TEOBResumS` [11, 57, 146, 147] and `SEOBNR` [58–60]. We will discuss EOB models in more detail in the next section, focusing in particular on `TEOBResumS`.

A different method is the gravitational self-force (GSF) approach [69–75], which uses as an expansion parameter the mass ratio of the binary. Therefore, this method is reliable for intermediate or extreme mass-ratio binaries, where one of the two black holes is much more massive than the other one. Note that while the linear Kerr and Schwarzschild perturbations discussed in the previous chapter are an aspect of this formalism, in general the GSF computation also involves the study of the dynamics. Calculations in this approximation are currently being performed at second order in the mass ratio. Note that this approach is particularly relevant for the description of EMRIs, and thus for the LISA mission [102, 152]. The GSF information can be also used to improve EOB models in the intermediate/high mass ratio regimes [10, 153].

Finally, a rather practical approach used to generate waveform is to build phenomenological models [61–66]. These models generate waveforms in the frequency domain using PN approximants for the inspiral and NR-calibrated templates for the merger-ringdown. While their accuracy is comparable to current NR-calibrated EOB models, they strongly depend on the availability of numerical simulations. Thanks to their computational efficiency, these models are often used in data analysis, since a full Bayesian analysis requires the generation of a large number of waveforms. Recently, phenomenological models have been developed also in the time domain [67, 68].

2.2 Effective-one-body approach

As anticipated, the basic idea behind the EOB model is to create a map between the two-body problem and the motion of an effective particle in a certain effective metric. To create such a map in the non-spinning case at 2PN, Buonanno and Damour [51] started from the PN equations of motion (EOM) written in harmonic coordinates (i.e. coordinates that satisfy the gauge condition $\Box x^\mu = 0$) and found the associated Lagrangian. However, this Lagrangian does not depend only on the coordinates and the velocities but, starting from 2PN, also depends on the accelerations. To eliminate this dependence, one can work in the Arnowitt-Deser-Misner (ADM) coordinates[1] and, with a Legendre transformation, it is possible to find the corresponding 2PN Hamiltonian $\hat{H} = \hat{H}_{0\mathrm{PN}} + c^{-2}\hat{H}_{1\mathrm{PN}} + c^{-4}\hat{H}_{2\mathrm{PN}}$. Due to the symmetries of the problem, it is convenient to rewrite it using polar coordinates (r, φ) in the plane of motion. Then, since the Hamiltonian is invariant under time-translation and spatial rotations, a natural ansatz for the Jacobi principal function $\hat{S}$ can be constructed using the two constants of motion related to these symmetries, that are the non-relativistic energy E^{NR} and the angular momentum $\mathcal{J}$. Explicitly, we have $\hat{S} = -\mathcal{E}^{\mathrm{NR}}t + j\varphi + \hat{S}_r(r; \mathcal{E}^{\mathrm{NR}}, j)$, where $j \equiv \mathcal{J}/(\mu M)$, while $M = m_1 + m_2$ and $\mu = m_1 m_2/(m_1+m_2)$ are the total and reduced mass of the system, respectively. Subsequently, one can use the Hamilton-Jacobi equation (1.87) and the PN Hamiltonian written in ADM coordinates to determine the unknown part $\hat{S}_r$. The author of Ref. [51] found an expression of the relativistic energy $\mathcal{E}^{\mathrm{R}} = \mathcal{E}^{\mathrm{NR}} + Mc^2$ as a function of the symmetric mass ratio $\nu = \mu/M$, the angular momentum $\mathcal{J}$, and the principal number $\mathcal{N} \equiv \mathcal{J} + I_R$ (where I_R is a radial action variable). The explicit expression can be found in Eq. (2.15) of Ref. [51]. Since $\mathcal{E}^{\mathrm{R}}$, $\mathcal{J}$, and $\mathcal{N}$ are observables, the expressions for $\mathcal{E}^{\mathrm{R}}(\nu, \mathcal{J}, \mathcal{N})$ is invariant under coordinates transformations. Moreover, in this expression there is also a coupling $\alpha = G\mu M$ that makes Eq. (2.15) of Ref. [51] reminiscent of a quantum Coulomb problem. The next step is now to consider the problem of a particle with mass μ moving in an effective metric

$$\begin{aligned} ds^2_{\mathrm{eff}} &= g^{\mathrm{eff}}_{\mu\nu} dx^\mu_{\mathrm{eff}} dx^\nu_{\mathrm{eff}} = -A(R_{\mathrm{eff}})c^2 dt^2_{\mathrm{eff}} + B(R_{\mathrm{eff}}) dR^2_{\mathrm{eff}} \\ &\quad + R^2_{\mathrm{eff}} \left(d\theta^2_{\mathrm{eff}} + \sin^2\theta_{\mathrm{eff}} d\varphi^2_{\mathrm{eff}} \right), \end{aligned} \tag{2.1}$$

where the metric functions have the generic form

$$A(R) = 1 + \frac{a_1}{c^2 R} + \frac{a_2}{c^4 R^2} + \frac{a_3}{c^6 R^3} + O\left(\frac{1}{R^4}\right), \tag{2.2a}$$

$$B(R) = 1 + \frac{b_1}{c^2 R} + \frac{b_2}{c^4 R^2} + O\left(\frac{1}{R^3}\right), \tag{2.2b}$$

and the coefficients a_i and b_i have to be determined. The coefficient a_1 can be immediately fixed at -2 to reproduce, at low order, the Schwarzschild metric. The Hamilton-Jacobi equation for a particle of mass μ in the effective metric $g^{\mathrm{eff}}_{\mu\nu}$ reduces to

$$g^{\mu\nu}_{\mathrm{eff}} p^{\mathrm{eff}}_\mu p^{\mathrm{eff}}_\nu + \mu^2 c^2 = 0. \tag{2.3}$$

where $p^{\mathrm{eff}}_\mu = \frac{\partial S_{\mathrm{eff}}}{\partial x^\mu}$. Then Buonanno and Damour required that the motion of such a test particle in this effective metric is equivalent to the two-body problem characterized by the

[1] The ADM coordinate system is also of primary importance in NR simulations, as we will discuss in Sec. 2.4.

expression $\mathcal{E}^{\rm R}(\nu,\alpha,\mathcal{J},\mathcal{N})$ discussed before. To create this map they exploited analogies with the Bohr-Sommerfeld quantization used in the Coulomb problem and found that the map between the energy of the real two-body problem, $\mathcal{E}_{\rm real}$, and the effective one, $\mathcal{E}_{\rm eff}$, simply reduces to

$$\frac{\mathcal{E}_{\rm eff}}{\mu c^2} = \frac{\mathcal{E}^2_{\rm real} - m_1^2c^4 - m_2^2c^4}{2m_1m_2c^4}. \tag{2.4}$$

Then one can write the relation between the EOB Hamiltonian of the two-body problem in terms of the Hamiltonian of the particle moving in the effective metric, that in geometrized units reads

$$\hat{H}_{\rm EOB} \equiv \frac{H_{\rm EOB}}{\mu} = \frac{1}{\nu}\sqrt{1+2\nu\left(\hat{H}_{\rm eff}-1\right)}. \tag{2.5}$$

This map has been proven to hold also at higher PN order, and also for binaries with aligned or anti-aligned non-vanishing spins. However, starting from 3PN, one has to modify the on-shell condition (2.3) to conserve Eq. (2.5):

$$g^{\mu\nu}_{\rm eff}p^{\rm eff}_\mu p^{\rm eff}_\nu + \mu^2c^2 + \mu^2 Q(x^\mu, p^{\rm eff}_\mu) = 0, \tag{2.6}$$

where Q is a term that takes into account higher-than-quadratic momenta contributions. The effective Hamiltonian $\hat{H}_{\rm eff}$ in the general spinning case can be written as

$$\hat{H}_{\rm eff} = \sqrt{A(r;\nu)\left(1+\frac{p_\varphi^2}{r^2}+\frac{p_r^2}{B(r;\nu)}+Q(r,p_r;\nu)\right)} + \hat{H}^{\rm SO}_{\rm eff} + \hat{H}^{\rm SS}_{\rm eff}, \tag{2.7}$$

where Q is an EOB potential introduced to keep the map (2.5) valid also beyond 2PN, $\hat{H}^{\rm SO}_{\rm eff}$ is the spin-orbit Hamiltonian, and $\hat{H}^{\rm SS}_{\rm eff}$ is the spin-spin Hamiltonian. We also dropped the pedices "eff" for notation simplicity and we have uses rescaled coordinates and momenta as already done in Sec. 1.6.2, i.e. $t = T_{\rm eff}/M$, $r = R_{\rm eff}/M$, $p_r = P_{R,\rm eff}/\mu$, and $p_\varphi = P_{\varphi,\rm eff}/(\mu M)$. Note that this Hamiltonian is similar to the one of a test mass orbiting around a Kerr black hole, cfr. with Eq. (1.95).

Once the Hamiltonian is specified, the dynamics of an EOB model is complete introducing a prescription for a radiation reaction (RR) $\mathcal{F}$, that parametrizes the loss of energy and angular momentum of the system due to the GWs emission. The leading-order contribution of the RR is at 2.5PN. Once that $\mathcal{F} = \left(\mathcal{F}_r, \mathcal{F}_\varphi\right)$ is specified, the dynamics can be computed by solving the Hamilton equations

$$\dot{\varphi} = \frac{\partial \hat{H}_{\rm EOB}}{\partial p_\varphi} \equiv \Omega, \tag{2.8a}$$

$$\dot{r} = \left(\frac{A}{B}\right)^{1/2}\frac{\partial \hat{H}_{\rm EOB}}{\partial p_{r_*}}, \tag{2.8b}$$

$$\dot{p_\varphi} = \hat{\mathcal{F}}_\varphi, \tag{2.8c}$$

$$\dot{p}_{r_*} = \left(\frac{A}{B}\right)^{1/2}\left(\hat{\mathcal{F}}_r - \frac{\partial \hat{H}_{\rm EOB}}{\partial r},\right), \tag{2.8d}$$

where we have defined the orbital frequency Ω, and we have introduced $\hat{\mathcal{F}}_{r,\varphi} = \mathcal{F}_{r,\varphi}/\nu$ and $p^2_{r_*} = \frac{A}{B}p_r^2$. The tortoise coordinate r_* is defined according to the relation between p_r and p_{r_*}.

Now that we have included both conservative (the Hamiltonian) and non-conservative (radiation reaction) effects, we can compute the EOB dynamics by solving the Hamilton EOM (2.8) with a standard numerical ODE solver. For this reason, EOB models are often referred to as *semi*-analytical models Finally, the last ingredient that completes an EOB model is a prescription that, given the EOB dynamics, allows us to compute the waveform at infinity. In conclusion, each EOB model has three building blocks: a Hamiltonian, a radiation reaction, and a prescription to compute the waveform at infinity.

We now conclude this brief overview of the EOB approach by noting that the metric potentials A, B, and Q, the radiation reactions, and the EOB waveform are often resummed to make them more robust in the strong-field regime [134, 138–140]. Moreover, the conservative sector of the dynamics and the waveform are improved using information from numerical data, both using full-NR simulations and test mass data. We will further discuss these two aspects in the following section, where we introduce the state-of-the-art EOB model `TEOBResumS`.

2.3 The effective-one-body model `TEOBResumS`

We will discuss in the following `TEOBResumS` [11, 57, 134], a time-domain EOB model that is informed and completed using NR data. The model can also describe binaries with generic orbits [7, 11, 145–147]. We start by discussing the Hamiltonian, and we then move to the radiation reaction and the waveform. We also briefly discuss how the model is calibrated and completed using numerical information.

2.3.1 Hamiltonian

To better highlight the structure of the Hamiltonian used in `TEOBResumS`, we start by discussing the non-spinning part and then we discuss the spin contributions.

Non-spinning sector

The effective Hamiltonian for the non-spinning sector is written as

$$\hat{H}_{\rm eff}^{\rm orb} = \sqrt{\left(A_{\rm orb}(r)\left(1 + p_\varphi^2 u^2 + Q_{\rm orb}(r, p_{r_*})\right) + p_{r_*}^2\right.}, \tag{2.9}$$

where we have used the inverse of the radius $u = 1/r$. The metric potentials are known at 5PN and read [154]

$$\begin{aligned}
A_{\rm 5PN}(u) =& 1 - 2u + 2\nu u^3 + \nu a_4 u^4 + \nu\left[a_5^c + a_5^{\log}\log(u)\right]u^5 \\
&+ \nu\left[a_6^c + a_6^{\log}\log(u)\right]u^6, && \text{(2.10a)}\\
D_{\rm 5PN}(u) =& 1 - 6\nu u^2 - \left(52\nu - \nu^2\right)u^3 + d_4 u^4 + d_5 u^5, && \text{(2.10b)}\\
Q_{\rm 5PNloc}(u, p_{r_*}) =& 2\nu\left(4 - 3\nu\right)u^2 p_{r_*}^4 + \left[q_{43} u^3 p_{r_*}^4 + q_{62} u^2 p_{r_*}^6 + O(u p_{r_*}^8)\right] \\
&+ \left[q_{44\rm loc} u^4 p_{r_*}^4 + q_{63\rm loc} u^3 p_{r_*}^6\right. \\
&\left. + q_{82\rm loc} u^2 p_{r_*}^8 + O(u p_{r_*}^{10})\right], && \text{(2.10c)}
\end{aligned}$$

where the coefficients of this expansion can be found in Ref. [154]. The B-potential is then defined as $B_{\rm 5PN} \equiv D_{\rm 5PN}/A_{\rm 5PN}$. However, in Eq. (2.9) the A, B, and Q orbital potentials

are used in a Padé-resummed form. In Ref. [148] for example, the resummations used were

$$A_{\rm orb}(r) = P^3_3[A^{\rm eff}_{\rm 5PN}(r; a^c_6)], \tag{2.11a}$$
$$D_{\rm orb}(r) = P^3_2[D_{\rm 5PN}(r)], \tag{2.11b}$$
$$Q_{\rm orb}(r, p_{r_*}) = Q_{\rm 5PNloc}(r, p_{r_*}), \tag{2.11c}$$

where $P^n_d[f(x)]$ means that the polynomial-expanded function f is replaced with a Padé-approximant, that is a rational function where the numerator is an x-polynomial of order n, and the denominator is an x-polynomial of order d. The coefficients of these two polynomials are chosen so that the Taylor expansion of $P^n_d[f(x)]$ matches $f(x)$. The coefficients a^c_6 is an analytically unknown coefficient that is treated as a parameter to be effectively determined by calibrating the model on NR simulations. For more details on the resummation of the potentials and on the calibration of a^c_6, see Refs. [11, 148]; both aspects play a crucial role in ensuring the reliability of the model during the last few orbits of the coalescence.

Spinning sector

We now consider black hole binaries where the two objects have aligned or anti-aligned spins, denoted as S_i, where $i = 1, 2$. By convention, we choose $m_1 > m_2$. Then we can define the dimensionless spin quantities $\chi_i \equiv S_i/m_i^2$ and $\tilde{a}_i \equiv S_i/(m_i M)$. We further define $\tilde{a}_0 \equiv \tilde{a}_1 + \tilde{a}_2$, $\tilde{a}_{12} \equiv \tilde{a}_1 - \tilde{a}_2$, and $X_{12} \equiv \sqrt{1-4\nu}$. Then the orbital part of `TEOBResumS` Hamiltonian in the more general spinning case is written in a Kerr form as [134]

$$\hat{H}^{\rm orb}_{\rm eff} = \sqrt{A(r)\left(1 + p^2_\varphi u^2_c + Q(r, p_{r_*})\right) + p^2_{r_*}}, \tag{2.12}$$

where u_c is the inverse of the centrifugal radius r_c that includes the spin-spin contributions; its explicit form is [134]

$$r^2_c \equiv r^2 + \tilde{a}^2_0\,(1 + 2u) + \delta a^2_{\rm NLO} u + \delta a^2_{\rm NNLO} u^2, \tag{2.13}$$

where the next-to-leading-order and next-to-next-to-leading order contributions $\delta a^2_{\rm NLO}$ and $\delta a^2_{\rm NNLO}$ can be found in Refs. [134, 148, 155]. The metric potentials in Eq. (2.12) are defined as

$$A(r; \chi_i) = \frac{1 + 2u_c}{1 + 2u} A_{\rm orb}(r_c) \tag{2.14a}$$
$$D(r; \chi_i) = D_{\rm orb}(r_c) \tag{2.14b}$$
$$B(r; \chi_i) = \frac{r^2}{r^2_c} \frac{D(r; \chi_i)}{A(r; \chi_i)}. \tag{2.14c}$$

With these choices, the orbital effective Hamiltonian contains also even-parity spin contributions. The complete effective Hamiltonian is then given by

$$\hat{H}_{\rm eff} = \hat{H}^{\rm orb}_{\rm eff} + p_\varphi \left(G_S \hat{S} + G_{S_*} \hat{S}_*\right), \tag{2.15}$$

where the spin-orbit coupling terms G_S and G_{S_*} are called gyro-gravitomagnetic functions, and

$$\hat{S} \equiv \frac{S_1 + S_2}{M^2}, \tag{2.16}$$

$$\hat{S}_* \equiv \frac{1}{M^2}\left(\frac{m_2}{m_1}S_1 + \frac{m_1}{m_2}S_2\right). \tag{2.17}$$

In `TEOBResumS` the gyro-gravitomagnetic functions are written in the DJS (Damour-Jaranowski-Schäfer) gauge [156] and are functions of r and p_{r_*}:

$$G_S = 2uu_c^2\hat{G}_S, \tag{2.18}$$

$$G_{S_*} = \frac{3}{2}u_c^3\hat{G}_{S_*}. \tag{2.19}$$

The explicit expressions for $\hat{G}_S$ and $\hat{G}_{S_*}$ can be found in Ref. [148]. These expressions are known at (next-to)^3-leading-order (N^{3}LO), i.e. at 4.5PN, but in `TEOBResumS` these terms are used considering the analytically-known expressions up to NNLO and adding a N^{3}LO free coefficient c_3 that is calibrated using NR simulations. In the effective Hamiltonian, we have thus two parameters that are fitted on NR data: a_6^c and c_3.

We conclude this section by noting that setting $\nu = 0$ and $S_2 = 0$, we recover the Hamiltonian for a non-spinning test particle in equatorial Kerr, cfr. with Eq. (1.95). However, if one sets $\nu = 0$ and $S_1 = 0$, G_{S_*} does not reduce to the spin-orbit coupling for a spinning particle in Schwarzschild. This is linked to the fact that the exact test mass limit expression of G_{S_*} has a light-ring singularity in the DJS gauge [134] and thus it has been expanded at 4PN.

2.3.2 Inspiral Waveform

For reasons that will be clear soon, we first discuss the EOB waveform and then we focus on the radiation reaction force. The EOB waveform is decomposed in multipoles on the spin-weighted spherical harmonics ${}_{-2}Y_{\ell m}(\Theta,\Phi)$ as in Eq. (1.39), and then each multipole is factorized. If we consider only the circular part of the inspiral waveform, the explicit factorization is [140]

$$h_{\ell m}^{\rm inspl} = h_{\ell m}^{(N,\epsilon)_{\rm c}}\hat{h}_{\ell m}^{(\epsilon)_{\rm c}} = h_{\ell m}^{(N,\epsilon)_{\rm c}}\hat{S}_{\rm eff}^{(\epsilon)}T_{\ell m}e^{i\delta_{\ell m}}(\rho_{\ell m})^{\ell}, \tag{2.20}$$

where ϵ denotes the parity of the multipole ($\epsilon = 0$ if $\ell + m$ is even, $\epsilon = 1$ otherwise), $h_{\ell m}^{(N,\epsilon)_{\rm c}}$ is the circular Newtonian contribution and $\hat{h}_{\ell m}^{(\epsilon)_{\rm c}}$ is the circular PN correction. The Newtonian factor in the circular limit reads

$$h_{\ell m}^{(N,\epsilon)_{\rm c}} = M\nu n_{\ell m}^{(\epsilon)}c_{\ell+\epsilon}(\nu)x^{\frac{(\ell+\epsilon)}{2}}Y^{\ell-\epsilon,-m}\left(\frac{\pi}{2},\varphi\right), \tag{2.21}$$

where $x = (M\Omega)^{2/3}$ and the coefficients are given by

$$\begin{aligned} n_{\ell m}^{(0)} &= (im)^{\ell}\frac{8\pi}{(2\ell+1)!!}\sqrt{\frac{(\ell+1)(\ell+2)}{\ell(\ell-1)}}, \\ n_{\ell m}^{(1)} &= -(im)^{\ell}\frac{16\pi i}{(2\ell+1)!!}\sqrt{\frac{(2\ell+1)(\ell+2)\left(\ell^2-m^2\right)}{(2\ell-1)(\ell+1)\ell(\ell-1)}}, \\ c_{\ell+\epsilon} &= X_2^{\ell+\epsilon-1} + (-1)^m X_1^{\ell+\epsilon-1}, \end{aligned} \tag{2.22}$$

and $X_i = m_i/M$. Note that in Ref. [140] there is also the distance from the source in the expression of $h_{\ell m}^{(N,\epsilon)_{\rm c}}$ (cfr. with Eq. (1)), but here we have already factorized the distance

in Eq. (1.39). To improve the behavior of the Newtonian factor is it useful to replace x with the tangential velocity $v_\varphi \equiv r_\Omega \Omega$, where r_Ω is defined as [134]

$$r_\Omega \equiv \left\{ \frac{\left(r_c^3 \psi_c\right)^{-1/2} + \tilde{G}}{\hat{H}_{\rm EOB}} \right\}^{-2/3}_{p_{r_*}=0}, \tag{2.23}$$

$$\psi_c = -\frac{2}{A'}\left(u_c' + \frac{\tilde{G}'}{u_c A}\sqrt{\frac{A}{p_\varphi^2} + u_c^2 A} \right), \tag{2.24}$$

$$\tilde{G} = G_S S + G_{S_*} S_*, \tag{2.25}$$

and the prime indicates a derivative with respect to r. This definition of r_Ω is valid for binaries of any mass ratio and satisfies the third circular Kepler law $1 = \Omega^2 r_\Omega^3$. However, when discussing the motion in equatorial Kerr, we obtain r_Ω from the Kerr generalization of the third Kepler law for circular orbits [157], so that r_Ω is simply given by

$$r_\Omega = r\left(1 + \hat{a} r^{-3/2}\right)^{2/3}. \tag{2.26}$$

Therefore, aside from numerical factors, the circular Newtonian quadrupolar contribution is $h_{22}^{(N,0)} \propto v_\varphi^2 e^{-2i\varphi}$. The PN contributions included in $\hat{h}_{\ell m}^{(\epsilon)_{\rm c}}$ of Eq. (2.20) are, in principle, written in the form $\hat{h}_{\ell m} = 1 + h_{\rm 1PN} x + h_{\rm 1.5PN} x^{3/2} + ...$ and are [134, 140]:

- the source term $\hat{S}_{\rm eff}^{(\epsilon)}$, that is the effective Hamiltonian for even-parity multipoles and the Newtonian-normalized angular momentum for odd-parity ones. Explicitly we have

$$\hat{S}_{\rm eff}^{(\epsilon)} = \begin{cases} \hat{H}_{\rm eff}(x) & \text{if} \quad \epsilon = 0 \\ \frac{p_\varphi}{r_\Omega v_\varphi} & \text{if} \quad \epsilon = 1 \end{cases} \tag{2.27}$$

- the resummation of the leading logarithmic contributions of the tail factor $T_{\ell m}$, which is generated by the back-scattering of the GWs with the curved spacetime associated with the mass of the binary. The explicit formula is

$$T_{\ell m} = \frac{\Gamma(\ell + 1 - 2i\hat{\hat{k}})}{\Gamma(\ell+1)} e^{\pi \hat{\hat{k}}} e^{2i\hat{\hat{k}}\ln(2kr_0)}, \tag{2.28}$$

  where $\hat{\hat{k}} = m H_{\rm EOB}\Omega$, $k = m\Omega$, $r_0 = 2M/\sqrt{e}$ and $\Gamma(z)$ is the Euler Gamma function.

- the residual phase of the tail factor $e^{i\delta_{\ell m}}$, that takes into account the fact that $T_{\ell m}$ includes only the leading contributions. The $\delta_{\ell m}$ are truncated at a certain PN order and therefore are not written in closed form, as opposed to the factors $\hat{S}_{\rm eff}^{(\epsilon)}$ and $T_{\ell m}$.

- the residual relativistic amplitude corrections $\rho_{\ell m}$ that, as the $\delta_{\ell m}$, are given at a certain PN order. To define the $\rho_{\ell m}$, we can start by defining

$$f_{\ell m} \equiv T_{\rm PN}\left[\frac{\left|\hat{h}_{\ell m}^{(e)}\right|}{\hat{S}_{\rm eff}^{(\epsilon)} \left|T_{\ell m}\right|} \right] \tag{2.29}$$

where $T_{\rm PN}$ denotes an expansion in the PN parameter x, and then we finally define

$$\rho_{\ell m} \equiv T_{\rm PN}\left[f_{\ell m}^{1/\ell}\right]. \tag{2.30}$$

It is preferable to use the $\rho_{\ell m}$ instead of the $f_{\ell m}$ because the expansion of the latter has terms $\propto \ell x$ that might be problematic for higher-order multipoles. A resummation scheme that has strongly improved the agreement with numerical data for spinning binaries of the analytical $\rho_{\ell m}$ is the one proposed in Refs. [158, 159]. We will see in more detail this procedure in the next chapters.

We conclude this discussion by recalling that the Newtonian contribution of the multipoles is obtained for even-parity modes from the ℓth-time derivative of the symmetric-trace-free (STF) mass Newtonian multipole, $I_{\ell m} \propto \nu r^\ell e^{-im\varphi}$, and for odd-parity modes from the current Newtonian multipole, $J_{\ell m} \propto \nu r^{\ell+1}\Omega e^{-im\varphi}$. In the case of circular motion, the radius and the orbital frequency are constant and, therefore, their derivatives vanish, leading to the expressions mentioned above. However, if we consider generic planar orbits, the terms $\dot{r}$ and $\dot{\Omega}$ do not vanish. We can thus easily generalize the circular Newtonian contribution $h_{\ell m}^{(N,\epsilon)_{\rm c}}$ and obtain a *generic* Newtonian prefactor [145]

$$h_{\ell m}^{(N,\epsilon)} = h_{\ell m}^{(N,\epsilon)_{\rm c}} \hat{h}_{\ell m}^{(N,\epsilon)_{\rm nc}}, \tag{2.31}$$

where

$$\hat{h}_{\ell m}^{(N,0)_{\rm nc}} = \left(h_{\ell m}^{(N,0)_{\rm c}}\right)^{-1} I_{\ell m}^{(\ell)}, \tag{2.32}$$

$$\hat{h}_{\ell m}^{(N,1)_{\rm nc}} = \left(h_{\ell m}^{(N,1)_{\rm c}}\right)^{-1} J_{\ell m}^{(\ell)}, \tag{2.33}$$

$$\tag{2.34}$$

and (ℓ) denotes a ℓth-time derivative. The correction for the quadrupolar waveform reads

$$\hat{h}_{22}^{(N,0)_{\rm nc}} = 1 - \frac{\ddot{r}}{2r\Omega^2} - \frac{\dot{r}^2}{2r^2\Omega^2} + \frac{2i\dot{r}}{r\Omega} + \frac{i\dot{\Omega}}{2\Omega^2}. \tag{2.35}$$

These Newtonian corrections contain time-derivatives of the radius and the orbital frequency that are evaluated numerically, i.e. considering the complete EOM. We will come back to this in Chapter 3, and we will also discuss the generalization of this procedure at 2PN in Chapter 4. The inspiral waveform with Newtonian noncircular corrections thus reads

$$h_{\ell m}^{\rm inspl} = h_{\ell m}^{(N,\epsilon)_{\rm c}} h_{\ell m}^{(N,\epsilon)_{\rm nc}} \hat{S}_{\rm eff}^{(\epsilon)} T_{\ell m} e^{i\delta_{\ell m}} (\rho_{\ell m})^\ell. \tag{2.36}$$

The analogous noncircular Newtonian corrections for the $(2,1)$, $(3,3)$, $(3,3)$, and $(4,4)$ multipoles are reported in Appendix A.

2.3.3 Radiation reaction

We now discuss the radiation reaction force that enters the Hamilton equations (2.8). To obtain the analytical expression, we require that the energy and angular momentum losses of the system are equal to the energy flux $\dot{E}$ and angular momentum flux $\dot{J}$ carried away by the emitted GWs. In this work, we consider only the fluxes at infinity, and we

neglect the fluxes absorbed by the horizons. The balance equations along generic orbits are [160]

$$\dot{r}\mathcal{F}_r + \Omega\mathcal{F}_\varphi + \dot{E} + \dot{E}_{\rm Schott} = 0, \tag{2.37a}$$

$$\mathcal{F}_\varphi + \dot{J} = 0, \tag{2.37b}$$

where the Schott energy is a term related to the interaction of the system with the local field. It identically vanishes along circular orbits, and the same happens to its radial average on generic bound orbits. The Schott contribution to the angular momentum in the balance laws (2.37) can be set to zero with a gauge fix [160].

We now focus on circular orbits, where we have $\dot{r} = 0$, $\dot{E}_{\rm Schott} = 0$, and thus $\dot{E} = \Omega\dot{J}$. Then using this latter relation, Eq. (1.42), and the fact that $h_{\ell,-m} = (-1)^\ell h^*_{\ell m}$, we can write

$$\dot{J} \equiv \frac{1}{\Omega}\sum_{\ell=2}^{\infty}\sum_{m=1}^{\ell} F_{\ell m} = \frac{2}{16\pi\Omega}\sum_{\ell=2}^{\infty}\sum_{m=1}^{\ell}|\dot{h}_{\ell m}|^2 = \frac{1}{8\pi}\sum_{\ell=2}^{\infty}\sum_{m=1}^{\ell} m^2\Omega|h_{\ell m}|^2, \tag{2.38}$$

where $F_{\ell m}$ are the multipoles of the energy flux. We can then factorize the Newtonian quadrupolar contribution and write $\hat{\mathcal{F}}_\varphi = \mathcal{F}_\varphi/\nu$ as

$$\hat{\mathcal{F}}_\varphi = -\frac{32}{5}\nu x^{7/2}\hat{f}, \tag{2.39}$$

where we have used

$$\hat{f} = \sum_{\ell=2}^{\infty}\sum_{m=1}^{\ell}(F^N_{22})^{-1}F_{\ell m}, \tag{2.40}$$

$$F = \frac{1}{8\pi}m^2\Omega^2|h_{\ell m}|^2 \tag{2.41}$$

and, in particular, $F^N_{22} = \frac{32}{5}x^5$. We can then use the generalized third Kepler law (2.23) to rewrite $x^{7/2}$ as

$$x^{7/2} = v^7_\varphi = r^7_\Omega\Omega^7 = r^4_\Omega\Omega^5. \tag{2.42}$$

We thus finally obtain the expression for the quasi-circular angular radiation reaction with the Newtonian leading contribution factorized,

$$\hat{\mathcal{F}}_\varphi = -\frac{32}{5}\nu r^4_\Omega\Omega^5\hat{f}. \tag{2.43}$$

Since in the quasi-circular case the radial component of the radiation reaction force $\mathcal{F}_r$ can be set to zero, we have that Eq. (2.43) is the only dissipative contribution in the quasi-circular dynamics of `TEOBResumS`.

We now turn our attention to the more generic noncircular case. To start with, we can use the dominant generic Newtonian prefactor of Eq. (2.35) to generalize $\mathcal{F}_\varphi$. We thus include a noncircular correction $\hat{f}^{\rm N_{nc}}_{\varphi,22}$ that is directly obtained from Eq (2.35) and Eq. (1.42a). This correction reads

$$\begin{aligned}\hat{f}^{\rm N_{nc}}_{\varphi,22} = 1 &+ \frac{3}{4}\frac{\ddot{r}^2}{r^2\Omega^4} - \frac{\ddot{\Omega}}{4\Omega^3} + \frac{3\dot{r}\dot{\Omega}}{r\Omega^3} \\ &+ \frac{4\dot{r}^2}{r^2\Omega^2} + \frac{\ddot{\Omega}\dot{r}^2}{8r^2\Omega^5} + \frac{3}{4}\frac{\dot{r}^3\dot{\Omega}}{r^3\Omega^5} + \frac{3}{4}\frac{\dot{r}^4}{r^4\Omega^4} + \frac{3}{4}\frac{\dot{\Omega}^2}{\Omega^4}\end{aligned} \tag{2.44}$$

$$- \dddot{r} \left(\frac{\dot{r}}{2r^2\Omega^4} + \frac{\dot{\Omega}}{8r\Omega^5} \right) + \ddot{r} \left(-\frac{2}{r\Omega^2} + \frac{\ddot{\Omega}}{8r\Omega^5} + \frac{3}{8}\frac{\dot{r}\dot{\Omega}}{r^2\Omega^5} \right).$$

In the radiation reaction presented in the Chiaramello-Nagar work [145], this contribution was included as a global factor, i.e.

$$\hat{\mathcal{F}}_\varphi = -\frac{32}{5}\nu r_\Omega^4 \Omega^5 \hat{f}^{\rm N_{nc}}_{\varphi,22} \hat{f}. \tag{2.45}$$

However, this expression has been improved in more recent works (see e.g. Refs. [1, 147]) including the factor $\hat{f}^{\rm N_{nc}}_{\varphi,22}$ *only* in the (2,2) multipole, as it should be. We will further discuss this point in Sec. 3.2.4. Note that the insertion of the flux-correction $\hat{f}^{\rm N_{nc}}_{\varphi,22}$ in the rhs of the EOM (2.8) makes the latter system of equations not solvable with a standard ODE solver. To overcome this complexity, `TEOBResumS` uses an iterative procedure to compute the time-derivatives in the rhs of the EOM that is a straightforward generalization of the procedure outlined in Appendix A of Ref. [56]. Finally, we mention that Ref. [160] presented a 2PN prescription for $\mathcal{F}_\varphi$. However, Ref. [145] showed that the angular radiation reaction computed from Eq. (2.45) is more reliable. This is a consequence of the fact that the time-derivatives in $\hat{f}^{\rm N_{nc}}_{\varphi,22}$ are computed using the complete equation of motion, rather than the PN-expanded ones.

For the radial component of the radiation reaction, $\hat{\mathcal{F}}_r$, we used the 2PN results of Ref. [160] Padé resummed as in [145]

$$\hat{\mathcal{F}}_r = \frac{32}{3}\nu \frac{p_{r_*}}{r^4} P^0_2[\hat{f}^{\rm BD}_r], \tag{2.46}$$

where the explicit expressions for the 2PN terms read

$$\hat{f}^{\rm BD}_r = \hat{f}^{\rm N}_r + \hat{f}^{\rm 1PN}_r + \hat{f}^{\rm 2PN}_r, \tag{2.47}$$

and (see also Ref. [147])

$$\hat{f}^{N}_r = -\frac{8}{15} + \frac{56}{5}\frac{p^2_\varphi}{r}, \tag{2.48a}$$

$$\hat{f}^{\rm 1PN}_r = -\frac{1228}{105}p^2_{r_*} - \frac{1984}{105}\frac{1}{r} - \frac{124}{105}\frac{p^2_{r_*}p^2_\varphi}{r} + \frac{1252}{105}\frac{p^4_\varphi}{r^3} - \frac{1696}{35}\frac{p^2_\varphi}{r^2}, \tag{2.48b}$$

$$\hat{f}^{\rm 2PN}_r = \frac{323}{315}p^4_{r_*} + \frac{59554}{2835}r^2 - \frac{1774}{21}\frac{p^2_{r_*}p^2_\varphi}{r^2} - \frac{628}{105}\frac{p^2_{r_*}p^4_\varphi}{r^3} - \frac{29438}{315}\frac{p^2_\varphi}{r^3} - \frac{461}{315}\frac{p^4_{r_*}p^2_\varphi}{r} + \frac{20666}{315}\frac{p^2_{r_*}}{r} - \frac{3229}{315}\frac{p^6_\varphi}{r^5} - \frac{35209}{315}\frac{p^4_\varphi}{r^4}. \tag{2.48c}$$

Finally, for the Schott energy we also use the results of Ref. [145],

$$E_{\rm Schott} = \frac{16}{5}\frac{p_{r_*}}{r^3} P^0_2[E^{\rm c}_{\rm Schott}] P^0_2[E^{\rm nc}_{\rm Schott}], \tag{2.49}$$

where the circular and noncircular parts, taken at 2PN accuracy, are also Padé resummed. The two contributions are explicitly reported, for example, in Eq. (31) and Eq. (32) of

Ref. [1]. The noncircular radiation reaction discussed in this section has been tested systematically in the test mass limit in Ref. [1]. We will come back to this in Chapter 3. However, note that when testing the analytical energy instantaneous fluxes with numerical results, the Schott contribution cannot be disentangled from the radial component. This means that there is an intrinsic ambiguity in the analytical choice of the radial component.

In the eccentric version of the model `TEOBResumS`, often referred to as `TEOBResumS-Dalì`, the radial radiation reaction has been changed to improve the quasi-circular limit of the model. In particular, the radiation used in Refs. [147] and subsequent `TEOBResumS` avatars is

$$\hat{f}_r^{\rm 2PN} = 1 - \left(\frac{573}{280} + \frac{118}{35}\nu\right) u + \left(-\frac{33919}{2160} + \frac{6493}{560}\nu + \frac{1311}{280}\right) u^2. \tag{2.50}$$

However, when discussing binaries in the test mass limit in this thesis, we will consider $\hat{f}_r$ as in Eq. (2.47).

2.3.4 Numerical completion for the radiation

All the terms of `TEOBResumS` that we have discussed so far are purely analytical, except for the NR-calibrated parameters a_c^6 and c_3 in the Hamiltonian. We now want to complete the model so that we can describe the full evolution of binaries, up to the ringdown. The goal is to have a waveform for the ringdown, $h_{\ell m}^{\rm rng}$, correct the inspiral waveform of Eq. (2.36) with some numerically-informed corrections $\hat{h}_{\ell m}^{\rm NQC}$, and then to match the two solutions at a certain time $t_{\ell m}^{\rm match}$. We will thus have a waveform that reads

$$h_{\ell m} = \theta(t_{\ell m}^{\rm match} - t) h_{\ell m}^{\rm inspl} \hat{h}_{\ell m}^{\rm NQC} + \theta(t - t_{\ell m}^{\rm match}) h_{\ell m}^{\rm rng}, \tag{2.51}$$

where θ is the Heaviside step-function.

We start by discussing the ringdown waveform that is typically defined, for each multipole, as the post-amplitude-peak waveform[2], i.e. the portion of waveform after $t_{A_{\ell m}}^{\rm peak}$. While it is true that the spacetime oscillations produced by the remnant of the merger can be described with a superposition of QNMs as in Eq. (1.78), it is not trivial to determine from which time this description, that is based on the homogeneous linearized solution, is valid. The first important consideration is that, at relatively early times after merger, the solely fundamental QNM is not sufficient to provide an accurate description of the waveform, and higher harmonics have to be taken into account [161–163]. However, while some works suggested that the inclusion of these overtones allows the description of the whole post-merger waveform in terms of QNMs [162, 163], others showed that nonlinear effects have to be taken into account in the early ringdown [164–168]. As a consequence, the pure QNM ansatz can be consistently used only starting from later times. In Sec. 5.4 we will argue that, even when considering linear perturbations generated by a particle falling in a Schwarzschild black hole, the pure QNM ansatz cannot be used to describe the whole postpeak waveform. In this case, the failure of this ansatz in the early ringdown is due to the non-vanishing source term at merger time, so that the non-homogeneous RWZ equations have to be considered.

We thus use the phenomenological ringdown model introduced in Ref. [169], which is based on the idea of factorizing the contribution of the fundamental QNM. The QNM-rescaled waveform is

$$\bar{h}_{\ell m}(\tau) = e^{\sigma_{\ell m 1}\tau + i\phi_{\ell m}^{\rm peak}} h_{\ell m}^{\rm rng}(\tau), \tag{2.52}$$

[2]Note that in the literature the merger time $t_{\rm mrg}$ is often defined as the peak of the quadrupolar amplitude $t_{A_{22}}^{\rm peak}$.

where $\tau = t - t^{\rm peak}_{A_{\ell m}}$, $\phi^{\rm peak}_{\ell m}$ is the value of the phase at the amplitude peak, $\sigma_{\ell m 1}$ is the fundamental QNM frequencies associated with the spin of the remnant, and $h^{\rm rng}_{\ell m}$ is the actual ringdown waveform. The QNM-rescaled waveform $\bar{h}_{\ell m}(\tau)$ is then written using two templates for the amplitude and the phase, $\bar{h}(\tau) = A_{\bar{h}}(\tau) e^{i\phi_{\bar{h}}(\tau)}$. Part of the coefficients of these templates are constrained by requiring the continuity between the ringdown and the inspiral-plunge waveform. The other coefficients are instead determined by fitting the templates on some numerical waveforms. These fits are called *primary* fits, and they are repeated for a sufficiently large number of numerical waveforms. The coefficients found with the primary fits and some quantities extracted from the numerical data (such as $A_{\rm peak}$, $\ddot{A}_{\rm peak}$, $\omega_{\rm peak}$, etc. for each multipole) are fitted over the parameter space; these latter fits are called *global*. From these fits are we able to reconstruct $\bar{h}_{\ell m}$ and thus $h^{\rm rng}_{\ell m}$ for every point in the parameter space. We will discuss these ringdown-modeling in more detail in Sec. 5.

The correcting factor $\hat{h}^{\rm NQC}_{\ell m}$ is instead known as Next-to-Quasi-Circular (NQC) correction. The name is linked to historical reasons, since for the quasi-circular EOB-NR models this correction was non-vanishing only during the plunge, when the motion was no longer quasi-circular. The NQC correction is written as

$$\hat{h}^{\rm NQC}_{\ell m} = \left(1 + \sum_{i=1}^{3} a^{\ell m}_i n_i\right) \exp\left(i \sum_{j=1}^{3} b^{\ell m}_j n_{j+3}\right), \tag{2.53}$$

where n_i are functions that are combinations of quantities negligible during the quasi-circular inspiral but relevant during the plunge. It is thus natural to write them in terms of time-derivatives of the radius or in terms of p_{r_*}. For all the higher modes, in Ref. [6] we used

$$n_1 = \frac{p^2_{r_*}}{r^2\Omega^2}, \tag{2.54a}$$
$$n_2 = \frac{\ddot{r}}{r\Omega^2}, \tag{2.54b}$$
$$n_3 = n_1\, p^2_{r_*}, \tag{2.54c}$$
$$n_4 = \frac{p_{r_*}}{r\Omega}, \tag{2.54d}$$
$$n_5 = n_4\, \Omega, \tag{2.54e}$$
$$n_6 = n_5\, p^2_{r_*}. \tag{2.54f}$$

For the (2,2) mode, we used the same n_i with $i \leq 4$, but we changed $n_5 = n_4\, r^2\Omega^2$ and, consequently, $n_6 = n_5\, p^2_{r_*}$. Note that in `TEOBResumS` only the first derivatives of A and ω are typically considered, so that n_3 and n_6 are set to zero. Moreover, in `TEOBResumS` the n_5 function for the higher modes is different than the one considered here. The coefficients a_i and b_i are determined at a specific time $t^{\rm NQC}_{\ell m}$. If we consider $t^{\rm NQC}_{\ell m} > t^{\rm peak}_{A_{\ell m}}$, as typically done in EOB models, then we can determine the coefficients by solving the linear system

$$A^{\rm EOB}_{\ell m}(t^{\rm NQC}_{\ell m}) = A^{\rm rng}_{\ell m}(t^{\rm NQC}_{\ell m}), \tag{2.55a}$$
$$\dot{A}^{\rm EOB}_{\ell m}(t^{\rm NQC}_{\ell m}) = \dot{A}^{\rm rng}_{\ell m}(t^{\rm NQC}_{\ell m}), \tag{2.55b}$$
$$\ddot{A}^{\rm EOB}_{\ell m}(t^{\rm NQC}_{\ell m}) = \ddot{A}^{\rm rng}_{\ell m}(t^{\rm NQC}_{\ell m}), \tag{2.55c}$$
$$\omega^{\rm EOB}_{\ell m}(t^{\rm NQC}_{\ell m}) = \omega^{\rm rng}_{\ell m}(t^{\rm NQC}_{\ell m}), \tag{2.55d}$$

$$\dot{\omega}^{\rm EOB}_{\ell m}(t^{\rm NQC}_{\ell m}) = \dot{\omega}^{\rm rng}_{\ell m}(t^{\rm NQC}_{\ell m}), \tag{2.55e}$$
$$\ddot{\omega}^{\rm EOB}_{\ell m}(t^{\rm NQC}_{\ell m}) = \ddot{\omega}^{\rm rng}_{\ell m}(t^{\rm NQC}_{\ell m}), \tag{2.55f}$$

where on the lhs the amplitude, frequency, and corresponding time-derivatives are computed from $h^{\rm inspl}_{\ell m}\hat{h}^{\rm NQC}_{\ell m}$, while on the rhs they are computed from the ringdown waveform $h^{\rm rng}_{\ell m}$. In Ref. [6] we explored also the option $t^{\rm NQC}_{\ell m} < t^{\rm peak}_{A_{\ell m}}$; in this case we have to consider, in the rhs of Eqs. (2.55), quantities extracted from numerical data at $t^{\rm NQC}_{\ell m}$. The choice $t^{\rm NQC}_{\ell m} > t^{\rm peak}_{A_{\ell m}}$ is, in principle, preferable since it reduces the number of numerical-informed parameters in the model. However, as we will discuss in Chapter 5 when studying the eccentric insplunge in Schwarzschild, choosing $t^{\rm NQC}_{\ell m} < t^{\rm peak}_{A_{\ell m}}$ works better for the higher modes. Finally, note that when we consider noncircularized orbits, the n_i functions are non-vanishing during the inspiral, and we have to switch off the NQC corrections with a sigmoid function before the beginning of the plunge (we will clarify in Chapter 5 how to precisely identify the plunge time for eccentric configurations).

We have thus all the ingredients to compute the complete EOB-NR waveform of Eq. (2.51). In `TEOBResumS` the matching time used is related to the peak of the *pure*-orbital frequency (i.e. the frequency associated with $\hat{H}^{\rm orb}_{\rm eff}$).

We conclude this section by highlighting that the quadrupolar NQC contribution is also included in the radiation reaction, see e.g. Ref. [8] and Eqs. (13-15) therein.

2.3.5 Summary and test mass limit

We have thus introduced the Hamiltonian, the radiation reaction, and the multipolar waveform of the EOB model `TEOBResumS`. Each of these pieces is informed with numerical results, both from perturbation theory and from full-GR simulations. The model exists in two branches: `GIOTTO`, which can describe quasi-circular binaries with spin-aligned, and `DALI`, which can describe generic planar orbits. Note that the quasi-circular limit of the latter does not exactly reduce to the former model. However, in this thesis, we will often consider the test mass limit of the eccentric avatar of `TEOBResumS`, and, in this case, we will use the Kerr Hamiltonian of Eq. (1.95) instead of the EOB one from Eq. (2.15). In other words, when working in the test mass limit, we neglect the ν-corrections in the conservative part of the dynamics. The study of the test mass limit is a common practice because it allows to test EOB prescriptions in a controlled laboratory, and thus to decide which prescriptions are good candidates also for generic mass ratios [55, 118, 122–125]. We consider only the leading order contributions in ν, both in the radiation reaction force and in the waveform, to be consistent with the numerical results obtained from the linear perturbation theory in Schwarzschild and Kerr. Therefore, the EOB EOM that we will consider when discussing the dynamics of test particles in Kerr and Schwarzschild are

$$\dot{r} = \left(\frac{A}{B}\right)^{1/2} \frac{\partial \hat{H}^{\rm eq}_{\rm Kerr}}{\partial p_{r_*}}, \tag{2.56a}$$
$$\dot{\varphi} = \frac{\partial \hat{H}^{\rm eq}_{\rm Kerr}}{\partial p_{\varphi}} \tag{2.56b}$$
$$\dot{p}_{r_*} = \left(\frac{A}{B}\right)^{1/2} \left(\hat{\mathcal{F}}_r - \frac{\partial \hat{H}^{\rm eq}_{\rm Kerr}}{\partial r}\right), \tag{2.56c}$$
$$\dot{p}_{\varphi} = \hat{\mathcal{F}}_{\varphi}, \tag{2.56d}$$

where the metric potentials A and B are given by Eq. (1.97). If we want to study geodesics, it is sufficient to set $\mathcal{F} = 0$ in the above Hamiltonian equations (and thus recover Eqs. (1.99)).

Note that if the goal is, instead, to accurately describe real astrophysical systems, the ν corrections in the Hamiltonian cannot be neglected, as shown, for example, in Fig. 7 of Ref. [10]. The tests and implementations in the test mass limit proposed in the papers at the base of this thesis [1, 3–6], have to be intended as a base for future improvements of `TEOBResumS-Dalì`.

2.4 Numerical Relativity

If we want to solve the EFE for binary black holes without relying on a perturbative approach, numerical methods are unavoidable. During the final stages of the coalescence, where the EFE exhibit strong non-linearity, numerical approaches stand out as the sole viable method of investigation. For this reason, NR simulations of binary black holes play a crucial role in validating and completing semi-analytical models. This has been already mentioned in Sec. 2.1, and was further discussed in Sec. 2.3 in the context of EOB models.

To numerically evolve a dynamical spacetime, it is necessary to establish a suitable concept of time and reformulate the EFE into a well-posed system of partial differential equations (PDEs). Subsequently, one must employ initial data that accurately reproduces the physical system under investigation and evolve them. Proper handling of singularities is also essential, necessitating the use of appropriate approaches and gauges. Once the problem is well-formulated on the mathematical side, the application of efficient numerical techniques becomes crucial for solving the EFE. Given the computational costs involved, high-performance computing clusters are typically employed. Before delving into these points in the following sections, it is useful to remind that, while this thesis will primarily focus on simulating black hole binaries in GR, the numerical approach is also fundamental for studying gravitational collapses, the coalescence of compact binaries where one or both objects have matter fields (e.g., neutron stars), the dynamical stability of stationary solutions, and compact binaries in alternative theories of gravity.

2.4.1 3+1 decomposition of General Relativity

We start by considering a globally hyperbolic spacetime $\mathcal{M}$, i.e. a spacetime that admits a spacelike hypersurface Σ from which it is possible, loosely speaking, to predict the past and the future. Such a surface is said to be a Cauchy surface. We can then foliate $\mathcal{M}$ by a family of nonintersecting spatial hypersurfaces Σ_t identified by a scalar function $t(p) = x^0(p)$ such that $\mathcal{M} = \cup\Sigma_t$. The future-pointing normal vector in then defined as $n^\mu \equiv -\alpha\,(\nabla t)^\mu$, where α is the lapse function, given by $\alpha = \left(-g^{\mu\nu}\nabla_\mu t \nabla_\nu t\right)^{-1/2}$, and $g_{\mu\nu}$ is the metric on $\mathcal{M}$. One can then define the projector $P^\mu_\nu = \delta^\mu_\nu + n^\mu n_\nu$ and easily show that the induced 3-metric[3] is given by

$$\gamma_{\mu\nu} = P^\sigma_\mu P^\rho_\nu g_{\sigma\rho} = g_{\mu\nu} + n_\mu n_\nu. \tag{2.57}$$

[3]Note that in Eq. (2.57) the 3-metric $\boldsymbol{\gamma}$ is a 4-dimensional tensor. While this might look confusing, one has to consider that the time components vanish in adaptive coordinates (that we will discuss in a moment).

Then, defining the extrinsic curvature as $K_{\mu\nu} \equiv -\gamma^{\sigma}_{\mu}\gamma^{\rho}_{\nu}\nabla_{\sigma}n_{\rho}$ and the vector $m^{\mu} = \alpha n^{\mu}$, simple algebra leads to an evolution equation for the 3-metric:

$$\mathcal{L}_m \gamma_{\mu\nu} = -2\alpha K_{\mu\nu}. \tag{2.58}$$

Note that Eq. (2.58) is a pure geometrical relation and we have not used any physical information in its derivation.

To write Eqs. (1.1) in the 3+1 formalism, it is possible to use the Gauss-Codazzi equations (Eq. (2.95) and (2.101) of Ref. [170]), that are relations between the 4-dimensional Riemann tensor ${}^4R_{\mu\nu\sigma\rho}$ of $\mathcal{M}$ and the 3-dimensional one of Σ_t. These equations "live" on a single spatial hypersurface Σ or, stated in an alternative way, they do not require a complete foliation of $\mathcal{M}$. Using the Gauss-Codazzi relations on $\left({}^4G_{\mu\nu} - 8\pi T_{\mu\nu}\right) n^{\mu} = 0$, one can find the Hamiltonian and the momentum constraints, that contains only spatial quantities and spatial derivatives. Finally, using the Ricci equation that relates ${}^4R^{\sigma}_{\ \mu\nu\rho}$ to 3-quantities but also contains derivatives in the normal direction to Σ_t (see Eq. (3.44) of Ref. [170]), we can find an evolution equation for K_{ij}. The equations read

$$\begin{aligned}
\mathcal{L}_m \gamma_{ij} =& -2\alpha K_{ij}, && \text{(2.59a)}\\
\mathcal{L}_m K_{ij} =& -D_i D_j \alpha + \alpha \Big(R_{ij} + K K_{ij} - 2K_{ik}K^{k}_{\ j} + \\
& 4\pi \left[(S-E)\,\gamma_{ij} - 2S_{ij} \right] \Big), && \text{(2.59b)}\\
C_0 \equiv& R + K^2 - K_{ij}K^{ij} - 16\pi E = 0, && \text{(2.59c)}\\
C_i \equiv& D_j K^{j}_{\ i} - D_i K - 8\pi P_i = 0, && \text{(2.59d)}
\end{aligned}$$

where $K = \gamma^{\mu\nu}K_{\mu\nu}$ is the trace of the extrinsic curvature, D_i is the covariant derivative associated with the 3-metric, $E = n^{\mu}n^{\nu}T_{\mu\nu}$ is the matter energy density, $P_{\mu} = -\gamma^{\sigma}_{\mu}n^{\rho}T_{\sigma\rho}$ is the matter momentum density, $S = g^{\mu\nu}S_{\mu\nu}$ is the trace of $S_{\mu\nu} = \gamma^{\sigma}_{\mu}\gamma^{\rho}_{\nu}T_{\sigma\rho}$. Note that the trace of stress-energy tensor is $T = S - E$. Equations (2.59) are the Arnowitt-Deser-Misner equations [171] written à la York [172], also known as the ADMY equations. The typical coordinates used in Eq. (2.59) are the *adapted coordinates* $x^{\mu} = (t, x^i)$, where x^i are the coordinates on Σ_t and ∂_t is the normal vector to Σ_t. We can write the latter as

$$(\partial t)^{\mu} = m^{\mu} + \beta^{\mu} = \alpha n^{\mu} + \beta^{\mu}, \tag{2.60}$$

where we have introduced the shift vector β^{μ}, which satisfies $n_{\mu}\beta^{\mu} = 0$. Note that $\partial \boldsymbol{t}$ is not necessarily time-like, but this is not a problem since there are no observers associated with it. In these coordinates, the line element reads

$$ds^2 = g_{\mu\nu}dx^{\mu}dx^{\nu} = -\alpha^2 dt^2 + \gamma_{ij}\left(dx^i + \beta^i dt\right)\left(dx^j + \beta^j dt\right), \tag{2.61}$$

and also clarifies why β^i is called *shift* vector (see also Fig. 4.1 of Ref. [170]). Note that α and β^i just describe how we move from one foliation to the next one; that is, they are just gauge degrees of freedom.

However, J. York showed that all the 3-metric that are conformally equivalent to $\boldsymbol{\gamma}$ have the same gravitational wave content [173, 174]. This brings us to the 3+1 *conformal* decomposition of GR. Indeed, among all the 3-metric conformal to $\boldsymbol{\gamma}$, we could choose $\tilde{\gamma}_{ij} = \Psi^{-4}\gamma_{ij}$ such that $\det \tilde{\gamma}_{ij} = 1$. The issue is that, within this choice, Ψ would not

be a scalar and $\tilde{\boldsymbol{\gamma}}$ would not be a tensor (it would be a tensor density with weight -2/3). Therefore, it is useful to define Ψ in terms of a background metric f_{ij} on Σ_t with determinant f, so that

$$\Psi \equiv \left(\frac{\gamma}{f}\right)^{1/12}, \tag{2.62a}$$

$$\tilde{\gamma}_{ij} = \Psi^{-4}\gamma_{ij}. \tag{2.62b}$$

The metric f_{ij} must have signature $(+,+,+)$ and its component must be time-independent, $\partial_t f_{ij} = 0$. We denote the corresponding covariant derivative as $\mathcal{D}_i$ (and $\mathcal{D}^i = f^{ij}\mathcal{D}_j$). In Cartesian coordinates the natural choice is the flat metric $f_{ij} = \mathrm{diag}(1,1,1)$, so that $f = 1$ and the Christoffel symbols are trivial. The relation between the physical and the conformal derivatives can be obtained from the general relations between two connections

$$D_k T^{i_1,\ldots,i_p}_{j_1,\ldots,j_q} = \tilde{D}_k T^{i_1,\ldots,i_p}_{j_1,\ldots,j_q} + \sum_{r=1}^{p} C^{i_r}_{kl} T^{i_1,\ldots,l,\ldots,i_p}_{j_1,\ldots,j_q} - \sum_{r=1}^{q} C^{l}_{kj_r} T^{i_1,\ldots,i_p}_{j_1,\ldots,l,\ldots,j_q}, \tag{2.63}$$

where $C^k_{ij} = \Gamma^k_{ij} - \tilde{\Gamma}^k_{ij}$. One can then define the trace-free part of the extrinsic curvature $A_{ij} = K_{ij} - \frac{1}{3}K\gamma_{ij}$, and then

$$A^{ij} \equiv \Psi^p \tilde{A}^{ij}, \tag{2.64}$$

where natural choices for the conformal rescaling p are $p = -4$, suggested by the kinematical Eq. (2.58), and $p = -10$, suggested by the momentum constraint (2.59d). With the latter choice one can find the Lichnerowicz equation [175] for the conformal factor Ψ, which reads

$$C_0 = \tilde{D}_i\tilde{D}^i\Psi - \frac{1}{8}\tilde{R}\Psi + \hat{A}_{ij}\hat{A}^{ij}\Psi^{-7} + \left(-\frac{1}{12}K^2 + 2\pi E\right)\Psi^5 = 0, \tag{2.65}$$

where $\hat{A}_{ij} \equiv \Psi^{10}A^{ij}$, and $\tilde{R}$ is the Ricci scalar associated with the $\tilde{\gamma}_{ij}$ metric. Similarly, one can conformally-decompose the other equations. With this procedure one finds: i) an evolution equation for the conformal factor from the kinematical equations, ii) evolution equations for K and $\tilde{A}_{ij}$ (with scaling $p = -4$), iii) Hamiltonian and momentum constraints. These constraints can be written either using $\hat{A}^{ij}$ and $p = -10$ (as in the Hamiltonian constraint (2.65)), or $\tilde{A}^{ij}$ and $p = -4$. Energy and momentum are usually rescaled as $\tilde{E} = \Psi^8 E$ and $\tilde{P}^i = \Psi^{10}P^i$.

2.4.2 Global quantities

If we are considering an asymptotic flat spacetime, it is possible to define some global quantities that characterize the spacetime itself and that are useful to build initial data for NR simulations. To start with, we recall that a spacetime is asymptotically flat (AF) if and only if for every hypersurface Σ_t exists a background metric f_{ij} that satisfies the following conditions [170]: i) f_{ij} is flat except for a compact region, ii) there is a coordinate system x^i such that $f_{ij} = \mathrm{diag}(1,1,1)$ for $r = \sqrt{x^i x_i} \to \infty$, and iii) in the asymptotic region $r \to \infty$ we have

$$\gamma_{ij} = f_{ij} + O(r^{-1}), \tag{2.66a}$$

$$\partial_k \gamma_{ij} = O(r^{-2}), \tag{2.66b}$$

$$K_{ij} = O(r^{-2}), \tag{2.66c}$$
$$\partial_k K_{ij} = O(r^{-3}). \tag{2.66d}$$

The asymptotic region $r \to \infty$ is called *spatial infinity*, i_0. Kerr and Schwarzschild are examples of AF spacetimes. Note that the presence of GWs at i_0 would violate Eq. (2.66a). However, we can include GWs in the spacetime by requiring that GWs are emitted at a finite time in the past. We can now define the ADM mass $M_{\rm ADM}$ at i_0 as [170, 171]

$$M_{\rm ADM} = -\frac{1}{8\pi} \lim_{r\to\infty} \oint_{\partial\Sigma_t} \sqrt{q}\,(\kappa - \kappa_0)\,, \tag{2.67}$$

where the integral is on the boundary of the hypersurface, $\partial\Sigma_t = \partial\mathcal{M} \cap \Sigma_t$, q is the determinant of the induced metric of $\partial\Sigma_t$ embedded in (Σ, γ_{ij}), and κ is the trace of the corresponding extrinsic curvature; κ_0 is the trace of extrinsic curvature of $\partial\Sigma_t$ embedded in (Σ, f_{ij}). Using the normal vector to $\partial\Sigma_t$, s^i, and the conformal decomposition we can also write [170]

$$M_{\rm ADM} = -\frac{1}{2\pi} \lim_{r\to\infty} \oint_{\partial\Sigma_t} \sqrt{q}\left(\mathcal{D}_i\Psi - \frac{1}{8}\mathcal{D}^j\tilde{\gamma}_{ij}\right) \tag{2.68}$$

In the Schwarzschild case one finds $M_{\rm ADM} = M$. Moreover, if the dominant energy condition $E^2 \geq P_i P^i$ is satisfied, then $M_{\rm ADM} \geq 0$, where the equality is obtained if and only if Σ_t is a foliation of Minkowski. We also have that $\dot{M}_{\rm ADM} = 0$. In NR simulations, $M_{\rm ADM}$ is computed at a large finite radius and therefore the integral is in general not conserved. However, if we also consider the radiation traveling to future null infinity that crosses the sphere at which $M_{\rm ADM}$ is computed, then the integral is approximately conserved. We can further define the ADM momentum as [170, 171]

$$P_k^{\rm ADM} = \frac{1}{8\pi} \lim_{r\to\infty} \oint_{\partial\Sigma_t} \sqrt{q}(\boldsymbol{\partial}_k)^i s^j \left(K_{ij} - K\gamma_{ij}\right). \tag{2.69}$$

The 4-momentum $(-M_{\rm ADM}, P_k^{\rm ADM})$ transforms as a 1-form under coordinate changes that preserve the asymptotic flatness. Note that the index k is associated with the vector $\boldsymbol{p}$ and is not tensor index.

Finally, considering the Killing vectors associated with rotations $\boldsymbol{\phi}$, we could try to define an angular momentum similarly to the linear momentum case. We can thus write [170]

$$J_k = \frac{1}{8\pi} \lim_{r\to\infty} \oint_{\partial\Sigma_t} \sqrt{q}\,(\boldsymbol{\phi}_k)^i \left(K_{ij} - K\gamma_{ij}\right). \tag{2.70}$$

However, this quantity does not transform as a 1-form (as opposed to $P_k^{\rm ADM}$), and moreover, the AF conditions do not guarantee the existence of the integral (as opposed to the cases of $M_{\rm ADM}$ and $P_k^{\rm ADM}$). To cure this problem, one could impose even stronger asymptotic conditions:

$$\partial_k \tilde{\gamma}_{ij} = O(r^{-3}), \tag{2.71a}$$
$$K = O(r^{-3}). \tag{2.71b}$$

Despite these conceptual difficulties, the notion of ADM angular momentum is often used in the literature for binary black holes, see e.g. [176–178]. For this reason, we will use the notation[4] $J_{\rm ADM}$, even if Eq. (2.70) was not presented in the original ADM article [171].

[4]Since in this thesis we focus only spin-aligned or anti-aligned binaries, the z-index is understood since $J_x^{\rm ADM} = J_y^{\rm ADM} = 0$.

The initial values of $M_{\rm ADM}$ and $J_{\rm ADM}$ are also fundamental to study the dynamics of binaries. Indeed, these two values, together with the fluxes computed from the NR waveforms, can be used to construct the energetic curves $E(J)$, where typically E is the binding energy, defined as the total energy minus the rest mass of the system. These gauge-invariant relations can be then exploited also to validate EOB models as done, for example, in Ref. [179].

2.4.3 Initial data

We can now turn our attention to the initial data problem. We now want to set up some initial conditions that satisfy the constraints of Eq. (2.59c) and (2.59d) (or equivalent) and that, at the same time, have a physical meaning. Since we have to determine 12 components (for γ_{ij} and K_{ij}), we have to prescribe 8 quantities and solve for the remaining 4. In this thesis, we focus on the Bowen-York initial data for black holes [172, 180, 181]. One can start by prescribing on Σ_0 conformally and asymptotically flat vacuum data: $\tilde{\gamma}_{ij} = f_{ij}$, $K = 0$, and $\tilde{E} = \tilde{P}^i = 0$. The condition $K = 0$ is known as *maximal slicing* because it implies that Σ_t has the maximum volume. One can then write the extrinsic curvature in terms of a vector potential $\boldsymbol{V}$ (see e.g. Eq. (23) of Ref. [182]) and obtain two elliptic equations for Ψ and $\boldsymbol{V}$. The vector potential can be given as a sum of terms that are singular at N_p spatial points, known as *punctures* (see e.g. Eq. (26) of Ref. [182]). Each of these terms depends on six parameters (P_i, S_i) that can be identified as the linear momenta and spins of the punctures. In the case of a single puncture, these parameters reduce to the aforementioned ADM linear and angular momentum. The conformal factor is then written isolating the Brill-Lindquist singular part $\Psi_{\rm BL}$ as

$$\Psi = \Psi_{\rm BL} + u = 1 + \sum_{n=1}^{N_p} \frac{m_n}{2|\boldsymbol{x}_n|} + u \tag{2.72}$$

with $u \to 0$ as the Euclidean distance from the puncture goes to infinity, $|\boldsymbol{x}_n| \to \infty$. The parameter m_n is known as the *bare mass* of the puncture. Then one can solve numerically the Hamiltonian constraints for u, which is generally C^2 at the puncture locations, using for example spectral methods [182]. The puncture approach has been used in the seminal paper of 2005 [77] and it is still used in NR simulations nowadays [85, 183, 184]. Other approaches for the initial data include the conformal thin-sandwich [185, 186], its extended version [187], and methods that exploit helical symmetry [188, 189].

2.4.4 Gauge conditions

As mentioned before, the lapse function α and β^i are gauge degrees of freedom. However, to successfully simulate BH spacetimes, these quantities have to be chosen carefully. In particular, one has to choose a gauge that has singularity-avoiding properties and that minimizes, in some way, the coordinate distortion.

Indeed, if one uses the simplest choice, known as *geodesic* gauge, that consists of setting $\alpha = 1$ and $\beta^i = 0$ everywhere, the simulations crash after a short time. For example, in Schwarzschild, the simulation would crash at $t \sim \pi M$, when the innermost grid point reaches the fundamental singularity [190]. However, we have already discussed a gauge condition that has singularity-avoiding properties. Indeed, the extrinsic curvature, and therefore its trace $K = -\nabla n^\mu$, measures how much n^μ bends when transported along

Σ_t. We have thus that the maximal slicing condition $K = 0$, that can be written as an equation for the lapse α, prevents the Eulerian observers associated with n^μ from converging towards a singularity (in the eventuality that it forms at some point during the evolution). This gauge leads to the so-called *collapse of the lapse*, i.e. $\alpha \to 0$ near singularities for $t \to \infty$. A general evolution equation for α is the Bona-Masso slicing [191]

$$\mathcal{L}_m \alpha = -\alpha^2 f(\alpha) K, \tag{2.73}$$

that for $f(\alpha) = 0$ reduces to the geodesic gauge, for $f(\alpha) = 1$ reduces to the so-called *harmonic* gauge, where the name is because the same equation can be obtained by considering $\Box x^0 = (-g)^{-1/2} \partial_\mu \left[(-g)^{1/2} g^{\mu\nu} \partial_\nu t \right] = 0$, and finally by setting $f(\alpha) = 2/\alpha$ one obtains the so-called 1+log gauge. The name of the last gauge is because if one sets $\beta^i = 0$, then $\alpha = 1 + \log(\gamma)$ is a solution of the evolution equation (2.73). Both the harmonic and 1+log gauges have singularity-avoiding properties [188].

While the singularity-avoiding properties are useful to avoid crashes of the simulations, the collapse of the lapse near the singularities leads to large coordinate gradients that would require too many grid points to be resolved. We want therefore to choose β^i so that the distortion is minimal. Then, defining the trace-free part of the distortion $Q_{ij} = \partial_t \gamma_{ij} - \frac{1}{3} Q \gamma_{ij}$, one can extremize the associated functional $I\left[\beta^i\right] = \int_{\Sigma_t} Q_{ij} Q^{ij} \sqrt{\gamma} d^3x$ and find an elliptic equation for β^i. This latter condition is automatically satisfied by stationary spacetimes since if $\boldsymbol{\partial}_t$ is a Killing vector, the distortion tensor identically vanishes. However, for practical purposes, evolution equations are always preferred to elliptic equations. For this reason, it is more common to use parabolic and hyperbolic gauge conditions for β^i with minimal distortion properties, known as Gamma-freezing and Gamma-driver [192]. The latter, after an integration, can be written as [193, 194]

$$\partial_t \beta^i = \mu_s \tilde{\Gamma}^i - \eta \beta^i + \beta^j \partial_j \beta^i, \tag{2.74}$$

where μ_s and ν are parameters whose values has to been chosen carefully in order to not spoil the well-posedness of the evolution scheme considered [194] (see also discussion in the next section). A typical choice for the former is $\mu_S = 1$, while the damping $\eta = 2/M$ works well for binaries with mass ratio close to one. The 1+log slicing and the hyperbolic Gamma-driver are typical choices for NR codes that evolve binaries using the punctures approach [77, 85, 183, 184, 195]. The typical initial values for the lapse and the shift vector on the initial slice are $\alpha = \Psi_{\rm BL}^{-2}$ and $\beta^i = 0$.

2.4.5 Free evolution schemes

If the initial data satisfy the energy and momentum constraints at $t = 0$, then the system can be evolved by solving numerically the evolution equations and, aside from numerical errors, the constraints remain satisfied during the evolution. We thus find initial data that satisfy the constraints, and then we evolve the system without enforcing the constraints during the evolution (but they have to be monitored to ensure that they remain small). However, to evolve the initial data, the 3+1 scheme employed must be well-posed, i.e. the solution of the associated Cauchy problem is unique and depends continuously on the initial data. More formally, a well-posed initial value problem exists if and only if there is a norm $||.||$ and a class of initial data so that the solution $u(t, x)$ is always bounded as $||u(t, x)|| \leq K e^{\alpha t} ||u(0, x)||$ for some α, K that do not depend on the initial data. The existence of a well-posed Cauchy problem is guaranteed if the second-order PDE system

under investigation is strongly hyperbolic, i.e. if and only if the principal part (the highest derivatives) is in the form $\Box_g u \simeq 0$. The evolution ADMY equations (2.59) are strongly hyperbolic if the lapse α is of the Bona-Masso family (Eq. (2.73)) and the momentum constraint identically vanishes during the evolution. If one drops this latter condition, then the system is only weakly hyperbolic[5], and thus the problem is ill-posed. Since the momentum constraint is inevitably violated during the evolution due to numerical approximations, the ADMY formulation cannot be used in numerical simulations. We thus mention in the following some common free-evolution schemes that are used by the NR community.

The first scheme for evolutions that we mention is the generalized harmonic gauge (GHG) [196–198], which has been used by Pretorius in the first complete evolution of a binary black hole merger [76] and is also used nowadays (in first-order symmetric hyperbolic formulation) by the SXS collaboration [83]. This formulation is used in numerical codes where regions inside the event horizons and around the fundamental singularities are excised by the computational domain. We have already encountered the (not generalized) harmonic gauge a few times, which can be written as $\Box x^\alpha = -g^{\mu\nu}\Gamma^\alpha_{\mu\nu} 0 \equiv -\Gamma^\alpha = 0$. If one set this gauge, the EFE are strongly (even symmetric) hyperbolic. One can then generalize this condition as $\Gamma_\alpha = H_\alpha$, where H_α is some given function, and define the constraint $Z_\alpha \equiv H_\alpha - Z_\alpha = 0$. The lhs of the EFE in this formulation can be written as $g^{\sigma\rho}\partial_\sigma\partial_\rho g_{\mu\nu} + (\dots)$, where the dots denote a non-linear part with first-order metric derivatives. Then the vacuum EFE in the GHG can be written as $R_{\mu\nu} - \nabla_{(\mu} Z_{\nu)} = 0$ with $Z_\mu = 0$. From the Bianchi identities one can find that the constraint evolves as linear wave equation, $\Box_g Z_\mu + R_{\mu\nu} Z^\nu = 0$, so that if $Z_\mu = \dot{Z}_\mu = 0$ initially, the constraint vanishes for the whole evolution. In actual evolutions, the constraints are damped, see e.g. Ref. [76].

A different free-evolution scheme that is typically used in codes that use the punctures approach is the Baumgarte-Shapiro-Shibata-Nakamura (BSSN) formulation [199, 200]. The first successful binary black evolution with this scheme has been achieved in Ref. [77], within four months from the result of Ref. [76]. If one considers the ADMY equations (2.59), then it is possible to define an auxiliary variable ($f^i = \partial_j \gamma^{ij}$) whose time-evolution is linked to the momentum constraint. Using thus the momentum constraint, one can re-write the ADMY equations so that the principal part is a wave-like equation. To obtain the BSSN equations, one starts from the conformal ADMY equations and define the auxiliary conformal variable $\tilde{\Gamma}^i \equiv \left(\tilde{\Gamma}^i_{jk} - F^i_{jk}\right)\tilde{\gamma}^{jk}$, where we recall that F^i_{jk} are the Christoffel symbols of the background metric f_{ij}. Then an evolution equation is found for this variable, so that the BSSN has evolution equations for Ψ, $\tilde{\gamma}_{ij}$, K, $\tilde{A}_{ij}$, Γ^i. Together with some classes of gauges, including the 1+log slicing and the Gamma-driver shift, the BSSN are strongly hyperbolic [194]. We also mention that typically, instead of using Ψ, it is common to use $\chi \equiv \Psi^{-4}$. The equations obtained in this way have some $1/\chi$ terms that are in principle singular, but numerical experiments showed that they are not problematic if one uses a numerical floor for χ. One can then find the positions of the punctures by searching for curves along which the variable χ vanishes. From the evolution equation for the conformal factor χ, one can find that the velocity of the puncture is simply given by the shift vector evaluated at the puncture locations,

$$v^i_p = -\beta^i|_{x_p}. \tag{2.75}$$

[5]That is, the principal symbol has real eigenvalues but not a complete set of eigenvectors.

A free-evolution scheme that is closely related to the BSSN one is the Z4c scheme [201–203], which improves the constraints-violation by introducing an additional field that transforms the constraints in evolution equations. More precisely, one can add (in a fully covariant way) an extra 4-vector Z_μ to the lhs of the EFE as $R_{\mu\nu} \to R_{\mu\nu} + 2\nabla_{(\mu} Z_{\nu)} +$ (damping terms for Z_μ). For $Z_\mu = 0$, one recovers GR. Moreover, from the Bianchi identities we have that Z_μ evolves according to a wave-like equation as discussed in the GHG case, so that if Z_μ vanishes at the beginning, then it vanishes at all times. As anticipated, the advantage of introducing Z_μ is that the constraints are now hyperbolic equations. This scheme is the one implemented, for example, in `GR-Athena++` [14, 85].

Chapter 3

Eccentric dynamics and inspirals in the test mass limit

From this chapter, we start to present original results. We begin by discussing the phenomenology of eccentric binaries in the test particle limit, focusing on the dynamics and on the eccentric inspiral. In particular, we will analyze the analytical Newtonian noncircular prescriptions for the EOB eccentric radiation. The following sections are mostly based on Ref[1]. [1]. The discussion of 2PN noncircular corrections [3–5] is postponed to Chapter 4, while we will analyze in detail the transition from the inspiral to the merger-ringdown phase in Chapter 5, following Ref. [6].

As discussed in Sec. 2.2, the EOB description of comparable mass binaries is smoothly connected by the symmetric mass ratio ν to the test particle limit. In other words, the time-like geodesics are naturally included in the EOB formulation and, therefore, one can obtain geodesic orbits by solving Eqs. (2.56) setting the radiation reaction $\mathcal{F}$ to zero (that is, solving Eqs. (1.99)). Given a certain test particle dynamics, even a geodesic one, we can compute the associated waveform, either numerically by solving the RWZ equations (1.57) or the Teukolsky equation (1.80) (in appropriate coordinates), or analytically by using the EOB prescription (2.36). Note that in a realistic scenario, one should impose the conservation of energy, and thus consider the back-reaction due to the GW emission on the dynamics; in other words, one should take into account the non-conservative effects parametrized by $\mathcal{F}$. However, if our goal is to test the goodness of the analytical prescriptions for the inspiral in the test particle limit, we can just ignore the back-reaction and compare the EOB analytical waveform to the numerical one obtained from linear perturbation theory. More importantly, one can use the numerical waveforms to compute the numerical fluxes at infinity through Eqs. (1.42), and compare them to the analytical radiation reaction $\mathcal{F}$ computed using the balance equations (2.37). For these reasons, as a first step, one can consider the waveform associated with geodesic motion and study the non-conservative dynamics only in a second moment.

The test particle limit is, therefore, a controlled laboratory that we can exploit to test the analytical model. If a certain prescription works well in the test particle limit, then it is probable (but not guaranteed) that will work well also in the comparable mass case. On the other hand, if a prescription underperforms in the test particle limit, there is little or no hope that it will be reliable in the comparable mass scenario. Note that the

[1]Ref. [1] has been concluded and submitted to the editor a few months after the beginning of my Ph.D., but some of the results of that paper have been already discussed in my master thesis. However, to make the discussion more self-consistent, we discuss these results also in this thesis.

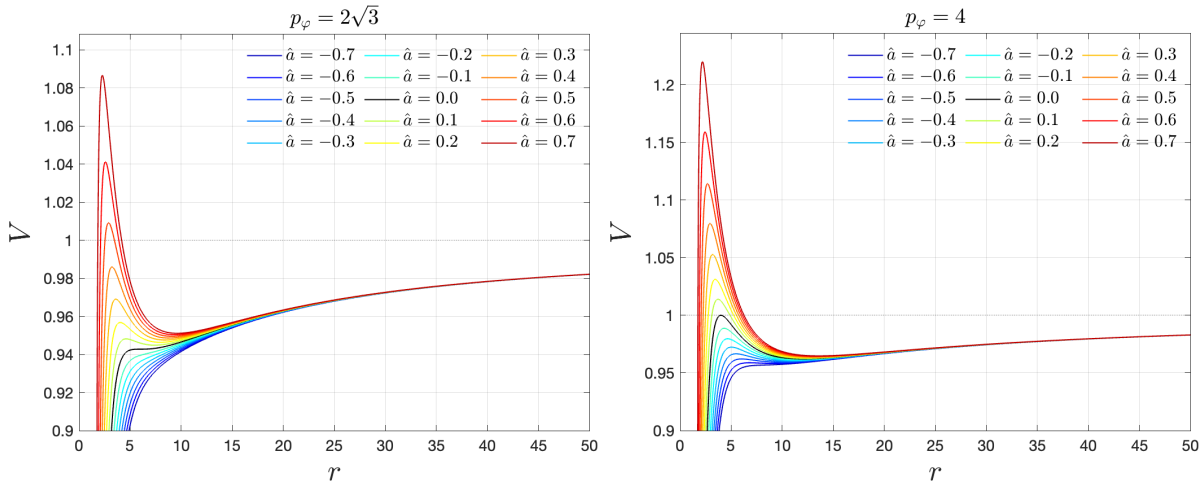

Figure 3.1: Kerr effective potentials for $p_\varphi = (2\sqrt{3}, 4)$ and different spins. The Schwarzschild potentials are highlighted in black.

analytical/numerical comparisons in the test particle limit are performed using the same dynamics, and therefore there is no ambiguity in the waveform/fluxes comparisons. In the general case, when one considers mass ratios close to $q = 1$, the analytical/numerical comparisons are performed considering EOB and NR waveforms. However, choosing EOB initial data that reproduces the same physical system simulated by the NR simulation is far from trivial and, indeed, there is no clear procedure of how to perform this initial data matching for generic orbits. The comparison is easier (but not trivial) in the quasi-circular case, but it becomes more difficult for eccentric or even hyperbolic-like orbits. It is thus evident that the extreme mass ratio regime is not only useful for practical purposes (since, as can be imagined, the numerical solution of RWZ/Teukolsky equation is much less computationally expensive than full-GR numerical simulations), but it is also useful from the conceptual point of view. We will come back to the EOB/NR comparison issue later. For the moment, we focus on the test particle scenario, first studying the conservative (geodesic) dynamics, and then the non-conservative ones.

3.1 Kerr planar orbits and eccentricity

We start by discussing the geodesics in Schwarzschild and equatorial Kerr. Since the orbits are planar, they are fully characterized by two constants of motion. The most natural choice is to consider the μ-normalized energy $\hat{E}$ and the angular momentum[2] p_φ. The type of orbit that corresponds to a certain pair $(\hat{E}, p_\varphi)$ can be easily understood by looking at the effective potential

$$V(r; p_\varphi) \equiv \hat{H}^{\rm eq}_{\rm Kerr}|_{p_{r_*}=0}. \tag{3.1}$$

In Figure 3.1 we show the potential for different values of spin and two values of angular momentum, $p_\varphi = (2\sqrt{3}, 4)$. If the potential has a local minimum, then bound orbits are allowed. In particular, it is possible to have circular geodesics with radius $r_{\rm qc}$, where $r_{\rm qc}$ is the radius at which the potential has the minimum. More generally, since $V \sim$

[2]We recall that we are considering mass-rescaled phase space variables related to the physical ones as discussed in Sec. 1.6.2 (see also Sec. 2.2).

$1-2/r+O(1/r^2)$, bound orbits can be obtained for any energy in the range $\hat{E}_{\rm qc} \leq \hat{E} < \min(1, V_{\rm max})$; the limiting case $\hat{E} = V_{\rm max} < 1$ is marginally stable. The two radial turning points of the orbit, the periastron r_- and the apastron r_+, are defined by the condition $\hat{E} = V(r_\pm; p_\varphi)$. If the potential barrier has a maximum bigger than one, then unbound orbits (scatterings) are allowed for $1 \leq \hat{E} \leq V_{\rm max}$. If $\hat{E} > V_{\rm max}$, then the particle will inevitably plunge toward the black hole. Note that for a certain value $p_\varphi^{\rm LSO}$, the local maximum and the local minimum degenerate in an inflection point, and therefore no stable bound orbits with $p_\varphi < p_\varphi^{\rm LSO}$ are allowed. In the Schwarzschild case, this happens for $p_\varphi^{\rm LSO} = 2\sqrt{3}$, and the inflection point is located at $r_{\rm LSO} = 6$. Circular orbits are allowed only for $r \geq r_{\rm LSO}$, and for this reason, the orbit with radius $r_{\rm LSO}$ is known as the *last stable orbit* (LSO). In the case of extremal black holes, we have $r_{\rm LSO} = 9$ for retrograde orbits (i.e. when the orbital angular momentum is anti-aligned with the Kerr spin), and $r_{\rm LSO} = 1$ for prograde orbits [204].

While energy and angular momentum allow us to completely describe planar geodesics, we would like to define some constants of motion with a more immediate geometrical meaning. It is well known that the two-body problem in Newtonian gravity has an exact solution and the orbits are given by conic sections. These orbits can be parametrized as $r(\varphi) = p/(1 - e\cos\varphi)$, where p is the semilatus rectum and e is the eccentricity. For $0 \leq e < 1$ we have elliptical orbits, of which the circular ones ($e = 0$) are a particular case. For $e \geq 1$ we have unbound orbits: parabolic for $e = 1$, hyperbolic for $e > 1$. In the case of bound orbits, the periastron r_- and the apastron r_+ can be found as $r_\pm = p/(1 \mp e)$. Then, by simply inverting these relations, we find that the Newtonian eccentricity and semilatus rectum can be written in terms of the two radial turning points as

$$e = \frac{r_+ - r_-}{r_+ + r_-}, \qquad p = \frac{2 r_+ r_-}{r_+ + r_-}. \tag{3.2}$$

We adopt Eqs. (3.2) to define the eccentricity and the semilatus rectum also in the general-relativistic case, where the two radial turning points are defined, as discussed above, by the condition $\hat{E} = V(r; p_\varphi)$. Then for each pair of $(\hat{E}, p_\varphi)$, we can compute (e, p). Note that, by construction, this definition of eccentricity in the full relativistic case is valid only for bound orbits. To have bound orbits, the Kerr potential $\tilde{V}$, defined as $\dot{r}^2 + \tilde{V}(r; \hat{E}, p_\varphi) = 0$ (see e.g. Eq. (1) of Ref. [205]), must have three roots: $(\bar{r}, r_-, r_+)$. If $\bar{r} = r_-$, then the bound orbit is only marginally stable. In terms of semilatus rectum, this stability condition translates in the constraint $p \geq p_s(e, \hat{a})$, where $p_s(e, \hat{a})$ is known as the *separatrix*, and its expression for planar orbits is implicitly given by [205, 206]

$$\begin{aligned} &p_s^2 (p_s - 6 - 2e)^2 + \hat{a}^4 (e-3)^2 (e+1)^2 \\ &- 2\hat{a}^2 (1+e) p_s \left[14 + 2e^2 + p_s (3 - e)\right] = 0. \end{aligned} \tag{3.3}$$

In the non-spinning case, Eq. (3.3) simply reduces to $p_s = 6 + 2e$, while in the circular case p_s reduces to $r_{\rm LSO}$. In other words, the separatrix is an eccentric generalization of the LSO. In terms of energy, angular momentum, and radial potential V, the separatrix corresponds to the condition $\hat{E} = V_{\rm max}(r; p_\varphi)$. Note that, in general, it is not possible to provide a dynamical definition of eccentricity in GR. However, it is useful to use (e, p) to label geodesics or even non-conservative orbits (see discussion below), since they provide a clear geometrical intuition of the orbit considered. We mention, en passant, that the effects of eccentric motion on waveforms and fluxes have been first studied in a seminal article by Peters and Mathews [207], and that the PN quasi-Keplerian parametrization [208] uses

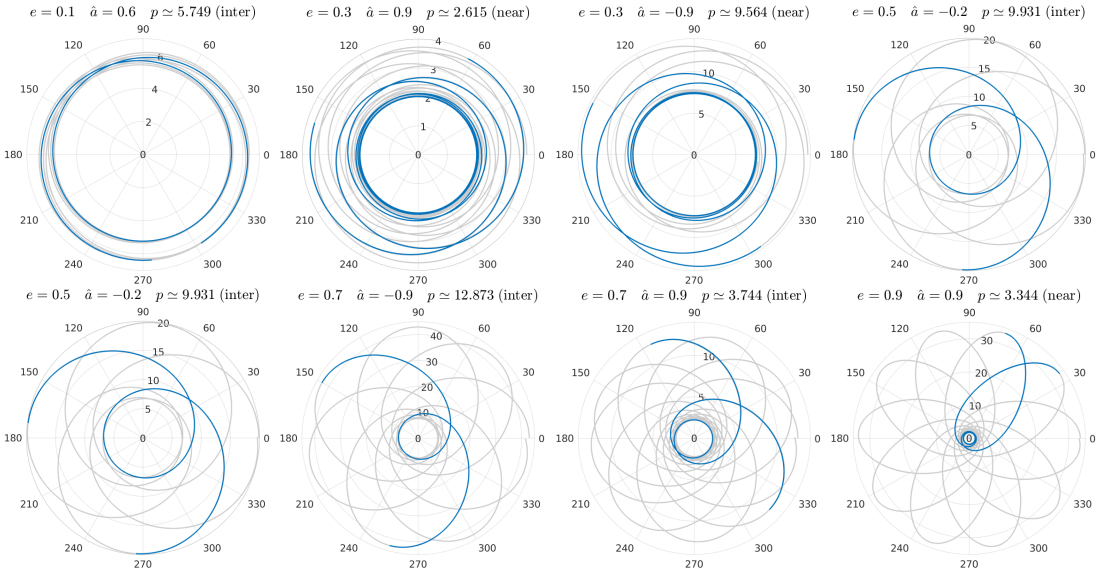

Figure 3.2: Examples of eccentric geodesic configurations considered in Ref. [1]. We have highlighted in blue a single radial orbit. The corresponding (2,2) and (4,4) multipoles for the configurations with $(e, \hat{a}) = (0.7, -0.9)$, $(0.1, 0.6)$, $(0.7, 0.9)$, and $(0.9, 0.9)$ are shown in Fig. 3.5.

three different eccentricities to describe bound orbits, but in this work we will not use them since in our EOB formalism we use the notion of eccentricity almost exclusively for labeling purposes.

In Ref. [1], we have run 144 geodesic configurations with eccentricities $e = (0, 0.1, 0.3, 0.5, 0.7, 0.9)$ and spins in the range $\hat{a} \in [-0.9, 0.9]$, typically $\hat{a} = (0, \pm 0.2, \pm 0.6, \pm 0.9)$. For each pair of spin and eccentricity $(\hat{a}, e)$, we have chosen three different semilatera recta: $p = p_s(e, \hat{a}) + 0.01$, $p = 9\, p_s(e, \hat{a})/p_s(e, 0)$, and $p = 13\, p_s(e, \hat{a})/p_s(e, 0)$. Depending on the value of the semilatus rectum, we referred to these simulations as, respectively, *near*, *intermediate*, and *distant*. The complete list of eccentric geodesic configurations in Kerr that we consider can be found in Table A.1. Moreover, some trajectories are shown in Fig. 3.2, where we have highlighted a radial orbit in blue. As can be seen, the bound orbits considered exhibit a strong periastron precession. The effect is mitigated in the case of orbits with large semilatus rectum. In the case of near simulations, i.e. those with $p = p_s + 0.01$, the precession becomes so relevant that the particle has a circular whirl near the periastron. After this whirl, the particle zooms out and continues on an elliptic-like orbit until the next periastron passage. For this reason, orbits of this kind are called *zoom-whirl* orbits; see e.g. Ref. [209].

If non-conservative effects are taken into account when solving the Hamilton equations (i.e. if $\mathcal{F} \neq 0$), both energy and angular momentum cease to be constants of motion. During the later stages of evolution, a point is reached where the condition $\hat{E} = V_{\rm max}(r; p_\varphi)$ is satisfied, so that the periastron is no longer defined. We refer to this time as the separatrix-crossing time $t_{\rm sep}$. As a consequence, both e and p cannot be longer computed after $t_{\rm sep}$. However, at each $t \leq t_{\rm sep}$ we can compute both e and p, so that we can have time-evolutions of these two quantities. The final measurable eccentricity is identified as $e_{\rm sep} = e(t_{\rm sep})$. We will come back to non-conservative dynamics in Chapter 5, where we will discuss the transition from inspiral to plunge for the Schwarzschild case in more detail. While eccentricity and semilatus rectum serve as valuable labels for configurations and contribute to an intuitive comprehension of the types of bound orbits under examination,

they are not suitable variables for the late inspiral in non-conservative cases, since they are not defined for $t \geq t_{\rm sep}$. For this reason, while we will label also the non-conservative configurations using the initial values of eccentricity and semilatus rectum, in practice we will always convert (e_0, p_0) in the initial values of energy and angular momentum, $(\hat{E}_0, p^0_\varphi)$, and use these quantities to start the evolution. Furthermore, we will always start our evolutions from the apastron, so that the initial radius is $r_0 = p_0/(1-e_0)$ and $p^0_{r_*} = 0$.

We conclude this discussion by noting that the definition of eccentricity discussed above for orbits in Kerr can be easily extended to the comparable mass case. Indeed, one can always find e and p using Eqs. (3.2), where the radial turning points $r_\pm$ are obtained from two equations $\hat{E} = H_{\rm EOB}(r_\pm, p_\varphi, p_{r_*} = 0)$. Solving these two equations creates a map $(\hat{E}, p_\varphi) \leftrightarrow (r_-, r_+)$, and thus through Eqs. (3.2) a map $(\hat{E}, p_\varphi) \leftrightarrow (e, p)$. Note that the eccentricity is not gauge invariant (nor is the semilatus rectum), and therefore to have an apples to apples EOB/NR comparison, it is not sufficient to consider EOB configurations with the same initial eccentricity (and initial frequency) as in the NR case. That is, the EOB eccentricity is not the same eccentricity considered in NR simulations, and could not be otherwise. See for example the comparisons in Table III of Ref. [147]. In Ref. [210], an attempt has been made to map various eccentric definitions, focusing in particular on the two EOB models `TEOBResumS` and `SEOBNR`.

3.2 Waveform and fluxes from eccentric geodesics

In this section we analyze waveforms and fluxes generated by eccentric conservative dynamics. We start by discussing how the numerical results are obtained and how accurate they are. We then briefly discuss how we improved the *circular* sector of the EOB multipolar waveform. Finally, we discuss and test the analytical waveforms and fluxes obtained by applying the Newtonian generic prefactor discussed in Sec. 2.3.2. Note that some of these results have been already discussed in my master thesis, but we reexamine and elaborate on them in this section to ensure a comprehensive and self-contained discussion. For the moment, we neglect the 2PN noncircular corrections to the waveform and radiation reaction; these effects will be discussed in Chapter. 4.

3.2.1 Numerical test mass waveforms

We now discuss the numerical waveforms that can be obtained from `RWZHyp` and `Teukode` using, in the source terms, the dynamics discussed in Sec. 3.1. We also provide some comparisons between the two time-domain codes and with other results present in the literature. The `RWZHyp` simulations that we will consider in this section have been performed by Danilo Chiaramello, while the `Teukode` have been performed by myself. Both computations have been performed on the Virgo "Tullio" server in Torino, supported by INFN. The discussion below is taken from Ref. [1], with minimal changes.

At the time of Ref. [1], both `RWZHyp` and `Teukode` were not systematically tested for eccentric configurations, even if some eccentric configurations performed with `RWZHyp` were considered in Ref. [145]. For this reason, we need to test the consistency of our results with published results. With this goal in mind, we compare the fluxes averaged along a radial orbit, $\langle \dot{E} \rangle$ and $\langle \dot{J} \rangle$, for both Schwarzschild and Kerr backgrounds. The mean is computed as an integral average of the fluxes from Eqs. (1.42) on a radial orbit,

Table 3.1: Table from Ref. [1]. Averaged numerical fluxes computed with `RWZHyp` and `Teukode` compared with results present in the literature, see discussion in the text.

		`Teukode` (TD) 3600×160	`Teukode` (TD) 5400×320	`RWZHyp` (TD)	Martel (TD)	Barack (GSF)	Fujita (FD)
$p = 7.50478$	$\langle \dot{E} \rangle \cdot 10^4$	3.16885	3.16888	3.17077	3.1770	3.1691	3.16899989184
$e = 0.188917$	$\langle \dot{J} \rangle \cdot 10^3$	5.96731	5.96737	5.96998	5.9329	5.967608	5.96755215608
$p = 8.75455$	$\langle \dot{E} \rangle \cdot 10^4$	2.12276	2.12269	2.12718	2.1484	2.1243	2.12360313326
$e = 0.764124$	$\langle \dot{J} \rangle \cdot 10^3$	2.77643	2.77635	2.78077	2.7932	2.77746	2.77735938996

whose corresponding radiation is not contaminated by the junk radiation. This latter phenomenon is a spurious signal generated by the fact that we use conformally-flat initial data, and therefore the linearized constraints are violated at the beginning of the simulation. The spurious signal propagates towards the central black hole and generates a sort of spurious ringdown signal. The junk is however damped and, within the configurations considered in this work, becomes typically negligible after $t \sim 200 - 300$ (here t is M-rescaled, as usual).

For the nonspinning case, the comparisons are shown in Table 3.1, where our ν-normalized averaged fluxes are compared with the classic time-domain (TD) results of Martel [209], as well as to more recent GSF calculations of Barack and Sago [211] and frequency-domain(FD) results of Fujita [212]. For the `RWZHyp` runs shown in Table 3.1, the computational domain used for the lower eccentricity case was $[R_*^-, S^+]_{R_*^+} = [-50, 70]_{50}$, while for the other configuration it was $[-50, 90]_{70}$; in both cases the radial resolution was $N_r = 6001$. For `Teukode` we used $N_r \times N_\theta = 3600 \times 120$. In both codes, the CFL factor used was 0.5. We verified that in the `Teukode` case the difference between resolutions 3600×120 and 5400×320 is negligible. Since in the second case the computational time is significantly higher, we stuck with the lower resolution. Note that we sum the multipoles up to $\ell_{\rm max} = 8$, but in the other works $\ell_{\rm max}$ assumes different values. Despite these differences, the agreement with previous calculations remains satisfactory due to the higher multipoles being highly subordinate. It is worth noting that, among the TD codes, `Teukode` stands out as the most accurate, at least for the resolutions considered. Additionally, we conducted a comparison of the instantaneous (i.e. not averaged) energy and angular momentum fluxes for `Teukode` and `RWZHyp` in cases where $(e, p) = (0.3, 9), (0.5, 11)$, and $(0.8, 13)$. The analysis revealed that the relative difference between the two numerical instantaneous fluxes peaks at periastron, reaching a maximum of only 0.3%.

In the case of a Kerr background, we have compared the averaged fluxes for $\hat{a} = 0.5$ and $e = 0.5$ obtained using `Teukode` with the results of Glampedakis and Kennefick [213]. The comparison, shown in Table 3.2, highlights the good agreement, with discrepancies below 0.2%. Note however that, as above, we fixed $\ell_{\rm max} = 8$, while Ref. [213] sums up to $\ell_{\rm max} = 10 - 17$ and this affects the comparison. In fact, in the first case reported in Table 3.2, the $\ell = 8$ modes have a relative contribution of $\sim 0.25\%$ to the total fluxes, therefore including also the multipoles with $\ell > 8$ would probably improve the agreement. Note also that when the semilatus rectum is increased, the agreement improves, because the higher modes become less and less relevant at large separations. We have also considered a configuration with $\hat{a} = 0.9$, $e \simeq 0.3731$, and $p \simeq 12.152$, calculated both in Ref. [214] and Ref. [213]. In this case, the contribution of the $\ell = 8$ modes is only of the order of $2 \cdot 10^{-5}$ due to the large value of p used, and, as a consequence, the discrepancy is smaller. Nonetheless, comparing the energy and angular momentum fluxes with the

Table 3.2: Table from Ref. [1]. Numerical averaged fluxes in Kerr spacetime. We compare the results of `Teukode` ($\ell_{\rm max} = 8$) with the results obtained by Ref. [213] ($\ell_{\rm max} = 10 - 17$). For the last simulation, only $\langle \dot{E}_{GK} \rangle$ is reported in Ref. [213].

$\hat{a}$	e	p	$\langle \dot{E}_{\rm teuk} \rangle$ $\cdot 10^3$	$\langle \dot{J}_{\rm teuk} \rangle$ $\cdot 10^2$	$\langle \dot{E}_{GK} \rangle$ $\cdot 10^3$	$\langle \dot{J}_{GK} \rangle$ $\cdot 10^2$
0.5	0.5	5.1	4.20753	3.25791	4.21594	3.26383
0.5	0.5	5.5	2.11538	1.89340	2.11797	1.89546
0.5	0.5	6.0	1.19519	1.22870	1.19638	1.22973
0.9	0.3731	12.152	0.023571	0.080743	0.023570	/

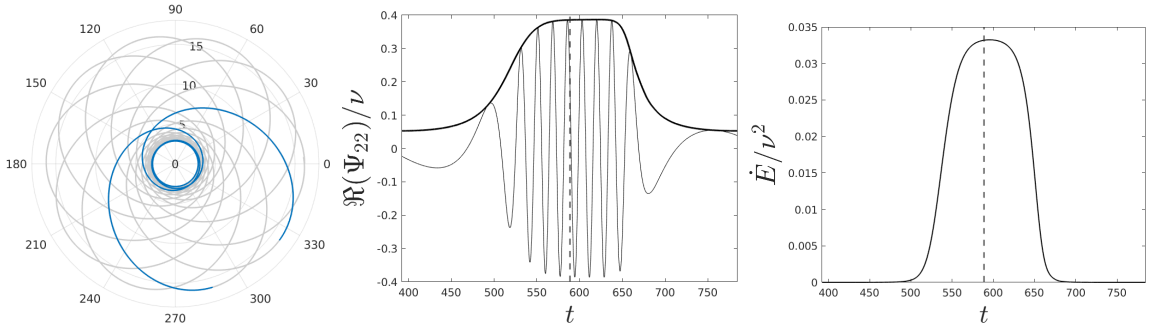

Figure 3.3: Trajectory, quadrupolar waveform, and instantaneous energy flux for $\hat{a} = 0.6$, $e = 0.7$, and $p = p_s + 0.01 \simeq 4.858$. The radiation is computed using `Teukode`. The dashed vertical line marks the periastron passage. From Ref. [1].

results of Ref. [214], we have found, respectively, discrepancies of 1.4% and of 0.8%, confirming the $\sim 1\%$ disagreement already found by Ref. [213]. We can thus conclude that our numerical computations of the fluxes along eccentric orbits are consistent with the results already present in the literature. We therefore expect that our numerical methods can reproduce accurate fluxes (and therefore waveforms) from eccentric orbits, both in Schwarzschild and Kerr spacetimes.

Before diving into the comparisons between analytical and numerical results, we show an eccentric zoom-whirl configuration in Fig. 3.3. The quasi-circular whirl that happens at the periastron passage at $r_- = p/(1+e) \simeq 2.8576$ is in a region that would not be allowed by circular stable orbits. Indeed, for $\hat{a} = 0.6$ we have that the last stable orbit is at $r_{\rm LSO} \simeq 3.8291$. This means that stable eccentric (and also hyperbolic-like) geodesics can explore regions that are more extreme than the ones experienced by circular stable orbits. This has clear consequences on the phenomenology of the radiation. Indeed, the energy flux and the waveform have an evident asymmetry with respect to the periastron passage (highlighted with a dashed vertical line). The same feature is observed in the angular momentum flux and becomes even more evident for higher spins and higher eccentricities. This effect is related to the close passage of the particle to the light-ring, and in the most extreme cases, it is even possible to observe QNM-excitations (called wiggles), even if we are only considering stable bound orbits. We will come back to this phenomenon in Secs. 3.2.3 and 3.2.4.

3.2.2 Analytical improvements in the circular sector

The strong-field quasi-circular whirls that occur in orbits with p close to the separatrix made us realize that we also needed to improve the *circular* sector of the analytical waveform in order to faithfully describe eccentric orbits.

In Ref. [1] we started by improving the $\rho_{\ell m}$, i.e. the general relativistic corrections to the circular amplitude of Eq. (2.30). Refs. [158, 159] proposed a resummation scheme whose basic ideas are: (i) first factorize out the orbital, spin-independent, part of the $\rho_{\ell m}$, and (ii) resum the orbital and spinning factors using, respectively, a Padé approximant and an inverse Taylor resummation scheme. The choice of the Padé approximant is partly arbitrary and is guided by the comparisons with the numerical results. The scheme was already applied up to $\ell = 6$; we extended it to the multipoles with $\ell = 7, 8$. This analytical enhancement has been further discussed in Sec. IIIC of Ref. [1]. We do not repeat here the complete discussion, but we point to the results reported in Fig. 2 and Fig. 3 of Ref. [1], which show the relevance of this resummation scheme.

In Ref. [1] we also explored the accuracy of the circular residual phase $\delta_{\ell m}$; we briefly report this discussion in the following. We have exploited various PN truncations of the 11 PN series for a test-particle on circular orbits around a Kerr black hole [215], and we have also tested the resummation scheme introduced in [56], where the resummed phases are obtained by factorizing the leading order $\delta^{\rm LO}_{\ell m}$ contribution and then using a Padé approximant P^i_j for the remaining correcting factor $\hat{\delta}_{\ell m}$, explicitly:

$$\delta_{\ell m} = \delta^{\rm LO}_{\ell m} + \delta^{\rm NLO}_{\ell m} + \cdots = \delta^{\rm LO}_{\ell m}\hat{\delta}_{\ell m}, \tag{3.4}$$

$$\bar{\delta}_{\ell m} = \delta^{\rm LO}_{\ell m} P^i_j[\hat{\delta}_{\ell m}]. \tag{3.5}$$

We show in Fig. 3.4 the phase differences (in absolute value) between numerical and analytical circular waveforms, either with the PN-expanded $\delta_{\ell m}$ (at various PN truncations) or with the resummed $\bar{\delta}_{\ell m}$. We consider some of the most relevant modes and only consider radii close to the LSO ($r = r_{\rm LSO} + 0.01$). For moderate spins ($\hat{a} \lesssim 0.5$), we see that the analytical/numerical phase agreement of the dominant mode is improved by increasing the PN order of δ_{22}. Nonetheless, when the spin increases, the series beyond 8 PN become unreliable. For the subdominant modes, the PN series at high order are reliable also for $\hat{a} \gtrsim 0.5$, even if for δ_{21} and δ_{33} some series at lower order give similar (or better) agreements.

Applying the resummation scheme of Eq. (3.5) at 5.5 PN, we have found that the most suitable choice is the Padé P^2_2. The resummation provides a better numerical/analytical agreement than the corresponding Taylor-expanded series at the same PN order. Nonetheless, the Taylor expanded δ_{22} at 6 or 7.5 PN yields comparable, or even better, agreement with numerical waveforms. For prograde orbits with $\hat{a} \gtrsim 0.3$, the resummation of the $\ell = m$ subdominant modes provides a more faithful description than the Taylor expanded series at 6.5 PN, as shown in Fig. 3.4. For even higher spins ($\hat{a} \gtrsim 0.8$), the resummed $\bar{\delta}_{\ell m}$ outperform also the series beyond 7 PN. The hierarchy of the analytical/numerical phase difference is different for the (2,1) mode, but in that case all the phase differences are smaller and remain below 0.01 radians. A similar argument holds at larger radii, even if for *distant* simulations is less straightforward to evaluate the goodness of the analytical choice, since the comparisons are affected by larger numerical errors.

Note in passing that, while spurious poles are absent in $\ell = m$ and $(2, 1)$ modes of the resummed $\delta_{\ell m}$ with Padé P^2_2, they may occasionally appear in some other subdominant modes. Finally, we have also successfully applied the resummation scheme at 6.5 PN

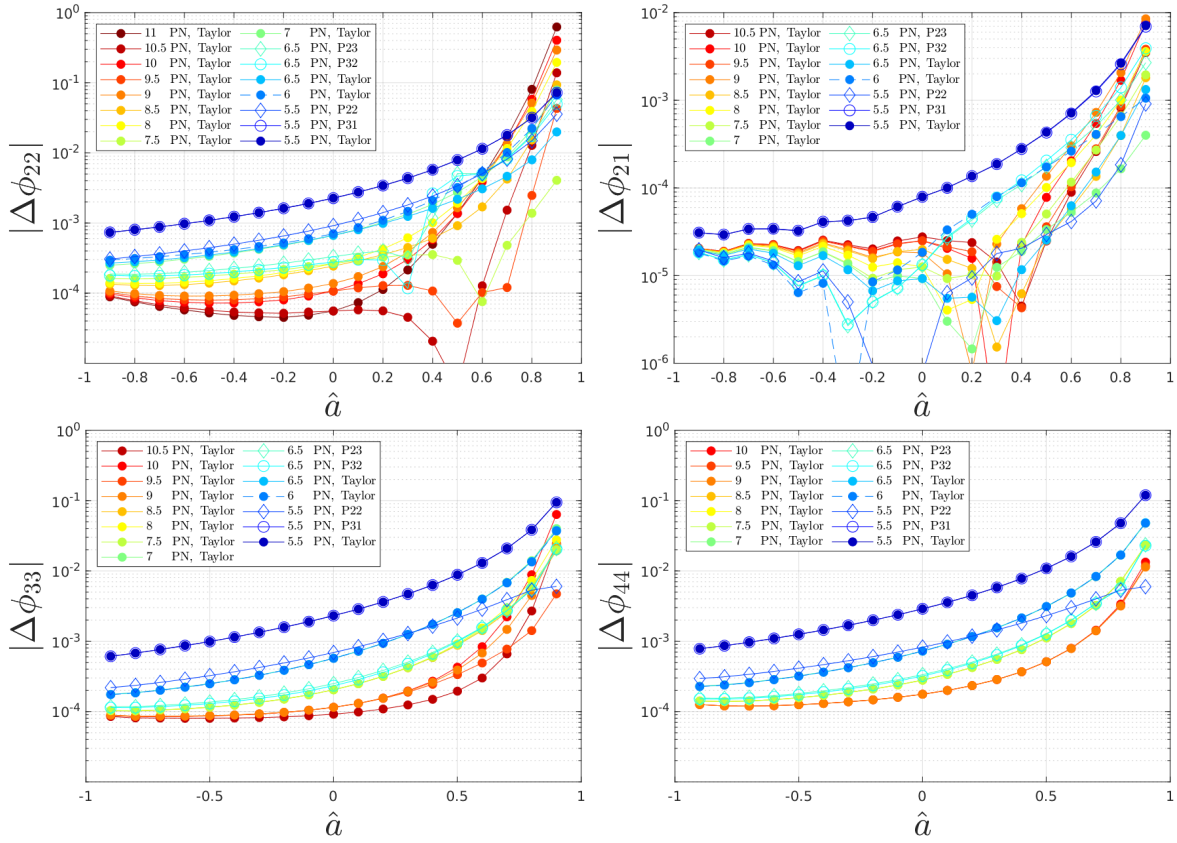

Figure 3.4: Phase difference between numerical and analytical waveform multipoles for different truncation of the $\delta_{\ell m}$ series (filled markers) and Padé resummations obtained with Eq. (3.5) (empty markers) for the *near* circular simulations ($r = r_{\rm LSO} + 0.01$). Note the different vertical scale for the (2,1) mode and the vertical logarithmic scale.

accuracy as shown in Fig. 3.4. By contrast, when working at 7.5 PN, one finds spurious poles even in the $(2,2)$ mulitpole, either with Padé P_2^4 or P_3^3, so that the resummation is not robustly applicable in this case. Generally speaking, the resummed $\bar{\delta}_{\ell m}$ yield a better phasing agreement with the numerical results. In particular they are more robust than the high-order PN truncations for prograde orbits around fast-spinning black hole. Nonetheless, in order to choose a compromise between accuracy and analytical simplicity, we have decided to consider the series truncated at 7.5 PN as our preferred choice. For noncircular simulations, the $\delta_{\ell m}$ are relevant during the circular whirl of zoom-whirl orbits, but are less significant for the other eccentric orbits. For higher spins, the analytical choice is more relevant since the separations reached are closer to the light ring, and thus the PN series are employed in stronger fields.

3.2.3 Generic Newtonian prefactor: waveform

We now consider the analytical waveform of Eq. (2.36), where the noncircular corrections are included in the *generic* Newtonian prefactor $h_{\ell m}^{(N,\epsilon)} = h_{\ell m}^{(N,\epsilon)_{\rm c}} \hat{h}_{\ell m}^{(N,\epsilon)_{\rm nc}}$. The noncircular contribution for the quadrupole is reported in Eq. (2.35), while the corrections for the (2,1), (3,3), (3,2), and (4,4) modes are written in Appendix A.

While Ref. [145] already pointed out a fairly good analytical/numerical agreement of the Newtonian-corrected quadrupolar waveforms in the nonspinning case, in Ref. [1] we carried out a systematic analysis in test particle limit considering the spin, more eccentric

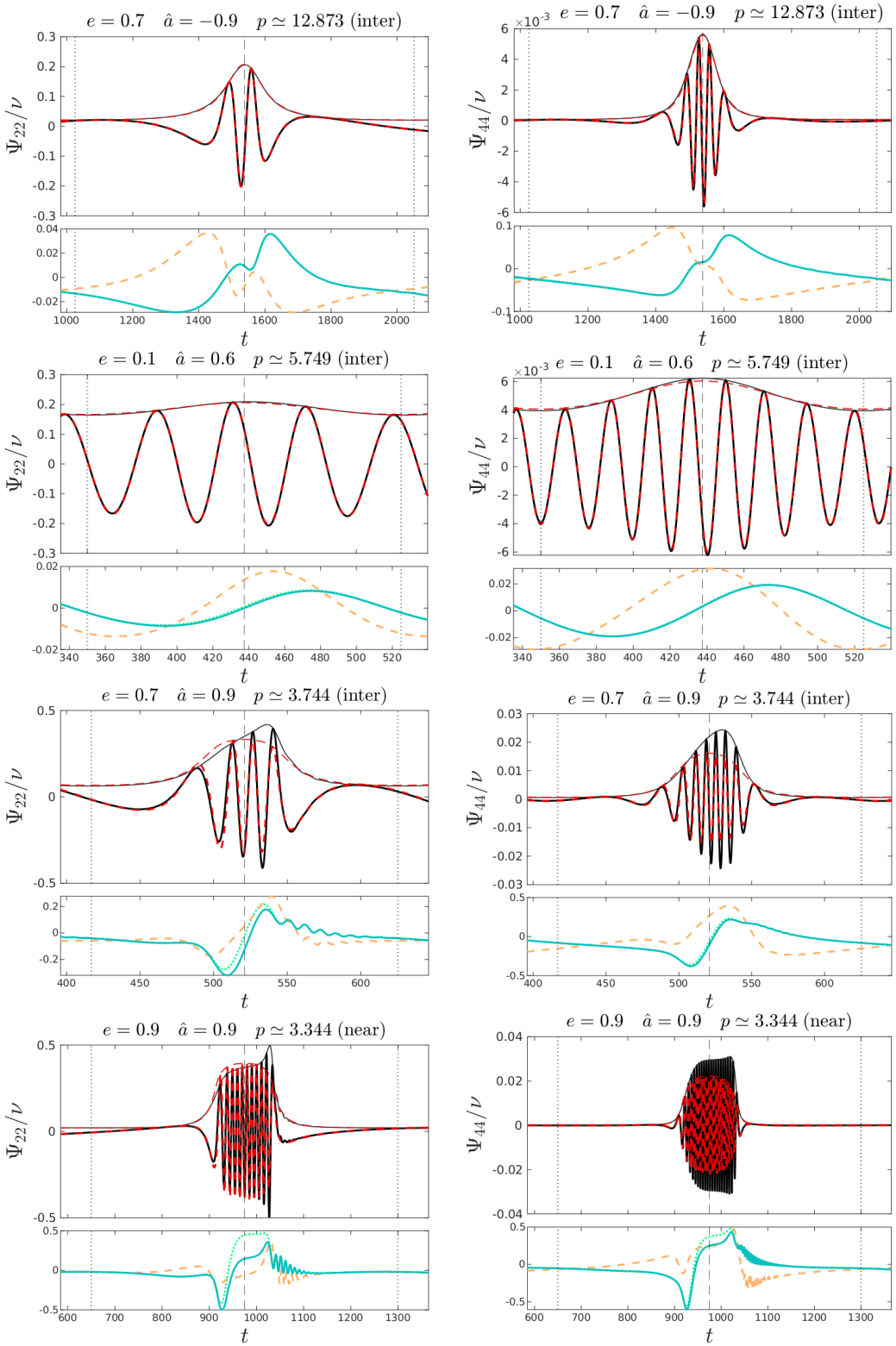

Figure 3.5: Numerical (black) and EOB (red dashed) waveforms for the (2,2) and (4,4) multipoles. The corresponding orbits can be found in Fig. 3.2. For each multipole, we report the relative amplitude difference (dashed orange) and the phase difference (light blue). We report also the phase differences for the waveform with the residual tail factor $\delta_{\ell m}$ at 6PN (dotted green). The vertical lines mark the periastron (dashed) and the apastron (dotted).

configurations, and also higher multipoles. This analysis, performed considering planar geodesics in Kerr, showed that the relative discrepancies increase in the subdominant multipoles. In Figure 3.5 we report the analytical/numerical comparisons for the $\ell = m = 2$ and $\ell = m = 4$ modes obtained for three illustrative configurations. The corresponding orbits are shown in Fig. 3.2. For each configuration we compare, in the top panel, the real part of the analytical (red) and numerical (black) waveform produced along a radial orbit. In the bottom panel, we show the analytical/numerical phase difference $\Delta\phi = \phi^{\rm numerical}_{\ell m} - \phi^{\rm analytical}_{\ell m}$ in radians (solid azul line) and the relative amplitude difference $1 - A^{\rm analytical}_{\ell m}/A^{\rm numerical}_{\ell m}$ (dashed orange lines). The residual waveform phases $\delta_{\ell m}$ are kept at 7.5PN accuracy, which is our default choice as discussed in Sec. 3.2.2. However, in order to establish the relevance of the PN-information used, we also show the phase differences obtained with $\delta_{\ell m}$ at 6PN accuracy (green dotted lines). As shown by the last configuration, such high PN-accuracy is relevant for circular or zoom-whirl orbits , but it is less important for eccentric configurations without circular whirls. Indeed, for the first two configurations of Fig. 3.5 the two phase differences, obtained considering 6 or 7.5PN information in the $\delta_{\ell m}$, overlap. Moreover, note that the phase difference reaches its minimum near periastron. This suggests that in the eccentric case, this quantity is dominated by the lack of high-order noncircular information in the waveform beyond the Newtonian order.

More waveform comparisons are reported in Ref. [1], in particular in Fig. 10, 16 and 17. In the last two figures, we show the most relevant multipoles up to $\ell = 8$. Note that we do not consider the $m = 0$ modes, that have been instead studied in Ref. [3] (see also Chapter 4). We concluded that the waveform with the generic Newtonian prefactor is reliable in the majority of cases considered, when the particle does not experience too strong gravitational fields. From the practical point of view, the generic Newtonian prefactor (used both in the waveform and in the radiation reaction) is already sufficient to obtain an EOB/NR unfaithfulness well below the 1% for comparable mass configurations with moderate eccentricity [147, 148].

However, from Fig. 3.5 it is impossible to not note that for $\hat{a} = 0.9$, the numerical waveforms develop a peak after the periastron passage, when the motion of the particles is outgoing. This peak is then followed by high-frequency oscillations, that are especially visible in the zoom-whirl case. The oscillations are even more visible in the fluxes, as we will see in Sec. 3.2.4. This interesting feature arises from the fact that, when a corotating test particle gets close to the light ring at high velocity, the QNMs of the central black hole can be excited, producing high-frequency oscillations (usually addressed as *wiggles*) in the radiated GWs at infinity [216]. This phenomenon has been recently analyzed in detail both using TD and FD codes [217, 218]. Moreover, the QNM excitation leads to strongly asymmetric fluxes with respect to the periastron passage. Since the damping time of the QNMs increases significantly for high spins, these excitations are mostly of interest for extremal black holes ($\hat{a} \gtrsim 0.99$). Nonetheless, QNMs excitations are present also in less extreme cases, as pointed out in [218] and shown in Fig. 3.5. These effects are particularly relevant for prograde zoom-whirl orbits with high eccentricity around fast-spinning black holes since the periastron can get very close to the light ring, well below the radius of the last stable orbit, as already discussed at the end of Sec. 3.2.1. The closer the periastron is to the central black hole, the more pronounced this effect becomes. These phenomena, which are not taken into account in EOB models, prevent achieving high accuracy in the presence of such conditions. Nevertheless, in most scenarios where radiation back-reaction is considered, zoom-whirl orbits are rare events. This is because

the burst of GW emission at the periastron passage often leads the particle to plunge toward the central black hole. While it would be interesting to model and incorporate these effects into the EOB waveform, this goal has not been pursued yet.

3.2.4 Generic Newtonian prefactor: fluxes

In Sec. 2.3.3 we argued that the quasi-circular angular component of the radiation reaction $\mathcal{F}_\varphi$ of Eq. (2.43) can be improved using the generic Newtonian correction $\hat{f}^{\rm N_{nc}}_{\varphi 22}$ of Eq. (2.44), obtained by combining Eqs. (2.35) and (1.42b). This procedure was used in Ref. [145] to obtain the radiation reaction angular component of Eq. (2.45), which we rewrite here using the notation adopted in Ref. [1] (see Eq. (22) therein),

$$\hat{\mathcal{F}}^{\rm old}_\varphi = -\frac{32}{5}\nu r^4_\Omega \Omega^5 \hat{f}^{\rm N_{nc}}_{\varphi,22}\hat{f}. \tag{3.6}$$

As already noticed in Ref. [147], the above formula can be improved by inserting the noncircular corrections $\hat{f}^{\rm N_{nc}}_{\varphi,22}$ only in the (2,2) mode. The improved RR thus reads

$$\hat{\mathcal{F}}^{\rm NP}_\varphi = -\frac{32}{5}\nu r^4_\Omega \Omega^5 \hat{f}_{\rm nc_{22}}, \tag{3.7a}$$

$$\hat{f}_{\rm nc_{22}} \equiv \hat{F}_{22}\hat{f}^{\rm N_{nc}}_{\varphi,22} + \hat{F}_{21} + \sum_{\ell=3}^{8}\sum_{m=1}^{\ell}\hat{F}_{\ell m}, \tag{3.7b}$$

where $\hat{F}_{\ell m} = F_{\ell m}/F^N_{22}$ are the Newton-normalized energy fluxes defined in Eq. (5.20). Note that $\hat{F}_{22}$ is not 1, but rather 1 + PN corrections. In practice, the global factor $\hat{f}^{\rm N_{nc}}_{\varphi,22}$ of Eq. (3.6) is now a factor of the $\ell = m = 2$ multipole, and we are neglecting the noncircular corrections of all the subdominant multipoles. A straightforward generalization of Eq. (3.7) can be obtained by considering also the noncircular corrections from the subdominant multipoles. For simplicity, we add these corrections up to $\ell = 6$, so that the generalized angular component of the radiation reaction reads

$$\begin{aligned}\hat{\mathcal{F}}^{\rm ANP}_\varphi = &-\sum_{\ell=2}^{6}\sum_{m=1}^{\ell}\dot{J}^{(N_{\rm qcirc},\epsilon)}_{\ell m}\hat{f}^{\rm N_{nc}}_{\varphi,\ell m}|\hat{h}^{(\epsilon)_{\rm c}}_{\ell m}|^2 \\ &-\sum_{\ell=7}^{8}\sum_{m=1}^{\ell}\dot{J}^{(N_{\rm qcirc},\epsilon)_{\rm c}}_{\ell m}|\hat{h}^{(\epsilon)}_{\ell m}|^2,\end{aligned} \tag{3.8}$$

where $J^{(N_{\rm qcirc},\epsilon)}_{\ell m} \propto \nu r^{2(\ell+\epsilon)}_\Omega \Omega^{2(\ell+\epsilon)+1}$ is the quasi-circular Newtonian contribution to the angular momentum flux[3], $\hat{f}^{\rm N_{nc}}_{\varphi,\ell m}$ is the Newtonian noncircular factor and $\hat{h}^{(\epsilon)_{\rm c}}_{\ell m}$ is the full PN (circular) correction introduced in Eq. (2.20). The factors are easy to obtain from the corresponding waveform corrections, but their expressions are quite long, so we do not report them here in the main text. The corrections for the (2,1), (3,3), (3,2), and (4,4) modes can be found in Appendix A. Note that the inclusion of Eq. (3.8) in the rhs of the Hamilton equations would require to extend the iterative procedure discussed in Sec. 2.3.3 also to higher time-derivatives of the radius and the orbital frequency, making the solving procedure more involved.

To establish the accuracy of these prescriptions for the radiation reaction, one can consider the fluxes computed by plugging $\mathcal{F}$ in Eqs. (2.37) and compare the output with

[3]For the $\ell = m = 2$ mode this is the already discussed term $\dot{J}^{(N_{\rm qcirc},0)}_{22} = 32/5\ \nu r^4_\Omega \Omega^5$.

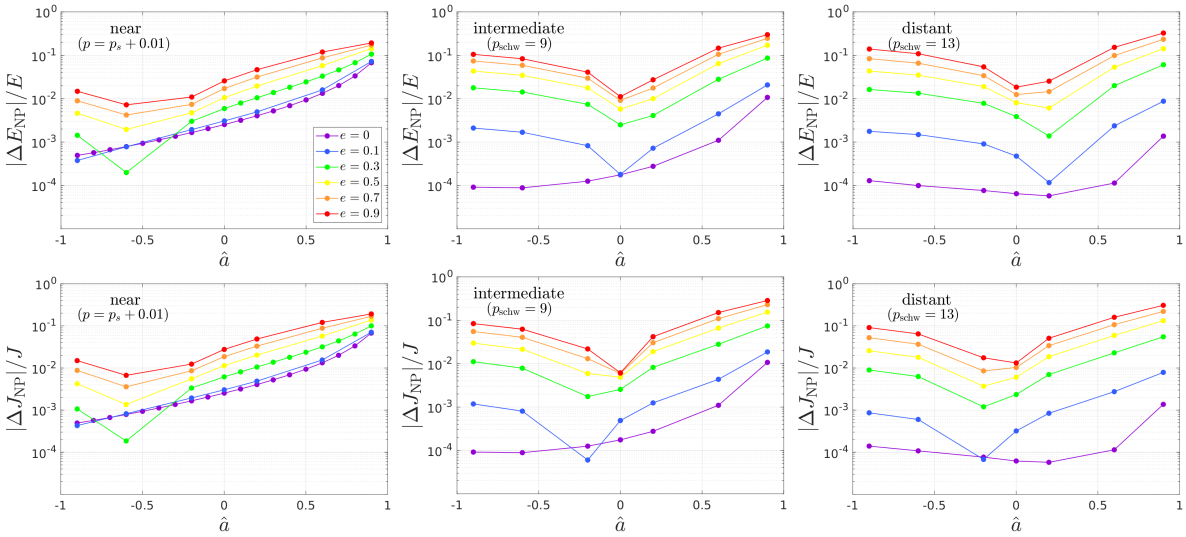

Figure 3.6: Relative differences between numerical and analytical averaged fluxes plotted against the spin (absolute value, logarithmic scale). Different colors highlight different eccentricities, see the legend in the first plot. We consider $\dot{E}_{\rm NP}$ and $\dot{J}_{\rm NP}$, i.e. the fluxes with the (2,2) general Newtonian prefactor of Eq. (2.44) in the (2,2) multipole. These relative differences are also reported in Table A.1.

the analytical results. Note that while the angular momentum flux is directly linked to $\mathcal{F}_\varphi$, the energy flux involves also $\mathcal{F}_r$ and $\dot{E}_{\rm Schott}$, as discussed in Sec. 2.3.3. One could also consider the fluxes computed plugging the analytical waveform of Eq. (2.36) in Eqs. (1.42). These fluxes are not directly linked to a radiation reaction, but give an idea of how the fluxes could be if all the waveform effects were included. The angular momentum fluxes computed from this latter prescription are denoted as $\dot{J}_{h_{\ell m}}$, while the fluxes computed from the different prescriptions of the angular radiation reaction are denoted as $\dot{J}_{\rm old}$ for $\hat{\mathcal{F}}_\varphi^{\rm old}$ from Eq. (3.6), $\dot{J}_{\rm NP}$ for $\hat{\mathcal{F}}_\varphi^{\rm NP}$ from Eq. (3.7), and $\dot{J}_{\rm ANP}$ for $\hat{\mathcal{F}}_\varphi^{\rm ANP}$ from Eq. (3.8). The same notation scheme is adopted for the energy fluxes.

To start with, we could consider the instantaneous fluxes associated with the geodesic orbits. Some analytical/numerical comparisons are shown in Fig. 6 of Ref. [1], but they do not provide a clear insight on the accuracy of the analytical prescriptions. It is however interesting to note that the analytical fluxes computed directly from the analytical waveform $h_{\ell m}$ are slightly more accurate, at least for large separations, but the three fluxes computed from using the radiation reactions $\mathcal{F}$ provide similar (but not equivalent) agreements. However, from these kinds of comparisons, it is not easy to understand which $\mathcal{F}_\varphi$ is the most accurate. For this reason, in Ref. [1] we based our conclusions on the averaged fluxes, which allow us to have a more global insight into the problem. The discussion of Ref. [1] is reported below, mutatis mutandis. All the values for the relative differences between numerical and analytical averaged fluxes can be found in Appendix D of Ref. [1], while in Table A.1 we report the analytical/numerical differences for the fluxes computed using Eq. (3.7).

As one would expect a priori, the analytical/numerical disagreement grows both with spin and eccentricity for every analytical prescription, since the periastron of prograde orbits can get very close to the light ring for high spin parameters and high eccentricity. In strong fields, the PN series employed in our model lose their reliability, even if strengthened by a resummation. In particular, from the relative differences between numerical and $(\dot{J}_{\rm NP}, \dot{E}_{\rm NP})$ fluxes reported in Fig. 3.6, it is possible to see that the spin is a relevant source of disagreement regardless of eccentricity. Conversely, eccentricity is also

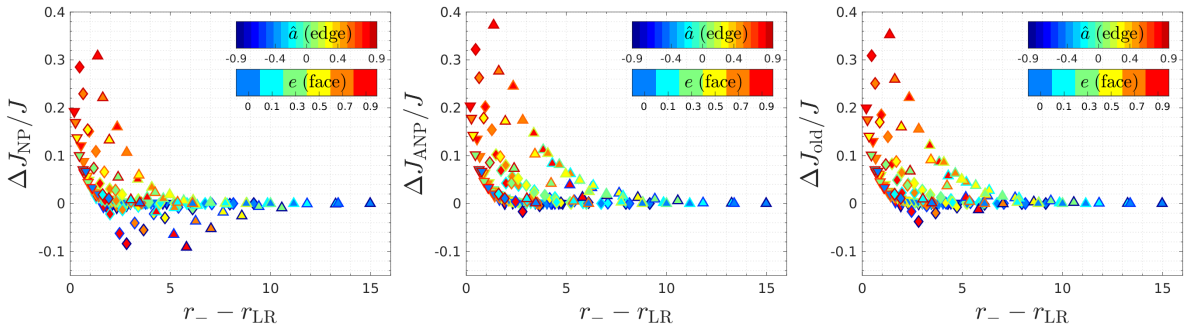

Figure 3.7: Left panel: relative differences $\Delta J_{\rm NP}/J \equiv (\langle \dot{J}_{\rm teuk}\rangle - \langle \dot{J}_{\rm NP}\rangle)/\langle \dot{J}_{\rm teuk}\rangle$ for the fluxes with the (2,2) general Newtonian prefactor in the (2,2) multipole plotted against the distance between the light ring and the periastron. The face color of the markers indicates the eccentricity, while the edge color indicates the spin. The shape of the markers is related to the rule used for the semilatus rectum: the reverse triangle indicates the near simulations, the diamond is for the intermediate simulations and the triangle pointing upward indicates the distant simulations. Other two panels: same scheme, but for $J_{\rm ANP}$ and $J_{\rm old}$. See Fig. 21 and Fig. 22 of Ref. [1] for analogous plots with $\dot{J}_{h_{\ell m}}$ and also with the energy fluxes.

crucial for the reliability of the fluxes, both for the lack of noncircular information in the angular radiation reaction beyond the Newtonian order and for the approaching of the periastron to stronger fields for higher eccentricities. The last issue can be easily seen in Fig. 3.7, where in the first panel we have plotted the same numerical/analytical relative differences of the angular momentum fluxes versus the distance between the light ring and the periastron. In the other two panels of Fig. 3.7 we have shown the differences for the other radiation reactions of Eq. (3.8) and Eq. (3.6). The analogous plots for the energy fluxes can be found in Appendix D of Ref. [1], but the general features discussed so far remain valid.

In order to decide which radiation reaction employ in the rhs of the Hamilton equations, we focus on the three analytical angular momentum fluxes that are strictly linked to an analytical prescription of the radiation reaction: $\dot{J}_{\rm NP}$, $\dot{J}_{\rm old}$, and $\dot{J}_{\rm ANP}$. Note that the analytical prescription of $\hat{\mathcal{F}}_r$ is the same in all the radiation reactions tested in this work. The fluxes computed from the EOB waveform (i.e. $\dot{J}_{h_{\ell m}}$) are less informative since, as already discussed, they are not related to a radiation reaction; for this reason, we will not discuss them in detail. As a first step, we focus on the two averaged analytical fluxes with only the (2,2) noncircular Newtonian prefactor $\hat{f}^{\rm Nnc}_{\varphi,22}$, $\langle \dot{J}_{\rm old}\rangle$ and $\langle \dot{J}_{\rm NP}\rangle$, which are computed with the angular radiation reaction $\hat{\mathcal{F}}^{\rm old}_{\varphi}$ from Eq. (3.6), and with $\hat{\mathcal{F}}^{\rm NP}_{\varphi}$ from Eq. (3.7), respectively. As mentioned above, $\hat{\mathcal{F}}^{\rm NP}_{\varphi}$ is theoretically more consistent than $\hat{\mathcal{F}}^{\rm old}_{\varphi}$ since the former includes the (2,2) noncircular Newtonian prefactor only in the (2,2) multipole, while in the older prescription the noncircular correction is treated as a global factor, and therefore affects even the subdominant modes. Nonetheless, for retrograde orbits, $\langle \dot{J}_{\rm old}\rangle$ has a better numerical/analytical agreement than $\langle \dot{J}_{\rm NP}\rangle$. In fact, the latter overestimates significantly the numerical fluxes, especially at high eccentricity, as can be seen from Fig. 3.7. This can be explained by noting that the dominant contribution to the averaged fluxes occurs at periastron, where we have $\hat{f}^{\rm Nnc}_{\varphi,22} < 1$. Then, the lack of noncircular corrections in the subdominant multipoles of $\langle \dot{J}_{\rm NP}\rangle$ leads to an overestimate of the numerical result. On the other hand, in $\langle \dot{J}_{\rm old}\rangle$ the noncircular correction $\hat{f}^{\rm Nnc}_{\varphi,22}$ is a global factor and thus artificially reduces the contribution of the subdominant modes, fixing the overestimate. Nonetheless, this is just an artificial effect and the old radiation

Table 3.3: Averaged analytical fluxes for test particle on eccentric orbits around a Schwarzschild black hole compared with numerical results, $\Delta J_{\rm NP}/J = 1 - \langle \dot{J}_{\rm NP}\rangle/\langle \dot{J}_{\rm num}\rangle$. For $p \leq 13$, the numerical fluxes in this table are obtained with `Teukode` and are a subset of the ones reported in Table A.1. The fluxes with greater semilatera recta are computed with `RWZHyp`.

e	p	$\langle \dot{J}_{\rm num}\rangle$	$\langle \dot{J}_{\rm NP}\rangle$	$\Delta J_{\rm NP}/J$	e	p	$\langle \dot{J}_{\rm num}\rangle$	$\langle \dot{J}_{\rm NP}\rangle$	$\Delta J_{\rm NP}/J$
0.1	6.21	10.5396	10.5076	$3.0 \cdot 10^{-3}$	0.7	7.41	10.5483	10.3521	$1.9 \cdot 10^{-2}$
0.1	9	0.85442	0.85401	$4.9 \cdot 10^{-4}$	0.7	9	1.69513	1.68505	$5.9 \cdot 10^{-3}$
0.1	13	0.30867	0.30857	$3.2 \cdot 10^{-4}$	0.7	13	0.50634	0.50113	$1.0 \cdot 10^{-2}$
0.1	21	0.10208	0.10207	$7.9 \cdot 10^{-5}$	0.7	21	0.15477	0.15408	$4.4 \cdot 10^{-3}$
0.1	31	0.04445	0.04446	$-7.0 \cdot 10^{-5}$	0.7	31	0.06542	0.06562	$-3.1 \cdot 10^{-3}$
0.3	6.61	8.73092	8.67715	$6.2 \cdot 10^{-3}$	0.9	7.81	12.5209	12.1752	$2.8 \cdot 10^{-2}$
0.3	9	0.97246	0.96998	$2.6 \cdot 10^{-3}$	0.9	9	2.49117	2.47585	$6.1 \cdot 10^{-3}$
0.3	13	0.33935	0.33855	$2.3 \cdot 10^{-3}$	0.9	13	0.65853	0.64984	$1.3 \cdot 10^{-2}$
0.3	21	0.11055	0.11048	$5.9 \cdot 10^{-4}$	0.9	21	0.19258	0.19098	$8.3 \cdot 10^{-3}$
0.3	31	0.04786	0.04789	$-6.6 \cdot 10^{-4}$	0.9	31	0.08011	0.08041	$-3.8 \cdot 10^{-3}$
0.5	9	1.23262	1.22659	$4.9 \cdot 10^{-3}$					
0.5	13	0.40329	0.40085	$6.0 \cdot 10^{-3}$					
0.5	21	0.12784	0.12760	$1.9 \cdot 10^{-3}$					
0.5	31	0.05479	0.05488	$-1.8 \cdot 10^{-3}$					

reaction is not theoretically solid. Moreover, in the Schwarzschild case or for prograde orbits, the new prescription is more accurate, as shown in Fig. 3.7. In fact, for spins aligned with the orbital angular momentum, the two analytical prescriptions generally underestimate the numerical fluxes, and therefore a global factor that is smaller than 1 at periastron worsen the numerical/analytical agreement, making the older prescription less accurate. Finally, we consider the averaged fluxes $\langle \dot{J}_{\rm ANP}\rangle$, that are computed using $\hat{\mathcal{F}}^{\rm ANP}_{\varphi}$ from Eq. (3.8) and thus include all the noncircular corrections up to $\ell = 6$. Comparing them with the $\langle \dot{J}_{\rm NP}\rangle$ fluxes, we can see that the ANP prescription is more reliable for retrograde orbits, but produces bigger relative differences with numerical data in the nonspinning case and for prograde orbits. The reason of this behavior is again related to the fact that at periastron we have $\hat{f}^{\rm N_{nc}}_{\varphi,\ell m} < 1$, as discussed above.

We also find that the fluxes $\langle \dot{J}_{\rm NP}\rangle$ are the most accurate in the Schwarzschild case. As can be seen from Table 3.3, in the nonspinning case this prescription is highly reliable for every configuration, yielding relative differences always below 3%, even for orbits with high eccentricity. Instead, for the other analytical prescriptions, the relative difference can be even $> 7\%$, as shown in Table VIII and Table IX of Ref. [1]. Note that for $p \geq 9$, the accuracy of our analytical model is consistent with the averaged eccentric fluxes at 10PN computed in Refs. [219, 220], but the EOB model remains solid even for smaller semilatera recta thanks to a robust resummation of the PN series.

In conclusion, considering that (i) the old prescription is not theoretically accurate, (ii) the radiation reaction with all the multipoles does not drastically improve the model for moderate eccentricities and moderate spins despite being more complicated, (iii) the fluxes $\langle \dot{J}_{\rm NP}\rangle$ are the most faithful in the nonspinning case, we decided to use in our model the angular radiation reaction $\hat{\mathcal{F}}^{\rm NP}_{\varphi}$ from Eq. (3.7). With this choice, the energy and angular momentum fluxes have an agreement of a few percent for moderate eccentricities

($e \lesssim 0.3$), even if for prograde orbits the spin reduces the maximum eccentricity up to which the model has good agreement with the numerical results. In the worst-case scenario that we consider, i.e. the one with $\hat{a} = 0.9$, $e = 0.9$, and "distant" semilatus rectum ($p \simeq 5.557$), we get relative differences of 33% and 31% for the energy and angular momentum fluxes, respectively (see Table VII of Ref. [1]). Note that the worst case does not correspond to a simulation with semilatus rectum close to the separatrix, since in those cases the lack of noncircular information is compensated by the zoom-whirl behavior.

3.3 Non-conservative eccentric dynamics

Now that we have tested the reliability of the angular radiation reaction proposed in Eq. (3.7), we can use this prescription, together with the radial component (2.46), to compute eccentric dynamics that take into account the loss of energy and angular momentum due to the GW emission. We thus solve the Hamilton equations (2.56), considering for all the eccentric cases a symmetric mass ratio of $\nu = 10^{-3}$. The dissipative contribution linked to $\mathcal{F}$ drives the particle to eccentric orbits with decreasing semilatus rectum. At the separatrix-crossing, the orbit is no longer stable, and the particle is doomed to plunge towards the central black hole at the next close encounter. We will discuss the transition from the inspiral to the plunge and the corresponding waveform in more detail in Chapter 5, but there we will focus on the nonspinning scenario. In this section, instead, we analyze the more generic planar spinning case, but we complete the waveform with the rather simple ringdown model that has been presented in Ref. [1].

3.3.1 A simple ringdown model

The EOB inspiral waveform (2.36) is completed as described in Eq. (2.51), where the NQC correction $\hat{h}^{\rm NQC}_{\ell m}$ has the form written in Eq. (2.53) and it is written using the base (2.54). The ringdown model $h^{\rm rng}_{\ell m}$ is obtained following the procedure introduced in Ref. [169]. In short, the procedure consists of (i) factorizing the fundamental corotating QNM contribution from the ringdown waveform; this leads to the QNM-rescaled waveform $\bar{h}$ as shown in Eq. (2.52), (ii) providing templates for the amplitude $A_{\bar{h}}$ and the phase $\phi_{\bar{h}}$ of the QNM-rescaled waveform, (iii) using continuity conditions to link some of the coefficients of these templates to numerical quantities at merger, (iv) fitting the remaining free coefficients on a set of numerical waveforms, (v) providing global fits (i.e. fits over the parameter space) of the numerical quantities at merger and of the free coefficients. This procedure has to be repeated for each multipole.

We start by discussing the ringdown model, and then the NQC correction follows from it. The following discussion is taken from Ref. [1], where we started by showing that the template for the amplitude proposed in Ref. [169] and used in `TEOBResumS` is not reliable in the test particle limit when the spin of the central black hole is large. On the other hand, the old phase template turns out to be reliable also in this regime. We thus proposed a more flexible amplitude ansatz, so that the QNM-rescaled waveform $\bar{h} = A_{\bar{h}} e^{i\phi_{\bar{h}}}$ from Eq. (2.52) is written as

$$A_{\bar{h}}(\tau) = \left(\frac{c_1^A}{1 + e^{-c_2^A \tau + c_3^A}} + c_4^A \right)^{\frac{1}{c_5^A}} , \tag{3.9a}$$

$$\phi_{\bar{h}}(\tau) = -c_1^\phi \ln\left(\frac{1 + c_3^\phi e^{-c_2^\phi \tau} + c_4^\phi e^{-2c_2^\phi \tau}}{1 + c_3^\phi + c_4^\phi}\right), \tag{3.9b}$$

where $\tau \equiv t - t^{\rm peak}_{A_{\ell m}}$. The only parameters to be fitted on numerical data are c_2^A, c_3^A, c_3^ϕ and c_4^ϕ, while the others are determined requiring the correct late-time behavior. Note however that now the amplitude is fitted using *two* parameters, contrary to Ref. [169], that employed a single fitting parameter. The constraints given by the request for continuity at merger and by correct late-time behavior of the ringdown are

$$c_1^A = \frac{c_5^A \alpha_1}{c_2^A} (A_{\rm mrg})^{c_5^A} e^{-c_3^A} \left(1 + e^{c_3^A}\right)^2, \tag{3.10}$$

$$c_4^A = (A_{\rm mrg})^{c_5^A} - \frac{c_1^A}{1 + e^{c_3^A}}, \tag{3.11}$$

$$c_5^A = -\frac{\ddot{A}_{\rm mrg}}{A_{\rm mrg}\alpha_1^2} + \frac{c_2^A}{\alpha_1}\frac{e^{c_3^A} - 1}{1 + e^{c_3^A}}, \tag{3.12}$$

$$c_2^\phi = \alpha_2 - \alpha_1, \tag{3.13}$$

$$c_1^\phi = \frac{1 + c_3^\phi + c_4^\phi}{c_2^\phi (c_3^\phi + 2c_4^\phi)} \Delta\omega_{\rm mrg}, \tag{3.14}$$

where α_i are the real parts of the QNM complex frequencies $\sigma_i \equiv \alpha_i + {\rm i}\omega_i$ (i.e., the inverse of the damping time), $A_{\rm mrg}$ and $\ddot{A}_{\rm mrg}$ are the amplitude and its second-time derivative at merger, $\Delta\omega_{\rm mrg} \equiv \omega_1 - \omega_{\rm mrg}$ is the difference between the imaginary part of the fundamental QNM frequency, ω_1, and the merger waveform frequency $\omega_{\rm mrg}$. Note that the merger is defined as the time at which the peak of the quadrupolar waveform occurs.

The aforementioned numerical quantities, together with the not-constrained coefficients of the templates, are extracted from numerical data and fitted over the parameter space. For the subdominant modes, one has to follow the same procedure, but all the quantities have to be evaluated at $t^{\ell m}_{\rm peak} = t_{\rm mrg} + \Delta t_{\ell m}$, where $\Delta t_{\ell m} \geq 0$ is the delay of each multipole peak with respect to the dominant mode. The $\Delta t_{\ell m}$ are also extracted from numerical data and are then fitted over the parameter space. To construct a complete ringdown model we have employed 97 numerical simulations with different values of eccentricity and spin. The global fits of the primary parameters found with the phase and amplitude templates are performed over $(\hat{a}, e) = [-0.6, 0.8] \times [0, 0.9]$, even if for high positive spins the global fits are reliable only at moderate or low eccentricity. Note that in Ref. [1], we used $e_{\rm sep}$ for the global fits, but this is not an optimal choice, for the reasons detailed in Sec. 3.1. In Ref. [6] we used a more reliable quantity, which is strictly related to the energy and the angular momentum; we will describe it in Chapter 5.

Once the ringdown model is completed, the NQC waveform is obtained as discussed in Sec. 2.3.4 using, for each mode, $t_{\rm NQC} = t^{\ell m}_{\rm peak} + 2 = t_{\rm mrg} + \Delta t_{\ell m} + 2$. The merger time $t_{\rm mrg}$ is determined using the peak of the orbital frequency following the same prescription adopted for the comparable mass case in the `TEOBResumS` model [134], i.e. using

$$t_{\rm mrg} = t^{\rm peak}_{\Omega_{\rm orb}} - 3, \tag{3.15}$$

where $\Omega_{\rm orb}$ is obtained from the orbital frequency Ω removing the spin-orbit contribution (but keeping the spin-spin terms). It was pointed out long ago in Ref. [126] that, in

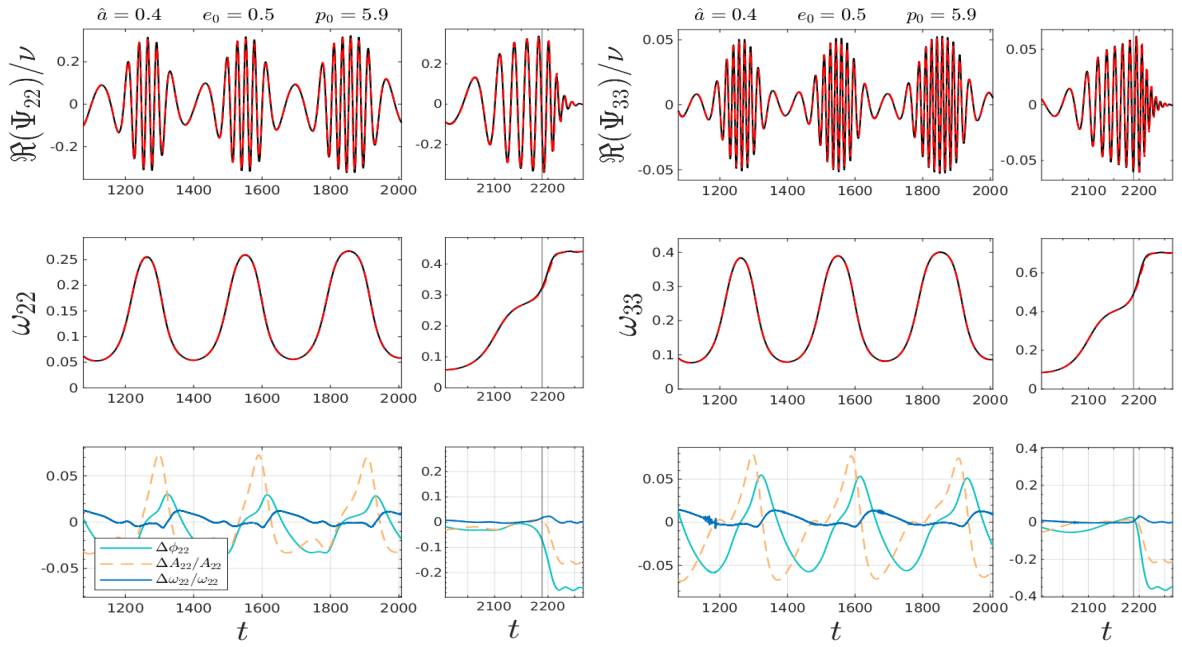

Figure 3.8: Comparison between numerical (black) and analytical (red dashed) complete waveform generated by a non-geodesic prograde orbit with initial eccentricity $e_0 = 0.5$ and semilatus rectum $p_0 = 5.9$ around a Kerr black hole with $\hat{a} = 0.4$. The vertical line marks the merger time. In the last panel of each mode, we report the relative difference of the amplitude (orange) and frequency (blue) together with the phase difference (light blue) in radians.

the transition from inspiral to plunge, the peak $t^{\rm peak}_{\Omega_{\rm orb}}$, is very close to the peak of the $\ell = m = 2$ waveform mode (for any subextremal value of the Kerr spin), and as such it offers an excellent reference point to attach the ringdown part when constructing EOB models. This observation is one of the key features behind the robustness and simplicity of the `TEOBResumS` waveform model [134]. In Ref. [6] we improved this description, but here with stick with this prescription, since we just want to emphasize that the waveform prescriptions analyzed in this chapter are reliable also during the plunge, and that it is possible to compute complete EOB waveforms incorporating merger and ringdown *also* in the case of eccentric inspirals.

The performance of the model for the (2,2) multipole in three quasi-circular cases can be observed in Fig. 12 of Ref. [1], while here we report an eccentric case with $\hat{a} = 0.4$ and $e_0 = 0.5$ in Fig. 3.8, showing the (2,2) and (3,3) multipoles. The (2,1) mode is shown in Fig. 13 of Ref. [1], but consider that for that multipole the post-merger parameters have been obtained with fits performed only on quasi-circular data. Note that while the analytical/numerical agreement is visibly good, the amplitude and phase differences are not negligible after the merger, showing that there is room for improvement. One simple way to improve this would be to calibrate the guess for $t_{\rm mrg}$ rather than using the ansatz of Eq. (3.15). However, the ringdown model discussed in this section has to be intended only as a proof of principle which shows that the EOB waveform can be completed using the usual NQC corrections and a ringdown model based on the idea of Ref. [134]. A more systematic analysis of the different pieces that enter both in the NQC and in the ringdown waveform has been performed in Ref. [6], but only for the non-spinning case. The complete and accurate modeling for the Kerr case is still under development, but we mention that one of the main challenges is that for retrograde orbits the peaks of some higher modes are strongly delayed with respect to the peak of the quadrupole, so

that the NQC are not strong enough to correct the waveforms for these higher modes. In these cases, one can perform the matching between the "ringdown" model and the inspiral waveform at $t^{\rm peak}_{A_{22}}$ (i.e. at $t_{\rm mrg}$) rather than at $t^{\rm peak}_{A_{\ell m}}$ also for the higher modes, as proposed in Ref. [58] and applied and discussed, for example, in Refs. [11, 60].

3.4 Summary

In this chapter, we have mainly discussed the results of Ref. [1] for eccentric (bound) orbits. Using eccentric planar geodesics in Kerr, we have discussed the accuracy of the waveform in Sec. 3.2.3, and of the radiation reaction in Sec. 3.2.4. The radiation reaction of Eq. (3.7), which is accurate enough for our purposes, is the one that is currently used in `TEOBResumS-Dalì` [146–148]. Note that in this model, the noncircular information is included:

- in the angular radiation reaction $\mathcal{F}_\varphi$ at Newtonian level, which includes only the noncircular *quadrupole* correction, as detailed in Eq. (3.7);
- at 2PN level in the non-vanishing radial radiation reaction of Eq. (2.46); in the test mass model we use $\hat{f}_r$ from Eq. (2.47), while in the eccentric avatar of `TEOBResumS` we use $\hat{f}_r$ from Eq. (2.50) in order to improve the quasi-circular limit of the model;
- at Newtonian level in each waveform multipole by generalizing the Newtonian prefactor $h^{(N,\epsilon)_{\rm c}}_{\ell m}$ of Eq. (2.36);

The Newtonian noncircular information that we include has explicit derivatives of r and Ω, that are not rewritten using the Newtonian-expanded EOM. Therefore, even if these corrections are formally Newtonian, their time derivatives are computed with the complete Hamilton equations.

Finally, in Sec. 3.3 we have discussed a simple ringdown model that is usable for a considerable portion of the parameter space. While there is clear room for improvement, this shows that the ringdown model of `TEOBResumS` can be extended also to eccentric configurations. The ringdown model discussed will be also used in Chapter 4 to complete the 2PN-corrected inspirals that we will analyze. However, in Chapter 4 we will naturally focus on the inspiral, since the 2PN corrections enter in the inspiral analytical EOB waveform.

Chapter 4

Noncircular 2PN corrections

We now introduce the 2PN noncircular corrections for the EOB waveform and the related corrections for the angular radiation reaction $\mathcal{F}_\varphi$. The results that we are going to discuss were presented in Refs. [3–5] and were obtained in strict collaboration with the other authors of the aforementioned references, in particular with Andrea Placidi. Note that these terms are not included in the public version of `TEOBResumS-Dali` yet.

We will consider instantaneous and hereditary noncircular contributions to the waveform and their influence on the radiation reaction. We will present two prescriptions for the instantaneous term: the first was introduced in Ref. [3], while the second in Ref. [5]. While the latter is preferable for several reasons that we will discuss later, we proceed in chronological order. Therefore, we start by discussing the instantaneous contribution of Ref. [3] in Sec. 4.1, and then the contribution of Ref. [5] in Sec. 4.3.

4.1 Instantaneous and hereditary corrections

The 2PN noncircular waveform in EOB coordinates was first obtained by Khalil *et al.* [150] by translating to EOB coordinates the results of Refs. [221, 222], which are originally expressed in harmonic coordinates. The tail (or hereditary) contributions, instead, are derived from the results of Ref. [223], which were subsequently extended in Ref. [150] to include higher-order corrections in the eccentricity and also to higher modes. However, the final result in Ref. [150] is written using the standard factorization of the circular part, *adding* the noncircular contribution as a correction. In Ref. [3] we used the PN-expanded results of Ref. [150] (considering only the nonspinning part), but we employed a rather different factorization scheme that leaves the generic Newtonian prefactor in the form that we have discussed before. However, we briefly recall here the steps needed to obtain these contributions (see also discussion in Sec. II of Ref. [3]).

Each waveform multipole can be written, before factorization, as

$$h_{\ell m} = 4\nu\sqrt{\frac{\pi}{5}}e^{-im\varphi}\hat{H}_{\ell m}, \tag{4.1}$$

where $\hat{H}_{\ell m}$ is the sum of an instantaneous contribution and a tail,

$$\hat{H}_{\ell m} = \hat{H}^{\rm inst}_{\ell m} + \hat{H}^{\rm tail}_{\ell m}. \tag{4.2}$$

The tail term is said to be *hereditary* because it is related to integrals that extend up to $t \to -\infty$, i.e. that take into account the whole history of the binary. We discuss the two addends of Eq. (4.2) in the following.

4.1.1 Instantaneous contributions

The instantaneous contributions to the modes for nonspinning binaries were derived in Ref. [224, 225] up to 2PN order and in Ref. [221] up to 3PN order, where the results are expressed in harmonic coordinates. The explicit form of $\hat{H}_{22}$ can be found in Eq. (4.4) of Ref. [221], but note that r and ϕ are harmonic coordinates in that expression. In Ref. [3] we denoted the harmonic coordinates with r_h and φ_h to avoid confusion with the EOB coordinates that are denoted, as usual, with r and φ. The transformation between harmonic and EOB coordinates can be found in Appendix A of Ref. [150], which has been derived following Ref. [160]. Following the same procedure, we wrote the quadrupolar instantaneous contribution in Eq. (4) of Ref. [3] in terms of the EOB phase-space variables (u, p_r, p_φ), where we recall that $u = 1/r$. The explicit expression for the quadrupolar instantaneous contribution is

$$
\begin{aligned}
\hat{H}_{22}^{\rm inst} &= u - p_r^2 + 2ip_r p_\varphi u + p_\varphi^2 u^2 + \frac{1}{c^2}\Bigg\{ i\left(\frac{\nu}{7} - \frac{5}{7}\right) p_r^3 p_\varphi u \\
&- ip_r p_\varphi u^2 \left[\left(\frac{4\nu}{7} + \frac{185}{21}\right) - \left(\frac{\nu}{7} - \frac{5}{7}\right) p_\varphi^2 u\right] \\
&+ \left(\frac{\nu}{14} - \frac{5}{14}\right)(p_\varphi^4 u^4 - p_r^4) + \left(\frac{3\nu}{14} + \frac{64}{14}\right) p_r^2 u \\
&+ u^2\left[(\nu - 4) + \left(\frac{31\nu}{14} - \frac{157}{42}\right) p_\varphi^2 u\right]\Bigg\} \\
&+ \frac{1}{c^4}\Bigg\{\left(\frac{17\nu^2}{168} + \frac{13\nu}{168} - \frac{5}{24}\right)(p_r^6 + p_r^4 p_\varphi^2 u^2 - p_\varphi^6 u^6) \\
&- i\left(\frac{17\nu^2}{84} + \frac{13\nu}{84} - \frac{5}{12}\right) p_r p_\varphi u (p_r^4 + p_\varphi^4 u^4)\Bigg] \\
&- p_r^2 u^2\Bigg[\left(\frac{13\nu^2}{63} + \frac{151\nu}{18} + \frac{1055}{252}\right) + \left(\frac{17\nu^2}{504} + \frac{13\nu}{504} - \frac{5}{72}\right) p_\varphi^4 u^2 \\
&+ \left(\frac{313\nu^2}{252} + \frac{85\nu}{252} - \frac{101}{252}\right) p_\varphi^2 u\Bigg] - \left(\frac{85\nu^2}{168} + \frac{55\nu}{168} + \frac{425}{168}\right) p_r^4 u \\
&+ ip_r^3 p_\varphi u^2\Bigg[\left(\frac{62\nu^2}{63} + \frac{11\nu}{126} + \frac{695}{126}\right) - \left(\frac{17\nu^2}{42} + \frac{13\nu}{42} - \frac{5}{6}\right) p_\varphi^2 u \\
&- ip_r p_\varphi u^3\Bigg[\left(\frac{523\nu^2}{189} + \frac{2452\nu}{189} - \frac{193}{27}\right) + \left(\frac{8\nu^2}{21} - \frac{29\nu}{14} - \frac{67}{28}\right) p_\varphi^2 u\Bigg] \\
&+ u^3\Bigg[\left(\frac{205\nu^2}{126} - \frac{49\nu}{18} + \frac{190}{63}\right) - \left(\frac{671\nu^2}{504} + \frac{1375\nu}{504} - \frac{481}{72}\right) p_\varphi^4 u^2 \\
&+ \left(\frac{127\nu^2}{27} - \frac{2710\nu}{189} - \frac{5519}{1512}\right) p_\varphi^2 u\Bigg]\Bigg\} + \mathcal{O}\left(\frac{1}{c^6}\right).
\end{aligned}
\tag{4.3}
$$

This is equivalent to Eq. (83) of Ref. [150] if one replaces the angular momentum with $p_\varphi^2 u^2 = p^2 - p_r^2$ (just to avoid confusion, here p is the modulus of the linear momentum). We applied the same procedure also to the other multipoles up to $\ell = 6$, confirming the results of Ref. [150]. We performed an additional check by using these multipoles,

together with the energy balance equations (2.37) and Eq. (1.42b), to obtain the 2PN angular momentum flux given by Eq. (3.70) of Ref. [160].

4.1.2 Hereditary contributions

The hereditary components $\hat{H}^{\rm tail}_{\ell m}$ are taken from Ref. [150]. These contributions were computed as an expansion in eccentricity and using the Keplerian parametrization (KP), according to the method outlined in Ref. [223]. The resulting tail contributions are initially expressed in terms of the frequency parameter $x = \Omega^{2/3}$, the eccentricity e, and the phase variable χ, which together with the semilatus rectum p parametrize the motion as $r = p/(1 + e\cos\chi)$. The semilatus rectum p and the eccentricity e used in Refs. [3, 150, 223] are defined in terms of the radial turning points using the $(e, p) \leftrightarrow (r_-, r_+)$ Newtonian relations, i.e. they are defined as in Eqs. (3.2). Note that the KP tail contributions in Ref. [150] are given up to 2PN and expanded in the eccentricity, see e.g. Eq. (97), where $\hat{H}^{\rm tail}_{22}$ is written up to $O(e^6)$.

Similarly to the instantaneous case, we want to rewrite the hereditary contribution using the phase-space variables (u, p_r, p_φ). Since we are working at 2PN accuracy, we can use the following Newtonian relations:

$$x = \frac{1-e^2}{p}, \tag{4.4a}$$

$$u = \frac{1+e\cos\chi}{p}, \tag{4.4b}$$

$$p_\varphi = \sqrt{p}, \tag{4.4c}$$

$$p_r = \frac{e\sin\chi}{\sqrt{p}}. \tag{4.4d}$$

This is possible since corrections to the leading Newtonian order would enter only at 2.5PN in the waveform. Since the expression for $\hat{H}^{\rm tail}_{22}$ in Eq. (97) of Ref. [150] is given as an expansion in the eccentricity e, it is important to identify the proper variables, in terms of (u, p_r, p_φ), which are of the same order in the eccentricity. It is possible to show that $\hat{H}^{\rm tail}_{22}$ translates into an expansion in both p_r and $\dot{p}_r$, with the latter related to p_φ through the Newtonian equation of motion

$$\dot{p}_r = u^2(p_\varphi^2 u - 1). \tag{4.5}$$

Using Eqs. (4.4a)–(4.4d), one can see that $p_r \sim e$ and $(p_\varphi^2 u - 1) \sim e$. From this and Eq. (97) of Ref. [150], one obtains an expression in terms of $(u, p_r, \dot{p}_r)$ which contains also half-integer powers of u, and that is reported in Eq. (18) of Ref. [3]. These half-integer powers can be eliminated by using Eq. (4.5), which, after an expansion in $\dot{p}_r$ (i.e., in eccentricity) gives

$$\frac{1}{\sqrt{u}} = p_\varphi\left(1 - \frac{\dot{p}_r}{2u^2} + \frac{3\dot{p}_r^2}{8u^4} - \frac{5\dot{p}_r^3}{16u^6} + \frac{35\dot{p}_r^4}{128u^8} - \frac{63\dot{p}_r^5}{256u^{10}} + \frac{231\dot{p}_r^6}{1024u^{12}}\right) + \mathcal{O}(\dot{p}_r^7). \tag{4.6}$$

Using this expression in the tail contribution, one obtains $\hat{H}^{\rm tail}_{22}$ written in terms of $(u, p_r, p_\varphi, \dot{p}_r)$ (see Eq. (102) of Ref. [150] or Eq. (21) of Ref. [3]). In order to eliminate the dependence on $\dot{p}_r$, we can use again Eq. (4.5). The final result for the quadrupolar tail in terms of (u, p_r, p_φ) is

$$\hat{H}^{\rm tail}_{22} = \frac{2\pi}{c^3}\left[p_\varphi u^3\left(\frac{1931}{1440} - \frac{595p_\varphi^2 u}{384} + \frac{377p_\varphi^4 u^2}{128} - \frac{1747p_\varphi^6 u^3}{576}\right.\right.$$

$$
\begin{aligned}
&+\frac{347p_\varphi^8u^4}{192}-\frac{381p_\varphi^{10}u^5}{640}+\frac{97p_\varphi^{12}u^6}{1152}\Bigg)\\
&-ip_ru^2\left(\frac{9}{256}-\frac{29p_\varphi^2u}{48}+\frac{39p_\varphi^4u^2}{128}+\frac{5p_\varphi^6u^3}{64}-\frac{61p_\varphi^8u^4}{768}+\frac{p_\varphi^{10}u^5}{64}\right)\\
&-p_r^2p_\varphi u^2\left(\frac{53}{192}-\frac{13p_\varphi^2u}{64}-\frac{17p_\varphi^4u^2}{64}+\frac{49p_\varphi^6u^3}{192}-\frac{p_\varphi^8u^4}{16}\right)\\
&-ip_r^3u\left(\frac{47}{288}-\frac{77p_\varphi^2u}{128}+\frac{31p_\varphi^4u^2}{64}-\frac{137p_\varphi^6u^3}{1152}\right)\\
&-p_r^4p_\varphi u\left(\frac{35}{192}-\frac{125p_\varphi^2u}{384}+\frac{47p_\varphi^4u^2}{384}\right)\\
&+ip_r^5\left(\frac{227}{3840}-\frac{23p_\varphi^2u}{640}\right)+\frac{p_r^6p_\varphi}{96}\Bigg].
\end{aligned}
\tag{4.7}
$$

In this way, the tail and instantaneous terms are written with the same variables. The absence of logarithmic terms in Eq. (4.7), which typically appears in tail terms, is due to a phase redefinition performed at the level of the KP tail contribution (see Sec. III C of Ref. [223]).

4.1.3 Factorization

Now that we have the generic instantaneous and hereditary contributions up to 2PN for the (ℓ,m)-modes up to $\ell=6$, we want to reproduce the standard EOB factorization with some additional factors that incorporate the 2PN noncircular corrections. The factorization is achieved in three steps: (i) we factorize the generic Newtonian prefactor, (ii) we expand the residual using the 2PN EOM for the time-derivatives, (iii) we factor out the PN circular part so that we have residual noncircular PN corrections to include in Eq. (2.36).

Factorization for the $m\neq0$ modes

We start by discussing the factorization of the $m\neq0$ multipoles. We want to write the EOB waveform factorized as [3]

$$
h_{\ell m}=h_{\ell m}^{(N,\epsilon)_{\rm c}}\hat{h}_{\ell m}^{(N,\epsilon)_{\rm nc}}\hat{h}_{\ell m}^{(\epsilon)_{\rm c}}\hat{h}_{\ell m}^{\rm nc},
\tag{4.8}
$$

where $\hat{h}_{\ell m}^{\rm nc}$ is the new factor that includes the 2PN noncircular corrections, while the other terms have been already discussed in Sec. 2.3.2.

As anticipated, we start by factorizing the general Newtonian factor $h_{\ell m}^{(N,\epsilon)_{\rm c}}\hat{h}_{\ell m}^{(N,\epsilon)_{\rm nc}}$ from the waveform multipole, so that the residual generic PN corrections can be written as

$$
\hat{h}_{\ell m}^{(\epsilon)}\equiv T_{\rm 2PN}\left[\frac{h_{\ell m}}{\left(h_{\ell m}^{(N,\epsilon)_{\rm c}}\hat{h}_{\ell m}^{(N,\epsilon)_{\rm nc}}\right)_{\rm EOMs}}\right],
\tag{4.9}
$$

where $T_{\rm 2PN}$ indicates an expression at 2PN order. The subscript "EOMs" highlights that in the Newtonian term we replace the time-derivatives with the corresponding EOB EOM at 2PN. The first-time derivatives can be found in Appendix B of Ref. [160], the

higher-order derivatives follow easily. The expression (4.9) is thus a corrections in the form "1+PN terms" written in terms of (u, p_r, p_φ). Note that for the $m = 0$ modes, the circular Newtonian part vanishes, $h_{\ell 0}^{(N,\epsilon)_{\rm c}} = 0$. Therefore, we need a different factorization in those cases. We discuss the factorization of the $m = 0$ modes in the next subsection.

The circular PN contribution can be easily obtained as

$$\hat{h}_{\ell m}^{(\epsilon)_{\rm c}} \equiv \lim_{p_r \to 0} \hat{h}_{\ell m}^{(\epsilon)}, \tag{4.10}$$

and can be factorized from the generic PN corrections of Eq. (4.9) as

$$\hat{h}_{\ell m}^{\rm nc} \equiv T_{\rm 2PN} \left[\frac{\hat{h}_{\ell m}^{(\epsilon)}}{\hat{h}_{\ell m}^{(\epsilon)_{\rm c}}} \right], \tag{4.11}$$

The above equation contains thus 2PN noncircular corrections that were not previously included in the model. We can easily split this correction into instantaneous and hereditary parts since these two contributions enter a different PN order (cfr. Eq. (4.3) and Eq. (4.7), where we left explicit powers of c for clarity). We can thus write

$$\hat{h}_{\ell m}^{\rm nc} = \hat{h}_{\ell m}^{\rm nc_{tail}} \hat{h}_{\ell m}^{\rm nc_{inst}}. \tag{4.12}$$

We also rewrite the terms using the conjugate momentum of the tortoise coordinate rather than radial momentum, since the former is not singular at the event horizon. We thus replace p_r with $p_{r_*} = (A/B)^{1/2} p_r$ expanded at 2PN order. To further simplify the analytical structure of these terms, we further expand each term up to $p_{r_*}^4$. We have explicitly verified that the result expanded in p_{r_*} is practically equivalent to the not-expanded result, even for highly eccentric and hyperbolic-like dynamics.

For the quadrupolar 2PN noncircular tail contribution, we find

$$\begin{aligned} \hat{h}_{22}^{\rm nc_{tail}} = 1 + \frac{1}{c^3} \frac{\pi}{(p_\varphi^2 u + 1)^2} \Bigg[- i \left(\frac{9 p_{r_*} u}{64} \hat{t}_{p_{r_*}}^{22} + \frac{457}{456} \frac{p_{r_*}^3}{(p_\varphi^2 u + 1)^2} \hat{t}_{p_{r_*}^3}^{22} \right) \\ + \frac{5729}{1440} \frac{p_{r_*}^2 p_\varphi u}{(p_\varphi^2 u + 1)} \hat{t}_{p_{r_*}^2}^{22} + \frac{133}{80} \frac{p_{r_*}^4 p_\varphi}{(p_\varphi^2 u + 1)^3} \hat{t}_{p_{r_*}^4}^{22} \Bigg], \end{aligned} \tag{4.13}$$

where $(\hat{t}_{p_{r_*}}^{22}, \hat{t}_{p_{r_*}^3}^{22}, \hat{t}_{p_{r_*}^2}^{22}, \hat{t}_{p_{r_*}^4}^{22})$ are the following alternate-sign polynomials in $y \equiv p_\varphi^2 u$:

$$\begin{aligned} \hat{t}_{p_{r_*}}^{22} &= 1 + \frac{24341}{405} y - \frac{290}{3} y^2 + \frac{1606}{9} y^3 - \frac{13979}{81} y^4 \\ &\quad + 101 y^5 - \frac{1504}{45} y^6 + \frac{388}{81} y^7, \end{aligned} \tag{4.14}$$

$$\begin{aligned} \hat{t}_{p_{r_*}^3}^{22} &= 1 + \frac{46372}{2285} y - \frac{134587}{2285} y^2 + \frac{45492}{457} y^3 \\ &\quad - \frac{54397}{457} y^4 + \frac{43924}{457} y^5 - \frac{112697}{2285} y^6 \\ &\quad + \frac{32212}{2285} y^7 - \frac{776}{457} y^8, \end{aligned} \tag{4.15}$$

$$\begin{aligned} \hat{t}_{p_{r_*}^2}^{22} &= 1 - \frac{27552}{5729} y + \frac{2910}{337} y^2 - \frac{70015}{5729} y^3 \\ &\quad + \frac{61785}{5729} y^4 - \frac{34674}{5729} y^5 + \frac{10952}{5729} y^6 - \frac{1455}{5729} y^7, \end{aligned} \tag{4.16}$$

$$\hat{t}^{22}_{p^4_{r_*}} = 1 - \frac{35260}{1197}y + \frac{78500}{1197}y^2 - \frac{34825}{342}y^3 + \frac{265975}{2394}y^4 - \frac{96727}{1107}y^5 + \frac{6305}{171}y^6 - \frac{3245}{342}y^7 + \frac{2425}{2394}y^8. \tag{4.17}$$

For the instantaneous factor, we separate amplitude and phase as

$$h^{\rm nc_{inst}}_{22} = f^{\rm nc_{inst}}_{22} e^{{\rm i}\delta^{\rm nc_{inst}}_{22}}, \tag{4.18}$$

which, respectively, are given by

$$\begin{aligned} f^{\rm nc_{inst}}_{22} =& 1 - \frac{p^2_{r_*}}{c^2\left(p^2_\varphi u+1\right)^3}\left[\left(\frac{1}{14}-\frac{31\nu}{14}\right)\hat{f}^{22}_{1^{\rm 1PN}} + \frac{p^2_{r_*}}{u\left(p^2_\varphi u+1\right)^2}\left(\frac{5}{7}-\frac{8\nu}{7}\right)\hat{f}^{22}_{p^{\rm 1PN}_{r_*}}\right] \\ &+ \frac{p^2_{r_*}}{c^4\left(p^2_\varphi u+1\right)^4}\left[u\left(\frac{65}{252}+\frac{211\nu}{126}+\frac{139\nu^2}{63}\right)\hat{f}^{22}_{u^{\rm 2PN}}\right. \\ &\left. + \frac{p^2_{r_*}}{\left(p^2_\varphi u+1\right)^2}\left(\frac{1613}{504}-\frac{1567\nu}{504}-\frac{71\nu^2}{72}\right)\hat{f}^{22}_{p^{\rm 1PN}_{r_*}}\right], \end{aligned} \tag{4.19}$$

$$\begin{aligned} \delta^{\rm nc_{inst}}_{22} =& \frac{1}{c^2}\frac{p_{r_*}p_\varphi}{(p^2_\varphi u+1)^2}\left[u\left(\frac{25}{21}-\frac{18}{7}\nu\right)\hat{\delta}^{22}_{u^{\rm 1PN}} + \frac{p^2_{r_*}}{(p^2_\varphi u+1)^2}\left(\frac{55}{21}-\frac{34\nu}{7}\right)\hat{\delta}^{22}_{p^{\rm 1PN}_{r_*}}\right] \\ &+ \frac{1}{c^4}\frac{p_{r_*}p_\varphi u}{(p^2_\varphi u+1)^3}\left[u\left(\frac{7}{27}-\frac{416}{189}\nu-\frac{652}{189}\nu^2\right)\hat{\delta}^{22}_{u^{\rm 2PN}}\right. \\ &\left. + \frac{p^2_{r_*}}{(p^2_\varphi u+1)^2}\left(\frac{20945}{2646}-\frac{17321}{1323}\nu+\frac{134}{1323}\nu^2\right)\hat{\delta}^{22}_{p^{\rm 2PN}_{r_*}}\right]. \end{aligned} \tag{4.20}$$

Similarly to the tail factor, the functions $(\hat{f}_i, \hat{\delta}_i)$ are polynomials in y. For the amplitude contribution we have

$$\hat{f}^{22}_{1^{\rm 1PN}} = 1 - \frac{7(1+3\nu)}{1-31\nu}y - \frac{(451-177\nu)}{3-93\nu}y^2 - \frac{3(3+5\nu)}{1-31\nu}y^3, \tag{4.21}$$

$$\hat{f}^{22}_{p^{\rm 1PN}_{r_*}} = 1 - \frac{65-216\nu}{3(5-8\nu)}y - \frac{5(115-72\nu)}{3(5-8\nu)}y^2 + \frac{305-264\nu}{3(5-8\nu)}y^3, \tag{4.22}$$

$$\begin{aligned} \hat{f}^{22}_{u^{\rm 2PN}} =& 1 - \frac{44767+28618\nu-7276\nu^2}{42\left(65+422\nu+556\nu^2\right)}y \\ &+ \frac{132507-87244\nu-29672\nu^2}{14\left(65+422\nu+556\nu^2\right)}y^2 \\ &- \frac{134789+27920\nu+9472\nu^2}{42\left(65+422\nu+556\nu^2\right)}y^3 \\ &- \frac{3\left(637-1448\nu+512\nu^2\right)}{2\left(65+422\nu+556\nu^2\right)}y^4 \end{aligned}$$

$$- \frac{3\left(418+355\nu+710\nu^2\right)}{7\left(65+422\nu+556\nu^2\right)}y^5, \tag{4.23}$$

$$\begin{aligned}\hat{f}^{22}_{p^{\rm 2PN}_{r_*}} = 1 &- \frac{16399-169738\nu-9902\nu^2}{7\left(1613-1567\nu-497\nu^2\right)}y \\ &- \frac{256835-145513\nu+7405\nu^2}{4839-4701\nu-1491\nu^2}y^2 \\ &+ \frac{4\left(292018-194489\nu-76057\nu^2\right)}{21\left(1613-1567\nu-497\nu^2\right)}y^3 \\ &- \frac{449937+29671\nu-80119\nu^2}{7\left(1613-1567\nu-497\nu^2\right)}y^4 \\ &- \frac{34361-33826\nu-3518\nu^2}{7\left(1613-1567\nu-497\nu^2\right)}y^5 \\ &+ \frac{15\left(5-13\nu+\nu^2\right)}{1613-1567\nu-497\nu^2}y^6, \end{aligned} \tag{4.24}$$

while for the phase

$$\hat{\delta}^{22}_{u^{\rm 1PN}} = 1 + \frac{125-102\nu}{25-54\nu}y, \tag{4.25}$$

$$\hat{\delta}^{22}_{p^{\rm 1PN}_{r_*}} = 1 + \frac{42\left(5-2\nu\right)}{55-102\nu}y - \frac{35\left(7-6\nu\right)}{55-102\nu}y^2, \tag{4.26}$$

$$\begin{aligned}\hat{\delta}^{22}_{u^{\rm 2PN}} = 1 &+ \frac{39761-20950\nu-21236\nu^2}{14\left(49-416\nu-652\nu^2\right)}y \\ &- \frac{3\left(3709-2556\nu-408\nu^2\right)}{14\left(49-416\nu-652\nu^2\right)}y^2 \\ &- \frac{3\left(767-2551\nu-1070\nu^2\right)}{7\left(49-416\nu-652\nu^2\right)}y^3 \ , \end{aligned} \tag{4.27}$$

$$\begin{aligned}\hat{\delta}^{22}_{p^{\rm 2PN}_{r_*}} = 1 &+ \frac{66624-84120\nu+300789\nu^2}{41890-69284\nu+536\nu^2}y \\ &- \frac{292601-144464\nu^2-298528\nu}{41890-69284\nu+536\nu^2}y^2 \\ &+ \frac{7\left(28217+17672\nu-1664\nu^2\right)}{41890-69284\nu+536\nu^2}y^3 \\ &+ \frac{3\left(6473-23284\nu+6856\nu^2\right)}{41890-69284\nu+536\nu^2}y^4 \ . \end{aligned} \tag{4.28}$$

Note that $y = p_\varphi^2 u$ is not a small quantity, so the y-polynomials in the above expression need a proper resummation, as we will discuss in Sec. 4.1.4. Moreover, the factor in front of $\hat{f}^{22}_{p^{\rm 1PN}_{r_*}}$ in Eq. (4.19) has a $1/u = r$ contribution. Therefore, for large separations, this term starts to dominate the others and becomes source of inaccuracies. This is one of the reasons that led us to the new factorization proposed in Ref. [5]. However, this term is not problematic for the configurations considered in Refs. [3, 4], as we will see in a moment when testing these new analytical contributions against numerical results.

Factorization for the $m = 0$ modes

As mentioned in the previous subsection, the circular Newtonian prefactor vanishes for the $m = 0$ modes, and therefore cannot be factorized. In this case, we factorize the multipoles as [3]

$$h_{\ell 0} = \hat{S}_{\rm eff} \left(h_{\ell 0}^{(N,\epsilon)} + \hat{\hat{h}}_{\ell 0} \right), \tag{4.29}$$

where the PN correction, which indeed is fully noncircular, is given by

$$\hat{\hat{h}}_{\ell 0} = T_{\rm 2PN} \left[\left(\frac{h_{\ell 0} - h_{\ell 0}^{(N,\epsilon)}}{\hat{S}_{\rm eff}} \right)_{\rm EOMs} \right]. \tag{4.30}$$

The effective source term $\hat{S}_{\rm eff}$ is the one discussed in Sec. 2.3.2. We proceed to split instantaneous and a tail parts as done before,

$$\hat{\hat{h}}_{\ell 0} = \hat{\hat{h}}_{\ell 0}^{\rm tail} + \hat{\hat{h}}_{\ell 0}^{\rm inst}. \tag{4.31}$$

Here we prefer to express the PN corrections using $(r, p_{r_*}, \dot{p}_{r_*})$, without writing $\dot{p}_{r_*}$ in terms of (r, p_{r_*}, p_φ). The reason is that in this case writing the corrections in p_φ leads to terms that do not vanish in the circular limit since they are not proportional to powers of p_{r_*} (more precisely, some contributions vanish in the circular limit only when p_φ is replaced with its corresponding quasicircular PN expansion in terms of u). The corresponding PN corrections for the $(2,0)$ mode read

$$\begin{aligned}
\hat{\hat{h}}_{20}^{\rm tail} = & -\frac{\pi}{960u^{10}c^3}\sqrt{\frac{\dot{p}_{r_*}+u^2}{6u}}\Big[960\dot{p}_{r_*}u^{10} + 960\dot{p}_{r_*}^2u^8 + 240\left(-3\dot{p}_{r_*}^3u^6\right. \\
& \left. + p_{r_*}^2\dot{p}_{r_*}u^9\right) + 80u^4\left(7\dot{p}_{r_*}^4 + 2p_{r_*}^4u^6\right) - 5\left(95\dot{p}_{r_*}^5u^2 + 26p_{r_*}^2\dot{p}_{r_*}^3u^5\right. \\
& \left. + 11p_{r_*}^4\dot{p}_{r_*}u^8\right) + \left(417\dot{p}_{r_*}^6 + 110p_{r_*}^2\dot{p}_{r_*}^4u^3 - 45p_{r_*}^4\dot{p}_{r_*}^2u^6 + 2p_{r_*}^6u^9\right)\Big], \qquad (4.32) \\
\hat{\hat{h}}_{20}^{\rm inst} = & \frac{1}{14\sqrt{6}u^2c^2}\Big[\dot{p}_{r_*}u^2(-19+\nu) + 3\left(\dot{p}_{r_*}^2 - p_{r_*}^2u^3\right)(3+5\nu) \\
& + 6p_{r_*}^2\dot{p}_{r_*}u(3+5\nu) + 3p_{r_*}^4u^2(3+5\nu)\Big] + \frac{1}{504\sqrt{6}u^3c^4}\Big[\dot{p}_{r_*}u^4\left(1052-\right. \\
& \left. 2803\nu - 53\nu^2\right) + p_{r_*}^2u^5\left(-743 + 7009\nu - 571\nu^2\right) + 3\dot{p}_{r_*}^2u^2\left(545\right. \\
& \left. -430\nu + 28\nu^2\right) - 3\dot{p}_{r_*}^3\left(79 + 25\nu + 5\nu^2\right) + 18p_{r_*}^2\dot{p}_{r_*}u^3\left(81 + 404\nu\right. \\
& \left. +65\nu^2\right) - 9p_{r_*}^2\dot{p}_{r_*}^2u\left(115 + 121\nu + 65\nu^2\right) + 6p_{r_*}^4u^4\left(79\right. \\
& \left. +133\nu + 185\nu^2\right) - 9p_{r_*}^4\dot{p}_{r_*}u^2\left(151 + 217\nu + 125\nu^2\right) \\
& - 3p_{r_*}^6u^3\left(187 + 313\nu + 185\nu^2\right)\Big]. \qquad (4.33)
\end{aligned}$$

4.1.4 Resummation

In the previous sections, we have discussed a factorization for the 2PN noncircular corrections for the $m \neq 0$ modes. However, in order to include these corrections in the waveform and to improve its accuracy, we have to consider a proper resummation. Indeed, if one does not adopt any resummation scheme, these 2PN noncircular corrections

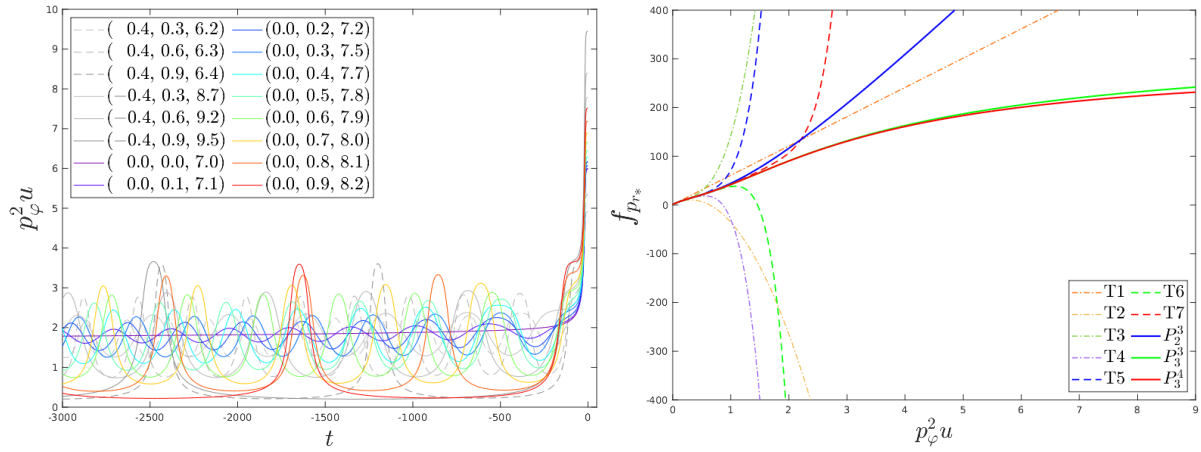

Figure 4.1: Left panel: last part of the time evolution of $p_\varphi^2 u$ for different combinations of $(\hat{a}, e_0, p_0)$; aligned with respect $t_{\rm mrg}$. Right panel: Behavior of various truncations of the $\hat{t}^{22}_{p_{r_*}}$ polynomial of Eq. (4.14). The various Taylor truncations of $\hat{t}^{22}_{p_{r_*}}$ oscillate and become very large for values of $p_\varphi^2 u$ of the order of those reached at periastron for large eccentricity or during the plunge. A diagonal Padé approximant P_d^n improves the behavior of the polynomials in strong-field regimes and eventually improves the behavior of the waveform there.

lead to a much worse analytical/numerical agreement with respect to the wave incorporating only Newtonian noncircular corrections. In particular, as shown in the left panel of Fig. 4.2 (see also Fig. 1 of Ref. [3] for more configurations), the non-resummed corrections are so unreliable during the plunge, that the NQC corrections are not able to correct their bad behavior. As a consequence, the accuracy of the analytical waveform is rather poor. Moreover, these non-resummed corrections strongly worsen the analytical/numerical phase agreement at apastron for highly eccentric inspirals.

The main issue can be traced back to the y-polynomials that appear in the hereditary contribution of Eq. (4.13). We recall that the original tail term was expanded in eccentricity up to $O(e^6)$; one can then rewrite this expansion in the radial momentum p_r and $\dot{p}_r$, which can be subsequently recast in a form where one is left with several polynomials in $y = p_\varphi^2 u$. Since y is a Newtonian order term (see also Eq. (4.4c)), we do not expect y to be small, especially during the last stages of the evolution of the binary. Values of y for different eccentric configurations are shown in Fig. 4.1. During the plunge we can even reach $y \sim 7$; note that y is also quite big at periastron for sufficiently eccentric binaries. As a consequence, these polynomials will grow drastically if we consider only a finite number of terms. However, since these polynomials have alternate signs, if we consider an infinite number of terms we can have term-by-term cancellations. A simple way to include this infinite number of terms is to replace the polynomials with Padé approximants. The efficacy of this resummation for $\hat{t}^{22}_{p_{r_*}}$ is shown in the right panel of Fig. 4.1, where we report various Taylor truncations and two Padé approximants. A completely analogous behavior is found for the other three functions $(\hat{t}^{22}_{p^3_{r_*}}, \hat{t}^{22}_{p^2_{r_*}}, \hat{t}^{22}_{p^4_{r_*}})$, which are thus also resummed. In practice, we replace the Taylor-expanded functions with $(P^4_3[\hat{t}^{22}_{p_{r_*}}], P^4_4[\hat{t}^{22}_{p^3_{r_*}}], P^4_3[\hat{t}^{22}_{p^2_{r_*}}], P^4_4[\hat{t}^{22}_{p^4_{r_*}}])$.

The improvement in the waveform due to the tail-resummation can be seen in the right panel of Fig, 4.2. The analytical/numerical phase agreement is not only better (and largely) during the plunge and merger phase, but also increases during the eccentric inspiral with respect to the waveform with expanded hereditary noncircular contribution. Moreover, the improvement for the phase with respect to the simple Newtonian prefactor

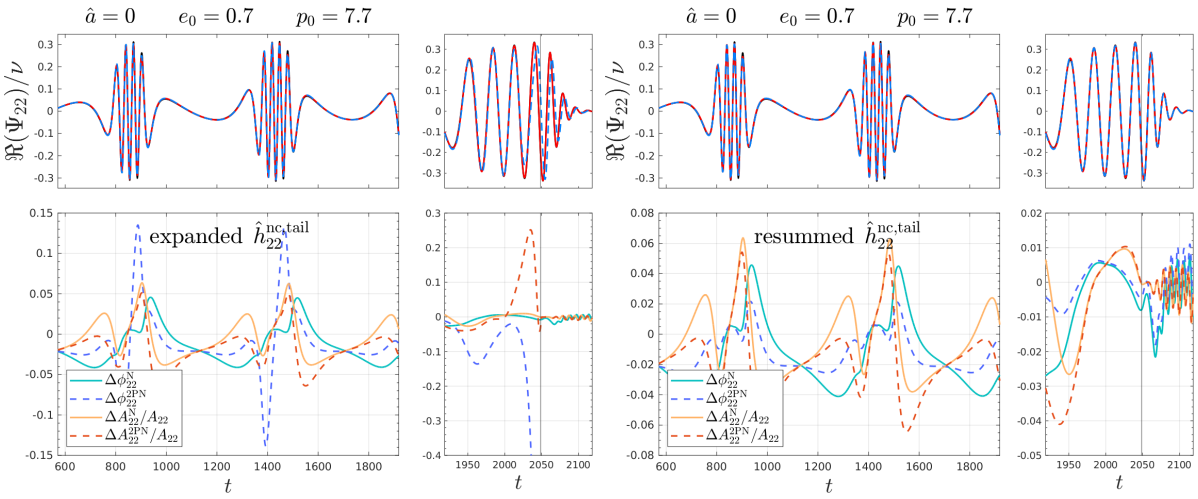

Figure 4.2: Left panel: comparisons with *nonresummed* noncircular tail factor: comparing analytical and numerical $\ell = m = 2$ waveforms for the transition from inspiral to plunge of a test particle on a Schwarzschild black hole with initial eccentricity $e_0 = 0.7$. We show the numerical waveform (black, indistinguishable) and two EOB waveforms: (i) the solid-red one with noncircular information only in the Newtonian prefactor and (ii) the dashed-blue one with noncircular 2PN corrections with the *nonresummed* tail $\hat{h}^{\rm nc_{tail}}_{22}$ of Eq. (4.13). The bottom panel shows both the phase differences and the relative amplitude differences with respect to the numerical waveform. We use dashed lines for the differences corresponding to the wave with 2PN corrections. The vertical line marks the merger time, corresponding to the peak of the numerical amplitude. Right panel: as the left one, but considering the *resummed* noncircular tail factor. The resummation strongly improves the analytical/numerical agreement, both at periastron and during the plunge-merger.

is evident all over, notably without pathological behaviors toward merger. On the contrary, the 2PN corrections do not seem to clearly improve (nor degrade) the accuracy of the amplitude.

Similarly, one can try to extend the resummation to the instantaneous contribution of Eqs. (4.19) and Eq. (4.20), that also contain y-polynomials. However, for the amplitude, we find that any choice of Padé approximant for the various residual polynomials in y develops spurious poles, so our resummation strategy cannot be pursued. By contrast, for the instantaneous residual noncircular phase given in Eq. (4.20), the procedure is robust. More precisely, we resum the y polynomials $\hat{\delta}^{22}$ of Eq. (4.20) using the Padé approximants $P^1_0[\hat{\delta}^{22}_{u^{\rm 1PN}}]$, $P^1_1[\hat{\delta}^{22}_{p^{\rm 1PN}_{r_*}}]$, $P^1_2[\hat{\delta}^{22}_{u^{\rm 2PN}}]$, and $P^1_1[\hat{\delta}^{22}_{p^{\rm 2PN}_{r_*}}]$. Note that the latter polynomial, written explicitly in Eq. (4.28), is at 4th-order in y, but we only use $O(y^2)$ terms since the P^2_1 approximant produces unphysical behaviors for large y and the other higher-order Padé approximants have spurious poles in the equal-mass case. The improvements introduced by this resummation are shown in Fig. 5 of Ref. [3] (green dashed lines), where we compare the analytical/numerical phase differences of the newly obtained waveform with the phase differences of the previous prescription, where the resummation was applied only to the eccentric hereditary terms. While a slight improvement in the phase accuracy can be seen in almost all the reported cases, the resummation of the instantaneous phase correction is much less relevant than the resummation of the eccentric tail. Nonetheless, in Ref. [3], we used the resummed instantaneous phase as our default option for the 2PN noncircular corrections written in terms of (u, p_{r_*}, p_φ).

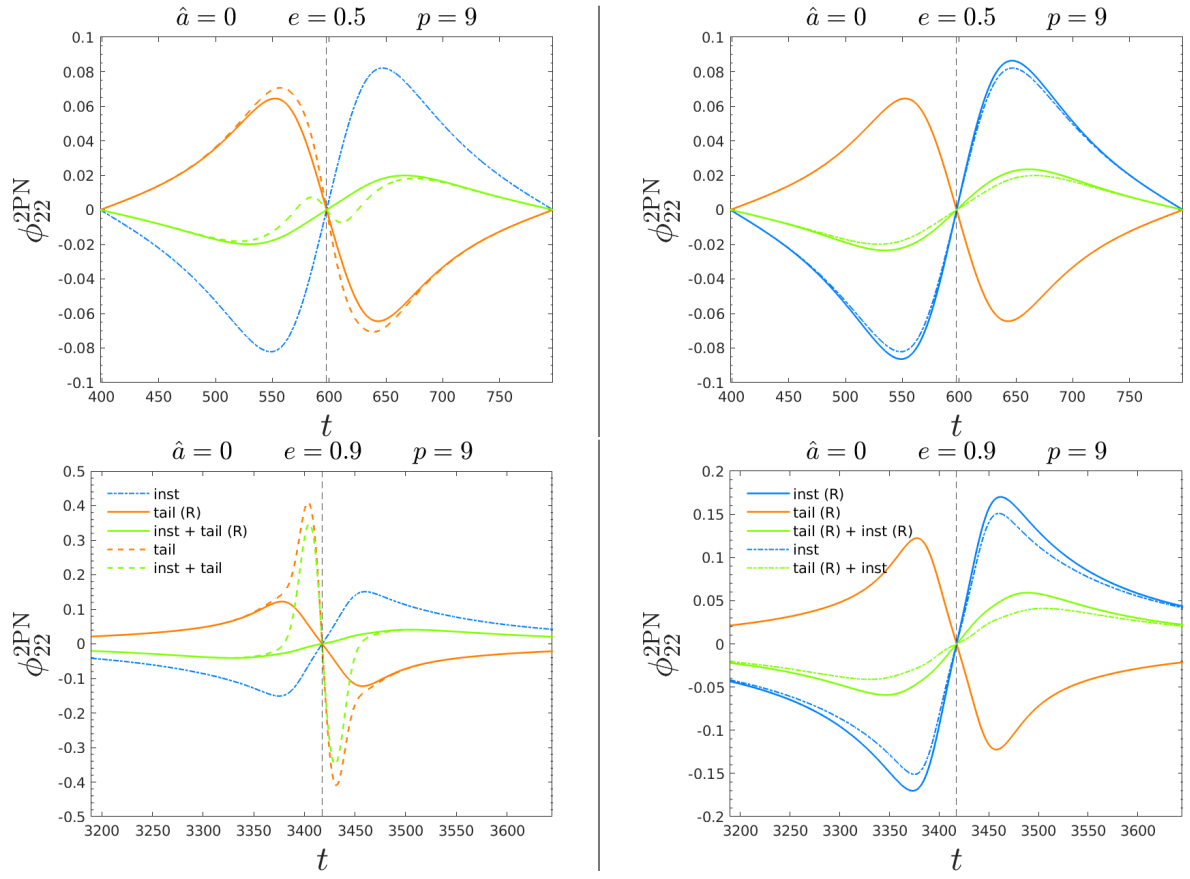

Figure 4.3: Left panels: instantaneous and hereditary noncircular 2PN corrections to the quadrupolar phase for two nonspinning geodesic cases with $e = (0.5, 0.9)$ and $p = 9$. The instantaneous phase corrections are shown with dot-dashed blue lines, while the orange lines are for the phase contributions of the resummed eccentric tail (dashed for the expanded results and solid for the resummed ones). The corresponding sums between instantaneous and hereditary are shown in green with the same style scheme of the considered tail. The vertical dashed line marks the periastron passage. For $e = 0.9$, we do not show the whole radial period in order to highlight the periastron. Right panels: analogous to left panels, but focusing on the relevance of the resummation for the instantaneous part. The orange solid line is the phase contribution of the resummed eccentric tail, while the blue lines correspond to the instantaneous phase contributions: dot-dashed for the nonresummed results and solid line for the resummed ones. The corresponding sums between tail and instantaneous are shown in green with the same style scheme of the instantaneous terms.

4.1.5 Compensation between instantaneous and tail terms

We now discuss a rather peculiar behavior of these noncircular corrections. We start by noting that, as shown in the previous section, the contribution of the 2PN corrections is quite small with respect to the improvement introduced by the generic Newtonian prefactor, see e.g. amplitude and phase differences for the Newtonian and 2PN corrected waveforms in the right panel of Fig. 4.2. An explanation of this effect can be obtained by separately analyzing the cumulative action of the instantaneous and hereditary contributions to the waveform: one finds that the good performance of our resummed waveform is due to *compensations* between the two. More importantly, one notices that the instantaneous contributions alone tend to *overestimate* the analytical phase, eventually yielding phase differences with the numerical waveform that are *larger* than those obtained with the simple Newtonian prefactor. This is very clear when inspecting the left panels of Fig. 4.3, which illustrates this effect for two different geodesic configurations with $e = (0.5, 0.9)$ and $p = 9$. Indeed, at high eccentricity and relatively small semilatus rectum, the resummation of the tail factor is a crucial aspect to have compensations between instantaneous and hereditary terms. The benefits of the resummation can be seen even at milder eccentricities or larger semilatera recta, even if it is less crucial. In the right panels of Fig. 4.3, we also show the effect of the resummation of the instantaneous factor for the same geodesic configurations considered in the left panels. While the effect of the resummation is clearly visible, it is also evident that the resummation of the instantaneous part is less relevant than the tail resummation, as we saw in the previous subsection.

Since the instantaneous and hereditary terms enter at different PN orders, we have compensation between different orders of the perturbative expansion. This aspect will be crucial while discussing the higher modes, in the next section. Indeed, since we are considering the global 2PN order, some higher modes do not have instantaneous corrections at relative 2PN order (see expressions in the next section). Finally, a consequence of this compensation between different PN orders is that higher PN corrections do not guarantee a more accurate analytical waveform.

4.1.6 Higher modes

So far, we focused on the quadrupolar contribution. We now discuss the 2PN corrections for the higher (subdominant) modes, that can be obtained as discussed in the previous sections. The modes that have corrections at 2PN global order are all the modes up to $\ell = 3$ and the $\ell = 4$ even modes. All the corrections for the relevant (at 2PN) $m \neq 0$ modes are reported in Appendix B.1. The (2,1), (2,0), (3,3), and (3,1) modes have a tail contribution at 1.5PN, as the (2,2) mode, while the (3,2) and (4,4), and higher modes do not. In particular, the tail contributions of the (2,1) and (3,3) modes read

$$\hat{h}^{\mathrm{nc_{tail}}}_{21} = 1 + \frac{1}{c^3}\pi\Bigg[- i \left(\frac{3029}{1920} u p_{r_*}\, \hat{t}^{21}_{p_{r_*}} + \frac{619}{576} p^3_{r_*}\, \hat{t}^{21}_{p^3_{r_*}} \right) + \frac{635}{768} \frac{p^2_{r_*}}{p_\varphi}\, \hat{t}^{21}_{p^2_{r_*}} - \frac{61}{256} \frac{p^4_{r_*}}{p_\varphi u}\, \hat{t}^{21}_{p^4_{r_*}} \Bigg], \tag{4.34}$$

$$\hat{h}^{\mathrm{nc_{tail}}}_{33} = 1 + \frac{1}{c^3} \frac{\pi}{p^2_\varphi (7 + 2p^2_\varphi u)^2} \Bigg[- i \left(\frac{4763}{384} p_{r_*} \hat{t}^{33}_{p_{r_*}} - \frac{4763}{24} \frac{p^2_\varphi p^3_{r_*}}{p^2_\varphi u^2 (7 + 2p^2_\varphi u)^2}\, \hat{t}^{33}_{p^3_{r_*}} \right)$$

$$+\frac{4763}{96}\frac{p_{r_*}^2}{p_\varphi u(7+2p_\varphi^2 u)}\hat{t}^{33}_{p^2_{r_*}}+\frac{4763}{6}\frac{p_\varphi^3 p_{r_*}^4}{p_\varphi^3 u^3(7+2p_\varphi^2 u)^3}\hat{t}^{33}_{p^4_{r_*}}\Bigg], \tag{4.35}$$

where

$$\hat{t}^{21}_{p_{r_*}}=1+\frac{6035y}{3029}-\frac{10870y^2}{3029}+\frac{8350y^3}{3029}-\frac{3215y^4}{3029}+\frac{511y^5}{3029}, \tag{4.36}$$

$$\hat{t}^{21}_{p^2_{r_*}}=1-\frac{1388y}{635}+\frac{666y^2}{635}-\frac{92y^3}{635}-\frac{13y^4}{635}, \tag{4.37}$$

$$\hat{t}^{21}_{p^3_{r_*}}=1-\frac{981y}{619}+\frac{573y^2}{619}-\frac{115y^3}{619}, \tag{4.38}$$

$$\hat{t}^{21}_{p^4_{r_*}}=1-\frac{82y}{183}-\frac{17y^2}{183}, \tag{4.39}$$

$$\begin{aligned}\hat{t}^{33}_{p_{r_*}}=1&+\frac{67183y}{23815}+\frac{721737y^2}{47630}-\frac{85973y^3}{9526}\\&+\frac{30812y^4}{4763}-\frac{10722y^5}{4763}+\frac{16769y^6}{47630}-\frac{337y^7}{47630},\end{aligned} \tag{4.40}$$

$$\begin{aligned}\hat{t}^{33}_{p^3_{r_*}}=1&+\frac{3125521y}{762080}+\frac{5675333y^2}{762080}-\frac{2623521y^3}{69280}\\&+\frac{3513777y^4}{95260}-\frac{2943211y^5}{152416}+\frac{7128059y^6}{762080}\\&-\frac{2725303y^7}{762080}+\frac{35247y^8}{95260}+\frac{5233y^9}{95260},\end{aligned} \tag{4.41}$$

$$\begin{aligned}\hat{t}^{33}_{p^2_{r_*}}=1&+\frac{1407963y}{381040}-\frac{343943y^2}{47630}+\frac{2036583y^3}{95260}-\frac{271775y^4}{19052}\\&+\frac{602219y^5}{76208}-\frac{268357y^6}{95260}+\frac{85037y^7}{190520}+\frac{918y^8}{23815},\end{aligned} \tag{4.42}$$

$$\begin{aligned}\hat{t}^{33}_{p^4_{r_*}}=1&+\frac{858779y}{190520}+\frac{92901791y^2}{6096640}+\frac{66769y^3}{7040}\\&-\frac{94475723y^4}{1219328}+\frac{9400891y^5}{152416}-\frac{82481269y^6}{3048320}\\&+\frac{17880961y^7}{1524160}-\frac{6096411y^8}{1524160}+\frac{2935y^9}{13856}+\frac{4009y^{10}}{76208}.\end{aligned} \tag{4.43}$$

Similarly to the quadrupole case, each residual y-polynomial is resummed using Padé approximants. The choices we made are summarized in Table 4.1. As we have discussed in Sec. 4.1.5, the compensations between instantaneous and tail terms are essential for provide a good analytical/numerical agreement. Therefore, we do not expect that the modes without tail correction will be reliable. In Fig. 4.4 we show the analytical/numerical comparisons for the (2,1), (3,3), (4,4), and (4,2) modes for a configuration with $e_0 = 0.5$. We start by noticing that the merger-ringdown waveform for the higher modes, in particular for the $(2,1)$ one, is far from being accurate. This is related to the next-to-quasicircular (NQC)/ringdown fit that we are using here (see Sec. 3.3) and that is not accurate. In Ref. [6] we presented a much more accurate NQC/ringdown model. However, here we focus on the inspiral, since we are interested in the performance of the 2PN corrections; a few comments follow. First, the phase and amplitude agreement during the inspiral phase for the $(2,1)$ and $(3,3)$ modes is comparable to the quadrupole, and the 2PN corrections

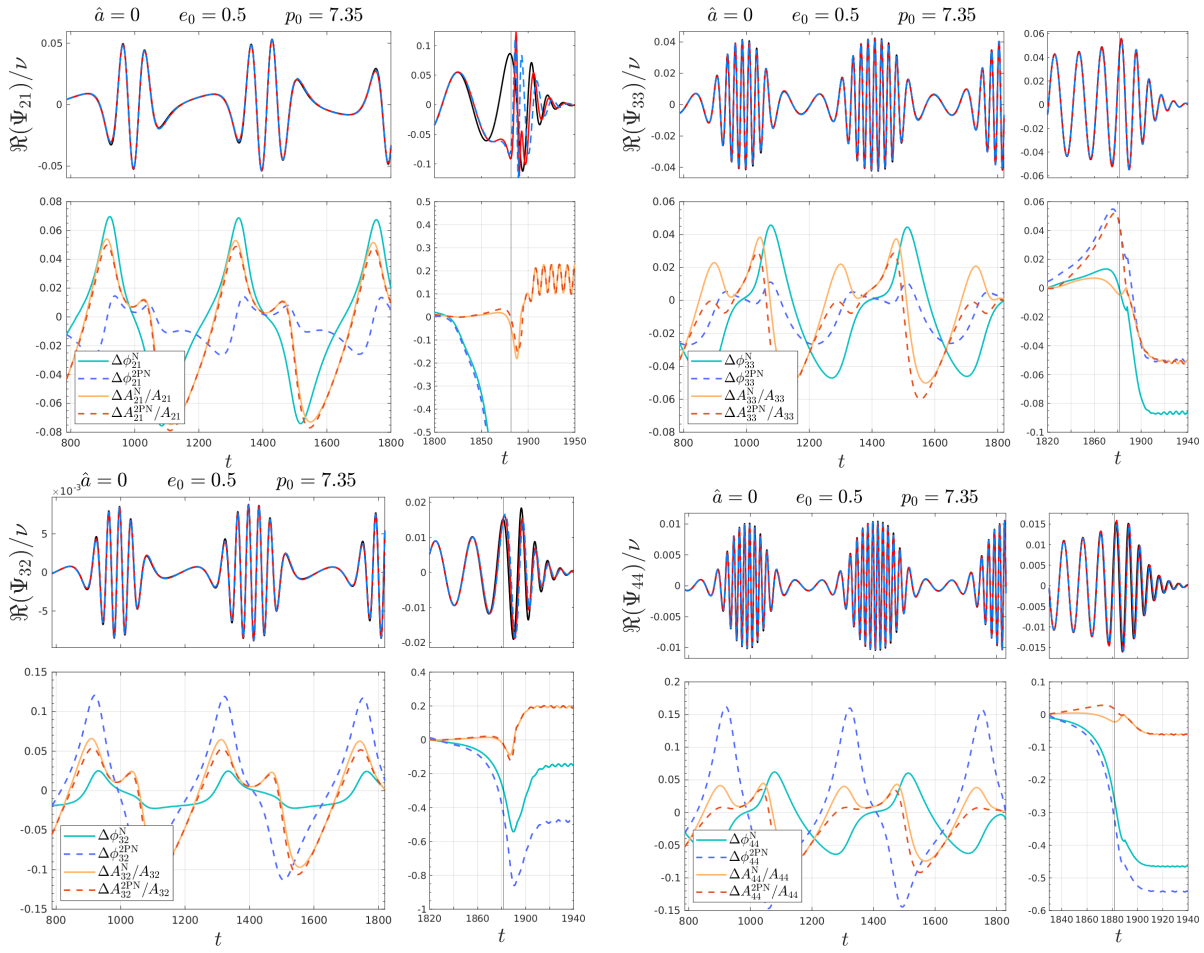

Figure 4.4: Same color scheme of Fig. 4.2, but here, in each row, we consider the subdominant modes (2,1), (3,3), (3,2), and (4,4) for a nonspinning configuration with $e_0 = 0.5$. The 2PN tail corrections in the (2,1) and (3,3) modes is resummed (it is zero for the (3,2) and (4,4) modes).

are found to yield a notable reduction of the analytical/numerical phase difference with respect to the simple Newtonian prefactor. This is true for any value of the eccentricity considered (see also other configurations in Fig. 8 of Ref. [3]). When moving to the $(3,2)$ and $(4,4)$ multipoles, one can see that the PN-corrected waveform performs *worse* than the leading-order one. As anticipated, we understand this result because these modes do not have a tail factor at 2PN order, in contrast to what happens for the $(2,2)$, $(3,3)$, and $(2,1)$ modes, where the aforementioned compensation between instantaneous and tail part can take place. An illustration of this effect for initial eccentricity $e_0 = 0.7$ can be found in Fig. 9 of Ref. [3]. Qualitatively, with 2.5PN accuracy, the same behavior should be found also for the $(3,2)$ and $(4,4)$ multipoles. These corrections have been computed in a more recent work [151], but their inclusion in our test mass EOB model has not been done yet.

We finally turn our attention to the $m = 0$ modes, analyzing, in particular, the (2,0) mode, that we analyze in the geodesic case, rather than along an inspiral-plunge dynamics. This is because we do not have a ringdown model for $m = 0$ modes. Indeed, the ringdown model discussed in Sec. 3.3 cannot be applied to $m = 0$ modes, since they are real rather than complex. We leave to future work the modelization of the ringdown for these modes. In Fig. 4.5, we test the factorization proposed in Eq. (4.29) for different geodesic configurations in Schwarzschild. The agreement between numerical and analytical results

Table 4.1: Padé used for the resummation of the tail 2PN noncircular corrections for the modes $(2,2)$, $(2,1)$, and $(3,3)$. Note that $\hat{t}^{33}_{p^3_{r_*}}$ has terms up to y^8, but we use the $(3,2)$ Padé.

	Padé			
(ℓ,m)	$\hat{t}^{\ell m}_{p_{r_*}}$	$\hat{t}^{\ell m}_{p^2_{r_*}}$	$\hat{t}^{\ell m}_{p^3_{r_*}}$	$\hat{t}^{\ell m}_{p^4_{r_*}}$
$(2,2)$	$(4,3)$	$(4,3)$	$(4,4)$	$(4,4)$
$(2,1)$	$(2,3)$	$(1,3)$	$(0,3)$	$(2,0)$
$(3,3)$	$(4,3)$	$(5,4)$	$(3,2)$	$(5,5)$

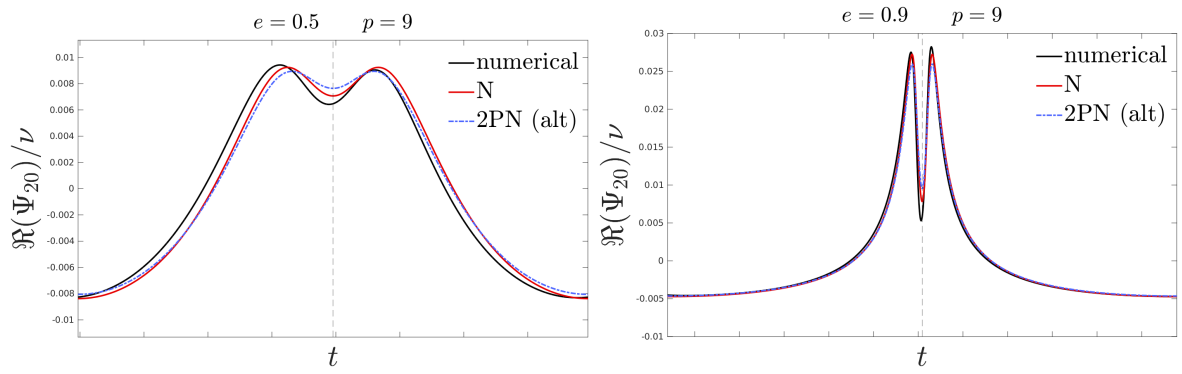

Figure 4.5: Comparisons for the mode $(2,0)$ on nonspinning geodesic orbits with $e = (0.5, 0.9)$ and $p = 9$. We show the numerical waveform (black), the EOB waveform with noncircular corrections only at Newtonian level (red online), and with corrections at 2PN as discussed in Sec. 4.1.3 (dashed blue).

is still qualitatively good, even if the other analytical modes discussed above are more accurate (both with only Newtonian and 2PN noncircular corrections). Here, a source of disagreement is that the asymmetry of the $m = 0$ numerical modes with respect to the apastron is not negligible, even in the geodesic case. In any case, the 2PN corrections do not seem to improve the analytical waveform for the $m = 0$ modes. The prescription with only the Newtonian prefactor is indeed more accurate. For this reason, we only consider Newtonian noncircular corrections for the $m = 0$ modes of our EOB waveform.

4.1.7 Comparison with other factorization schemes

During the development of Ref. [3], Ref. [150] appeared. Besides providing some of the analytical expressions used here (e.g., the explicit expression of the tail), Ref. [150] also proposed a different waveform factorization where (i) only the *quasicircular* Newtonian prefactor is factored out, (ii) all the noncircular effects are interpreted as corrections to the quasi-circular baseline expression, and (iii) the instantaneous and hereditary contributions are included in additive form. We now compare this prescription against ours. The discussion of this section is taken from Sec. VI of Ref. [3], with very minimal changes.

We start by carefully following Sec. IIIB of Ref. [150], and we report here all the equations needed for this aim. For $m > 0$, Ref. [150] proposes the factorized expression

$$h^{\rm 2PN_{qc}}_{\ell m} = h^{(N,\epsilon)_c}_{\ell m} \hat{S}_{\rm eff} \left(T_{\ell m} + T^{\rm ecc}_{\ell m}\right) e^{i\delta_{\ell m}} \left(f_{\ell m} + f^{\rm ecc}_{\ell m}\right), \tag{4.44}$$

where the eccentric terms $f^{\rm ecc}_{\ell m}$ and $T^{\rm ecc}_{\ell m}$ are written as functions of $(r,\ p_r,\ \dot{p}_r)$. For the leading-order quasicircular hereditary term $T_{\ell m}$, we use the standard prescription

introduced in Ref. [140], while for $\delta_{\ell m}$ and $f_{\ell m}$ we follow Refs. [1, 158, 159] (see also discussion in Sec. 2.3.2). Here we focus explicitly on the $(2,2)$ mode only, following the steps of Ref. [150]. More precisely, we use the full expression of $T_{22}^{\rm ecc}$ presented in its supplemental material, which reads [150]

$$
\begin{aligned}
T_{22}^{\rm ecc} =& \frac{\pi}{c^3}\Bigg[-\frac{3ip_r}{2r} - \dot{p}_r\sqrt{r} - \frac{p_r\left(2p_r + i\dot{p}_r r^{3/2}\right)}{4\sqrt{r}} + \frac{1}{48}\left(-5i\mathrm{p}\mathrm{r}^3\right. \\
& \left. -15\mathrm{p}\mathrm{r}^2\dot{p}_r r^{3/2} + 9i\mathrm{p}\mathrm{r}\dot{p}_r^2 r^3 - \dot{p}_r^3 r^{9/2}\right) + \frac{1}{32}\sqrt{r}\left(-10p_r^4 + 15ip_r^3\dot{p}_r r^{3/2}\right. \\
& \left. +8p_r^2\dot{p}_r^2 r^3 - ip_r\dot{p}_r^3 r^{9/2} + 2\dot{p}_r^4 r^6\right) + \frac{r}{1920}\left(589ip_r^5 + 1150p_r^4\dot{p}_r r^{3/2}\right. \\
& \left. -1060ip_r^3\dot{p}_r^2 r^3 - 505p_r^2\dot{p}_r^3 r^{9/2} + 55ip_r\dot{p}_r^4 r^6 - 116\dot{p}_r^5 r^{15/2}\right) \\
& + \frac{r^{3/2}}{11520}\left(1974p_r^6 - 4995ip_r^5\dot{p}_r r^{3/2} - 7470p_r^4\dot{p}_r^2 r^3 + 7240ip_r^3\dot{p}_r^3 r^{9/2}\right. \\
& \left. +3855p_r^2\dot{p}_r^4 r^6 - 669ip_r\dot{p}_r^5 r^{15/2} + 560\dot{p}_r^6 r^9\right)\Bigg]. \qquad (4.45)
\end{aligned}
$$

For the instantaneous contribution, $f_{22}^{\rm ecc}$, we use Eq. (122) of Ref. [150], which we rewrite here explicitly specified to the test mass limit ($\nu = 0$),

$$
\begin{aligned}
f_{22}^{\rm ecc} =& -\frac{p_r^2}{2v_0^2} + ip_r r v_0 + \frac{r^2 v_0^4}{2} + \frac{1}{2rv_0^2} - 1 + \frac{1}{c^2}\left(\frac{p_r^4}{4r^3 v_0^8} + \frac{29p_r^4}{84v_0^2} + \frac{ip_r^3}{4r^2 v_0^5}\right. \\
& -\frac{37}{84}ip_r^3 r v_0 - \frac{p_r^2}{12r^4 v_0^8} + \frac{1}{4}p_r^2 r^2 v_0^4 + \frac{31p_r^2}{14rv_0^2} - \frac{37}{84}ip_r r^3 v_0^7 + \frac{ip_r}{6r^3 v_0^5} \\
& \left. -\frac{209ip_r v_0}{84} - \frac{1}{6r^5 v_0^8} - \frac{2}{21}r^4 v_0^{10} - \frac{13}{12r^2 v_0^2} - \frac{59rv_0^4}{84} + \frac{43v_0^2}{21}\right) \\
& + \frac{1}{c^3}\left(-\frac{\hat{a}p_r^2}{3r^3 v_0^5} - \frac{4i\hat{a}p_r}{3r^2 v_0^2} + \frac{\hat{a}}{3r^4 v_0^5} - \frac{5\hat{a}v_0}{3r} + \frac{4\hat{a}v_0^3}{3}\right) \\
& + \frac{1}{c^4}\left(-\frac{\hat{a}^2 p_r^4}{6r^4 v_0^8} - \frac{i\hat{a}^2 p_r^3}{6r^3 v_0^5} + \frac{\hat{a}^2 p_r^2}{6r^5 v_0^8} - \frac{5\hat{a}^2 p_r^2}{6r^2 v_0^2} + \frac{i\hat{a}^2 p_r v_0}{r} + \frac{\hat{a}^2}{2r^3 v_0^2}\right. \\
& -\frac{\hat{a}^2 v_0^4}{2} - \frac{p_r^6}{4r^6 v_0^{14}} - \frac{31p_r^6}{112r^3 v_0^8} - \frac{277p_r^6}{1008v_0^2} - \frac{5ip_r^5}{32r^5 v_0^{11}} - \frac{3ip_r^5}{14r^2 v_0^5} + \frac{571ip_r^5 r v_0}{2016} \\
& -\frac{p_r^4}{12r^7 v_0^{14}} - \frac{179p_r^4}{144r^4 v_0^8} - \frac{85}{252}p_r^4 r^2 v_0^4 - \frac{1963p_r^4}{1008rv_0^2} - \frac{5ip_r^3}{24r^6 v_0^{11}} + \frac{349ip_r^3 r^3 v_0^7}{1008} \\
& -\frac{953ip_r^3}{1008r^3 v_0^5} + \frac{803}{504}ip_r^3 v_0 + \frac{2p_r^2}{9r^8 v_0^{14}} + \frac{79p_r^2}{168r^5 v_0^8} - \frac{71p_r^2 r^4 v_0^{10}}{1008} + \frac{43p_r^2}{42r^3 v_0^4} \\
& -\frac{31p_r^2}{168r^2 v_0^2} - \frac{31}{112}p_r^2 r v_0^4 - \frac{43p_r^2 v_0^2}{126} - \frac{5ip_r}{72r^7 v_0^{11}} + \frac{127ip_r r^5 v_0^{13}}{2016} \\
& -\frac{83ip_r}{504r^4 v_0^5} + \frac{5}{63}ip_r r^2 v_0^7 - \frac{9221ip_r v_0}{6048r} + \frac{1}{9r^9 v_0^{14}} - \frac{1}{126}r^6 v_0^{16} \\
& \left. +\frac{1}{6r^6 v_0^8} + \frac{43}{63r^4 v_0^4} + \frac{53r^3 v_0^{10}}{168} + \frac{13}{504r^3 v_0^2} - \frac{43r^2 v_0^8}{126} - \frac{43v_0^2}{126r} - \frac{11v_0^4}{18}\right), \qquad (4.46)
\end{aligned}
$$

where

$$v_0 = \frac{(1+\dot{p}_r r^2)^{1/6}}{\sqrt{r}}. \tag{4.47}$$

Note that in Eq. (4.46) we have also a correction at 1.5PN order, but this is proportional to the spin of the Kerr black hole, $\hat{a}$. Since in the previous sections we only considered non-spinning terms, we only have instantaneous corrections at 1PN and 2PN in Eq. (4.18). Moreover, note that $T_{22}^{\rm ecc}$ and $f_{22}^{\rm ecc}$ are written in terms of $(p_r,\, \dot{p}_r)$. However, following the practice introduced in Ref. [55], when considering the Hamiltonian formalism for a test particle around a Schwarzschild black hole, it is useful to replace p_r with p_{r_*} in order to avoid the presence of spurious numerical singularities toward the horizon. We thus rewrite the above equations replacing $(p_r,\, \dot{p}_r)$ with $(p_{r_*},\, \dot{p}_{r_*})$. Using Hamilton's equations, the radial momentum and its derivative are written as (see Appendix E of Ref. [150])

$$p_r = \sqrt{\frac{B}{A}} p_{r_*} \equiv \xi^{-1}(r) p_{r_*}, \tag{4.48}$$

$$\dot{p}_r = -\left[\left(\frac{\partial H}{\partial r} \right)_{p_{r_*}} + \left(\frac{\partial H}{\partial p_{r_*}} \right)_{r} \frac{p_{r_*}}{\xi(r)} \frac{d\xi(r)}{dr} \right]. \tag{4.49}$$

The explicit expressions for the Kerr metric functions A and B from Ref. [134] are reported in Eq. (1.97). In Figure 4.6 we consider two configurations with $e_0 = (0.1, 0.7)$ and show comparisons between (i) the numerical waveform from `Teukode` (black online, barely distinguishable in the top panels), (ii) the waveform with the generic Newtonian prefactor [145] (red online), and (iii) the 2PN-accurate waveform of Eq. (4.44) (dashed, green online). For each analytical waveform, the bottom panels of the figure report the corresponding phase differences and relative amplitude differences with the numerical counterpart. For simplicity, the $h_{\ell m}^{\rm 2PN_{qc}}$ is not completed through merger (via NQC corrections) and ringdown. As can be seen in the figure, the amplitude differences become relevant at large eccentricities during the inspiral at apastra. Moreover, even at small eccentricity, the waveform with only Newtonian noncircular corrections seems to perform globally better than the 2PN wave of Eq. (4.44).

Figure 4.6 also highlights an aspect that might be *a priori* unexpected: the largest amplitude differences occur at apastron and not at periastron. This might look puzzling, since PN expansions are more accurate in weak fields than in strong fields, while the plot seems to indicate the opposite. The reason for this behavior can be understood by inspecting Figs. 4.7. They refer to the same configuration ($e_0 = 0.7$) of the rightmost panel of Fig. 4.6. In the left panels of Fig. 4.7, we compare different analytical quadrupolar waveforms and their analytical/numerical relative amplitude differences. In particular (i) the quasicircular EOB waveform (gray online); (ii) the waveform with noncircular corrections included in the generic Newtonian prefactor (red online); (iii) the waveform of Eq. (4.8), where the 2PN noncircular effects are incorporated as a multiplicative correction to the Newtonian prefactor (blue online); and (iv) the waveform with quasicircular factorization and 2PN noncircular corrections as written in Eq. (4.44) (green online). In the right panels of the same figure, we illustrate the noncircular instantaneous corrections to the amplitude and to the phase for each analytical prescription. The instantaneous noncircular correction for the waveform of Eq. (4.44) is written as the multiplicative factor $1 + f_{22}^{\rm ecc}/f_{22}$, for formal consistency with the other analytical choices. All noncircular factors provide a relevant and coherent correction to the phase, as shown in the right middle panel of Fig. 4.7. The effect of these corrections is evident in the left top

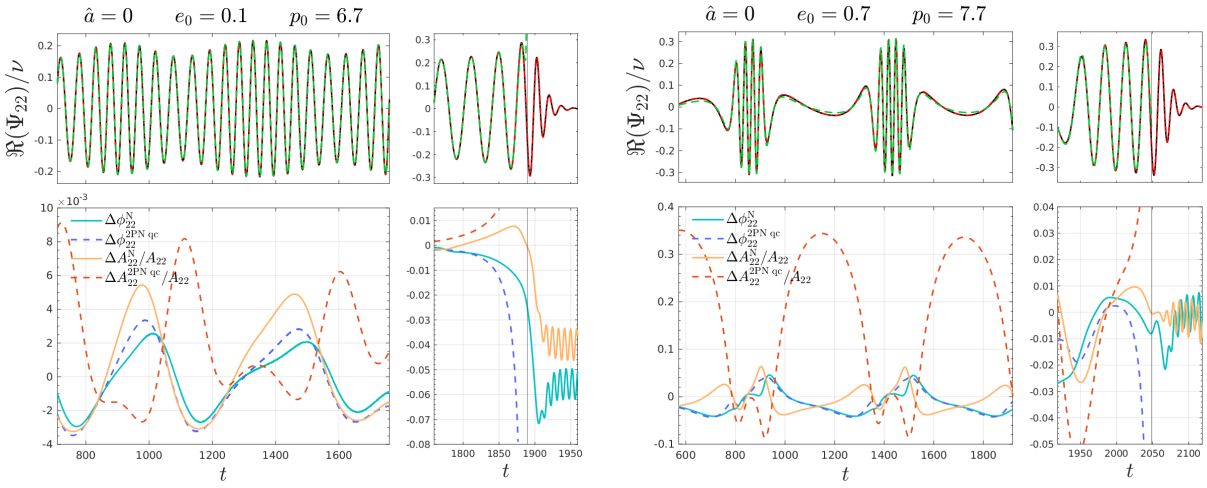

Figure 4.6: Testing the waveform factorization of Ref. [150], Eq. (4.44): comparisons between the $\ell = m = 2$ numerical and analytical waveforms emitted by the eccentric inspiral of a test particle on a Schwarzschild black hole. The initial eccentricities and semilatera recta are (e_0, p_0) =(0.1, 6.7), (0.7, 7.7). We show the numerical waveform (black), the EOB waveform with generic Newtonian prefactor (2.35) (dot-dashed red, labeled N), the 2PN-accurate waveform with the quasicircular factorization of Eq. (4.44) (labeled $\rm 2PN_{qc}$). The corresponding phase differences and relative amplitude differences are shown in the bottom panels. The vertical black line marks the merger time, corresponding to the peak of the numerical waveform amplitude.

panel, where the quasicircular waveform (gray online) is visibly dephased with respect to the other curves, This indicates that all noncircular phase corrections discussed in this work eventually yield an improved numerical/analytical phase agreement with respect to the quasicircular EOB waveform. By contrast, the noncircular correction provided by Eq. (4.44), at 2PN accuracy, does not provide a reliable amplitude at apastron, with differences that are rather close to those obtained using the standard circular waveform.

To understand this aspect, let us focus for a moment on the Newtonian noncircular prefactor of Eq. (2.35), whose time evolution is shown for the case considered in the right panels of Fig. 4.7 (red online). These panels show that the contribution of the Newtonian prefactor is larger at apastron than at periastron. This follows from the fact that in Eq. (2.35) the orbital frequency Ω appears squared and at the denominator of the noncircular correction, as a consequence of having factorized the circular Newtonian contribution. This eventually amplifies the contribution of the whole function in correspondence of the lowest values of Ω, i.e. at apastron. Note, however, that the only nonvanishing contribution of Eq. (2.35) at apastron is the one proportional to $\ddot{r}$, which is thus the main reason behind the behavior seen in the comparison shown in the left panels of Fig. 4.7. The hierarchy between $\ddot{r}$ and Ω^2 is clarified by the right bottom panel of Fig. 4.7. By contrast, when considering Eq. (4.44), without the crucial factorization of the Newtonian prefactor, the amplitude correction remains substantially constant, and small, for the whole radial evolution; see $1 + f_{22}^{\rm ecc}/f_{22}$ in Fig. 4.7 (green online, right panels). This leads to large analytical/numerical discrepancies for the amplitude, as shown in Figs. 4.6 and in the left panels of Fig. 4.7. In other words, this behavior is linked to the fact that Eq. (4.44) incorporates the PN expansion of Eq. (2.35) through the replacement of Ω and $\ddot{r}$ via the 2PN equation of motion, and so the crucial amplification related to the exact $\ddot{r}/\Omega^2$ contribution is lost.

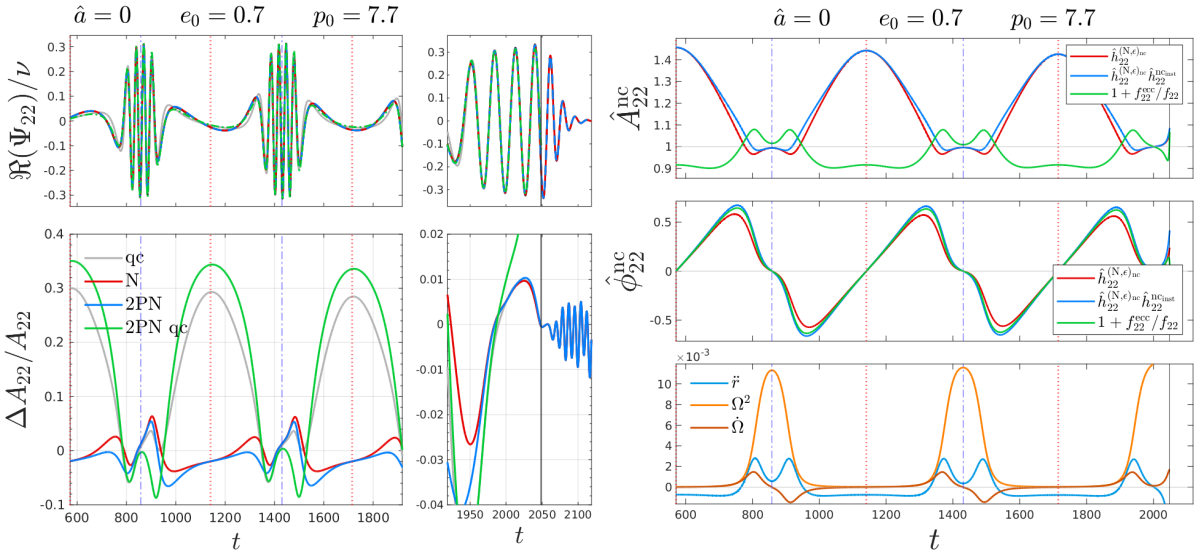

Figure 4.7: Left panels: numerical wave (black), quasicircular EOB wave (gray), wavewith Newtonian noncircular corrections (red), 2PN wave from Eq. (4.8) (blue), and 2PN wave of Eq. (4.44) (green, without merger/ringdown). Analytical/numerical relative amplitude differences in the bottom panel; vertical lines mark apastra (dotted red) and periastra (dash-dotted blue). Right panels: amplitude and phase contributions for different noncircular corrections: noncircular Newtonian prefactor $\hat{h}^{(\mathrm{N},\epsilon)_{\rm nc}}_{\ell m}$ of Eq. (2.35) (red); Newtonian-factorized instantaneous corrections up to 2PN, $\hat{h}^{(\mathrm{N},\epsilon)_{\rm nc}}_{\ell m}\hat{h}^{\rm nc_{inst}}_{\ell m}$, (blue); 2PN noncircular corrections of Eq. (4.44), written as $1+f^{\rm ecc}_{22}/f_{22}$ (green).

4.1.8 An alternative for $m \neq 0$ modes: $\dot{p}_{r_*}$

Inspired by the procedure followed for the $m=0$ modes, we also rewrote the 2PN noncircular corrections for the other modes ($m\neq 0$) by replacing p_φ with its expression in terms of $(u, p_{r_*}, \dot{p}_{r_*})$ using the 2PN-accurate EOM. We report here the expression for the quadrupole [3]:

$$
\begin{aligned}
\left[\hat{h}^{\rm nc_{tail}}_{22}\right]_{\dot{p}_{r_*}} &= 1-\frac{\pi}{c^3}\left(\frac{3}{2}ip_{r_*}u+\frac{ip_{r_*}\dot{p}_{r_*}}{4u}+\frac{p^2_{r_*}\sqrt{u}}{2}-\frac{3ip_{r_*}\dot{p}^2_{r_*}}{16u^3}+\frac{5p^2_{r_*}\dot{p}_{r_*}}{16u^{3/2}}\right.\\
&+\frac{5ip^3_{r_*}}{48}+\frac{ip_{r_*}\dot{p}^3_{r_*}}{32u^5}-\frac{p^2_{r_*}\dot{p}^2_{r_*}}{4u^{7/2}}-\frac{15ip^3_{r_*}\dot{p}_{r_*}}{32u^2}+\frac{5p^4_{r_*}}{16\sqrt{u}}-\frac{11ip_{r_*}\dot{p}^4_{r_*}}{384u^7}\\
&+\frac{101p^2_{r_*}\dot{p}^3_{r_*}}{384u^{11/2}}+\frac{53ip^3_{r_*}\dot{p}^2_{r_*}}{96u^4}-\frac{115p^4_{r_*}\dot{p}_{r_*}}{192u^{5/2}}-\frac{589ip^5_{r_*}}{1920u}-\frac{223ip_{r_*}\dot{p}^5_{r_*}}{3840u^9}\\
&+\frac{257p^2_{r_*}\dot{p}^4_{r_*}}{768u^{15/2}}+\frac{181ip^3_{r_*}\dot{p}^3_{r_*}}{288u^6}-\frac{83p^4_{r_*}\dot{p}^2_{r_*}}{128u^{9/2}}-\frac{111ip^5_{r_*}\dot{p}_{r_*}}{256u^3}\\
&\left.+\frac{329p^6_{r_*}}{1920u^{3/2}}\right),
\end{aligned}
\tag{4.50}
$$

$$
\begin{aligned}
[f^{\rm nc_{inst}}_{22}]_{\dot{p}_{r_*}} &= 1+\frac{1}{c^2}\left[\frac{(3\nu+62)p^2_{r_*}}{42}+\frac{(65-48\nu)p^2_{r_*}\dot{p}_{r_*}}{84u^2}+\frac{(114\nu-115)p^2_{r_*}\dot{p}^2_{r_*}}{168u^4}\right.\\
&+\frac{(10-9\nu)p^4_{r_*}}{21u}+\frac{(115-156\nu)p^2_{r_*}\dot{p}^3_{r_*}}{336u^6}+\frac{(144\nu-125)p^4_{r_*}\dot{p}_{r_*}}{168u^3}\\
&\left.+\frac{(174\nu-65)p^2_{r_*}\dot{p}^4_{r_*}}{672u^8}+\frac{(55-144\nu)p^4_{r_*}\dot{p}^2_{r_*}}{336u^5}+\frac{(6\nu-5)p^6_{r_*}}{24u^2}\right]\\
&+\frac{1}{c^4}\left[\frac{(1685-1506\nu-336\nu^2)p^2_{r_*}u}{504}\right.
\end{aligned}
$$

$$
\begin{aligned}
&- \frac{(76039 - 79256\nu + 29480\nu^2) p_{r_*}^2 \dot{p}_{r_*}}{42336u} \\
&- \frac{(40120 - 41507\nu + 6257\nu^2) p_{r_*}^2 \dot{p}_{r_*}^2}{10584u^3} \\
&+ \frac{(2609 + 4538\nu + 382\nu^2) p_{r_*}^4}{3024} \\
&+ \frac{(227327 - 281328\nu + 48696\nu^2) p_{r_*}^2 \dot{p}_{r_*}^3}{56448u^5} \\
&- \frac{(198001 - 378512\nu + 96248\nu^2) p_{r_*}^4 \dot{p}_{r_*}}{84672u^2} \\
&- \frac{11(9290 - 14020\nu + 3019\nu^2) p_{r_*}^2 \dot{p}_{r_*}^4}{42336u^7} \\
&+ \frac{(749981 - 1363564\nu + 247480\nu^2) p_{r_*}^4 \dot{p}_{r_*}^2}{169344u^4} \\
&- \frac{(4687 - 20688\nu + 5916\nu^2) p_{r_*}^6}{14112u} \Bigg], \qquad (4.51)
\end{aligned}
$$

$$
\begin{aligned}
[\delta_{22}^{\mathrm{nc_{inst}}}]_{\dot{p}_{r_*}} &= \frac{1}{c^2} \Bigg[\frac{(25 - 26\nu) p_{r_*} \sqrt{u}}{14} + \frac{(25 - 12\nu) p_{r_*} \dot{p}_{r_*}}{42u^{3/2}} - \frac{(25 - 18\nu) p_{r_*} \dot{p}_{r_*}^2}{48u^{7/2}} \\
&+ \frac{(6\nu + 5) p_{r_*}^3}{84\sqrt{u}} + \frac{5(10 - 9\nu) p_{r_*} \dot{p}_{r_*}^3}{168u^{11/2}} - \frac{5(31 - 30\nu) p_{r_*}^3 \dot{p}_{r_*}}{168u^{5/2}} \\
&- \frac{(775 - 918\nu) p_{r_*} \dot{p}_{r_*}^4}{5376u^{15/2}} + \frac{3(45 - 58\nu) p_{r_*}^3 \dot{p}_{r_*}^2}{224u^{9/2}} - \frac{(25 - 26\nu) p_{r_*}^5}{56u^{3/2}} \\
&+ \frac{(325 - 576\nu) p_{r_*} \dot{p}_{r_*}^5}{5376u^{19/2}} - \frac{(145 - 498\nu) p_{r_*}^3 \dot{p}_{r_*}^3}{1344u^{13/2}} + \frac{3(5 - 8\nu) p_{r_*}^5 \dot{p}_{r_*}}{56u^{7/2}} \Bigg] \\
&+ \frac{1}{c^4} \Bigg[\frac{(31259 - 10972\nu - 11360\nu^2) p_{r_*} u^{3/2}}{10584} \\
&- \frac{(30467 - 58216\nu - 26216\nu^2) p_{r_*} \dot{p}_{r_*}}{21168\sqrt{u}} \\
&- \frac{(197641 - 182480\nu + 20600\nu^2) p_{r_*} \dot{p}_{r_*}^2}{84672u^{5/2}} \\
&- \frac{(25213 - 81572\nu - 27568\nu^2) p_{r_*}^3 \sqrt{u}}{21168} \\
&+ \frac{(430967 - 462772\nu + 66832\nu^2) p_{r_*} \dot{p}_{r_*}^3}{169344u^{9/2}} \\
&- \frac{(15711 - 16846\nu + 11500\nu^2) p_{r_*}^3 \dot{p}_{r_*}}{14112u^{3/2}} \\
&- \frac{(2456467 - 2958740\nu + 594704\nu^2) p_{r_*} \dot{p}_{r_*}^4}{1354752u^{13/2}} \\
&+ \frac{(866783 - 1234624\nu + 221608\nu^2) p_{r_*}^3 \dot{p}_{r_*}^2}{169344u^{7/2}} \\
&- \frac{(38639 - 34420\nu + 21376\nu^2) p_{r_*}^5}{42336\sqrt{u}} \\
&+ \frac{(2807687 - 4018384\nu + 1077064\nu^2) p_{r_*} \dot{p}_{r_*}^5}{2709504u^{17/2}}
\end{aligned}
$$

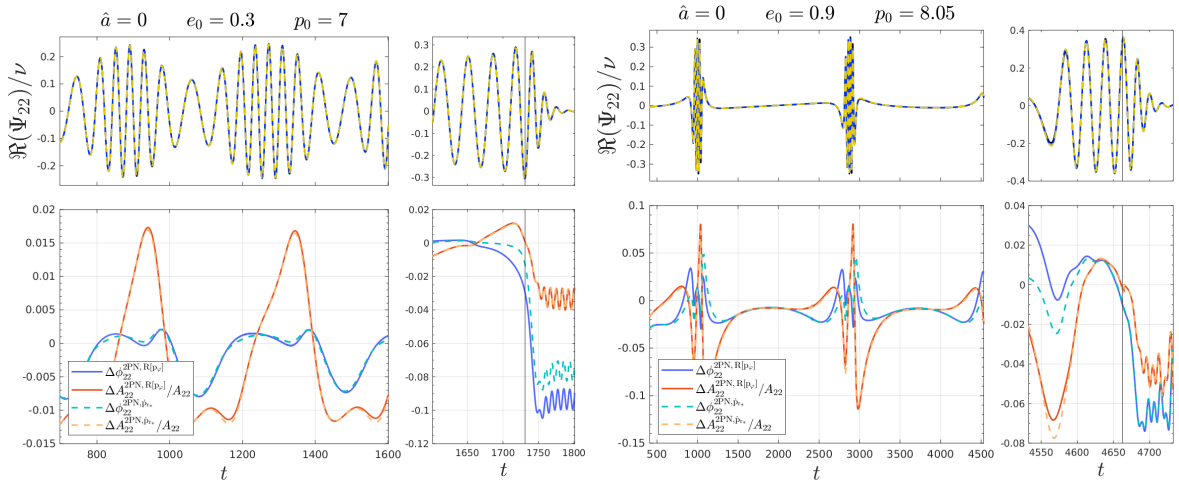

Figure 4.8: Analytical/numerical comparisons of the $\ell = m = 2$ mode for initial eccentricity $e_0 = (0.3, 0.9)$ and $\hat{a} = 0$. In the top panels, we show the real part of the numerical waveform (black, almost indistinguishable), the analytical waveform with resummed 2PN noncircular corrections written in terms of (p_{r_*}, p_φ) (solid blue), and the analytical one with corrections written in terms of $(p_{r_*}, \dot{p}_{r_*})$ (dashed yellow). The corresponding analytical/numerical phase differences and amplitude relative differences are shown in the bottom panels (solid lines for resummed corrections with p_φ, dashed lines for the corrections with $\dot{p}_{r_*}$).

$$- \frac{(149307 - 248258\nu + 44612\nu^2)p_{r_*}^3 \dot{p}_{r_*}^3}{37632u^{11/2}} + \frac{(324131 - 573220\nu + 81808\nu^2)p_{r_*}^5 \dot{p}_{r_*}}{84672u^{5/2}}\Bigg]. \tag{4.52}$$

Note that in these expressions there are half-integer powers of u, but since these corrections do not need any resummation (i.e. they are already reliable in non-resummed form), this is not a problem.

In Fig. 4.8, we look at the test particle case and compare the above corrections with those of Sec. 4.1.3, specifically those with the resummation both in the hereditary and instantaneous factors (see Fig. 19 of Ref. [3] for more eccentric configurations). As usual, in the bottom panels we report the phase difference and the relative amplitude difference; we use solid lines for resummed corrections with p_φ, and dashed lines for the corrections in terms of $\dot{p}_{r_*}$. Without the need of a resummation scheme, the accuracy of the $(u, p_{r_*}, \dot{p}_{r_*})$-corrections turns out to be practically equivalent to the one for the corrections written in terms of (u, p_{r_*}, p_φ), especially for low or moderate eccentricity. Nevertheless, the evaluation of $\dot{p}_{r_*}$ through Hamilton's equation in the comparable mass case is less efficient than using directly p_φ, and for this reason, in Ref. [3] we preferred to use the resummed corrections containing p_φ. However, in subsequent articles ([4, 5]), we employed the $(u, p_{r_*}, \dot{p}_{r_*})$-corrections due to their more simple analytical expressions.

4.1.9 Relevance in the comparable mass case

We conclude the discussion on the result of Ref. [3] with some remarks on the comparable mass case, where we test the accuracy of the (2,2) mode. We incorporated the 2PN-improved eccentric waveform in the EOB eccentric model presented in Ref. [148]. Note that in Ref. [148] (but also in more recent works), the calibration of the (a_6^c, c_3) parameters (see discussion in Sec. 2.3.1) is performed only on NR *quasicircular* simulations. Since

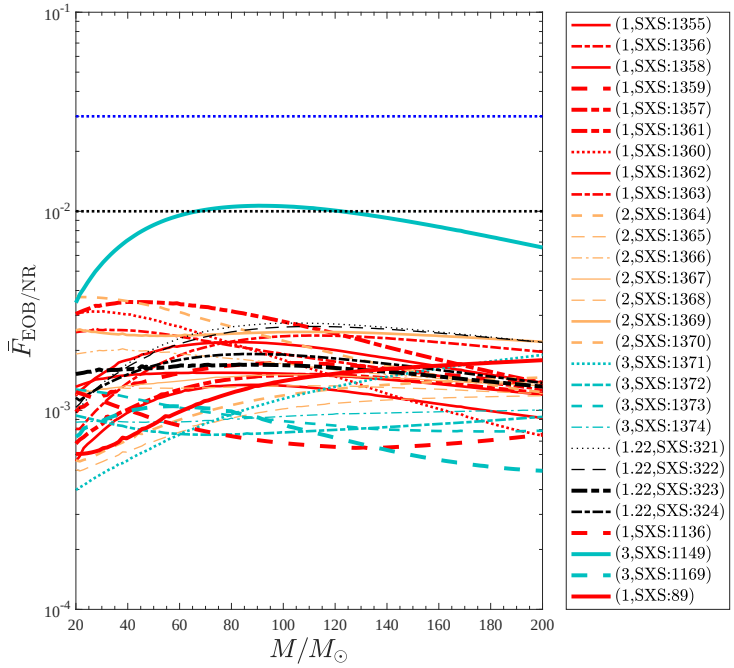

Figure 4.9: EOB/NR unfaithfulness for the $\ell = m = 2$ mode computed over the eccentric SXS simulations publicly available, Table IV of Ref. [3]. The horizontal lines mark the 0.03 and 0.01 values. The value of $\bar{F}^{\rm max}_{\rm EOB/NR}$ does not exceed the 0.7% except for the single outlier given by SXS:BBH:1149, corresponding to $(q, \chi_1, \chi_2) = (3, +0.70, +0.60)$ with $e^{\rm NR}_{\omega_a} = 0.037$, which is around 1%. This is consistent with the slight degradation of the model performance for large positive spins already found in the quasicircular limit, as pointed out in Ref. [148].

the 2PN noncircular corrections to the waveform have an essentially negligible impact on quasicircular configurations, we did not provide a new determination of (a^c_6, c_3). The EOB/NR comparisons are performed considering the public eccentric configurations of the SXS catalog [82], whose maximum initial eccentricity is $e^{\rm NR}_0 \sim 0.3$. The complete list of configurations considered can be found in Table IV of Ref. [3]. We explored the performance of the new waveform using both time-domain (phase-alignment) and frequency-domain comparison. The latter are obtained by computing the unfaithfulness, defined as

$$\bar{F}(M) \equiv 1 - F = 1 - \max_{t_0,\phi_0} \frac{\langle h_1, h_2\rangle}{||h_1||||h_2||}, \tag{4.53}$$

where (t_0, ϕ_0) are the initial time and phase. We used $||h|| \equiv \sqrt{\langle h, h\rangle}$, and the inner product between two waveforms is defined as

$$\langle h_1, h_2\rangle \equiv 4\Re \int_{f_{\rm min}}^{\infty} \frac{\tilde{h}_1(f)\tilde{h}^*_2(f)}{S_n(f)}\, df \tag{4.54}$$

where $\tilde{h}(f)$ denotes the Fourier transform of $h(t)$; $S_n(f)$ is the zero-detuned, high-power noise spectral density of Advanced LIGO [226], and $f_{\rm min}$ is the initial frequency approximately corresponding to the frequency of the first apastron on each NR simulation, after the initial junk radiation has cleared. In practice, the integral is done up to a maximal frequency $f_{\rm end}$ that corresponds to $|\tilde{h}(f_{\rm end})| \sim 10^{-2}$.

Nonetheless, certain factors complicate the EOB/NR comparisons, making them more difficult to interpret. To start with, in order to optimize the phase-alignment we determine the initial eccentricity and the initial frequency manually, by visually inspecting the

agreement between numerical and analytical waveforms (we recall that the eccentricity is not gauge-invariant, so we cannot just impose $e_0^{\rm NR} = e_0^{\rm EOB}$). Therefore, even if we see a small improvement in the time-domain comparisons of the quadrupole waveform with respect to Ref. [148], this may be a consequence of the better procedure used to identify the initial values. Secondly, when computing the unfaithfulness we have to consider the Fourier transforms of the NR/EOB waveforms, but this computation is quite delicate. For example, one has to consider a hyper-parameters-depending tapering for the time-domain waveforms (both NR and EOB) in order to reduce high-frequency oscillations in the corresponding Fourier transforms. The unfaithfulness obtained for the configuration considered is shown in Fig. 4.9. Even if the obtained results are slightly better than the ones presented in Ref. [148] where only Newtonian noncircular corrections were considered (see Fig. 14 therein), it is not clear if the improvement is a consequence of the new 2PN noncircular corrections or if it is a consequence of the improved EOB/NR initial data matching procedure.

To conclude, since Fig. 14 of Ref. [148] and our current Fig. 4.9 are quite similar, we are prone to conservatively state that the factorized and resummed 2PN noncircular corrections to the waveform are not especially important for the mildly eccentric configurations of the SXS catalog.

4.1.10 Summary

In this section we substantially revisited the results of Ref. [3] for the eccentric configurations. In Sec. 4.1.1 and Sec. 4.1.2 we have discussed the instantaneous and hereditary 2PN noncircular corrections, respectively. In Sec. 4.1.3 we have proposed a new factorization of the 2PN noncircular waveform corrections written in terms of (u, p_{r_*}, p_φ), that crucially factorizes the circular Newtonian prefactor *and* the noncircular one from Eq. (2.35). For the $m > 0$ modes, these corrections needed a proper resummation (especially for the hereditary contribution), as discussed in Sec. 4.1.4. For the $m = 0$ we considered an alternative factorization, since the circular Newtonian factor vanishes in this case.

We have then included these resummed corrections in the EOB waveform as shown in Eq. (4.8), and demonstrated that they yield a better analytical waveform phase in the test particle limit, but are substantially irrelevant for the amplitude. In Sec. 4.1.5 we have shown that the instantaneous and hereditary corrections crucially compensate (despite entering at different PN orders), so one has to consider both in order to have an accurate waveform. In Sec. 4.1.6 we have then discussed the higher modes.

In Sec. 4.1.7, we have also tested the factorization proposed in Ref. [150], showing that it is as accurate as ours for the phase, but it is unreliable for the amplitude, especially at apastron. This is linked to the fact that the waveform of Ref. [150] does not factorize the noncircular Newtonian prefactor, but instead uses the PN-expanded EOM to write the time-derivatives that appear in the noncircular correction.

We have also proposed an alternative way of writing the (Newtonian-factorized) 2PN corrections in Sec. 4.1.8, where we used the phase-space variables $(u, p_{r_*}, \dot{p}_{r_*})$ instead of (u, p_{r_*}, p_φ). We have also shown that this correction is practically equivalent to the one discussed in Sec. 4.1.3 (the latter resummed as detailed in Sec. 4.1.4).

We concluded the discussion of Ref. [3] by commenting on the comparable mass case scenario in Sec. 4.1.9, where we argued that these 2PN noncircular corrections do not seem to be crucial for the EOB accuracy in the case of mildly eccentric black hole binaries.

4.2 Assessment of the radiation reaction

In this section we discuss the results of Ref. [4], where we tested the effects of different radiation reactions of eccentric and hyperbolic orbits. The following discussion is taken, mutatis mutandis, from the aforementioned paper. Loosely speaking, this paper can be seen as an extension of Ref. [1] where we also considered 2PN corrections in $\mathcal{F}_\varphi$. We also considered the quasi-circular $\mathcal{F}_\varphi$, since it is the prescription used in `SEOBNRv4EHM` [149] (see Eq. (3) therein).

4.2.1 Testing radiation reactions employed in EOB models

We start by recalling the prescriptions for the radiation reaction forces $(\mathcal{F}_\varphi, \mathcal{F}_r)$ that are used in the `TEOBResumS` model (NCN) [3, 147, 148], in the `SEOBNRv4EHM` [149] model (QC), and proposed, but not implemented yet, in Ref. [150] (QC2PN). While we start by focusing on these three prescriptions, in Sec. 4.2.3 we will also discuss the 2PN extension of the `TEOBResumS` radiation reaction.

- **Noncircular Newtonian prefactor (`TEOBResumS`): NCN**. The first radiation reaction that we consider is the one of the `TEOBResumS` family. We recall that the quadrupolar noncircular Newtonian correction enters in the angular component $\mathcal{F}_\varphi$ as shown in Eq. (3.7), where $\hat{f}^{\rm N_{nc}}_{\varphi,22}$ is written explicitly in Eq. (2.44). The radial component here considered is the one reported in Eq. (2.46).

- **Quasicircular with $\mathcal{F}_r \neq 0$ (`SEOBNRv4EHM`): QC** The second prescription that we consider is denoted as QC and mimics what it is implemented in `SEOBNRv4EHM` [149]. While in `TEOBResumS` the radial component of the radiation reaction is set to zero for the quasicircular inspiral, it is not the case for `SEOBNRv4HM`, which has

$$\hat{\mathcal{F}}^{\rm QC}_\varphi = -\frac{32}{5}\nu r^4_\Omega \Omega^5 \hat{f}, \tag{4.55a}$$

$$\hat{\mathcal{F}}^{\rm QC}_r = \hat{\mathcal{F}}^{\rm QC}_\varphi \frac{p_r}{p_\varphi}. \tag{4.55b}$$

  This quasicircular radiation is also used in `SEOBNRv4EHM` [149], the eccentric extension of `SEOBNRv4HM`. We note, however, two aspects. The first one is that Refs. [149, 150] (and not even Refs. [58, 227], which define the `SEOBNRv4HM` model) do not write explicitly the leading-order (Newtonian) contribution to $\mathcal{F}_\varphi$. In particular it is not stated explicitly whether Kepler's constraint is relaxed as originally proposed in Refs. [55] to have a more faithful representation of the angular momentum losses during the plunge. This may induce the reader to think that the dominant term of the angular component is $\mathcal{F}^{\rm qc,LO}_\varphi = -32/5\nu\Omega^{7/3}$. Nonetheless, inspecting the public code it is possible to see that also in the `SEOBNRv4HM` models the Keplerian constraint is relaxed so that $\mathcal{F}^{\rm qc,LO}_\varphi = -32/5\nu r^4_\Omega \Omega^5$, as in `TEOBResumS`. The second aspect to consider is that through Ref. [4] (and also through this thesis) we consider $\hat{f}$ as implemented in the test mass version of `TEOBResumS`. While the term is formally the same of `SEOBNRv4HM`, there are some differences in PN orders adopted and in the related resummations that enter $\hat{f}$ and follow Refs. [1, 158, 159]. However, the reliability of the term $\hat{f}$ that we will use in this work is shown in Appendix A of Ref. [4]. With the aforementioned caveats, the radiation reaction of Eqs. (4.55) is a proxy of the one used in the actual `SEOBNRv4EHM` model.

- **Quasicircular with 2PN noncircular corrections: QC2PN** We finally turn to the QC2PN radiation reaction, which contains 2PN noncircular correction in factorized form as introduced by Khalil *et al.* [150]. The radiation reaction forces are factorized in quasicircular and eccentric parts:

$$\mathcal{F}_\varphi^{\rm QC2PN} = \hat{\mathcal{F}}_\varphi^{\rm QC}\hat{\mathcal{F}}_\varphi^{\rm ecc}, \tag{4.56a}$$
$$\mathcal{F}_r^{\rm QC2PN} = \hat{\mathcal{F}}_r^{\rm QC}\hat{\mathcal{F}}_r^{\rm ecc}, \tag{4.56b}$$

  where $\hat{\mathcal{F}}_\varphi^{\rm QC}$ and $\hat{\mathcal{F}}_\varphi^{\rm QC}$ are the quasicircular terms of Eq. (4.55), while $\hat{\mathcal{F}}_\varphi^{\rm ecc}$ and $\hat{\mathcal{F}}_r^{\rm ecc}$ are the noncircular corrections up to 2PN and reduce to unity in the circular case. Their explicit expressions in the test mass limit, written in terms of $(r, p_r, \dot{p}_r)$, are reported in Appendix B of Ref. [4].

Testing the reliability of the EOB radiation reaction

We now test the reliability of the RR described above. We use the method of Ref. [1], which we also recalled in Chapter 3. In short, we will consider geodesic configurations and we will compare the analytical fluxes, obtained from the balance equations (2.37) [160] and different analytical prescriptions for $\mathcal{F}_\varphi$ and $\mathcal{F}_r$ (the prescription of $\dot{E}_{\rm Schott}$ is given by Eq. (2.49)), with the numerical fluxes, obtained using Eqs. (1.42) and the numerical waveform from `Teukode`.

We use the same geodesic numerical simulations presented in Ref. [1] and in Sec. 3.1; therefore, we consider spins in the range $\hat{a} \in [-0.9, 0.9]$ and eccentricities up to $e = 0.9$. For each pair $(e, \hat{a})$, we compute the semilatus rectum p according to the separatrix $p_s(e, \hat{a})$. More precisely, we consider *intermediate* and *distant* configurations that have semilatus rectum $p = p_{\rm schw} p_s(e, \hat{a})/p_s(e, 0)$, where $p_{\rm schw}$ is 9 and 13, respectively. In Sec. 3.1 we considered also *near* simulations that had $p(e, \hat{a}) = p_s(e, \hat{a}) + 0.01$; however, we will not consider them in this work since they show a strong zoom-whirl behavior and thus are less significant for testing the noncircular terms.

Instantaneous fluxes for eccentric orbits

We start our tests by computing the analytical fluxes along bound geodesics with eccentricities up to $e = 0.9$. We report the trajectories and the instantaneous fluxes for some significant nonspinning cases in Fig. 4.10, while in Fig. 4.11 we show some spinning configurations. For each configuration we show the numerical fluxes (black), the NCN fluxes (red) computed using the radiation reaction of Eqs. (3.7) and (2.46), the QC fluxes (blue) computed using Eqs. (4.55), and the QC2PN fluxes (green). Figure 4.10 illustrates that the QC fluxes are the less accurate ones, even for $e = 0.1$. The discrepancies with the numerical results are more relevant for higher eccentricities. In particular, the QC fluxes overestimate the numerical flux at periastron in almost all the cases. However, for some cases with high eccentricity and high spin, the QC expressions incidentally provide the best approximation to the numerical fluxes at periastron, as shown in the case with $(e, \hat{a}, p) = (0.7, 0.6, 8.517)$ of Fig. 4.11. To better understand this aspect, one should note that for high spins (and high eccentricity) the periastron of the orbit is located in stronger field, and thus the numerical fluxes have general-relativistic contributions that are not included in the EOB analytical fluxes. Indeed, the last panel of Fig. 4.11 highlights that the numerical fluxes are not symmetric with respect to the periastron and that there are quasinormal-modes excitations of the Kerr black hole [216–218]. These excitations

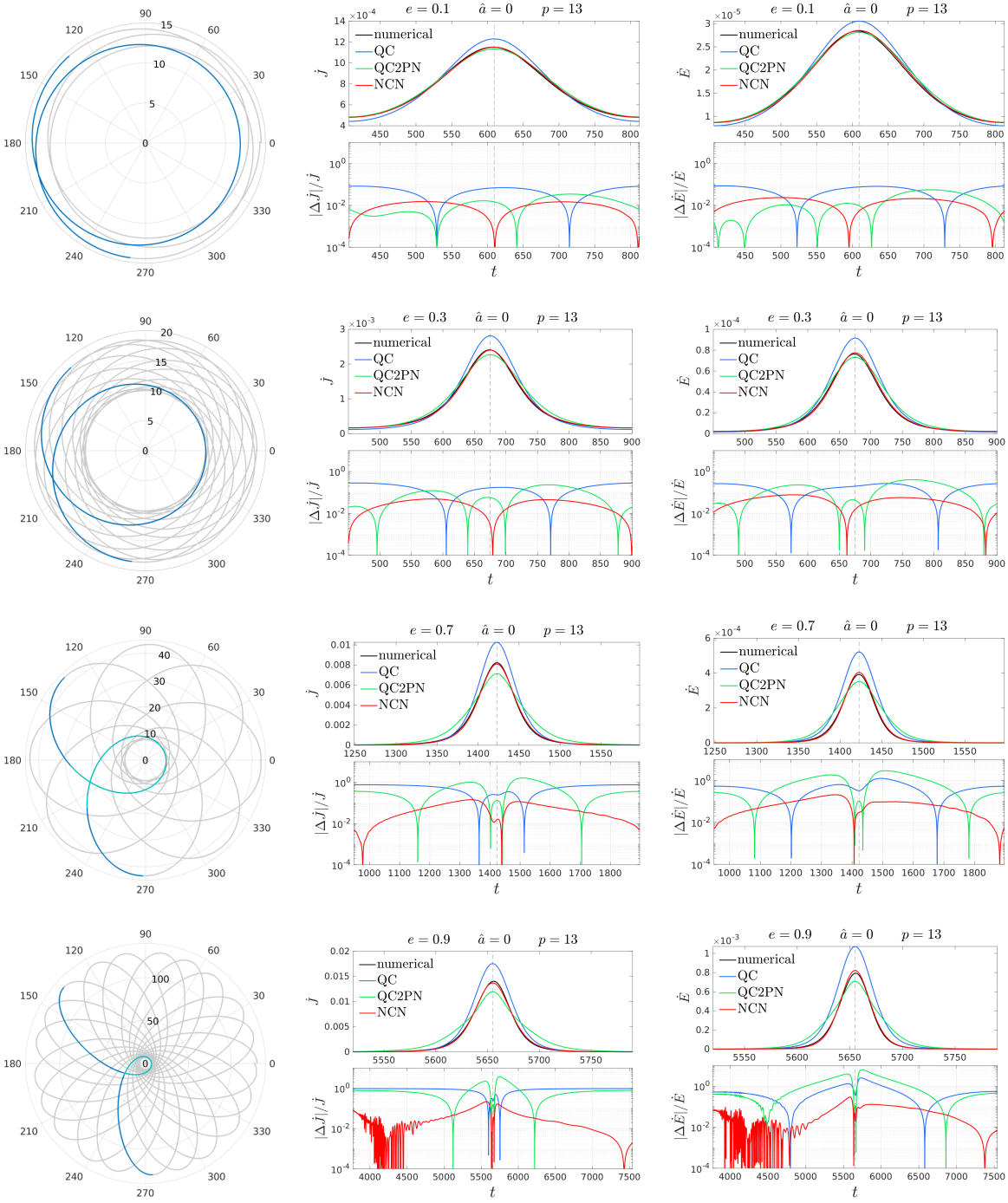

Figure 4.10: Geodesic configurations with $\hat{a} = 0$, $p = 13$ and $e = (0.1, 0.3, 0.7, 0.9)$. For each one we show the trajectories highlighting one radial period (blue) and the corresponding fluxes. We contrast the numerical fluxes (black) with the three analytical fluxes considered in this work: the NCN flux (red) computed using Eqs. (3.7) and (2.46); the QC flux (blue) from Eq. (4.55), which is a proxy of the `SEOBNRv4EHM` fluxes, and the QC2PN flux with 2PN noncircular corrections (green) from Eqs. (4.56). Each subpanel also reports the analytical/numerical relative difference. Note that while the relative differences in the lower panels are always shown over the complete radial period, the fluxes for $e \geq 0.7$ are shown on smaller time intervals (highlighted in aqua-green on the trajectories) in order to better highlight the burst of radiation at periastron passage (marked by a dashed vertical line).

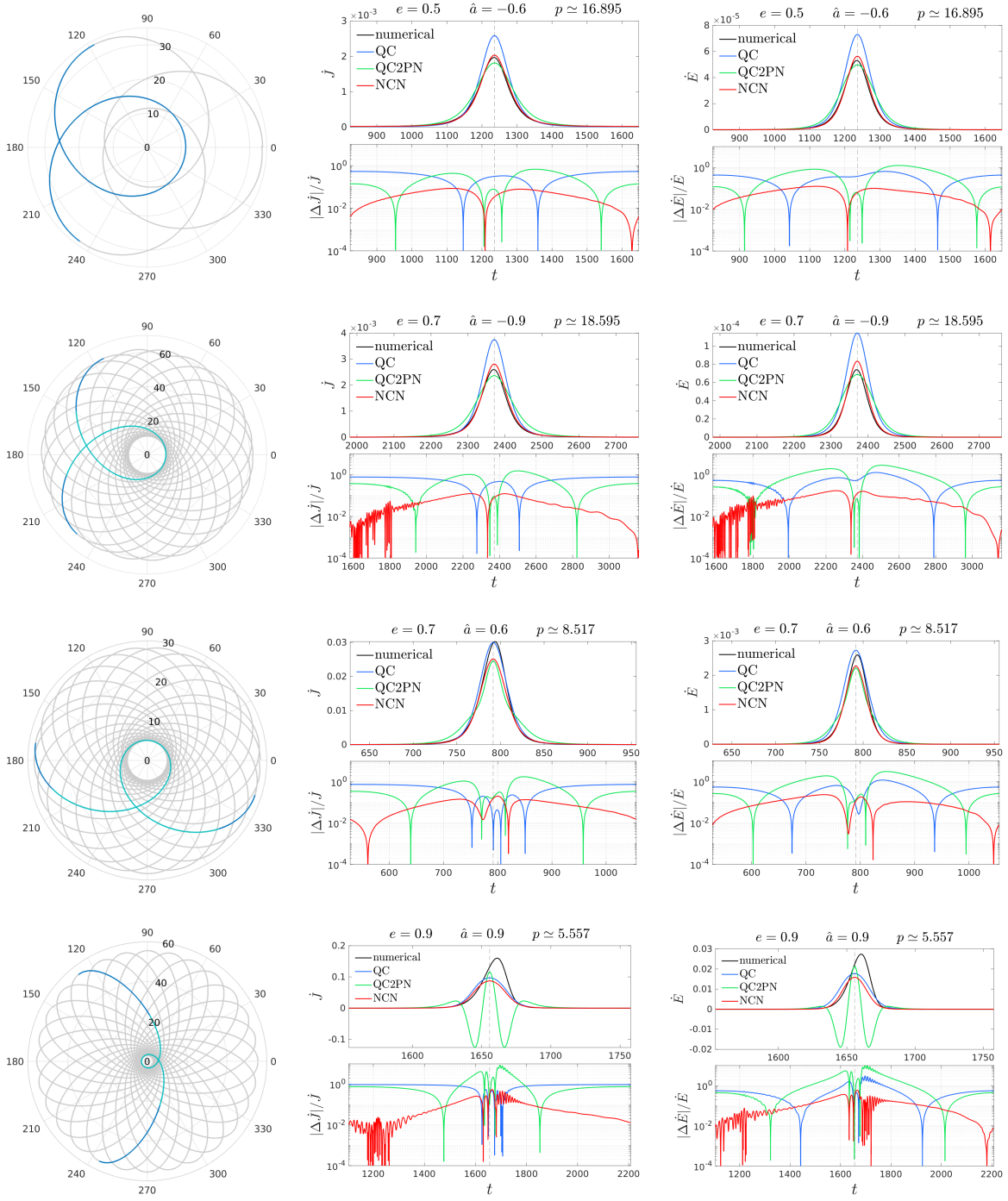

Figure 4.11: Analogous to Fig. 4.10, but for spinning configurations with different eccentricities. The semilatera recta are computed according to $p = 13p_s(e, \hat{a})/p_s(e, 0)$. For each configuration, we show the trajectories highlighting one radial period (blue) and the corresponding fluxes. We contrast the numerical fluxes (black) with the three analytical fluxes considered in this work: the NCN flux (red) computed using Eqs. (3.7) and (2.46); the QC flux (blue) from Eq. (4.55), which is a proxy of the `SEOBNRv4EHM` fluxes, and the QC2PN flux with 2PN noncircular corrections (green) from Eqs. (4.56). Each subpanel also reports the analytical/numerical relative difference. Note that while the relative differences in the lower panels are always shown over the complete radial period, the fluxes for $e \geq 0.7$ are shown on smaller time intervals (highlighted in aqua-green on the trajectories) in order to show better the burst of radiation at the periastron passage (marked by a dashed vertical line).

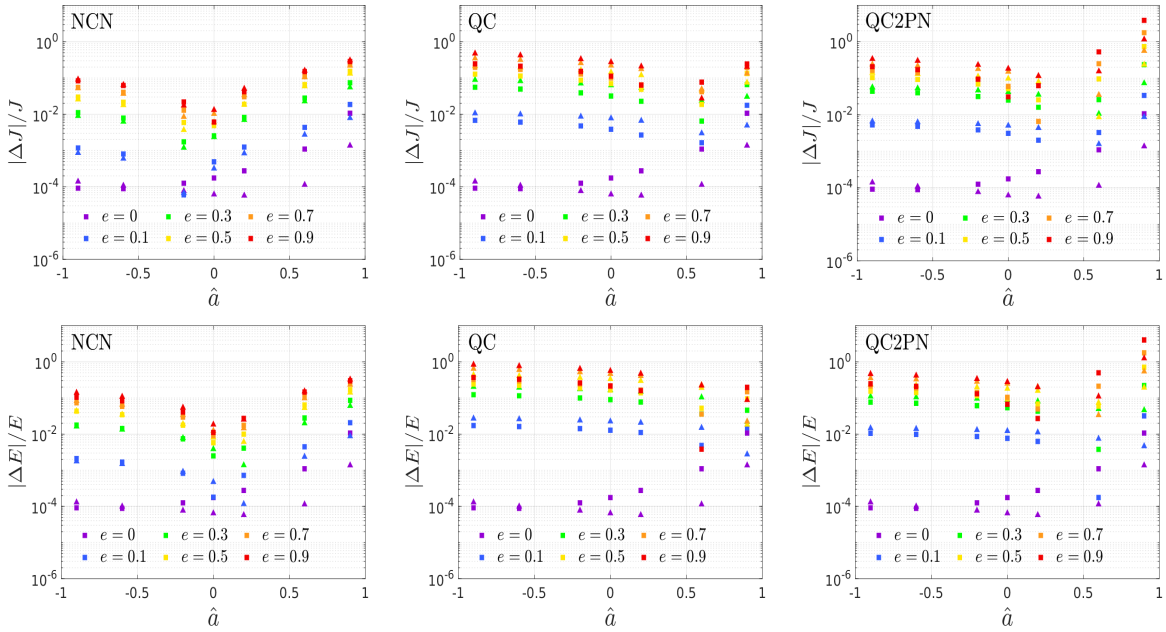

Figure 4.12: Analytical/numerical relative differences for the orbital averaged fluxes (angular momentum and energy) that correspond to eccentric configurations. For each configuration the semilatus rectum is computed according to $p = p_{\rm schw} p_s(e, \hat{a})/p_s(e, 0)$ where $p_{\rm schw} = 9$ (squares) or $p_{\rm schw} = 13$ (triangles).

are responsible for the oscillations in the relative differences after the periastron passage that can be clearly seen in the case with $(e, \hat{a}) = (0.9, 0.9)$ shown in Fig. 4.11. As a consequence, the analytical flux underestimates the numerical results in strong field, as already observed in Ref. [1] and Secs. 3.2.3 and 3.2.4. Therefore, considering that (i) the QC fluxes overestimate the numerical fluxes for all the cases with mild spins, and (ii) the numerical fluxes at periastron in the strong field regime naturally overestimate analytical fluxes, we have that there must be some configurations for which the quasicircular prescription will provide a good approximation at periastron. However, in all cases with mild or high eccentricity, the QC fluxes are not reliable at apastron, leading to comparatively large relative differences. While this is not relevant from a practical point of view since the main contribution of the radiation reaction to the dynamics happens at periastron, it is, however, an indication that the quasicircular prescription is not suited to describe eccentric dynamics, as *a priori* expected. We will further confirm this statement in the next subsection where we will analyze the fluxes more systematically considering the analytical/numerical differences between averaged fluxes over the whole parameter space $(e, \hat{a}) = [0, 0.9] \times [-0.9, 0.9]$. The fact that the QC radiation reaction overestimates the numerical fluxes at periastron generally results in an unphysical acceleration of the dynamics once the corresponding $\mathcal{F}_\varphi$ enters at the rhs of Hamilton's equations. We will further discuss the relevance of this aspect for comparable mass binaries in Sec. 4.2.2.

Let us now focus on the QC2PN prescription, which follows from Ref. [150] (green in Figs. 4.10 and 4.11). While for low eccentricity the corresponding fluxes are reliable, as shown in the $e = 0.1$ case of Fig. 4.11, the prescription starts to be less accurate for mild and high eccentricities. In particular, while this choice is generally more accurate than the QC case at apastron, the relative differences are still larger than the NCN ones. Moreover, when the particle is almost at the periastron, or shortly after the periastron passage (i.e. when the radial momentum is close to its maximum value along the orbit), the analytical/numerical relative differences for this prescription reach their maximum and are

even larger than for the QC case. This aspect can be clearly seen in all the configurations with $e \geq 0.5$ shown in Figs. 4.10 and 4.11. For large values of eccentricity and large spin, the fluxes associated with the QC2PN choice can show unphysical behaviors, developing multiple peaks and becoming negative. This can be clearly seen in the last configuration of Fig. 4.11, but we anticipate that a similar pathological behavior can occur even in the nonspinning case if the noncircularity of the orbit is high enough, as shown in the last hyperbolic scattering of Fig. 4.14 in Sec. 4.2.1. In Fig. 4.11 we consider configurations with semilatus rectum $p = 13p_s(e, \hat{a})/p_s(e, 0)$, but the pathologic behavior becomes even more relevant if we consider smaller semilatera recta like $p = 9p_s(e, \hat{a})/p_s(e, 0)$.

Let us finally turn to the analysis of the NCN analytical fluxes, repeating for completeness some of the analysis of Ref. [1]. Figure 4.10 shows that such analytical expressions are the most reliable among the three and this becomes especially evident for $e \geq 0.3$. Note that the NCN expressions are the only ones where the relative differences are smaller at apastron than at periastron, as one would naturally expect since the periastron is reached in a stronger gravitational field, and thus the accuracy of any PN-based expression (though resummed) should be reduced there.

Finally, we conclude with an observation on the numerical fluxes that could be relevant for the next subsection. As can be seen in the last plots of Fig. 4.10 or in Fig. 4.11, the relative differences of highly eccentric configuration are noisy for early times (i.e. near the apastron). This is linked to the fact that the numerical flux is still slightly contaminated by the junk radiation[1]. However, the highly eccentric fluxes have a small absolute magnitude near the apastron, and thus this contamination does not affect the averaged fluxes that we will consider in the next section. To be more quantitative, consider that for the case with $(e, \hat{a}, p) = (0.9, 0, 13)$ in the last row of Fig. 4.10, the angular momentum and energy fluxes have values of $5 \cdot 10^{-8}$ and $2 \cdot 10^{-11}$ at apastron, respectively.

Orbital averaged fluxes for eccentric orbits

To have a more systematic picture of the accuracy of the analytical expressions discussed above, it is useful to consider the fluxes averaged along a radial orbit and the corresponding relative differences with the numerical quantities. However, this method tests the reliability of the prescriptions in the neighborhood of the periastron, where there is the main contribution to the integrated flux. In other words, with this method it is not possible to see that the QC and QC2PN expressions are not accurate at apastron. We report the analytical/numerical relative differences in absolute value plotted against the Kerr spin parameter $\hat{a}$ in Fig. 4.12. We use squares as markers to indicate configurations with semilatus rectum $p = 9p_s(e, \hat{a})/p_s(a, 0)$, while we use triangles for $p = 13p_s(e, \hat{a})/p_s(a, 0)$. Note that the results for the NCN fluxes were already shown in Fig. 3.6.

Let us first note in Fig. 4.12 that the purple markers, corresponding to the circular configurations, are the same in all cases since the circular expressions are shared by the QC, QC2PN, and NCN expressions. Their accuracy is further discussed in Appendix A of Ref. [4]. Already for $e = 0.1$, the three prescriptions provide quite different results: both the QC and QC2PN choices yield significantly larger differences than the NCN one for both energy and angular momentum. This remains true also for larger eccentricities. On the other hand, for spins $\hat{a} \geq 0.6$, the relative differences of the quasicircular prescription are similar to the ones of the `TEOBResumS` fluxes, and even slightly better in

[1] The numerical simulations do not start necessarily from $t = 0$.

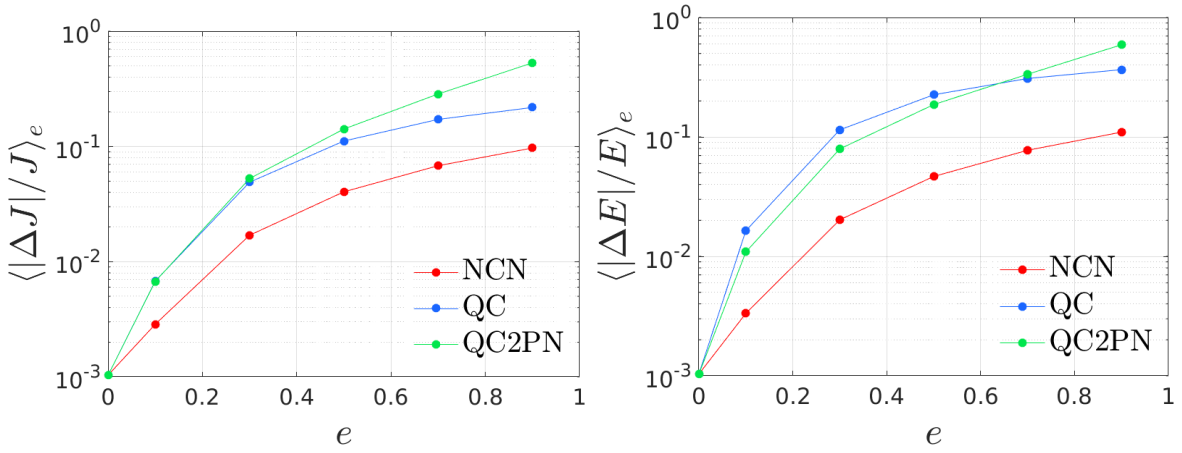

Figure 4.13: Means of the analytical/numerical relative differences of the orbital averaged fluxes, graphical representation of Table 4.2. Each point represents the mean of the averaged fluxes of all the configurations with a certain value of eccentricity, which we indicate as $\langle ... \rangle_e$. Note that we consider $\hat{a} = (0, \pm 0.2, \pm 0.6, \pm 0.9)$ and two semilatera recta for each pair $(e, \hat{a})$, so that each point is the mean value over 14 averaged fluxes. As can be seen, NCN is, on average, the most reliable radiation reaction.

some cases. Nonetheless, we have already discussed above that generally the quasicircular fluxes overestimate the numerical results, but for high spins the numerical fluxes include contributions that are not described by EOB models. For the last prescription shown in Fig. 4.12, the one that includes 2PN noncircular information, for $\hat{a} \geq 0.6$ we have greater relative differences than for the other two prescriptions, but we already argued that for high spins and/or high eccentricity this prescription shows pathological behavior. For smaller spins, instead, the analytical/numerical discrepancies are bigger for farther simulations, as happens also for the other radiation reactions independently of the spin considered (with few exceptions). This issue of the QC2PN choice can even lead to negative averaged fluxes; for example, this happens in the configurations with $\hat{a} = 0.9$, $e \geq 0.7$ and $p = 9p_s(e, \hat{a})/p_s(e, 0)$.

Finally, we can consider all the simulations for a certain value of eccentricity and we can obtain the mean of the corresponding averaged fluxes. We indicate this average at fixed eccentricity as $\langle ... \rangle_e$. In Fig. 4.13 we report these averages for the fluxes considered so far, showing once again that the NCN is the most reliable for every value of eccentricity.

To conclude, also the systematic study of the reliability of the three prescriptions considered so far suggests that the standard radiation reaction of `TEOBResumS` is the most accurate, both for low and high eccentricity.

Hyperbolic geodesic orbits

We now turn our attention to unbound orbits. We consider three hyperbolic geodesic scatterings in Schwarzschild spacetime whose orbits are shown in Fig. 4.14, together with the corresponding analytical/numerical angular momentum and energy fluxes. In all three cases considered, the initial separation is $r = 120$, but we show only the time interval that corresponds to $r \leq 40$. Since we define the eccentricity and the semilatus rectum in terms of turning points, our definitions of eccentricity and semilatus rectum are not valid for unbound orbits, see Eqs. (3.2). We use instead the energy E and the angular momentum p_φ to characterize our orbits. The selected values are also reported in Fig. 4.14 for each case.

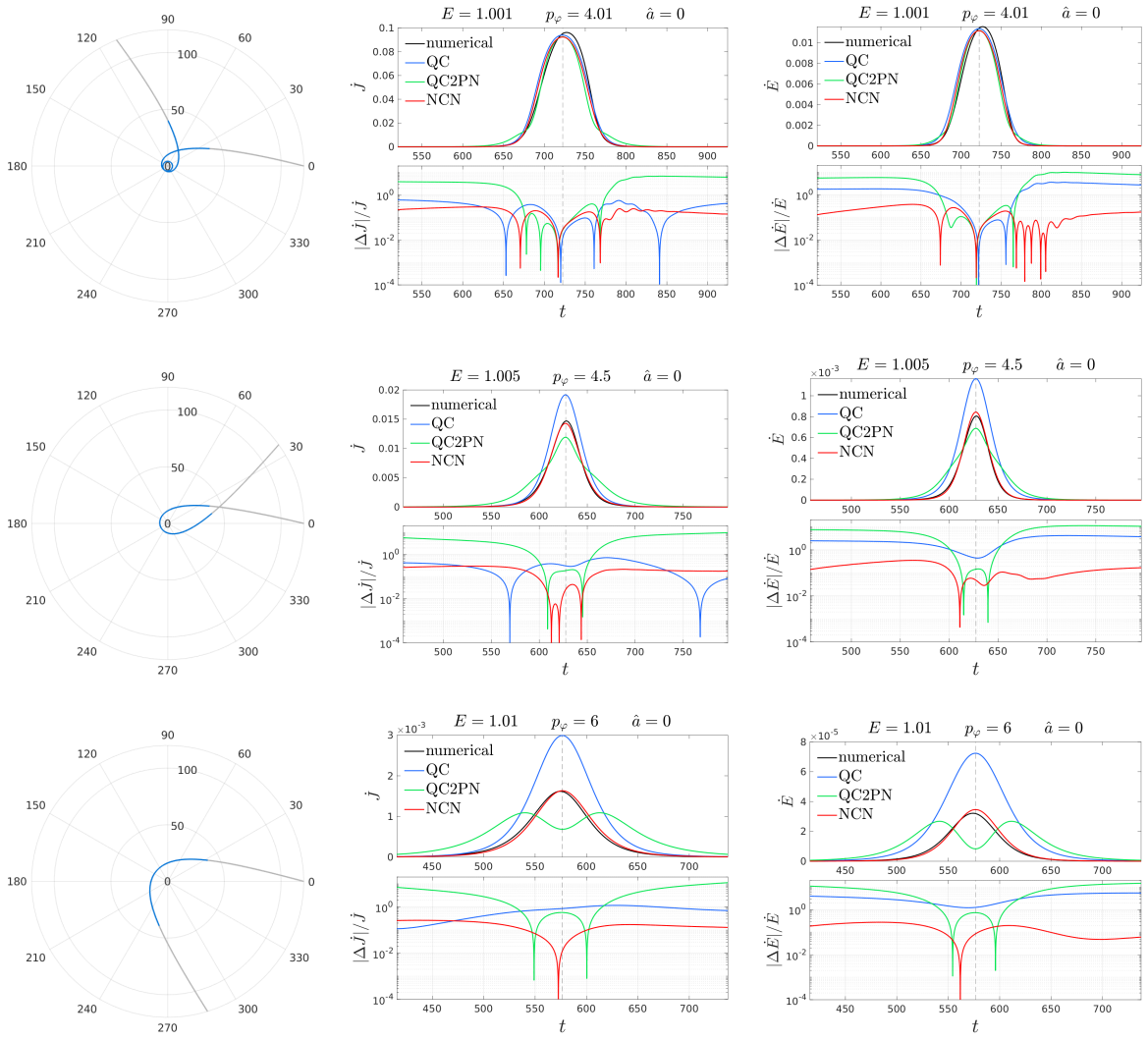

Figure 4.14: Hyperbolic geodesics in Schwarzschild spacetime. In the trajectories we highlight in blue the part that corresponds to $r \leq 40$; the fluxes are computed on this interval. We contrast the numerical fluxes (black) with the three analytical fluxes considered in this work: the NCN flux (red) computed using Eqs. (3.7) and (2.46); the QC flux (blue) from Eq. (4.55), which is a proxy of the `SEOBNRv4EHM` fluxes, and the QC2PN flux with 2PN noncircular corrections (green) from Eqs. (4.56). Each subpanel also reports the analytical/numerical relative difference. For each analytical flux, we also show the relative difference with the numerical result. The dashed vertical line marks the closest passage to the central black hole.

Table 4.2: Averaged analytical/numerical relative differences $\langle \delta F \rangle = \langle |\Delta F|/F \rangle$ for the fluxes averaged over a radial orbit for the three analytical possibilities, NCN, QC and QC2PN. We consider the means over the simulations with same eccentricity, the average for the nonspinning configurations, and the average for all the configurations. The values are reported in percentages. The relative differences averaged over the circular configurations are $\langle \delta J \rangle_c = \langle \delta E \rangle_c = 0.10\%$. The averages at fixed eccentricity are shown in Fig. 4.13.

[%]	NCN		QC		QC2PN	
	$\langle \delta J \rangle$	$\langle \delta E \rangle$	$\langle \delta J \rangle$	$\langle \delta E \rangle$	$\langle \delta J \rangle$	$\langle \delta E \rangle$
$e = 0.1$	0.29	0.33	0.68	1.64	0.67	1.09
$e = 0.3$	1.70	2.02	4.89	11.46	5.26	7.93
$e = 0.5$	4.04	4.66	11.15	22.53	14.17	18.65
$e = 0.7$	6.81	7.73	17.17	30.84	28.54	33.47
$e = 0.9$	9.69	10.97	21.80	36.60	53.15	59.08
$\hat{a} = 0$	0.44	0.60	8.60	18.72	5.43	9.49
all	3.77	4.30	9.30	17.20	16.98	20.05

The first configuration considered exhibits a strong zoom-whirl behavior. While during the circular whirl at periastron all three prescriptions provide similar results, the differences between them are clearly visible in the zoom part. Here, the less reliable prescription is the one using the QC2PN flux, as it gives differences well beyond the 100%, both before and after the whirl phase. This issue is even more evident when inspecting the other two configurations, which have larger energies and larger angular momenta. In particular, for $(E, p_\varphi) = (1.01, 6)$ the QC2PN fluxes even develop multiple peaks. The QC fluxes are more solid, but the relative differences with the numerical results are still very large and they always overestimate the numerical results at periastron, especially for the energy fluxes. Finally, the fluxes computed using the NCN choice are, once again, the most reliable and robust, showing smaller quantitative discrepancies with the numerical results for all three configurations considered.

4.2.2 Comparable mass case

In Sec. V of Ref. [4] we also discussed the comparable mass case. We focused on the EOB/NR comparison of a single equal mass black hole binary with nominal EOB initial eccentricity $e_0 \sim 0.2$. The EOB/NR comparisons were performed considering the SXS:BBH:1363 configuration discussed in Table IV of Ref. [3]. The findings are schematically listed in the following.

- If one considers the eccentric version of `TEOBResumS` as introduced in Ref. [148], and changes *only* the radiation reaction from NCN to QC, the new EOB waveform is much shorter than the NR one (see Fig. 8 of Ref. [4]). In other words, the QC radiation reaction leads to an unphysical acceleration of the system.

- On the other hand, if one changes the radiation reaction from NCN to QC but also calibrate again the model (finding $a_c^6 = -97$ instead of $a_6^c = -93.0366$) and recompute the optimal initial data $(e^{\rm EOB}_{\omega_a}, \omega^{\rm EOB}_a)$, then the EOB/NR comparison with this QC version of the model is similar (but not equivalent) to the one obtained using the eccentric model (see Fig. 9 of Ref. [4]). In other words, the unphysical

effects of the radiation reaction can be partially compensated by the calibration and the tuning of the initial data.

- Despite this partial compensation of the physical inaccuracy, the QC model is less accurate than the eccentric one. In particular, with the former we have an unfaithfulness (computed with LIGO noise) that can be slightly above 1%, while with the eccentric model we have at most 0.25% (see Fig. 10 of Ref. [4]).
- Finally, if one inspects the waveform frequency, it is clear that the QC model is less accurate than the eccentric model, as clearly shown in Fig. 11 of Ref. [4].

Given the above considerations, we conclude that the QC expression of $\hat{\mathcal{F}}_\varphi$ can introduce not-negligible systematics and it is thus *not suited* to construct faithful and robust EOB template waveforms for eccentric binaries. Crucially, standard phasing and faithfulness diagnostics can fail to capture these systematic errors, especially if a short NR waveform is employed. The faster circularization of the orbit given by the QC choice can be easily overlooked in the minimization of the initial data parameters, thus leading to large phase errors on longer signals.

4.2.3 2PN noncircular corrections in `TEOBResumS` radiation reaction

Reference [3] introduced high PN noncircular terms in the Newtonian-factorized waveform as a multiplicative correction to the generic Newtonian prefactor, which we also discussed in the previous section. After suitable resummations, this yielded an improved analytical/numerical waveform agreement with respect to the use of only the generic Newtonian prefactor, especially for the phase. This section aims to explore the performance of an analogous procedure applied to the flux. For simplicity, and since in any case our $\hat{\mathcal{F}}_\varphi$ is noncircular flexed only in the $\ell = m = 2$ mode, we limit here our analysis only to this mode. A more complete investigation is postponed to future work.

2PN-accurate quadrupolar flux

In Ref. [3] we recovered the full multipolar fluxes at 2PN accuracy in EOB coordinates as a consistency check of our waveform calculation. In particular, starting from the instantaneous part of the waveform we could explicitly recover the 2PN-accurate flux in EOB coordinates as obtained in Ref. [160]. For our current factorization purposes, we show here explicitly the $\ell = m = 2$ flux multipole up to 2PN order, including *both* the instantaneous (1PN and 2PN) and tail (1.5PN) parts,

$$
\begin{aligned}
F_{22}^{\rm 2PN} = {} & p_{r_*}^2 p_\varphi u^3 - 2p_\varphi^3 u^5 - 2p_\varphi u^4 + \frac{1}{c^2}\Bigg\{ p_\varphi u^5 \left[\frac{689}{42} - \frac{33\nu}{7} + \left(\frac{109}{7} - \frac{61\nu}{7}\right) p_\varphi^2 u \right. \\
& \left. + \left(\frac{17}{42} - \frac{12\nu}{7}\right) p_\varphi^4 u^2 \right] - p_{r_*}^2 p_\varphi u^4 \left[\frac{148}{21} - \frac{36\nu}{7} + p_\varphi^2 u \left(\frac{7}{3} - \frac{21\nu}{2}\right) \right] \\
& - p_{r_*}^4 p_\varphi u^3 \left(\frac{145}{42} + \frac{9\nu}{14}\right) \Bigg\} + \frac{\pi}{c^3}\Bigg[u^5 \left(\frac{9}{128} - \frac{173 p_\varphi^2 u}{10} + \frac{79309 p_\varphi^4 u^2}{5760} - \frac{889 p_\varphi^6 u^3}{32} \right. \\
& \left. + \frac{9157 p_\varphi^8 u^4}{384} - \frac{697 p_\varphi^{10} u^5}{72} + \frac{47 p_\varphi^{12} u^6}{640} + \frac{643 p_\varphi^{14} u^7}{480} - \frac{97 p_\varphi^{16} u^8}{288} \right) + p_{r_*}^2 u^4 \left(\frac{215}{192} \right.
\end{aligned}
$$

$$+\frac{91109p_\varphi^2u}{5760}-\frac{811p_\varphi^4u^2}{24}+\frac{14659p_\varphi^6u^3}{192}-\frac{51487p_\varphi^8u^4}{576}+\frac{22975p_\varphi^{10}u^5}{384}-\frac{3489p_\varphi^{12}u^6}{160}$$
$$+\frac{485p_\varphi^{14}u^7}{144}\Bigg)-p_{r_*}^4u^3\left(\frac{1219}{1152}-\frac{1471p_\varphi^2u}{576}+\frac{449p_\varphi^4u^2}{128}-\frac{3677p_\varphi^6u^3}{576}+\frac{769p_\varphi^8u^4}{144}\right.$$
$$\left.-\frac{49p_\varphi^{10}u^5}{32}\right)\Bigg]-\frac{1}{c^4}\Bigg\{p_\varphi u^6\left[\frac{8852}{189}-\frac{12335\nu}{378}+\frac{268\nu^2}{27}+p_\varphi^2u\left(\frac{21001}{882}-\frac{52147\nu}{588}\right.\right.$$
$$\left.+\frac{7661\nu^2}{294}\right)+p_\varphi^4u^2\left(\frac{59}{882}-\frac{60901\nu}{1764}+\frac{7663\nu^2}{1764}\right)+p_\varphi^6u^3\left(\frac{851}{882}-\frac{4987\nu}{882}\right.$$
$$\left.\left.-\frac{3295\nu^2}{1764}\right)\right]-p_{r_*}^2p_\varphi u^5\left[\frac{10277}{882}-\frac{60065\nu}{1764}+\frac{7799\nu^2}{441}+p_\varphi^2u\left(-\frac{6465}{392}\right.\right.$$
$$\left.-\frac{48385\nu}{441}+\frac{22237\nu^2}{441}\right)+p_\varphi^4u^2\left(\frac{709}{84}-\frac{685\nu}{24}+\frac{463\nu^2}{168}\right)\Bigg]-p_{r_*}^4p_\varphi u^4\left[\frac{6527}{441}\right.$$
$$\left.+\frac{6809\nu}{1764}-\frac{14921\nu^2}{1764}+p_\varphi^2u\left(\frac{2923}{588}-\frac{4889\nu}{588}-\frac{6317\nu^2}{294}\right)\right]\Bigg\}, \tag{4.57}$$

where, for the sake of simplicity, we considered an expansion in p_{r_*} up to order $\mathcal{O}(p_{r_*}^4)$. For completeness, Appendix C of Ref. [4] also reports the other flux multipoles relevant at 2PN order.

Factorization and resummation

Our aim here is to add 2PN-accurate noncircular corrections to the flux contribution of the mode $\ell = m = 2$. This is achieved by dressing the first term of Eq. (3.7b) with an additional correcting factor $\hat{F}^{\rm 2PN_{nc}}_{\varphi,22}$ derived from the full noncircular 2PN flux $\hat{F}^{\rm 2PN}_{22}$ written in Eq. (4.57). Following the same reasoning implemented for the waveform in Ref. [3], the procedure we use is the following:

(i) starting from the Taylor expanded flux $F^{\rm 2PN}_{22}$, we factorize the full Newtonian contribution $F^N_{22}\hat{f}^{\rm N_{nc}}_{\varphi,22}$, and we use in the latter the 2PN-accurate EOM to replace the time derivatives and expand the residual up to $\mathcal{O}(1/c^4)$,

(ii) we single out the circular part $\hat{F}^{\rm 2PN_c}_{22}$ of the Newton-factorized flux by simply taking the limit $p_{r_*}\to 0$,

(iii) we factorize the circular part computed in the previous step and compute the desired noncircular correction $\hat{F}^{\rm 2PN_{nc}}_{22}$.

In formulas we have

$$\hat{F}^{\rm 2PN_c}_{22}\equiv\lim_{p_{r_*}\to 0}T_{\rm 2PN}\left[\frac{F^{\rm 2PN}_{22}}{\left(F^N_{22}\hat{f}^{\rm N_{nc}}_{\varphi,22}\right)_{\rm EOMs}}\right], \tag{4.58}$$

$$\hat{F}^{\rm 2PN_{nc}}_{22}\equiv T_{\rm 2PN}\left[\frac{F^{\rm 2PN}_{22}}{\left(F^N_{22}\hat{f}^{\rm N_{nc}}_{\varphi,22}\right)_{\rm EOMs}\hat{F}^{\rm 2PN_c}_{22}}\right], \tag{4.59}$$

where the operator $T_{\rm 2PN}$ performs a Taylor expansion up to the 2PN order and the subscript "EOMs" manifests the replacement of the time derivatives in the Newtonian flux with the corresponding EOB EOM. The resulting noncircular factor (4.59) comes out naturally split in an instantaneous and a tail part, which appear at different PN orders. For this reason, one can readily factorize it further in an instantaneous and a tail factor,

$$\hat{F}_{22}^{\rm 2PN_{nc}} = \hat{F}_{22}^{\rm 2PN_{nc,inst}} \hat{F}_{22}^{\rm 2PN_{nc,tail}}, \tag{4.60}$$

which explicitly read

$$\begin{aligned}
\hat{F}_{22}^{\rm 2PN_{nc,inst}} &= 1 + \frac{1}{c^2}\left[\frac{p_{r_*}^2}{\left(1+p_\varphi^2 u\right)^2}\left(\frac{281}{168}+\frac{31\nu}{28}\right)\hat{f}^{\rm 1PN}_{p_{r_*}^2}\right.\\
&\left.+\frac{p_{r_*}^4}{u\left(1+p_\varphi^2 u\right)^3}\left(\frac{5-6\nu}{16}\right)\hat{f}^{\rm 1PN}_{p_{r_*}^4}\right]\\
&+\frac{1}{c^4}\left[\frac{p_{r_*}^2 u}{\left(1+p_\varphi^2 u\right)^3}\left(\frac{159697}{42336}-\frac{2081\nu}{10584}+\frac{20345\nu^2}{10584}\right)\hat{f}^{\rm 2PN}_{p_{r_*}^2}\right.\\
&\left.+\frac{p_{r_*}^4}{p_\varphi\left(1+p_\varphi^2 u\right)^4}\left(\frac{225067}{84672}+\frac{18119\nu}{10584}+\frac{6893\nu^2}{21168}\right)\hat{f}^{\rm 2PN}_{p_{r_*}^4}\right],
\end{aligned} \tag{4.61}$$

$$\begin{aligned}
\hat{F}_{22}^{\rm 2PN_{nc,tail}} &= 1 + \frac{\pi}{c^3}\left[-\frac{p_{r_*}^2}{p_\varphi\left(1+p_\varphi^2 u\right)^2}\frac{887}{1536}\hat{t}^{\rm 1.5PN}_{p_{r_*}^2}\right.\\
&\left.+\frac{p_{r_*}^4}{p_\varphi u\left(1+p_\varphi^2 u\right)^3}\frac{2215}{9216}\hat{t}^{\rm 1.5PN}_{p_{r_*}^2}\right].
\end{aligned} \tag{4.62}$$

Again, in the results reported above we expand in p_{r_*} up to order $\mathcal{O}(p_{r_*}^4)$. The terms $\hat{f}^{\rm PN}_{p_{r_*}^n}$ and $\hat{t}^{\rm 1.5PN}_{p_{r_*}^n}$ are polynomials in the Newtonian-order variable $y = p_\varphi^2 u$. For the instantaneous part the coefficients of the polynomials contain also the symmetric-mass ratio ν and read

$$\hat{f}^{\rm 1PN}_{p_{r_*}^2} = 1+\frac{2(571-54\nu)}{281+186\nu}y+\frac{1061-390\nu}{281+186\nu}y^2, \tag{4.63}$$

$$\hat{f}^{\rm 1PN}_{p_{r_*}^4} = 1+\frac{2(395-366\nu)}{21(5-6\nu)}y+\frac{295-234\nu}{7(5-6\nu)}y^2, \tag{4.64}$$

$$\begin{aligned}
\hat{f}^{\rm 2PN}_{p_{r_*}^2} = 1&+\frac{2\left(503861-236326\nu-42992\nu^2\right)}{159697-8324\nu+81380\nu^2}y\\
&+\frac{6\left(144635-100862\nu-59260\nu^2\right)}{159697-8324\nu+81380\nu^2}y^2\\
&-\frac{6\left(119807-50090\nu+28256\nu^2\right)}{159697-8324\nu+81380\nu^2}y^3\\
&-\frac{21\left(26487-19592\nu+428\nu^2\right)}{159697-8324\nu+81380\nu^2}y^4,
\end{aligned} \tag{4.65}$$

$$\begin{aligned}
\hat{f}^{\rm 2PN}_{p_{r_*}^4} = 1&+\frac{2\left(1028891+66902\nu-13616\nu^2\right)}{225067+144952\nu+27572\nu^2}y\\
&+\frac{6\left(670405+13630\nu+8948\nu^2\right)}{225067+144952\nu+27572\nu^2}y^2
\end{aligned}$$

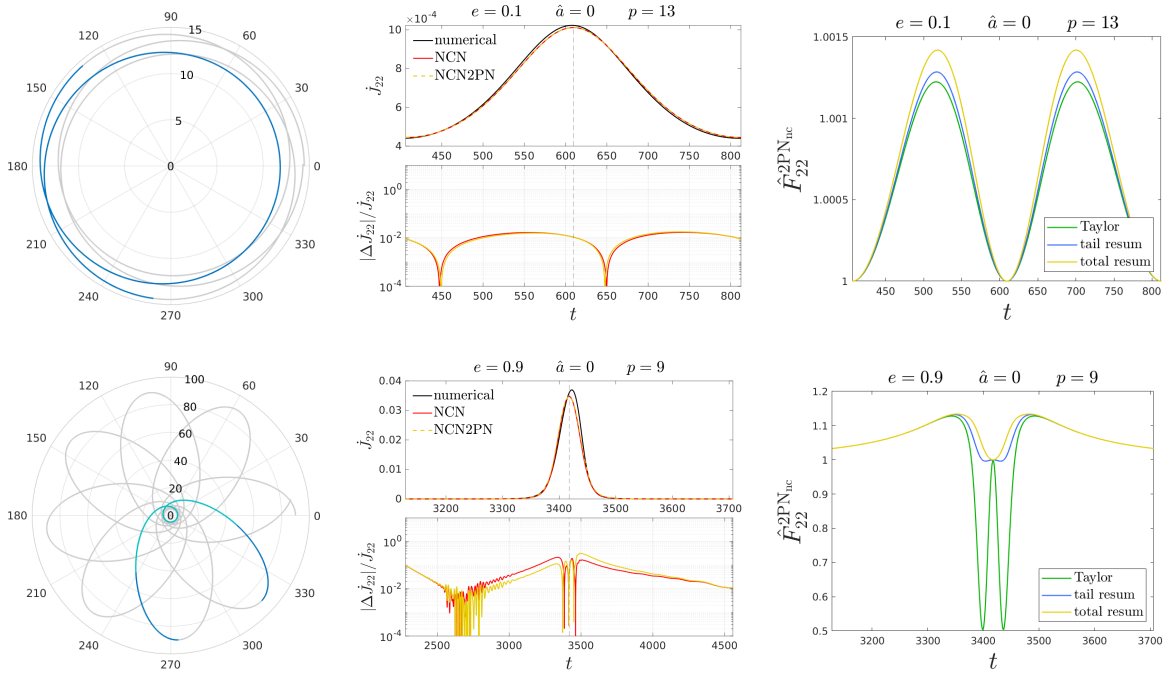

Figure 4.15: Trajectories, quadrupolar angular momentum fluxes, and 2PN corrections to the flux as discussed in Sec 4.2.3. We show the standard flux from `TEOBResumS` (red), the result with 2PN resummed corrections (yellow), and the numerical flux (black). The corresponding analytical/numerical relative differences reported in the bottom panel are shown over the radial period; the corresponding part of the trajectories is highlighted in blue. On the rightmost panels we show the 2PN corrections to the flux in Taylor expanded form, with resummation of the tail factor and with resummation of both the instantaneous and hereditary parts. The latter is used for the 2PN flux of the middle panels. For the second configuration with $e = 0.9$, the fluxes and the 2PN corrections are shown over a time interval that is shorter than the radial period in order to highlight the burst of radiation at periastron; the corresponding part of the trajectories is highlighted in aqua-green.

$$+\frac{6\left(548563+5454\nu+42912\nu^2\right)}{225067+144952\nu+27572\nu^2}y^3 +\frac{3\left(478421-54244\nu+40444\nu^2\right)}{225067+144952\nu+27572\nu^2}y^4, \tag{4.66}$$

while in the tail factor there are no ν-contributions and the two polynomials are

$$\begin{aligned}\hat{t}^{1.5\mathrm{PN}}_{p^2_{r_*}} &= 1+\frac{19094}{2661}y-\frac{127753}{13305}y^2+\frac{22016}{887}y^3 -\frac{2569}{2661}y^4-\frac{79250}{2661}y^5+\frac{29231}{887}y^6 -\frac{204692}{13305}y^7+\frac{7372}{2661}y^8, \end{aligned}\tag{4.67}$$

$$\begin{aligned}\hat{t}^{1.5\mathrm{PN}}_{p^4_{r_*}} &= 1-\frac{4222}{443}y+\frac{115273}{11075}y^2-\frac{74904}{2215}y^3 -\frac{15491}{2215}y^4+\frac{91994}{2215}y^5-\frac{77197}{2215}y^6 +\frac{169412}{11075}y^7-\frac{7372}{2215}y^8. \end{aligned}\tag{4.68}$$

Note that the analytical structure of the 2PN correction $\hat{F}^{2\mathrm{PN_{nc}}}_{22}$ is similar to the one of the 2PN corrections to the waveform multipoles discussed in Ref. [3]. As already argued

Table 4.3: Averaged analytical/numerical relative differences for averaged quadrupolar fluxes, $\langle \delta F_{22} \rangle = \langle |\Delta F_{22}|/F_{22} \rangle$. We consider the fluxes computed using NCN, NCN with 2PN corrections in Taylor expanded form, and NCN2PN that includes 2PN noncircular corrections in resummed form. For each flux we compute the averages over the simulations with same eccentricity, the average for the nonspinning configurations, and the average for all the configurations. The values are reported in percentages. The relative difference averaged over the circular cases is $\langle \delta J_{22} \rangle_c = \langle \delta E_{22} \rangle_c = 0.07\%$. The averages at fixed eccentricity are shown in Fig. 4.16.

[%]	NCN		NCN2PN (Taylor)		NCN2PN	
	$\langle \delta J_{22} \rangle$	$\langle \delta E_{22} \rangle$	$\langle \delta J_{22} \rangle$	$\langle \delta E_{22} \rangle$	$\langle \delta J_{22} \rangle$	$\langle \delta E_{22} \rangle$
$e = 0.1$	0.31	0.39	0.26	0.34	0.24	0.32
$e = 0.3$	2.03	2.52	1.70	2.23	1.47	1.98
$e = 0.5$	4.70	5.41	4.24	5.17	3.40	4.26
$e = 0.7$	7.41	8.10	8.75	10.05	5.45	6.49
$e = 0.9$	9.66	10.36	24.36	26.91	7.37	8.44
$\hat{a} = 0$	3.01	3.21	4.85	5.53	1.59	1.98
all	4.03	4.48	6.56	7.46	3.00	3.59

for the waveform, the polynomials in the y variable need to be resummed in order to provide reliable results in strong field regimes. We use diagonal Padé approximants for the polynomials in the tail and the 2PN instantaneous part, while we leave in Taylor-expanded form the polynomials in the 1PN instantaneous contribution.

Testing the 2PN noncircular correction in Newtonian-factorized angular radiation reaction

We test the reliability of the resummed factor $\hat{F}_{22}^{\rm 2PN}$ in the test mass limit, focusing on the quadrupolar contributions to the angular momentum and energy fluxes, $\dot{J}_{22}$ and $\dot{E}_{22}$. We start by considering two nonspinning configurations with eccentricities $e = (0.1, 0.9)$ in Fig. 4.15. In the rightmost panels we show the 2PN noncircular correction $\hat{F}_{22}^{\rm 2PN_{nc}}$ with different resummation procedures: in Taylor expanded form (green), with resummation only on the hereditary part $\hat{F}_{22}^{\rm 2PN_{nc,tail}}$ (blue), and with resummation on both $\hat{F}_{22}^{\rm 2PN_{nc,inst}}$ and $\hat{F}_{22}^{\rm 2PN_{nc,tail}}$ (yellow). The latter is used in the radiation reaction (and fluxes) that we label as NCN2PN. In the case with $e = 0.1$, the three 2PN circular corrections are similar, while in the other configuration with $e = 0.9$ the effects of the resummation become relevant. It is also possible to see that the resummation is more relevant for the hereditary part than for the instantaneous factor. This is a consequence of the fact that $\hat{t}^{\rm 1.5PN}_{p^n_{r_*}}$ are 8th-order y-polynomials, while $\hat{f}^{\rm 2PN}_{p^n_{r_*}}$ are 4th-order. However, the contribution of the resummed correction to $\dot{J}_{22}$ is small even for $e = 0.9$, as shown in the middle panels of Fig. 4.15.

Deeper insight into the problem is obtained by considering the analytical/numerical relative differences of the averaged quadrupolar fluxes and averaging over all the simulations with the same eccentricity, to obtain mean relative differences for each value of eccentricity, $\langle \Delta J_{22}/J_{22} \rangle_e$ and $\langle \Delta E_{22}/E_{22} \rangle_e$. In Table 4.3 and Fig. 4.16 we report these mean differences for three different radiation reactions: the standard prescription NCN, the prescription that includes in NCN the 2PN noncircular correction $\hat{F}_{22}^{\rm 2PN_{nc}}$ in Taylor-

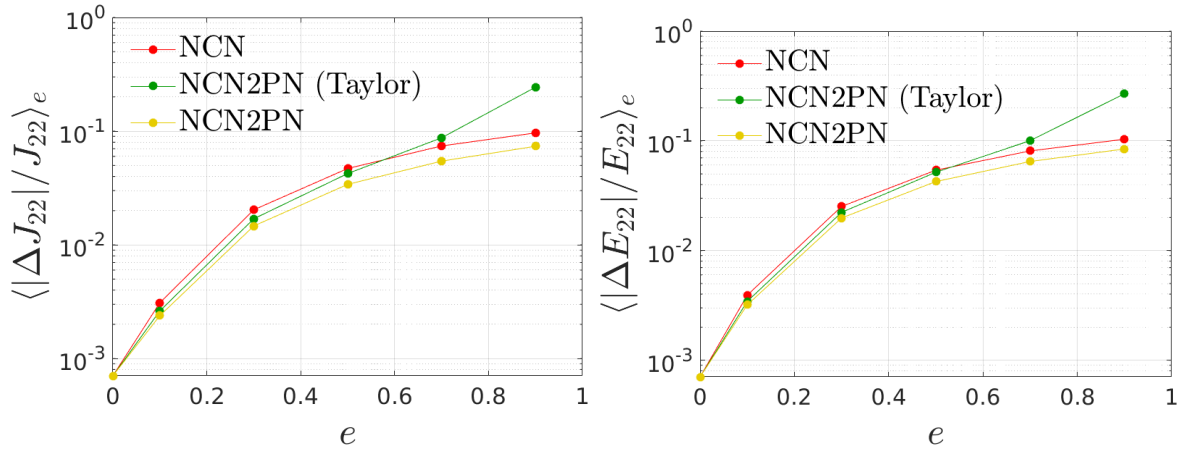

Figure 4.16: Means of the analytical/numerical relative differences of the averaged fluxes, graphical representation of Table 4.3. The mean $\langle ...\rangle_e$ is performed over all the simulations with the same eccentricity. Since we consider two semilatera recta for each pair $(e, \hat{a})$ and $\hat{a} = (0, \pm 0.2, \pm 0.6, \pm 0.9)$, each point is an average over 14 configurations.

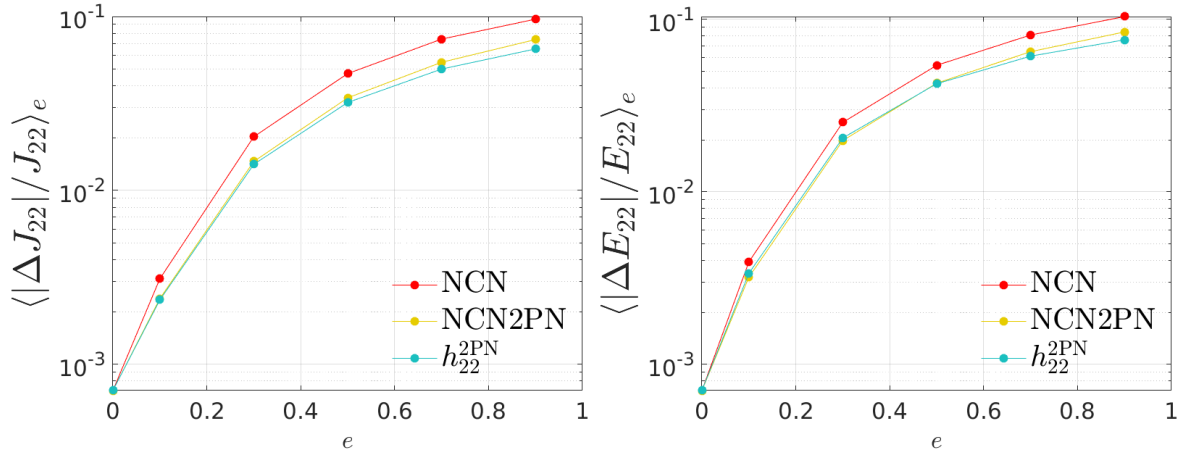

Figure 4.17: Means of the analytical/numerical relative differences of the averaged fluxes. The mean $\langle ...\rangle_e$ is performed over all the simulations with the same eccentricity. Since we consider two semilatera recta for each pair $(e, \hat{a})$ and $\hat{a} = (0, \pm 0.2, \pm 0.6, \pm 0.9)$, each point is an average over 14 configurations. We report the results for the NCN and NCN2PN fluxes, and also for the fluxes computed from the 2PN waveform of Ref. [3] using Eqs. (1.42). Complementary to Fig. 4.16

expanded form, and the prescription NCN2PN that includes the 2PN noncircular correction in NCN but with Padé resummation. As can be seen, the 2PN noncircular correction improves the radiation reaction NCN, but the resummation is needed in order to obtain more accurate results also for $e \gtrsim 0.6$. Indeed, for high eccentricity the periastron gets closer to the central black hole, making the y-polynomials of $\hat{F}_{22}^{\rm 2PN_{nc}}$ grow too much. The resummation prevents this issue and leads to better results also for low eccentricity.

However, note that with the factorization scheme here proposed the post-Newtonian noncircular corrections cannot improve the analytical/numerical agreement at periastron and apastron, since at the two radial turning points we have $p_{r_*} = 0$, and thus $\hat{F}_{22}^{\rm 2PN_{nc}}$ reduces to unity. This could be an indication that using the EOM at 2PN in the post-Newtonian noncircular corrections is not the best way to proceed, while leaving the explicit derivatives of coordinates and momenta could lead to more reliable fluxes. A first insight can be obtained by computing the analytical fluxes considering Eqs. (1.42)

and the waveform with resummed 2PN corrections[2] proposed in Ref. [3]. As can be seen from Fig. 4.17, this procedure is practically consistent with the flux at 2PN order discussed above. The exploration of this different procedure and the inclusion of higher multipoles is left to future work.

4.2.4 Summary

In this section we have revisited the results of Ref. [4]. In Sec. 4.2.1 we have compared the Noncircular-Newtonian (NCN) radiation reaction used in `TEOBResumS` [3, 147, 148] with the Quasi-Circular (QC) prescription used in `SEOBNRv4EHM` [149], and with the Quasi-circular-factorized one with 2PN noncircular corrections (QC2PN) proposed in Ref. [150]. We found that the first one is the most accurate in the test particle limit, both for eccentric and hyperbolic geodesic configurations. The reason of its accuracy is strictly related to the fact that the generic Newtonian prefactor has explicit time-derivatives that are not expanded using 2PN EOM. In Sec. 4.2.2 we have then argued that the QC radiation reaction in the comparable mass case leads to systematics in waveform models that could be particularly evident in EOB/NR comparisons for longer waveforms than the ones currently available. The NCN prescription is more accurate also in the comparable mass case. Finally, in Sec. 4.2.3 we have shown that including 2PN noncircular corrections in the quadrupolar contribution of the NCN radiation reaction leads to mild improvement, at least in the test mass limit.

4.3 Nouvelle Vague: an improved instantaneous correction

In this section we discuss the alternative formulation of the instantaneous 2PN noncircular corrections proposed in Ref. [5]. With this section, we conclude our discussion of the 2PN noncircular corrections.

We have previously seen that the analytical prescriptions for the EOB waveform and radiation reaction that are based on the Newtonian-factorization (with a 2PN correction) deliver the most faithful representation of the fluxes of a test mass around a Kerr black hole. References [3, 5] used the 2PN-truncated EOM to recast the noncircular correction in a simpler form, retaining explicit dependence on only the angular and radial momenta (p_φ, p_r). Unfortunately, with this approach the behavior at the orbit turning points (apastron and periastron) cannot be modified by higher PN corrections, since $p_r = 0$ there by definition, and all noncircular corrections vanish (see, e.g. Eq. (4.13), (4.19), and (4.20)). The accuracy at the radial turning points of the scheme is thus entirely determined by the Newtonian contribution, which explicitly depends on the, there nonvanishing, radial acceleration $\ddot{r}$ that appears in Eq. (2.35).

In Ref. [5] we proposed a new strategy to improve the behavior of the waveform at the radial turning points. The crucial element behind the accuracy of the generic Newtonian prefactor is that the derivatives (and notably $\ddot{r}$, see the right panels of Fig. 4.7) are evaluated using the *exact* EOM and not the PN-truncated ones. This is the important keystone that allows one to increase the accuracy of Newtonian-like expressions in strong

[2]More precisely, we consider the waveform with 2PN noncircular corrections where the noncircular tail factor and the instantaneous noncircular phase are resummed.

field (basically improving the Ruffini-Wheeler approximation [228], see also [55]). We extend here this idea to higher PN orders.

4.3.1 From the multipole moments to the factorized waveform

In Sec. 4.1 we reported $\hat{h}^{\rm nc}_{\ell m}$, the 2PN noncircular correction to the Newtonian-factorized waveform [3]. This correction is further factorized in a hereditary contribution (or tail) and in an instantaneous part, $\hat{h}^{\rm nc}_{\ell m} = \hat{h}^{\rm nc_{tail}}_{\ell m}\, \hat{h}^{\rm nc_{inst}}_{\ell m}$. The computation of the noncircular factors of Ref. [3] employs as initial input the PN expanded spherical multipoles of the waveform of Refs. [150, 221]. Depending on the parity of the multipole, these are obtained from the corresponding mass-type (when $\ell + m$ is even) or current-type (when $\ell + m$ is odd) radiative spherical multipoles, respectively called $U_{\ell m}$ and $V_{\ell m}$, [3] which in turn are related to the STF source multipole moments by nonlinear PN relations involving time derivatives of the latter. In the case of the $\ell = m = 2$ mode, at 2PN one has $h_{22} = -U_{22}/(\sqrt{2}c^4)$, $U_{22} = 2\sqrt{3}\,\alpha^{ij}_{22} U_{ij}$, and $U_{ij} = \ddot{I}_{ij}$, where α^{ij}_{22} is one of the STF tensors which connect the basis of spherical harmonics to the STF one (see, e.g., Eq.(2.5) of Ref. [221] for their definition), U_{ij} is the STF radiative mass quadrupole, and I_{ij} is the STF mass quadrupole of the source. A standard intermediate step in this computation is to systematically replace the time derivatives of the dynamical variables, which stem from the time derivatives of the STF source moments, like $\ddot{I}_{ij}$, with the PN-expanded EOM. In Ref. [5] we followed a different approach to obtain an alternative noncircular instantaneous factor where the time-derivatives are not replaced with the PN-expanded EOM. In practice: (i) we recover the 2PN accurate expressions for the STF source moments, valid for noncircular binaries, from Sec. IIIB of Ref. [221]; (ii) we trade the modified harmonic coordinates used therein for the EOB phase space variables $(r, \varphi, p_{r_*}, p_\varphi)$ using the transformations given in Eqs. (5)–(8) of Ref. [3]; (iii) we build the radiative multipoles following Secs. II and IIIA of Ref. [221], by taking the needed time derivatives but *without* replacing them with the PN-expanded EOM; (iv) we factorize the Newtonian part, which is precisely $h^{(N,\epsilon)}_{\ell m}$; (v) we factorize the generic source term $\hat{S}^{(\epsilon)}_{\rm eff}$, which corresponds to the mass-reduced EOB effective Hamiltonian $\hat{H}_{\rm eff}$ for even-parity multipoles and to the Newtonian-normalized angular momentum $\hat{j}_\varphi$ for odd-parity multipoles; finally (vi) we factorize also the non-eccentric part of the residual, which is obtained by setting to zero p_{r_*} and all the time derivatives of the EOB dynamical variable except $\dot{\varphi}$ (i.e., the orbital frequency Ω). Note that this non-eccentric part *does not* coincide with the exact circular limit, as we will explain below. The $\ell = m = 2$ PN-expanded instantaneous contribution reads

$$\begin{aligned} h^{\rm inst}_{22} &= h^{(N,0)}_{22}(r, \dot{r}, \ddot{r}, \Omega, \dot{\Omega}) \\ &\quad + \frac{1}{c^2} h^{(1{\rm PN},0)}_{22}(r, \dot{r}, \ddot{r}, \Omega, \dot{\Omega}, p_{r_*}, \dot{p}_{r_*}, \ddot{p}_{r_*}, p_\varphi, \dot{p}_\varphi, \ddot{p}_\varphi) \\ &\quad + \frac{1}{c^4} h^{(2{\rm PN},0)}_{22}(r, \dot{r}, \ddot{r}, \Omega, \dot{\Omega}, p_{r_*}, \dot{p}_{r_*}, \ddot{p}_{r_*}, p_\varphi, \dot{p}_\varphi, \ddot{p}_\varphi), \end{aligned} \tag{4.69}$$

where and $h^{(N,0)}_{22}$ is the Newtonian part and $(h^{(1{\rm PN},0)}_{22}, h^{(2{\rm PN},0)}_{22})$ formally addresses the contributions obtained by taking the time-derivative of the corresponding terms in the

[3] This separation takes place when the motion is planar, namely for spin-aligned configurations. In the general case, for each multipole one needs both $U_{\ell m}$ and $V_{\ell m}$.

radiative multipoles while keeping all derivatives explicit. We obtain

$$h_{22}^{(N,0)} \equiv -8\sqrt{\frac{\pi}{5}}\nu r^2\Omega^2 e^{-2\mathrm{i}\varphi}\hat{h}_{22}^{(N,0)_{\rm nc}}, \tag{4.70}$$
$$\hat{h}_{22}^{(N,0)_{\rm nc}} = 1 - \frac{1}{2}\left(\frac{\dot{r}^2}{r^2\Omega^2} + \frac{\ddot{r}}{r\Omega^2}\right) + \mathrm{i}\left(\frac{2\dot{r}}{r\Omega} + \frac{\dot{\Omega}}{2\Omega^2}\right),$$

with the noncircular part $\hat{h}_{22}^{(N,0)_{\rm nc}}$ isolated. The noncircular contribution is obtained from Eq. (4.69) as follows. First, we define the instantaneous, total, factorized correction as $f_{22}^{\rm total} \equiv h_{22}^{\rm inst}\left(h_{22}^{(N,0)}\hat{H}_{\rm eff}\right)^{-1}$, where we replaced $\hat{S}_{\rm eff}^{(0)} \equiv \hat{H}_{\rm eff}$. The non-eccentric limit of this function is defined according to point (iv) above, so to obtain (at 2PN)

$$\begin{aligned} f_{22}^{\rm circ} = 1 &+ \frac{u}{c^2}\left[-\frac{12}{7} - \frac{p_\varphi^2 u}{3} + \left(\frac{1}{7} + \frac{p_\varphi^2 u}{2}\right)\nu\right] \\ &+ \frac{u^2}{c^4}\left[-\frac{229}{252} - \frac{929 p_\varphi^2 u}{756} + \frac{19 p_\varphi^4 u^2}{63}\right. \\ &+ \left(\frac{289}{126} - \frac{1741 p_\varphi^2 u}{378} - \frac{235 p_\varphi^4 u^2}{504}\right)\nu \\ &\left.+ \left(\frac{65}{126} + \frac{31 p_\varphi^2 u}{54} - \frac{143 p_\varphi^4 u^2}{504}\right)\nu^2\right]. \end{aligned} \tag{4.71}$$

Note that p_φ *is not* replaced with its PN-expanded circular expression. The noncircular (instantaneous) contribution is obtained by factoring out this result as

$$\hat{h}_{22}^{\rm nc_{inst}} = T_{\rm 2PN}\left[f_{22}^{\rm total}(f_{22}^{\rm circ})^{-1}\right], \tag{4.72}$$

where $T_{\rm 2PN}$ indicates an expansion up to the 2PN order, as usual. This allows us to obtain a new noncircular factor that is analogous, though different, to that of Ref. [3]. A few more comments are in order to further clarify the structure of the non-eccentric (i.e. circular) part. First, we stress that taking the exact *circular limit* of the product $h_{22}^{(N,0)} f_{22}^{\rm circ}$ (i.e., replacing also the PN-expanded expression of p_φ along circular orbits) correctly delivers the 2PN-accurate f_{22} function of Eq. (B1) of Ref. [140]. The factorization procedure is thus such that the waveform is consistent with the quasi-circular waveform of `TEOBResumS`[4]. We note, however, that in practice we *do not* use the 2PN-accurate $f_{22}^{\rm circ}$ recovered above, but rather replace it with the quasi-circular function $\rho_{22} = f_{22}^{1/2}$ with the PN-accuracy and resummation used either in the standard `TEOBResumS` model (for comparable masses) or in its test mass version [1]. More precisely, ρ_{22} is resummed according to Refs. [158, 159], but while in `TEOBResumS` the orbital contribution $\rho_{22}^{\rm orb}$ is Taylor-expanded at 3^{+2}PN accuracy [229], in the test mass limit we use it at 6PN, resummed with a (4,2) Padé approximant.

The new noncircular factor is given explicitly in the supplemental `Mathematica` notebook of Ref. [5]. The noncircular tail contribution $\hat{h}_{\ell m}^{\rm nc_{tail}}$ is the one discussed in Ref. [3], while the circular tail contributions are incorporated according to standard procedure [140].

[4] In Ref. [3] we factorized the *circular* $\hat{S}_{\rm eff}^{(\epsilon)}$, but the procedure followed in this work is more consistent since in the full EOB waveform we have the generic factor $\hat{S}_{\rm eff}^{(\epsilon)}$, see e.g. Ref. [140].

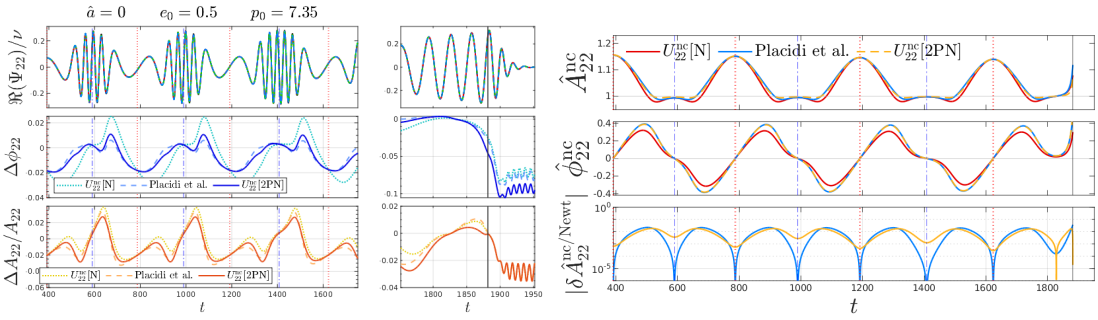

Figure 4.18: Left panel: quadrupolar waveform generated by a test mass plunging into a Schwarzschild black hole along an orbit with initial eccentricity $e_0 = 0.5$. Numerical waveform (black) compared to the EOB waveform with Newtonian noncircular corrections (red), to the one with 2PN noncircular corrections [3] (dashed green), and to the one proposed here (dash-dotted blue). Phase and relative amplitude differences are also shown. Right panel: comparing the 2PN-accurate instantaneous noncircular correction to the amplitude (top) and to the phase (middle) of this work with the one of Placidi et al.[3]. Relative differences with the Newtonian contribution are shown in the right-bottom panel. The noncircular factor introduced here is nonzero at the apastron (red dotted vertical lines) and periastron (blue dash-dotted vertical lines). The black vertical line marks the merger time.

4.3.2 Comparing analytical and numerical test mass results

The new prescription for the noncircular waveform correction is tested by following step-by-step the approach of Ref. [1, 3, 4]. This relies on extensive comparisons with waveform and fluxes emitted by a (nonspinning) particle orbiting around a Kerr black hole, considering various orbital configurations. To set the stage, we consider a particle inspiralling and plunging around a Schwarzschild black hole and compare the analytical waveform with the numerical one, considered exact, obtained by solving numerically the Teukolsky equation using `Teukode` [126] (see Ref. [1] for more numerical details). Figure 4.18 refers to a configuration with initial eccentricity $e_0 = 0.5$ and semilatus rectum $p_0 = 7.35$. The numerical waveform (black) is compared with the analytical waveform with Newtonian noncircular corrections (red), the waveform with 2PN noncircular corrections proposed in Ref. [3] (dashed green), and the waveform with 2PN noncircular corrections as proposed in this work (blue dash-dotted). The corresponding analytical/numerical differences for amplitude and phase are shown in the bottom panels. Regarding the phase, the performance of the new waveform and the one of Ref. [3] are substantially equivalent (see the dashed and solid blue lines in the middle left panel of Fig. 4.18). For the amplitude, instead, the new approach yields a reduced maximum analytical/numerical difference during the evolution, as well as a slight improvement as the orbital motion approaches the periastra (see bottom left panel of Fig. 4.18). This comes from the nonvanishing of the noncircular correction at the radial turning point. This is highlighted in the right panels of Fig. 4.18, which show the noncircular corrections. The bottom right panel exhibits the relative difference between the two 2PN noncircular amplitude corrections and the Newtonian noncircular amplitude correction, $|\delta\hat{A}_{22}^{\rm nc/Newt}|$. The correction at the two turning points is nonzero and is especially relevant at periastron. Note that the *instantaneous* phase noncircular corrections at 2PN differ sensibly from the Newtonian one. However, part of this difference is compensated by the hereditary phase correction, as already discussed in Sec. 4.1.5.

The improvement in the description of the waveform at periastron is even more important when the noncircular corrections are incorporated in the fluxes. Note in fact that the main contribution to the dynamics, through radiation reaction, happens due

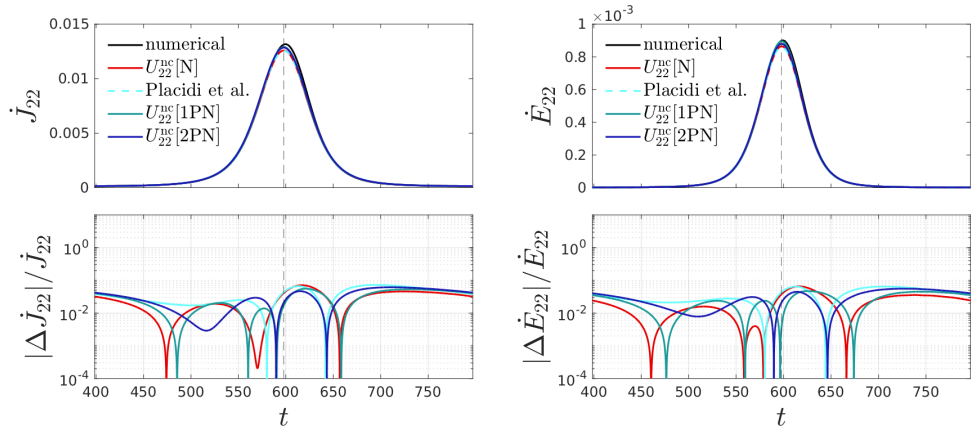

Figure 4.19: Angular momentum and energy quadrupolar fluxes at infinity generated by a test particle in Schwarzschild spacetime along a geodesic with $e = 0.5$ and $p = 9$. The relative differences in the bottom panels show that the PN waveform corrections with explicit derivatives improve the analytical/numerical agreement at periastron.

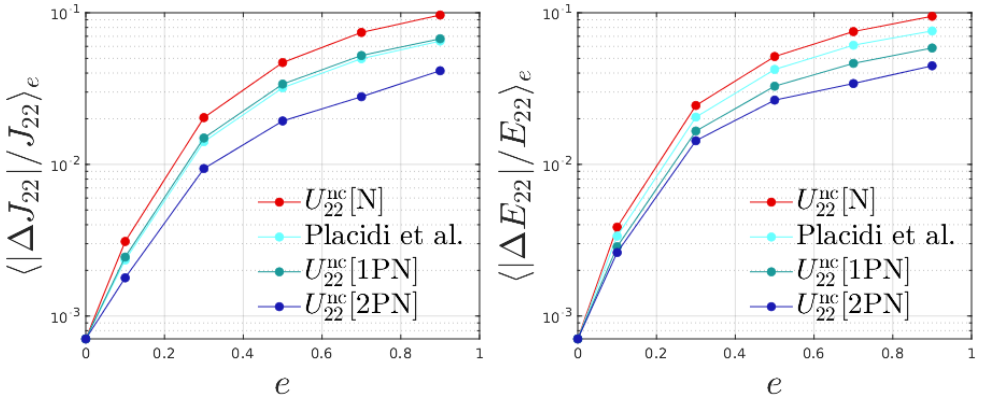

Figure 4.20: Analytical/numerical fractional differences between the averaged quadrupolar fluxes versus eccentricity that show convergence of PN corrections in the test mass limit. Each point is obtained from the mean of the orbital averaged fluxes of all the configurations considered at a given eccentricity e. See the main text for more details.

to the burst of radiation emitted at periastron. To show this effect systematically, we consider the usual set of geodesic eccentric orbits with eccentricity up to $e = 0.9$ and semilatera recta given by $p = p_{\rm schw} p_s(e, \hat{a})/p_s(e, 0)$, where p_s is the separatrix [205, 206] and $p_{\rm schw} = (9, 13)$; see also discussion in Sec. 3.1. In Fig. 4.19 we compare the fluxes for a case example with $e = 0.5$. From the analytical/numerical relative differences, one finds that the 2PN noncircular corrections with explicit derivatives perform better at periastron. As a radiation reaction, these fluxes will drive faster inspirals than those driven by the simple leading (Newtonian) noncircular correction of [1]. To draw a more global picture, it is useful to compare the orbital-averaged analytical fluxes with the corresponding, averaged, numerical ones obtained from the exact waveforms, calculated solving the Teukolsky equation. We compute the analytical/numerical relative difference and for each value of eccentricity e we compute its average over all the simulations sharing the same value of e. These averages are shown in Fig. 4.20, where each point has been obtained by averaging the analytical/numerical relative differences of 14 simulations with $\hat{a} = (0, \pm 0.2, \pm 0.6, \pm 0.9)$ and two different values of p. As shown in Fig. 4.20, the new 2PN waveform yields (on average) the best analytical/numerical agreement; even the

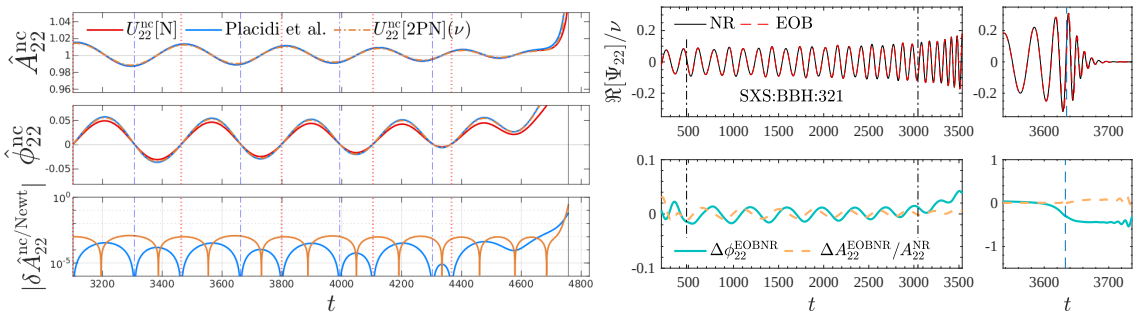

Figure 4.21: Left panels: same scheme as Fig. 4.18, but for an eccentric inspiral binary with $e_0 = 0.07621$ and $q = 1.22$ obtained with the full EOB dynamics of [3]. Right panels: corresponding EOB/NR phasing comparison with the NR dataset SXS:BBH:321 of the SXS catalog [230]. The EOB/NR phase difference is reduced during the plunge with respect to the corresponding plot in Fig. 13 of Ref. [3].

1PN energy flux calculation is better than the 2PN-accurate expression of Ref. [3]. Note, however, that the average over all spinning configurations can hide some information. In particular, for highly eccentric configurations ($e = 0.9$), the Newtonian prescription yields a better analytical/numerical agreement when averaged only on negative spins. This is clearer for the lowest spin, $\hat{a} = -0.9$, since the Newtonian flux yields a better analytical/numerical agreement even for mild eccentricities ($e \gtrsim 0.3$). However, in the Schwarzschild case, the hierarchy of the different prescriptions is the same as shown in Fig. 4.20.

The new noncircular correction factor is quantitatively superior to all other previous attempts of incorporating high PN noncircular information in the waveform and fluxes also in another aspect: the instantaneous amplitude correction presented in Eq. (4.19) contains a 1PN term $\propto -p_{r_*}^2 r$, that can become extremely large when considering hyperbolic or eccentric orbits with large radius. While this issue is not relevant for any of the configurations considered in Ref. [3], the correction can become even negative, and thus unphysical, for large separations, e.g. those occurring in hyperbolic encounters. By contrast, the new waveform is well-behaved *also* for a hyperbolic encounter or scattering configuration starting from any, arbitrarily large, initial separation.

4.3.3 Comparable mass case

The same behavior carries over to the comparable mass case, with the test mass dynamics replaced by the resummed EOB dynamics. We consider as a case study the NR configuration SXS:BBH:321 of the SXS catalog [230], row #23 in Table IV of Ref. [3]. Figure 4.21 exhibits the time-evolution of the noncircular waveform corrections along the corresponding EOB dynamics in the left panels and the EOB/NR comparisons in the right ones. In this case, the mass ratio is $q = 1.22$, while the dimensionless spins (χ_1, χ_2), aligned with the orbital angular momentum, are $\chi_1 = +0.33$ and $\chi_2 = -0.44$. The initial EOB eccentricity at the apastron is small, $e_{\omega_a}^{\rm EOB} = 0.07621$, but large enough to probe that our new waveform brings an improvement with respect to previous work. First of all, the left panels of Fig. 4.21 indicate that in the comparable mass case, the amplitude correction at the radial turning points is small but still relevant. It is informative to look at a standard EOB/NR phasing comparison for SXS:BBH:321, that we report in the right panels of Fig. 4.21. The EOB waveform is aligned to the NR one by minimizing the phase difference in the frequency interval corresponding to the two vertical lines in the left panels of the figure. The top panels compare the EOB and NR real parts of the waveform,

while the bottom panels show the EOB/NR phase difference $\Delta\phi_{22}^{\rm EOBNR} \equiv \phi_{22}^{\rm EOB} - \phi_{22}^{\rm NR}$ and relative amplitude difference, with $\Delta A_{22}^{\rm EOBNR} \equiv A_{22}^{\rm EOB} - A_{22}^{\rm NR}$. The picture illustrates that $\Delta\phi_{22}^{\rm EOBNR}$ is reduced, during the late-inspiral and plunge, with respect to the corresponding plot in Fig. 13 of Ref. [3], with the same waveform alignement interval used here. A similar behavior is also found with higher eccentricities. However, it must be noted that since the waveform is different, the choice of the initial parameters, which is not changed in this case, possibly might be optimized further. This study, together with the analysis of higher modes, is postponed to future work.

We finally point out that the waveform differences due to the new noncircular correction will yield fluxes that are *larger* at apastron than the current ones. Once recast in the form of radiation reaction force, and incorporated within the EOB dynamics, the new prescription will eventually yield an additional acceleration of the eccentric inspiral due to the stronger emission at periastron.

4.3.4 Summary

We have thus incorporated the discussion of Ref. [5] in this thesis. Inspired by the structure of the generic Newtonian prefactor, in Sec. 4.3.1 we have computed the instantaneous 2PN noncircular corrections of the waveform starting from the PN source multipoles and keeping explicit time-derivatives. In Sec. 4.3.2 we have shown that this procedure yields a better analytical/numerical agreement for the quadrupolar radiation with respect to other prescriptions for the instantaneous term present in the literature [3, 150]. We also tested the reliability of this framework for comparable mass binaries in Sec. 4.3.3.

However, we discussed only the quadrupolar term and we only considered a case study in the comparable mass case. Studies on the accuracy of the higher modes and a more systematic analysis for comparable mass binaries are postponed to future work. The development of the radiation reaction force and its influence on the inspiral (for any mass ratio) is also deferred to future work.

Chapter 5

Merger and ringdown for eccentric small-mass-ratio binaries

In Sec. 3.3 we have briefly discussed nonconservative eccentric Kerr dynamics, arguing that the back-reaction on the dynamics due to GW emission leads the particle to plunge toward the central black hole, and that the ringdown waveform can be modeled following the ideas proposed in Ref. [169] also in the eccentric case. We now discuss in more detail these topics, but focusing only on the Schwarzschild case. The following discussions are taken from Ref. [6].

More precisely, in this chapter we focus on the EOB prescription to compute the waveform at infinity for a non-spinning test particle plunging in a Schwarzschild black hole after an eccentric inspiral. The numerical data used to build the ringdown model, and thus complete the EOB waveform, are obtained by solving numerically the Regge-Wheeler and Zerilli (RWZ) equations [109, 110, 112, 114] using the time-domain code `RWZHyp` [122–124] discussed in Sec. 1.5.1. We argue that a description based exclusively on Quasi-Normal-Modes (QNMs) cannot be used to describe the ringdown waveform starting from the peak of the amplitude. We rather use a modified version of the phenomenologically agnostic ringdown model presented in Ref. [169]. We model the (2,2) multipole and also all the $m > 0$ higher modes up to $\ell = 4$, plus the (5,5) mode. The complete waveform obtained is, to our knowledge, the most accurate EOB waveform for a nonspinning test particle on quasi-circular inspirals in Schwarzschild spacetime, and also generalizes well to highly eccentric dynamics.

5.1 From eccentric inspiral to plunge, merger, and ringdown

The radiation-reaction-driven transition from eccentric inspiral to plunge, merger, and ringdown in the large mass ratio limit and the emitted gravitational waveform (computed using black-hole perturbation theory) were first discussed in Ref. [145] and then more in extenso in Sec. VB of Ref. [1] (notably also allowing the central black hole to spin). In the same Sec. VB of Ref. [1] we also presented a (preliminary) complete EOB-based waveform model including merger and ringdown for the $\ell = m = 2$ mode that we have also reported in Sec. 3.3 of this thesis.

In this chapter based on Ref. [6], we build upon Ref. [1] and complement the description of the dynamics and waveform phenomenology described there, but studying in

Table 5.1: Configurations considered in Ref. [6] and relevant quantities at merger time, defined as the peak of the orbital frequency. From left to right: initial semilatus rectum, initial eccentricity, eccentricity at the separatrix-crossing time, time difference between the peak of the orbital frequency and the peak of the quadrupolar amplitude, energy, angular momentum, and quadrupolar amplitude at the peak of the orbital frequency (that corresponds to the light-ring crossing).

#	p_0	e_0	$e_{\rm sep}$	$t^{\rm peak}_{\Omega_{\rm orb}} - t^{\rm peak}_{A_{22}}$	$\hat{E}^{\rm LR}$	$p^{\rm LR}_\varphi$	$A^{\rm LR}_{22}$
1	7.0	0.00	0.000	2.559	0.9422	3.4574	0.2928
2	7.3	0.05	0.061	2.585	0.9424	3.4598	0.2932
3	7.0	0.10	0.113	2.657	0.9429	3.4668	0.2942
4	8.0	0.15	0.141	2.708	0.9433	3.4717	0.2950
5	7.5	0.20	0.201	2.856	0.9444	3.4855	0.2970
6	8.0	0.25	0.229	2.925	0.9450	3.4932	0.2981
7	8.0	0.30	0.276	3.080	0.9462	3.5081	0.3003
8	8.0	0.35	0.321	3.240	0.9476	3.5243	0.3027
9	7.5	0.40	0.393	3.538	0.9503	3.5544	0.3070
10	8.0	0.45	0.415	3.651	0.9513	3.5644	0.3085
11	7.7	0.50	0.482	4.004	0.9545	3.5984	0.3133
12	8.0	0.55	0.514	4.189	0.9563	3.6159	0.3158
13	8.0	0.60	0.563	4.479	0.9592	3.6447	0.3199
14	8.0	0.65	0.615	4.839	0.9625	3.6768	0.3245
15	8.0	0.70	0.670	5.298	0.9665	3.7142	0.3298
16	8.0	0.75	0.728	5.877	0.9710	3.7554	0.3359
17	8.0	0.80	0.778	6.284	0.9751	3.7912	0.3408
18	8.2	0.85	0.818	6.628	0.9784	3.8202	0.3451
19	8.3	0.90	0.869	7.497	0.9839	3.8684	0.3523
20	8.5	0.95	0.904	8.160	0.9878	3.9004	0.3566

detail only the nonspinning case. In particular, we: (i) present a precise description of the transition from inspiral to plunge and its dependence on the eccentricity; (ii) explicitly present an analytical description of the postpeak waveform, that improves the one presented in Ref. [1] and that is crucial (as we will see) to construct a complete EOB waveform, that is the main goal of Sec. 5.2 below. Here we focus on the nonspinning case only, while the spinning case will be discussed elsewhere. The radiation-reaction-driven relative dynamics is obtained by solving Hamilton's equations in the presence of driving forces, i.e. by solving Eq. (2.56) specified for the nonspinning case. The explicit form of $\hat{\mathcal{F}}_\varphi$ and $\hat{\mathcal{F}}_r$ can be found in Eq. (3.6) and (2.46). Note that the $\mathcal{F}_\varphi$ of Eq. (3.6) is less accurate than the one of Eq. (3.7), but here the goal is just to complete the EOB waveform using numerical data for the plunge, merger, and ringdown waveform, so that the details of the radiation reaction used are not relevant.

We have already discussed in Sec. 3.1 that in order to have stable orbits, the semilatus rectum must satisfy the condition $p \geq p_s = 6 + 2e$, where p_s is the separatrix and reduces to the LSO in the quasi-circular case. In Ref. [6], and thus in this chapter, we consider configurations with initial eccentricities up to $e_0 = 0.95$ and semilatera recta such that the particle undergoes at least a few radial orbits before plunging in the black hole. The simulations considered are listed in Table 5.1. The dynamics is always started at the

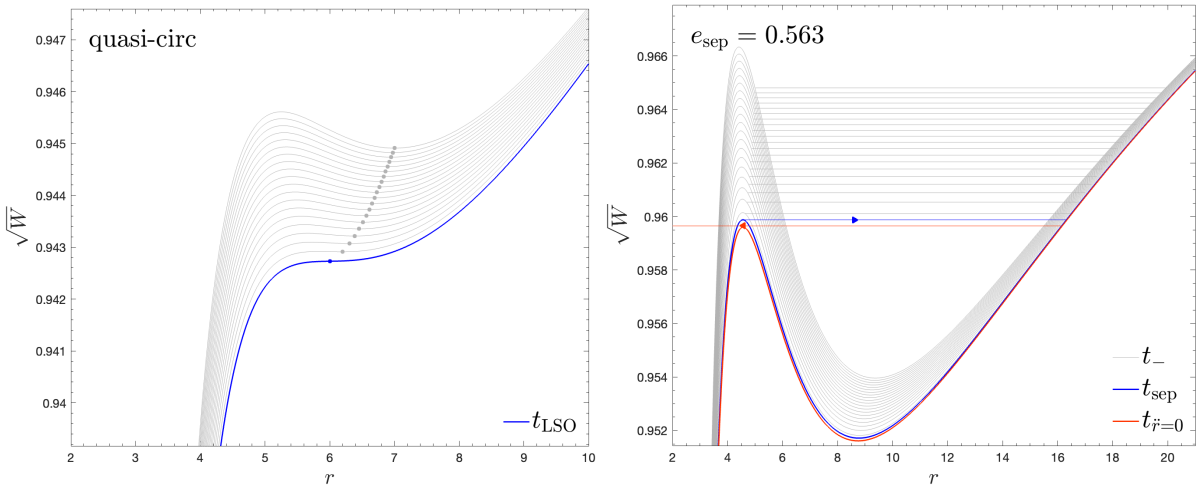

Figure 5.1: Left panel: the evolution of radial effective potential W, Eq. (5.1), along the transition from quasi-circular inspiral up to the Last Stable Orbit. The LSO potential is highlighted, while the minima (identified by visible markers) indicate the radius and energy of the particle. Right panel: eccentric case with initial eccentricity $e_0 = 0.6$ ($e_{\rm sep} = 0.563$). We show a sequence of potentials W (that change due to radiation reaction) and corresponding energies of the particle at the periastron (horizontal line, gray) during the bound motion of the inspiral. The quantities at the separatrix crossing are shown in blue, while the red lines correspond to the beginning of the plunge. Note that in this case one has $V_{\rm max} \lesssim E$. The horizontal arrows mark the radial location (and energy) of the particle along the orbit at $t = t_{\rm sep}$ and at $t = t_{\dot r=0}$. Note that the arrows point toward the corresponding direction of the radial motion, outgoing for $t = t_{\rm sep}$ and ingoing for $t = t_{\dot r=0}$. This latter point can be considered a *missed* periastron and practically marks the beginning of the plunge.

apastron, so that the initial radial momentum is zero. Note that we chose (e_0, p_0) in order to have a clear geometrical intuition of the orbit, but we immediately convert (e_0, p_0) in energy and angular momentum so that we have all the needed initial values to compute the dynamics from Hamilton's equations (see also discussion in Sec. 3.1). Note that since the dynamics is not conservative, e and p are not constants of motion and are not defined through the whole evolution of the binary. Indeed, after the separatrix-crossing time $t_{\rm sep}$, i.e. the time at which the condition $p(t) = p_s(t)$ is met, the periastron is no longer defined, and thus neither the eccentricity nor the semilatus rectum. Since in the next sections we will focus on the last part of the dynamics, we will often use $e_{\rm sep} = e(t_{\rm sep})$ to refer to a certain simulation, rather than e_0. Note however that this is only for labeling purposes, the eccentricity $e(t)$ is not actually used anywhere during the evolution.

The numerical waveform at linear order in ν is obtained by solving the Regge-Wheeler and Zerilli [109, 110] equations (1.57). The solutions $\Psi^{\rm (o/e)}_{\ell m}(t)$ are related to the waveform multipoles of Eq. (1.39) as $\Psi^{\rm (o/e)}_{\ell m}(t) = h_{\ell m}(t)/\sqrt{(\ell+2)(\ell+1)\ell(\ell-1)}$. The RWZ equations are solved using the time-domain code `RWZHyp` [122–124] discussed in Sec. 1.5.1. These simulations have been performed by Danilo Chiaramello on the INFN server `Tullio` (as the other `RWZHyp` simulations considered in Refs. [1, 145]).

5.1.1 Transition from eccentric inspiral to plunge

We now discuss the main qualitative features of the transition from an eccentric inspiral to plunge and merger. To make this section pedagogical and self-consistent, we start by reminding how this transition occurs in the quasi-circular case, which is approximately

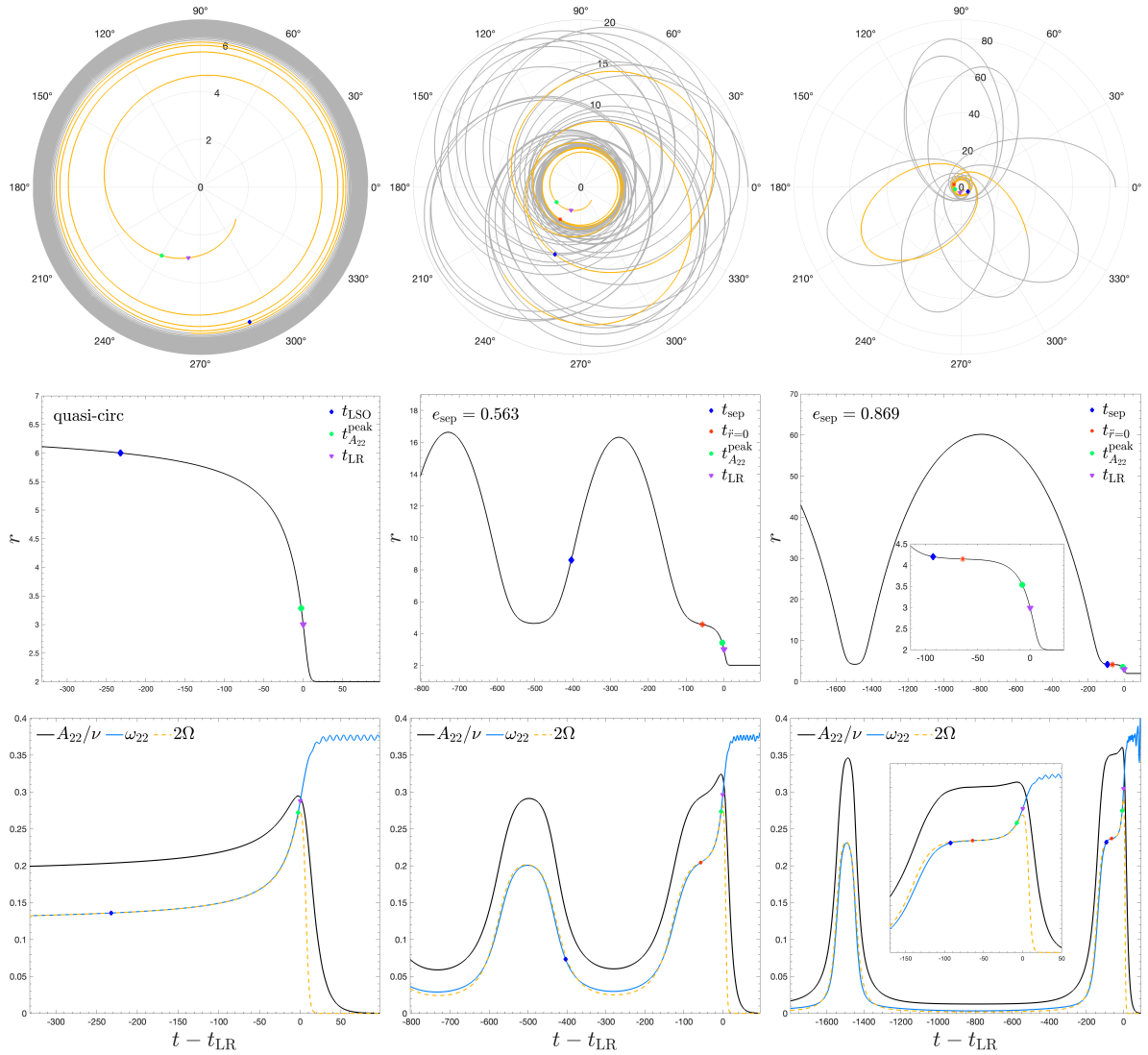

Figure 5.2: Top row: trajectories for the three configurations with initial eccentricity $e_0 = (0, 0.6, 0.9)$. We highlight in orange the portions that correspond to the parts shown in the lower panels. In all the cases we mark the separatrix crossing with a blue diamond (LSO in the quasi-circular case), the peak of the quadrupolar amplitude $t_{A_{22}}^{\rm peak}$ with a green circle, and the light-ring crossing time $t_{\rm LR}$ with a purple triangle. In the eccentric case, we also highlight the inflection point of the radius that marks the end of the last radial orbit, $t_{\dot{r}=0}$, with a red star. Middle row: radius versus time, same markers as above. Bottom row: corresponding amplitude (black) and frequency (blue) of the quadrupolar waveforms. We also show the orbital frequency (dashed orange).

representable as a sequence of circular orbits. The radius r_c of each circular orbit (with $r > r_{\rm LSO}$) corresponds to the local minimum of the radial potential

$$W = \left(1 - \frac{2}{r}\right)\left(1 + \frac{p_\varphi^2}{r^2}\right) \,, \tag{5.1}$$

i.e. defined by the condition $\partial_r(W)|_{r=r_c} = 0$, and its energy is $\hat{E} = \sqrt{W_{\rm min}}$, where $W(r_c) = W_{\rm min}$. Note that the relation with the effective potential V discussed in Sec. 3.1 is $V = \sqrt{W}$. Since the radiation reaction eliminates angular momentum from the system, the potential W is modified during the evolution, until the local maximum and minimum fuse together in an inflection point at the LSO, $r = r_{\rm LSO} = 6$, where $\partial_r W = \partial_r^2 W = 0$ and $p_\varphi^{\rm LSO} = 2\sqrt{3}$. The evolution of the potential and the energy for the quasi-circular case up to $t_{\rm LSO}$ are shown in the first panel of Fig. 5.1. We highlight in blue the potential at $t_{\rm LSO}$, after which the particle plunges into the black hole.

Eccentric orbits occur when $\sqrt{W_{\rm min}} < \hat{E} \leq \sqrt{W_{\rm max}}$, and the radial motion is confined between the two turning points, apastron and periastron. Since angular momentum is not conserved due to gravitational wave emission, the potential changes in time until the separatrix-crossing, identified by $\hat{E} = \sqrt{W_{\rm max}}$. After this, the periastron no longer exists (and thus e and p are no longer defined). As the energy of the particle approaches the maximum of the potential, the radial velocity eventually reaches a local minimum $|\dot{r}|_{\rm min} \neq 0$ and the radial acceleration $\ddot{r}$ changes sign, forcing the particle to plunge into the black hole. We identify this time, $t_{\ddot{r}=0}$, as the beginning of the plunge. The evolution of the potential for a configuration with initial eccentricity $e_0 = 0.6$ is shown in the right panel of Fig. 5.1. In this example the particle undergoes many eccentric orbits, then it crosses the separatrix while moving away from the central black hole (blue marker). The particle then reaches the apastron, inverts the motion, and eventually crosses the potential barrier at approximately $t_{\ddot{r}=0}$ (red marker), where the plunge starts. We also show the corresponding trajectory, the radial evolution, and the corresponding waveform in Fig. 5.2. Looking at $r(t)$, it is clear that $t_{\ddot{r}=0}$ can be thought as a *missed* periastron. In the same figure, we also show the quasi-circular configuration and another eccentric case with higher initial eccentricity, $e_0 = 0.9$. Note that in this highly eccentric case, there is a long-lasting circular whirl around the plunge, while in the previous case, the whirl around $t_{\ddot{r}=0}$ was much shorter. This phenomenology is linked to when $t_{\rm sep}$ occurs. In the $e = 0.9$ case, the particle crosses the separatrix slightly before the plunge and thus the energy at $t_{\ddot{r}=0}$ is quite close to the maximum of the radial potential. As a consequence, the particle undergoes a long-lasting quasi-circular whirl[1]. In the case with $e_0 = 0.6$, the separatrix crossing occurs slightly after the last periastron passage and thus the effect of the radiation reaction during the last radial orbit increases the difference between the energy and the maximum of the radial potential at the beginning of the plunge (in this case we have $\hat{E} - \sqrt{W_{\rm max}} \simeq 5 \times 10^{-5}$, while in the more eccentric one we had 2×10^{-6}). Therefore, in our $e_0 = 0.6$ case the particle has a shorter quasi-circular whirl before the plunge with respect to our $e_0 = 0.9$ case. For similar reasons, the configuration with $e_0 = 0.5$ has a longer whirl at $t_{\ddot{r}=0}$ than the configuration with $e_0 = 0.8$. We thus confirm that the length of the quasi-circular behavior occurring before the plunge does not simply depend on the value of eccentricity.

[1]We recall that if the energy is close to the peak of the radial potential, the orbits show a zoom-whirl behavior, see e.g. Ref [209].

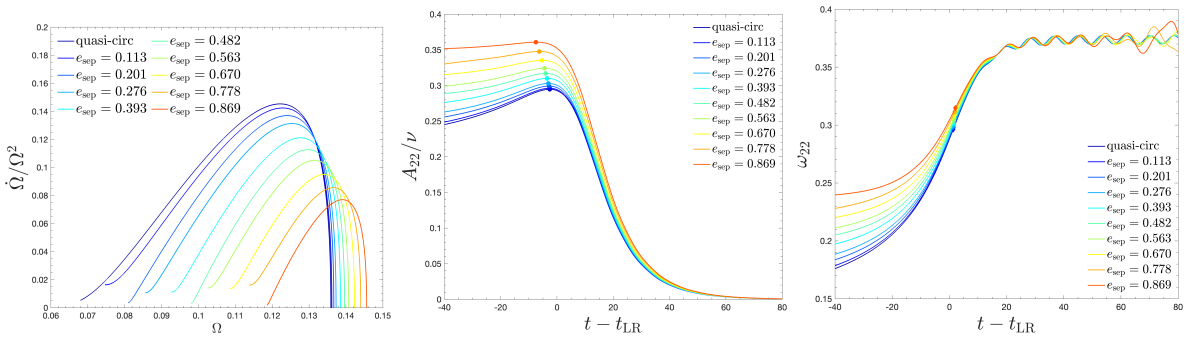

Figure 5.3: Adiabatic estimator, quadrupolar waveform amplitude and frequency for the quasi-circular case and different eccentric configurations. Left panel: measure of adiabaticity, $\dot{\Omega}/\Omega^2$. The horizontal axis is restricted between $\Omega_{\ddot{r}=0}$ and $\Omega_{\rm pk}$. Middle panel: quadrupolar Zerilli amplitudes, aligned with respect to the light-ring crossing. The dots mark the maxima of the amplitudes. Right panel: Zerilli frequencies for different eccentricities, always aligned using the light-ring crossing. The diamonds mark the inflection points of the frequencies.

Since the beginning of the plunge is a *missed* periastron and the eccentricity is a slowly varying quantity, the radius that marks the beginning of the plunge can be approximated as $r_{\rm plunge} \simeq (6 + 2e_{\rm sep})/(1 + e_{\rm sep})$ and it is always smaller than $r = 6$. The net result of this, together with the considerations above, is that the plunge is more adiabatic in the presence of eccentricity than in the quasi-circular case. This is made quantitative in the left panel of Fig. 5.3, which depicts the adiabatic estimator $\dot{\Omega}/\Omega^2$ as a function of Ω for some relevant configurations. For each dataset, the horizontal axis is restricted between $\Omega_{\ddot{r}=0}$ and $\Omega_{\rm pk}$, that corresponds respectively to the orbital frequency at the start of the plunge and at the light-ring crossing.

5.1.2 Waveform phenomenology

The features of the dynamics that we have just discussed clearly reflect on the waveform phenomenology, as shown by the Zerilli (2,2) waveforms reported in the bottom row of Fig. 5.2; the amplitude is shown in black, and the frequency in blue. The latter is also compared with the orbital frequency, Ω, shown in dashed orange. While in the circular case 2Ω is a remarkably good approximation of the waveform frequency ω_{22}, in the two eccentric cases the noncircular effects increase the differences between these two quantities during the inspiral. However, note that $\omega_{22} \simeq 2\Omega$ holds also during the plunge for the two eccentric cases, up to the time of the quadrupolar amplitude peak, $t^{\rm peak}_{A_{22}}$ (marked with a green circle), i.e. shortly before the light-ring crossing $t_{\rm LR}$ (marked with a purple triangle). This can be easily understood considering that the eccentric plunge is rather adiabatic.

In order to better highlight the properties of the waveform for different eccentricities, in Fig. 5.3 we plot the (2,2) mode of the waveforms for $e_0 \in [0, 0.9]$. As a consequence of the fact that in highly eccentric configurations the plunge starts at smaller radii, the amplitude grows as the eccentricity increases and the peaks become wider. Moreover, the peaks occur at earlier times with respect to the light-ring crossing, as shown by the markers in the left panel. In the right panel of Fig. 5.3 we show the corresponding frequencies. After the light-ring crossing, all the frequencies reach the fundamental positive quasi-normal frequency of the Schwarzschild black hole. Notably, also the beating between the positive and negative fundamental quasi-normal frequencies is not influenced

by the nature of the perturbation. However, at later time the oscillations in the frequencies tend to grow for high eccentricity, but this is only an effect of the power-law tail that begins to dominate on the quasi-normal-mode (QNM) contribution. We postpone the discussion of the tail to Sec. 5.4.4. We also highlight the inflection point of the frequencies using diamond markers. The location of this point is not strongly influenced by the eccentricity, but it is only slightly delayed with respect to the light-ring crossing. On the contrary, the location of the amplitude peak is strongly influenced by the eccentricity. This is a qualitative explanation of why the quasi-circular ringdown model used in `TEOBResumS` can correctly reproduce the frequency of highly eccentric comparable mass configurations, but not their amplitudes (see the supplemental material of Ref. [2] or the discussion in Chapter 6).

5.2 Waveform modeling

5.2.1 Ringdown (postpeak) modeling

During the ringdown, a relevant contribution to the waveform is given by the QNMs. If this is the only contribution, then each multipole can be written as Eq. (1.63), where we recall that $\sigma^{\pm}_{\ell n} = \alpha_{\ell n} \pm i\omega_{\ell n}$ are the complex QNM frequencies, and $C^{\pm}_{\ell mn}$ are complex constant coefficients. While the latter depend on the type of perturbation, the frequencies depend only on the mass of the Schwarzschild black hole. As argued in Sec. 2.3.4, we comply with the phenomenological ansatz introduced in Ref. [169], based on the idea of factorizing away the contribution of the fundamental quasi-normal mode. We thus consider the QNM-rescaled waveform $\bar{h}(\tau) = A_{\bar{h}}(\tau)e^{i\phi_{\bar{h}}(\tau)}$ of Eq. (2.52), where the amplitude and the phase are given by the templates of Eq. (3.9a) (introduced in Ref. [1]) and (3.9b) (from Ref. [169]). The sets of parameters c^A and c^ϕ are constrained by requiring the continuity of the waveform at $\tau = 0$ with the inspiral waveform. Requiring the continuity of the amplitude, its first two time derivatives, and the frequency, we get Eqs. (3.10), (3.11), (3.12), and (3.14). Note that in previous works also the condition of Eq. (3.13), $c^\phi_2 = \alpha_2 - \alpha_1$, was imposed. Here instead we leave c^ϕ_2 as a free parameter. The phase difference obtained with the constrained c^ϕ_2 using the damping times is shown in blue in the bottom-right panels of Fig. 5.4. The free c^ϕ_2 improves the phase, especially for $\ell = m$ modes.

With the templates from Eqs. (3.9a) and (3.9b) we are able to fit the numerical postpeak waveform for each multipole and every eccentricity considered in this work. In the first row of Fig. 5.4 we show the primary fits for the (2,2), (2,1), and (3,3) modes for the quasi-circular inspiral. The rescaled amplitude $A_{\bar{h}}$ and the rescaled phase $\phi_{\bar{h}}$ reach a plateau after $\simeq 2\tau_{\ell 1}$, where $\tau_{\ell 1} \equiv 1/\alpha_{\ell 1}$ is the QNM-damping time of the fundamental harmonic. This means that, at this stage of the evolution, the only relevant contribution to the waveform is given by the fundamental QNMs. Note that leaving c^ϕ_2 as a free parameter strongly improves the phase agreement for the (2,2) and (3,3) modes (cfr. red and blue lines in the phase difference of each plot), while it is not relevant for the (2,1) mode. Similar considerations hold for the configuration with $e_0 = 0.9$, that is shown in the bottom row of Fig. 5.4, and all the other eccentric configurations considered in this work.

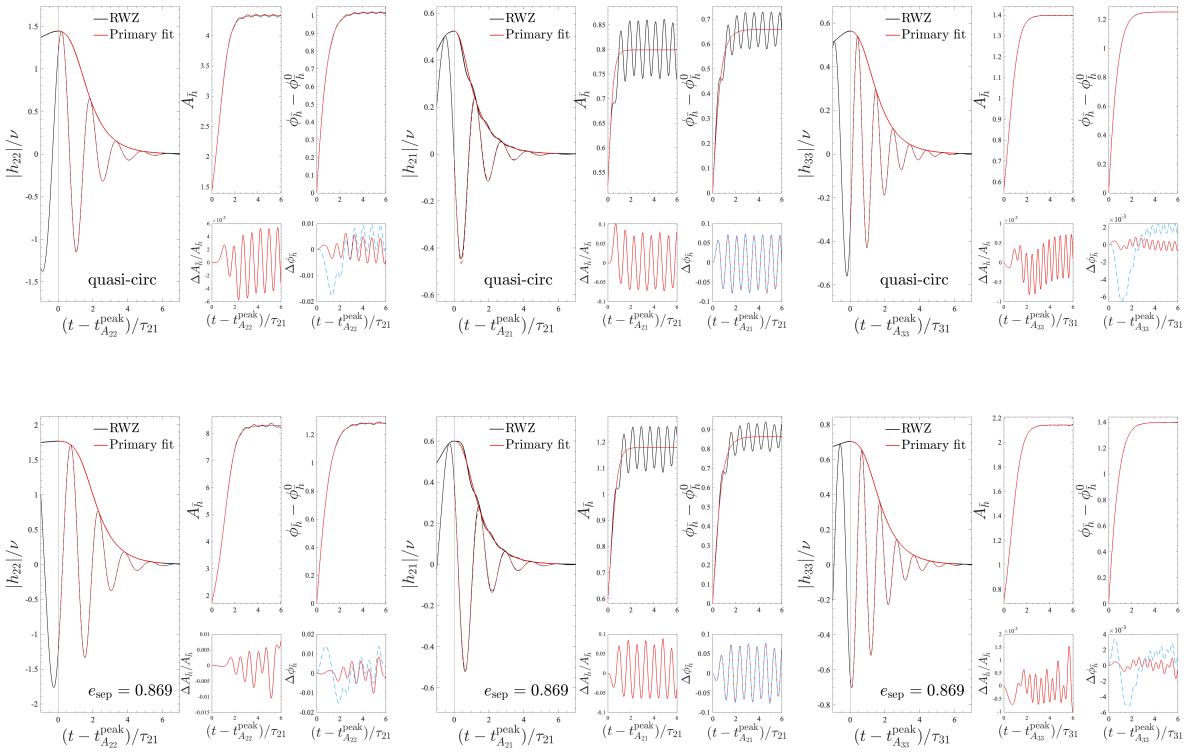

Figure 5.4: Numerical waveform (black) and postpeak primary fits (red) for the (2,2), (2,1), and (3,3) modes for the quasi-circular configuration (top row) and the configuration with $e_0 = 0.9$ (bottom row). We show the waveform $h_{\ell m}$ and its amplitude together with the QNM-rescaled amplitude $A_{\bar{h}}$ and phase $\phi_{\bar{h}}$. In the two small bottom panels we show the fit/numerical relative difference for the rescaled amplitude and the difference for the rescaled phase (red). Here $\phi^0_{\bar{h}}$ is the phase of $\bar{h}$ at $\tau = 0$, and $\tau_{\ell 1} = 1/\alpha_{\ell 1}$ is the QNM-damping time of the fundamental mode. We also show the RWZ/primary phase difference obtained by imposing the condition $c^\phi_2 = \alpha_2 - \alpha_1$ in the primary fit (dashed blue).

5.2.2 Modeling the mode-mixing

The templates discussed above catch all the main features of the numerical waveform, except the mode-mixing generated by the negative-frequency QNMs. This effect can be already seen in the (2,2) mode, but becomes particularly relevant in the $m = 1$ modes, as shown for the (2,1) mode in Fig. 5.4. We will discuss this effect in more detail in Sec. 5.4.2, here we just mention that it can be simply included in the ringdown model doing the substitution

$$h^{\rm rng}_{\ell m}(\tau) \to h^{\rm rng}_{\ell m}(\tau)\left(1 + \hat{a}_{\ell m 1} e^{2i\omega_{\ell,1}\tau}\sigma(\tau;\tau^{\rm mm}_0)\right), \tag{5.2}$$

where $\hat{a}_{\ell m 1} = C^-_{\ell m 1}/C^+_{\ell m 1} \equiv \hat{A}_{\ell m 1} e^{i\theta_{\ell m 1}}$ and $\sigma(t;\tau^{\rm mm}_0) = 1/(1 + e^{-(\tau-\tau^{\rm mm}_0)})$ is a sigmoid that activates the mode-mixing correction. The $\hat{a}_{\ell m 1}$ coefficients can be extracted fitting the late ringdown frequency with a fundamental-QNM ansatz as outlined in Ref. [122]; in this work we will follow a more refined procedure that we will discuss in Sec. 5.4.2. Note that, even though $C^\pm_{\ell m 1}$ depend on the nature of the perturbation, the modulus of their ratio, $\hat{A}_{\ell m 1}$, does not seem to change with the eccentricity, as shown for example for the (2,2) mode in Fig. 5.3. The values of $\hat{A}_{\ell m 1}$ can be found in Table 5.3, while the value of $\tau^{\rm mm}_0$ is chosen in order to introduce the oscillations in the analytical waveform only when they are also present in the numerical wave. For all the eccentricities, we use $\tau^{\rm mm}_0 = 25$

for the (2,2) multipole, $\tau_0^{\rm mm} = 20$ for the $\ell = m$ higher modes, $\tau_0^{\rm mm} = 8$ for (2,1), (3,2), (4,3), (4,2) and $t_0 = 3$ for (3,1) and (4,1).

5.2.3 Global fits for the postpeak waveform

In Sec. 5.2.1 and Sec. 5.2.2 we have discussed a phenomenological model that can be used to faithfully describe the postpeak waveform. This model depends on different free parameters that are found fitting RWZ postpeak waveforms. However, in order to describe any eccentric case, we need to provide global fits of these parameters as functions of some system-characterizing quantity. While the eccentricity would be an intuitive choice[2], it is not a gauge invariant quantity and it is not defined through the whole evolution of the system. We thus use the quantity $b \equiv p_\varphi/\hat{E}$ evaluated at the peak of the orbital frequency (i.e. at the light-ring crossing) and shifted with the corresponding quasi-circular value,

$$\hat{b}_{\Omega_{\rm pk}} = b_{\Omega_{\rm pk}} - b^{\rm QC}_{\Omega_{\rm pk}}, \tag{5.3}$$

where $b^{\rm QC}_{\Omega_{\rm pk}} = 3.6693$. Note that this parameter is gauge invariant since it is a combination of energy and angular momentum, and it vanishes in the quasi-circular case. The latter feature is useful because we impose that the fits reduce to the exact values in the quasi-circular case.

We thus proceed to perform the global fits for each multipole. Note that in our global fits we only use the simulations in Table 5.1 with odd identification number (#) (i.e. the simulations with "round" initial eccentricity), so that the eccentric simulations with even identification number can be thought of as a test-set for the analytical model. We need to fit the free parameters of amplitude and phase templates, $\left\{c_2^A, c_3^A, c_2^\phi, c_3^\phi, c_4^\phi\right\}$, the quantities $\left\{A_{\rm peak}, \ddot{A}_{\rm peak}, \omega_{\rm peak}\right\}$ that are needed to compute the constrained parameters, and the phase θ_1 of the mode-mixing complex factor $\hat{a}_{\ell m 1}$ (the modulus does not depend on the eccentricity). The primary fits are reported in Appendix C.2, and in particular in Table C.1. The fits for the mode-mixing are instead reported in Table 5.4.

5.2.4 Completing the EOB waveform with NQC corrections

In Sec. 2.3.4 we have seen that the EOB waveform for the full evolution of the system is given by Eq. (2.51). The ringdown waveform $h^{\rm rng}_{\ell m}$ is obtained as described in the previous subsections, while the inspiral waveform $h^{\rm inspl}_{\ell m}$ that we consider is the one of Eq. (4.8). More precisely, for the quadrupolar waveform we will consider the 2PN noncircular hereditary term $\hat{h}^{\rm tail_{nc}}_{22}$ written in terms of $\dot{p}_{r_*}$, Eq. (4.50), and the instantaneous corrections $\hat{h}^{\rm inst_{nc}}_{22}$ introduced in Ref. [5] and discussed in Sec. 4.3. The 2PN noncircular corrections are switched off at the beginning of the plunge using a sigmoid function, $\sigma(t) = 1/[1+e^{-\alpha(t_{\rm plunge}-t)}]$ with $\alpha = 0.2$, both for the eccentric and quasi-circular cases. The relevance of these corrections in the quasi-circular inspiral will be discussed in Sec. 5.3. For the higher modes, we will not consider the 2PN noncircular corrections and we will only include the Newtonian noncircular correction given by the generic Newtonian prefactor.

The NQC correction $\hat{h}^{\rm NQC}_{\ell m}$ in Eq. (2.51), that is a bridge between $h^{\rm inspl}_{\ell m}$ and $h^{\rm rng}_{\ell m}$, is given by Eq. (2.53), where n_i are functions that are combinations of quantities negligible

[2]The eccentricity at the separatrix-crossing was used in the global fits performed in Ref. [1].

during the quasi-circular inspiral but relevant during the plunge. They are explicitly given by Eqs. (2.54) (see also discussion below those equations). The coefficients a_i and b_i that appear in Eq. (2.53) are determined at a certain time $t^{\rm NQC}_{\ell m}$. If we consider $t^{\rm NQC}_{\ell m} > t^{\rm peak}_{A_{\ell m}}$, then these coefficients are determined by solving the linear system (2.55). If we want to use $t^{\rm NQC}_{\ell m} < t^{\rm peak}_{A_{\ell m}}$, we have to consider a similar system of equations where on the rhs we have to consider quantities extracted from numerical data at $t^{\rm NQC}_{\ell m}$. Due to this reason, the choice $t^{\rm NQC}_{\ell m} > t^{\rm peak}_{A_{\ell m}}$ is preferable since it reduces the number of numerical-informed parameters in the model, as already mentioned in Sec. 2.3.4. However, as we will see in more detail later, choosing $t^{\rm NQC}_{\ell m} < t^{\rm peak}_{A_{\ell m}}$ works better for the higher modes. While the NQC correction is negligible during the quasi-circular inspiral by construction, they are not negligible in eccentric inspirals since p_{r_*} is not small. For this reason, we switch off the NQC corrections during the eccentric inspiral using a sigmoid,

$$\hat{h}^{\rm NQC}_{\ell m} \to \hat{h}^{\rm NQC}_{\ell m} \frac{1}{1+e^{-\alpha^s (t - t_{\dot{r}=0})}}. \tag{5.4}$$

Given the discussion in Sec. 5.1.1, it is natural to center the sigmoid in $t_{\dot{r}=0}$ so that the NQC corrections are switched on in a region where the motion is indeed quasi-circular. Due to this choice, the relevance of the precise value of α^s is not crucial; in this work we will use $\alpha^s = 0.2$. Finally, consider that to correctly evaluate the lhs of Eqs. (2.55), an interpolation on a refined time grid is needed, see Appendix A of Ref. [6] for more details.

5.2.5 Matching point

The match of the plunge and ringdown waveform is performed at $t^{\rm NQC}_{\ell m}$ if $t^{\rm NQC}_{\ell m} > t^{\rm peak}_{A_{\ell m}}$, while it is performed at $t^{\rm peak}_{A_{\ell m}}$ if $t^{\rm NQC}_{\ell m} \leq t^{\rm peak}_{A_{\ell m}}$. The former prescription will be used for the (2,2) mode, while the latter will be used for the higher modes. In any case, in order to know the locations of $t^{\rm peak}_{A_{\ell m}}$, we need to link them to dynamical quantities. In the `TEOBResumS` model [11, 231] and also in Ref. [1], the heuristic used to find the peak of the quadrupolar amplitude was

$$t^{\rm peak}_{A_{22}} = t^{\rm peak}_{\Omega_{\rm orb}} - \Delta t_{\rm NQC} - 2, \tag{5.5}$$

where $t^{\rm peak}_{\Omega_{\rm orb}}$ is the peak of the orbital frequency[3] and $\Delta t_{\rm NQC} = 1$ (see e.g. Eq. (3.15)). We keep $\Delta t_{\rm NQC}$ in the notation for continuity with previous works. The heuristic (5.5) gives satisfactory results in the quasi-circular case, since the exact value of $t^{\rm peak}_{A_{22}}$ extracted from the Zerilli waveform is $\Delta t^{\rm exact}_{\rm NQC} \simeq 0.559$. Most importantly, Eq. (5.5) is reliable also for quasi-circular binaries of comparable mass. However, when dealing with highly eccentric binaries, the approximation $\Delta t_{\rm NQC} = 1$ is no longer valid and we thus perform a global fit as discussed in Sec. 5.2.3, finding

$$t^{\rm peak}_{A_{22}} = t^{\rm peak}_{\Omega_{\rm orb}} - \frac{2.559 + 7.574\,\hat{b}_{\Omega_{\rm pk}} - 18.830\,\hat{b}^2_{\Omega_{\rm pk}}}{1 - 2.160\,\hat{b}_{\Omega_{\rm pk}}}. \tag{5.6}$$

The peak amplitude of the other multipoles is delayed with respect to the quadrupolar one as

$$t^{\rm peak}_{A_{\ell m}} = t^{\rm peak}_{A_{22}} + \Delta t_{\ell m}, \tag{5.7}$$

[3] Consider that for spinning binaries, $t^{\rm peak}_{\Omega_{\rm orb}}$ is the peak of the *pure* orbital frequency, that is computed without considering the spin-orbit terms.

Table 5.2: Time delays of the amplitude peaks $\Delta t_{\ell m}$ for the higher modes with respect to the peak of the (2,2) amplitude, see definition in Eq. (5.7). The global fitting template is $\Delta t_{\ell m} = \left(C^{\ell m}_{\rm QC} + C^{\ell m}_1 \hat{b}_{\Omega_{\rm pk}} + C^{\ell m}_2 \hat{b}^2_{\Omega_{\rm pk}}\right) / \left(1 + D^{\ell m}_1 \hat{b}_{\Omega_{\rm pk}}\right)$, where $C^{\ell m}_{\rm QC}$ is the quasi-circular value; see also discussion in Sec. 5.2.3.

(ℓ, m)	$C^{\ell m}_{\rm QC}$	$C^{\ell m}_1$	$C^{\ell m}_2$	$D^{\ell m}_1$
(2,1)	11.960	51.831	...	2.704
(3,3)	3.563	5.507	21.215	...
(3,2)	9.396	11.549	28.933	...
(3,1)	13.100	15.132	28.765	...
(4,4)	5.384	7.032	23.973	...
(4,3)	9.766	11.101	27.870	...
(4,2)	12.090	13.150	28.396	...
(4,1)	13.280	15.033	28.667	...
(5,5)	6.679	7.803	24.818	...

with $\Delta t_{\ell m} > 0$ for all the higher modes. The values of $\Delta t_{\ell m}$ the quasi-circular case, together with their global fits, are listed in Table 5.2. The fact that $\Delta t_{\ell m}$ increases with m at fixed ℓ can be understood heuristically considering that all the m-modes have to reach the same final QNM frequency $\omega_{\ell,1}$ (modulo mode-mixing), but the waveform frequency during the inspiral is given, at leading order, by $\omega^{\rm inspl}_{\ell m} = m\Omega$. Therefore, the modes with small m will need more time to reach the final frequency $\omega_{\ell,1}$.

We also point out that the mode-mixing becomes more relevant in low-m higher modes (see e.g. Sec. 5.4.2), so that the position of the amplitude peak for the higher modes can be contaminated by the mode-mixing. Once the location of the amplitude peak is known, we can proceed to match, mode by mode, the inspiral waveform to the ringdown model. From a computational point of view, the matching is performed on a time grid that is finer than the one used to solve the dynamics, see Appendix A of Ref. [6] for technical (and not really interesting) details.

5.3 Probing the effective-one-body analytical waveform

We now proceed to test the reliability of the numerical-informed EOB waveform discussed in Sec. 5.2. We start by discussing in detail the quasi-circular case, and we then move to eccentric orbits.

5.3.1 Quasi-circular case

We start by analyzing in detail the quasi-circular case, testing the different prescriptions for the implementation of the NQC correction, and discussing the accuracy of each waveform mode. Focusing first on the $\ell = m = 2$ mode, we have to discuss three aspects:

(i) the impact of the precise location of the amplitude peak on the EOB temporal axis, $t^{\rm peak}_{A_{22}}$, as described by Eq. (5.6);

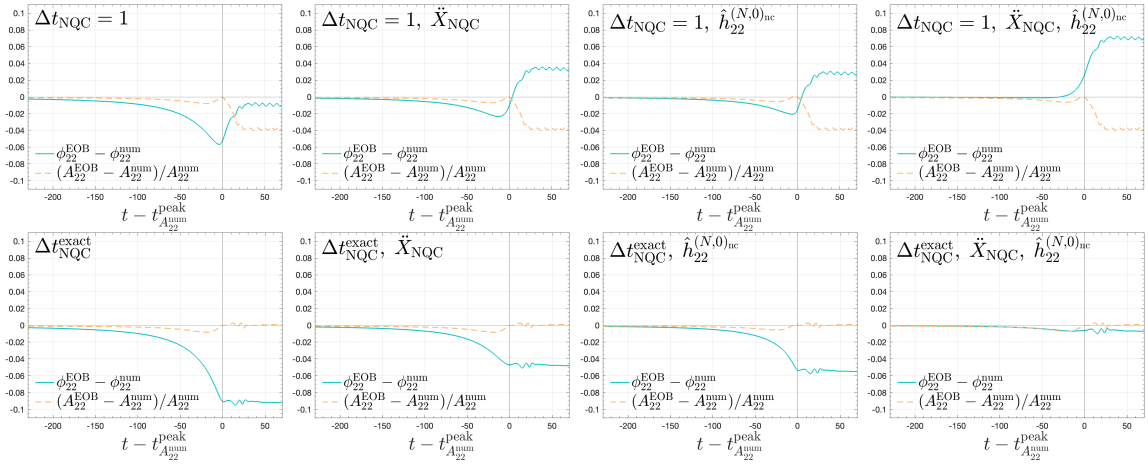

Figure 5.5: Analytical/numerical differences for the amplitude and the phase (in radians) of the quadrupolar waveform for the quasi-circular inspiral-plunge in Schwarzschild. We consider different inspiral-plunge and ringdown matching procedures. The differences are shown from the LSO crossing to $t^{\rm peak}_{A^{\rm num}_{22}}+70$. In the upper panels we consider the matching time according to Eq. (5.5), while in the lower panels we use Eq. (5.6). Then, from left to right, we progressively improve the model considering the second-time derivatives in the NQC base, $\ddot{A}_{22}$ and $\ddot{\omega}_{22}$, and then the Newtonian noncircular correction, $\hat{h}^{(N,0)_{\rm nc}}_{\ell m}$. The rightmost lower panel shows the differences for the state-of-the-art model.

(ii) the impact of the NQC correction determined imposing also continuity between the EOB and RWZ second-time derivatives $\ddot{X}_{\rm NQC}=\left\{\ddot{A}^{\rm NQC}_{22},\ddot{\omega}^{\rm NQC}_{22}\right\}$;

(iii) the impact due to the noncircular Newtonian prefactor of Eq. (2.35).

Note that here we are analyzing the plunge, therefore at this stage we do not consider the 2PN noncircular corrections discussed in Chapter 4. Figure 5.5 illustrates the analytical/numerical relative amplitude difference (dashed orange) and phase differences in radians (light blue) for all possible combinations. In the top row of the figure, the amplitude peak location is obtained according to Eq. (5.5), i.e. the prescription that is adopted, for simplicity, in the comparable mass case within the `TEOBResumS` model[4]. In the bottom row of the figure we consider instead its exact location according to Eq. (5.6). Then, moving from left to right, we add the second-time derivatives of amplitude and frequency in the NQC-corrections, the analytical generic Newtonian prefactor, and finally both effects together. In all the cases, the NQC corrections are obtained by solving the system given by Eqs. (2.55) using $t^{\rm NQC}_{22}=t^{\rm peak}_{A_{22}}+2$.

For the $\Delta t_{\rm NQC}=1$ case, we see that, as expected, the inclusion of both the improved NQC corrections and of the generic Newtonian prefactor brings a considerable reduction of the phase difference up to merger. Moreover, the phase difference now grows monotonically, to saturate at $\Delta\phi^{\rm EOBRWZ}_{22}\simeq 0.08$. As recently pointed out in Ref. [11], if such a behavior is reproduced for comparable mass waveforms, generally indicates that one will end up with excellent mismatches using actual detector power spectral density. This suggests that the use of $\hat{h}^{(\rm N,0)_{\rm nc}}_{22}$ and of $\ddot{X}_{\rm NQC}$ *also* for comparable mass binaries may result in a further reduction of the current EOB/NR disagreement (~ 0.2 rad) through merger and ringdown. By contrast, it is interesting to note that the amplitude difference during the ringdown is not negligible and remains substantially unchanged whatever choice is

[4]See however Ref. [56] for an early attempt to go beyond this simplifying choice.

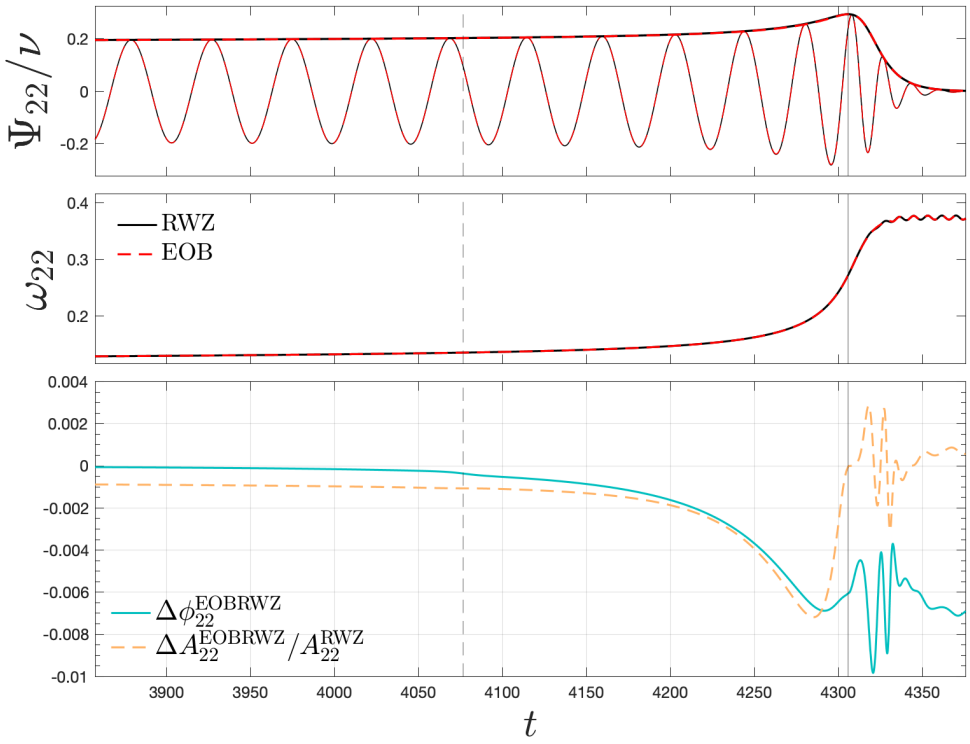

Figure 5.6: Quasi-circular case, $\ell = m = 2$ mode: RWZ waveform (black) compared to the complete EOB one (red, dashed). The vertical lines mark the LSO crossing and the peak of A_{22}. The bottom panel shows the relative amplitude difference (dashed orange) and the phase difference in radians (solid light blue). noncircular corrections to the waveform up to 2PN are included.

made. When $\Delta t_{\rm NQC}^{\rm exact}$ is used we are thus not surprised to find a consistent reduction of the amplitude difference during the ringdown (though evidently it remains unchanged up to merger). By contrast, the progressive inclusion of additional physical elements (i.e. $\hat{h}_{22}^{(\rm N,0)_{\rm nc}}$ and $\ddot{X}_{\rm NQC}$) brings phase differences below 0.01 rad through the full inspiral, merger and ringdown. The complete EOB/RWZ comparison for the final quadrupolar waveform, that incorporates also 2PN noncircular corrections, is shown in Fig. 5.6 and complements the rightmost bottom panel of Fig. 5.5 also showing the EOB frequency. One appreciates that the phase difference reaches the $\sim 4\cdot 10^{-4}$ rad at LSO crossing, and remains always below the 0.01 rad even at merger time. The relative amplitude difference is $\sim 1\times 10^{-3}$ at LSO crossing to reach at most $\sim 7\times 10^{-3}$ around merger time. Finally, we quantify the contribution of the 2PN noncircular corrections in Fig. 5.7, where we show the EOB/RWZ phase differences of the (2,2) mode for a quasi-circular inspiral starting from $r_0 = 9$. The waveforms have been computed (i) considering the complete waveform, as discussed above and shown in Fig. 5.6, (ii) considering only Newtonian noncircular corrections. As can be seen, the 2PN noncircular corrections improve the phase agreement through the whole inspiral of the binary, but they are not relevant for the amplitude.

Modeling higher modes correctly using NQC corrections determined using the standard paradigm implemented in `TEOBResumS` might be tricky. The main issue is that the amplitude peak of each mode is always delayed than the $(2,2)$ one [122], as reminded in Table 5.2. In the discussion above we have seen that the inclusion of the generic noncircular prefactor of Eq. (2.31) improves the EOB/RWZ agreement for the $(2,2)$ mode. We now proceed to evaluate the relevance of this term also for the other multipoles considering an illustrative higher mode, like the $(4,4)$. Figure 5.8 shows that the waveform with

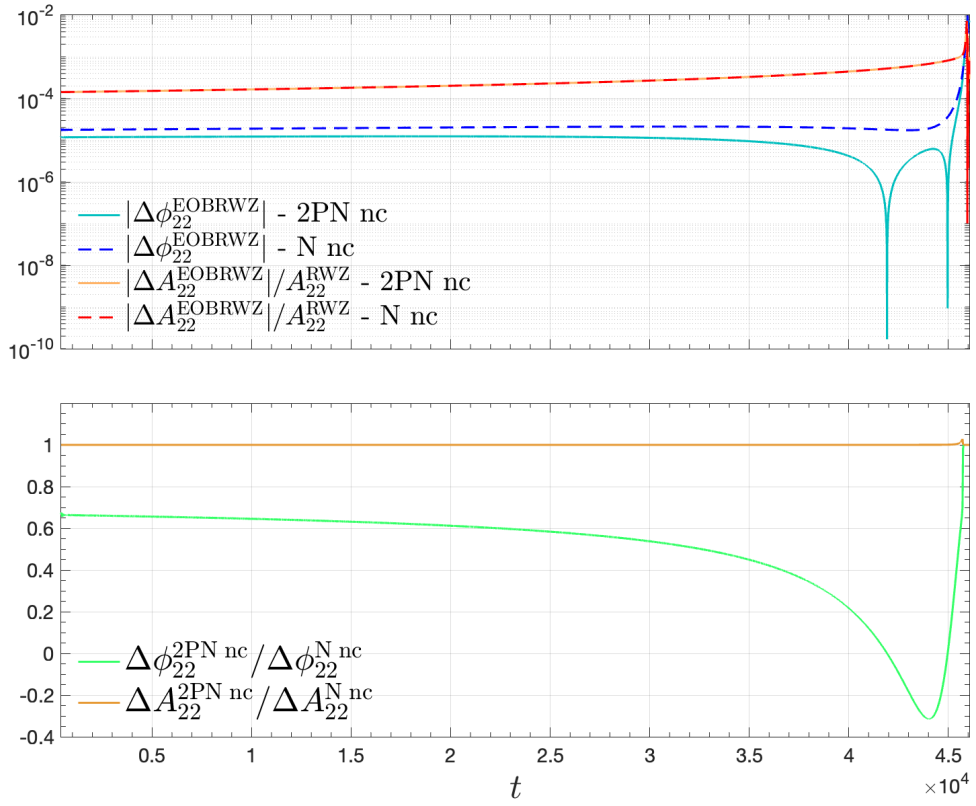

Figure 5.7: EOB/RWZ phase differences (radians) and relative amplitude differences for the (2,2) mode of a quasi-circular inspiral starting from $r_0 = 9$. In the upper panel we show the differences obtained with the waveform with noncircular corrections up to 2PN (solid, light blue for the phase and orange for the amplitude), and the ones obtained considering only the generic Newtonian prefactor (dashed, blue for the phase and red for the amplitude). In the bottom panel we show the ratios of these differences.

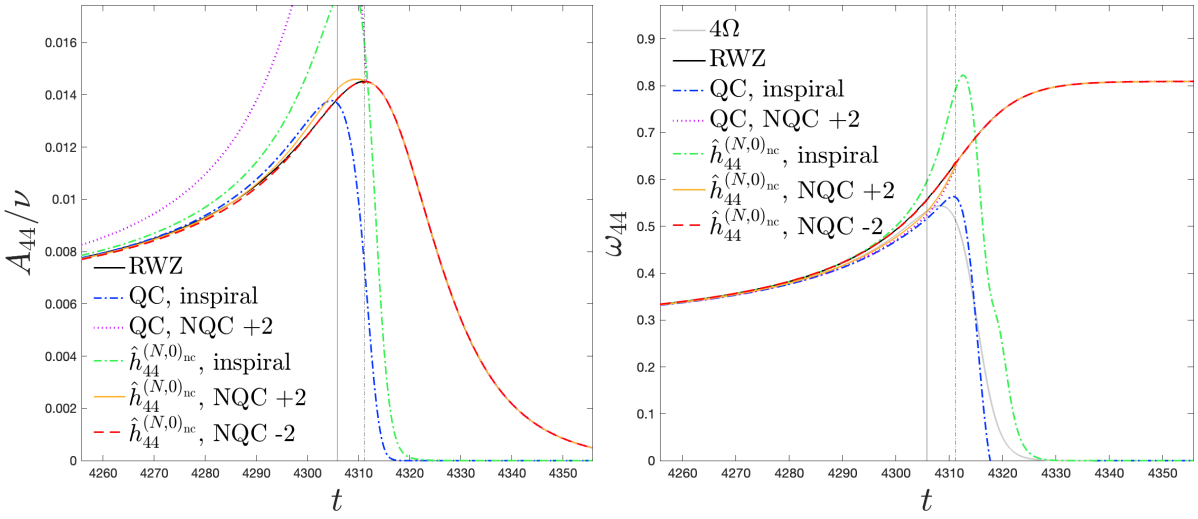

Figure 5.8: Quasi-circular case, mode $\ell = m = 4$: comparing various choices of analytical EOB waveform and different ways of determining the NQC corrections. Amplitude (left panel) and frequency (right panel) The best EOB/RWZ agreement is obtained by: (i) using the general, noncircular, Newtonian prefactor and (ii) when the NQC corrections are computed at $t_{44}^{\rm NQC} = t_{A_{44}}^{\rm peak} - 2$. We also show, as gray line, 4 times the orbital frequency. From left to right, the two vertical lines mark $t_{A_{22}}^{\rm peak}$ and $t_{A_{44}}^{\rm peak}$.

only the simple quasi-circular factor (dash-dotted blue line) underestimates the waveform amplitude toward merger. Starting from this, it is not possible for the waveform NQC correction to improve the waveform behavior and assure a reliable matching to the ringdown, especially for the amplitude, as shown by the NQC-corrected quasi-circular waveform (dotted purple) in Fig. 5.8. By contrast, one sees that when the noncircular Newtonian prefactor factor is used, the waveform visibly overestimates the waveform amplitude toward merger. This situation is preferable to the opposite because can be easily corrected by the NQC correction, as shown by the waveform obtained computing the NQC correction at $t_{44}^{\rm NQC} = t_{A_{44}}^{\rm peak} + 2$ (yellow solid line). We also find that, in order to considerably improve the NQC corrections, the system of Eqs. (2.55) has to be evaluated at $t_{\ell m}^{\rm NQC} < t_{A_{\ell m}}^{\rm peak}$. For all higher modes, we chose

$$t_{\ell m}^{\rm NQC} = t_{A_{\ell m}}^{\rm peak} - 2. \tag{5.8}$$

Therefore, to compute the rhs of Eqs. (2.55), we need to fit $A_{\ell m}^{\rm NQC}$, $\dot{A}_{\ell m}^{\rm NQC}$, $\ddot{A}_{\ell m}^{\rm NQC}$, $\omega_{\ell m}^{\rm NQC}$, $\dot{\omega}_{\ell m}^{\rm NQC}$, and $\ddot{\omega}_{\ell m}^{\rm NQC}$ from RWZ data. The global fits are discussed in Appendix C.2 and reported in Table C.2. The (4,4) multipole with the generic Newtonian prefactor and the NQC evaluated according to Eq. (5.8) is shown with a red dashed line in Fig. 5.8. As can be seen, both the amplitude and the frequency improves near the matching time with respect to the waveforms with NQC computed at $t_{44}^{\rm NQC} = t_{A_{44}}^{\rm peak} + 2$.

For $\ell = m$ modes, we use the same prescriptions of the (2,2) mode, except for the fact that the NQC corrections are computed before the peak amplitude, according to Eq. (5.8). The results for the (3,3), (4,4), and (5,5) modes are shown in the top row of Fig. 5.9, where we use the color black for the numerical waveform and frequency and red dashed lines for the complete EOB waveform. The absolute value of phase difference is always below 0.07, 0.035 and 0.05 radians for the (3,3), (4,4), and (5,5) modes, respectively. The relative amplitude difference, instead, is around at most of the 1% before the matching point for all three cases. However, the amplitude difference in the late ringdown is around 10^{-3} for the (3,3) and (4,4) modes and even smaller ($8 \cdot 10^{-4}$) for the (5,5) mode.

The $m < \ell$ modes are shown in the middle and bottom rows of Fig. 5.9. In this case we do not consider the second-time derivative of the frequency in the NQC corrections. As for the higher modes with $\ell = m$, the NQC are computed at $t_{\ell m}^{\rm NQC} = t_{A_{\ell m}}^{\rm peak} - 2$. However, for the $m < \ell$ we also apply a downsampling and spline procedure in the interval $t \in [t_{\ell m}^{\rm NQC}, t_{A_{\ell m}}^{\rm peak}]$ to improve the continuity of the waveform. Indeed, since the NQC corrections are determined at $t_{\ell m}^{\rm NQC}$, the waveform could be discontinuous at $t_{A_{\ell m}}^{\rm peak}$, where the NQC-corrected plunge waveform is matched to the ringdown. The downsampling and subsequent spline-patching solves this issue. While these higher modes are less accurate than the $\ell = m$ ones, the phase agreement is still good and generally below the 0.2 rad, except the (4,2) and (4,1) modes that are more dephased. The degradation of the accuracy is strictly linked to the higher delay of the matching point (i.e. $t_{A_{\ell m}}^{\rm peak}$); see Table 5.2. However, these modes are not as relevant as the others in the complete strain, that can be computed using Eq. (1.39). In the first panel of Fig. 5.12 we show the strain for the observational direction $(\Theta, \Phi) = (\pi/4, 0)$ computed considering all the modes shown so far, both in the numerical and analytical strain. During the inspiral, the relative amplitude difference reaches at most the $2 \cdot 10^{-3}$, while the absolute value of the phase difference never exceeds the $2 \cdot 10^{-3}$ radians. The differences oscillate more in the ringdown; the amplitude difference reaches at most 8% in the early ringdown, while the phase difference reaches at most 0.06 radians. Note however that, on average, during the ringdown both the amplitude and the phase difference are much smaller.

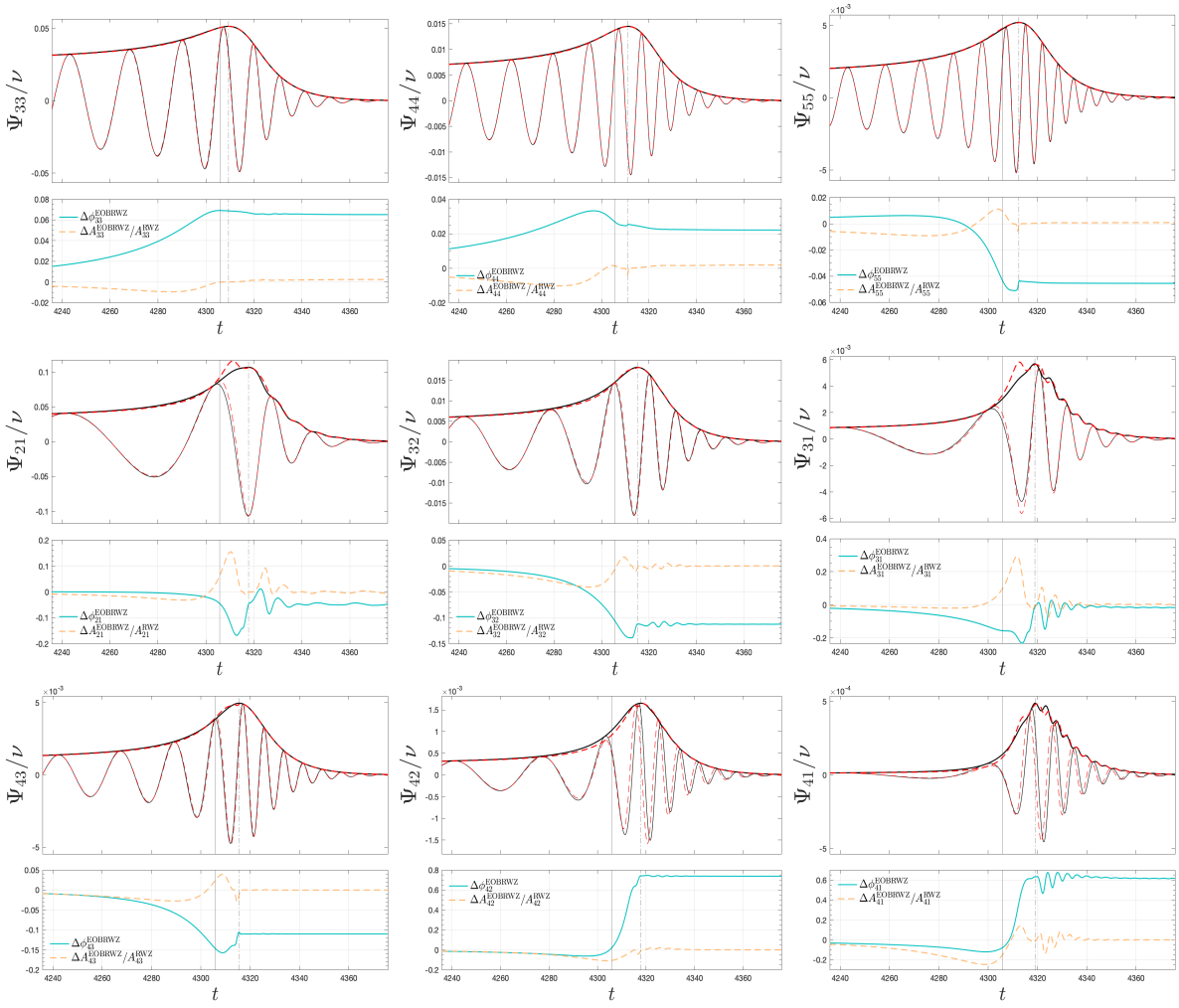

Figure 5.9: Quasi-circular configuration, higher modes, EOB/RWZ comparisons. The vertical solid black lines mark $t^{\rm peak}_{A_{22}}$, while the dash-dotted ones mark $t^{\rm peak}_{A_{\ell m}}$. Bottom panels: relative amplitude difference (orange, dashed) and phase difference (light blue). For each mode, the NQC corrections are determined according to the best prescription selected in Fig. 5.8.

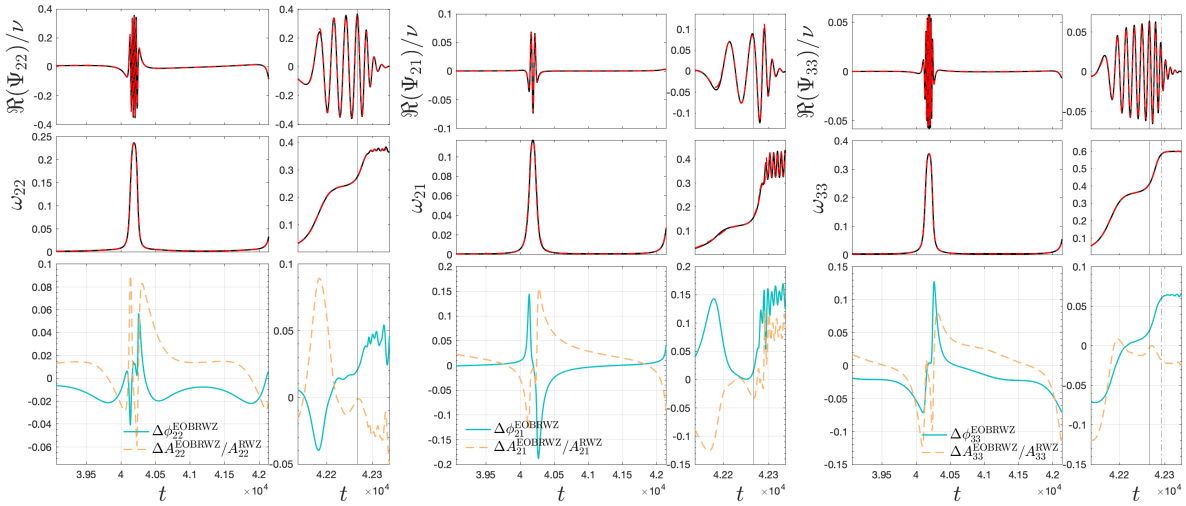

Figure 5.10: Analytical/numerical comparisons for the (2,2), (2,1), and (3,3) multipoles for the configuration with initial eccentricity $e_0 = 0.95$. We show the real part and the frequency of the RWZ waveform (black) and the complete EOB waveform (red, dashed). In the bottom panels we show the relative amplitude difference (orange dashed) and the phase difference in radians (light blue). The vertical solid lines mark the peak of A_{22}, while the dash-dotted ones mark $t^{\rm peak}_{A_{\ell m}}$.

5.3.2 Eccentric case

Let us move now to discussing the eccentric case. The same procedures considered optimal in the quasi-circular case are retained also in the presence of eccentricity to provide comparisons with the eccentric configurations listed in Table 5.1. As an explicit example that efficiently summarizes the performance of the model all over the parameter space, Fig. 5.10 shows the EOB/RWZ performance for configuration #20 of Table 5.1, that corresponds to initial eccentricity $e_0 = 0.95$. Note that this configuration is not used in the global fits, as discussed in Sec. 5.2.3. The figure includes modes $(2, 2)$, $(2, 1)$, and $(3, 3)$. The performance of the model all over the RWZ-covered points of the parameter space is assessed in Fig. 5.11, where we show the $(2, 2)$, $(2, 1)$, $(3, 3)$, and $(4, 4)$ multipoles. We report both relative amplitude differences and phase differences (in radians). Note that three specific configurations are highlighted in color, to point out that the performance of the model degrades (slightly) as eccentricity is increased.

The simplest route to have a handle on the accuracy of all multipoles is simply to compare the strain for EOB and RWZ. This is done in Fig. 5.12 for the quasi-circular case, for $e_0 = 0.55$ and $e_0 = 0.95$. It is interesting to note that, despite the EOB performance during the (eccentric) inspiral degrades with eccentricity, as expected, due to the lack of high-order corrections (see Refs. [3, 5]), the behavior during merger and ringdown is practically comparable among the three cases.

5.3.3 Improved description of ringdown for $m \neq \ell$ modes

So far, we have seen that the EOB waveform model gives more than satisfactory results also for the higher modes. However, if one carefully inspects the $m = 1$ EOB modes in the quasi-circular case (see Fig. 5.9), one sees the ubiquitous presence of a bump before the actual amplitude peak. Interestingly, this feature occurs in all modes and it is related to the NQC amplitude correction. In general, this is also true for other modes with

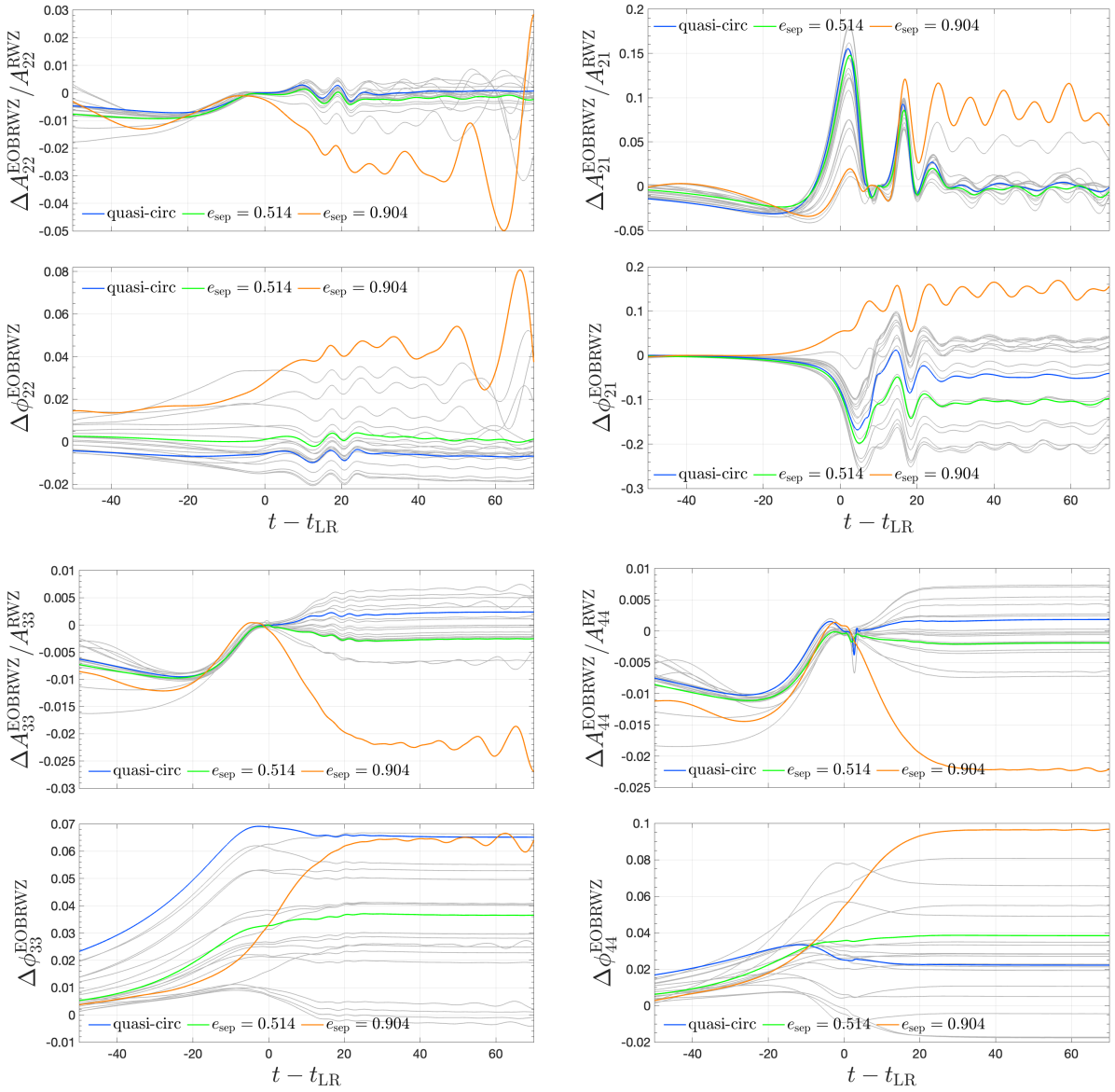

Figure 5.11: Analytical/numerical relative difference for the amplitude (upper panels) and phase difference (bottom panels) for the plunge-ringdown of all the configurations considered in this work. Modes (2,2), (2,1), (3,3), and (4,4). We highlight the quasi-circular configuration (blue) and the ones with $e_0 = (0.55, 0.95)$ (green and orange, respectively).

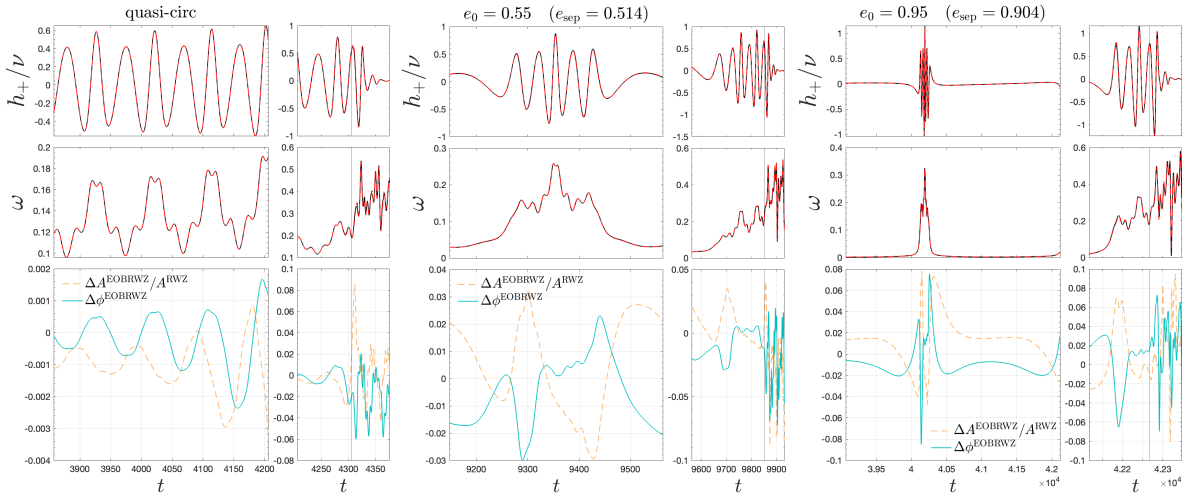

Figure 5.12: EOB (red dashed) versus RWZ (black, solid) strain comparison for $e_0 = (0, 0.55, 0.95)$. The direction is $(\Theta, \Phi) = (\pi/4, 0)$ and all modes with $m > 0$ are summed up to $\ell = 4$, plus the (5,5) one. Bottom panels: relative amplitude difference and phase difference (in radians). The vertical lines mark the peak of the quadrupolar amplitude.

$m \neq \ell$, though the effect is less visible. To overcome this difficulty, we decided to explore a different way to model the ringdown for higher modes. The procedure is substantially the same used in the EOB models of the `SEOBNR`-family, in particular `SEOBNRv4PHM` [58, 141] and `SEOBNRv5PHM` [60, 144], although the fitting template is different from the one used there. This approach is crucial to obtain very reliable waveforms when $t^{\rm peak}_{A_{\ell m}}$ is far from $t^{\rm peak}_{A_{22}}$, i.e. situations where the NQC corrections cannot guarantee a reliable match of the plunge waveform to the merger ringdown one modeled after $t^{\rm peak}_{A_{\ell m}}$. The main idea is to have the RWZ-informed part of the waveform starting directly from $t^{\rm peak}_{A_{22}}$ (and not from $t^{\rm peak}_{A_{\ell m}}$) for all modes with $\ell \neq m$. To do so, we consider the QNM-rescaled waveform similar to the one of Eq. (2.52), but where the time is shifted using $t^{\rm peak}_{A_{22}}$ for each (ℓ, m) mode. It thus reads

$$\bar{h}_{\ell m}(\bar{\tau}) = e^{\sigma^+_{\ell m 1}\bar{\tau} + i\phi^0_{\ell m}} h^{\rm rng}_{\ell m}(\bar{\tau}) \ , \tag{5.9}$$

where $\bar{\tau} \equiv t - t^{\rm peak}_{A_{22}}$ and $\phi^0_{\ell m}$ is the phase of the (ℓ, m) multipole at $t^{\rm peak}_{A_{22}}$. This rescaled waveform is then written as $\bar{h}^{\rm mod}_{\ell m}(\bar{\tau}) = A_{\bar{h}} e^{i\phi_{\bar{h}}}$, where the templates for $A_{\bar{h}}$ and $\phi_{\bar{h}}$ are given in Eqs. (3.9a) and (3.9b). We impose continuity conditions constraining c^A_1, c^A_2, c^A_4 and c^ϕ_1:

$$c^A_1 = \frac{e^{-c^A_3}\left(e^{2c^A_3} - 1\right) c^A_5 (A_{t^{\rm peak}_{A_{22}}})^{c^A_5} (\alpha_1 A_{t^{\rm peak}_{A_{22}}} + \dot{A}_{t^{\rm peak}_{A_{22}}})^2}{\alpha_1^2 (A_{t^{\rm peak}_{A_{22}}})^2 c^A_5 + A_{t^{\rm peak}_{A_{22}}} (2\alpha_1 c^A_5 \dot{A}_{t^{\rm peak}_{A_{22}}} + \ddot{A}_{t^{\rm peak}_{A_{22}}}) + (c^A_5 - 1)(\dot{A}_{t^{\rm peak}_{A_{22}}})^2}, \tag{5.10}$$

$$c^A_2 = \frac{c^A_5}{c^A_1} e^{-c^A_3} \left(e^{c^A_3} + 1\right)^2 \left(A_{t^{\rm peak}_{A_{22}}}\right)^{c^A_5 - 1} \left[\alpha_1 A_{t^{\rm peak}_{A_{22}}} + \dot{A}_{t^{\rm peak}_{A_{22}}}\right], \tag{5.11}$$

$$c^A_4 = (A_{t^{\rm peak}_{A_{22}}})^{c^A_5} - \frac{c^A_1}{e^{c^A_3} + 1}, \tag{5.12}$$

$$c^\phi_1 = \frac{1 + c^\phi_3 + c^\phi_4}{c^\phi_2 (c^\phi_3 + 2c^\phi_4)} \left(\omega_1 - \omega_{t^{\rm peak}_{A_{22}}}\right), \tag{5.13}$$

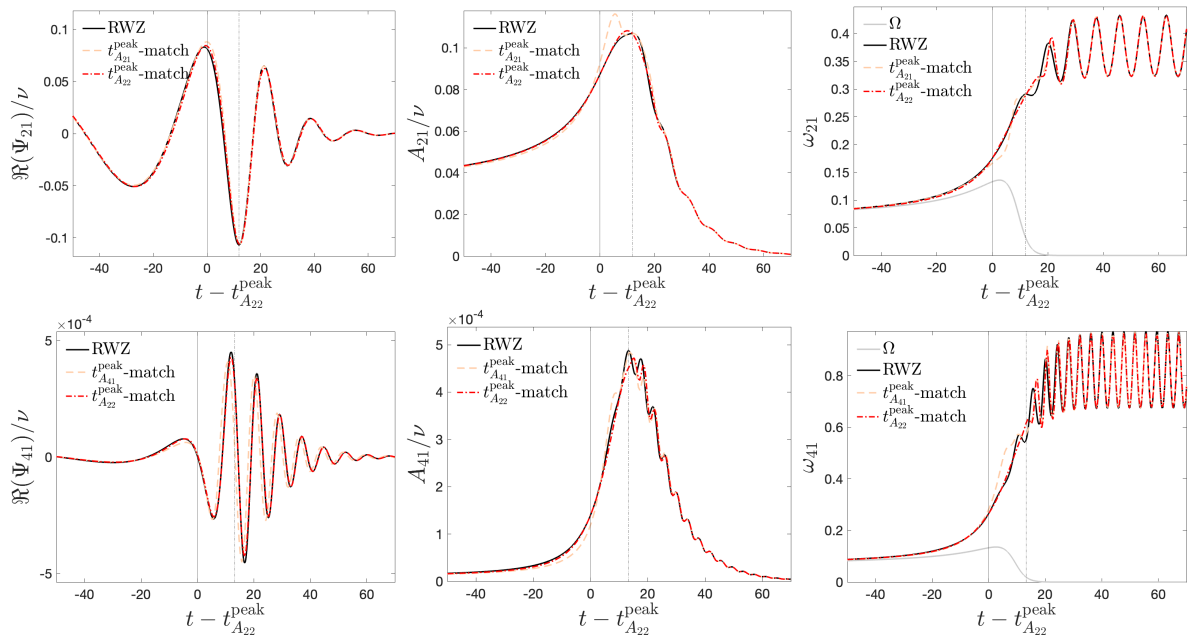

Figure 5.13: Nonspinning case. The new ringdown (red dashed) contrasted with the standard one discussed above (orange, dashed) for the $(2,1)$ and $(4,1)$ modes. The RWZ ringdown waveform is fitted from $t^{\rm peak}_{A_{22}}$ (solid vertical lines) rather than from $t^{\rm peak}_{A_{\ell m}}$ (dash-dotted vertical lines). This ensures a more accurate waveform description around $t^{\rm peak}_{A_{\ell m}}$.

where $A_{t^{\rm peak}_{A_{22}}}$, $\dot{A}_{t^{\rm peak}_{A_{22}}}$, $\ddot{A}_{t^{\rm peak}_{A_{22}}}$ and $\omega_{t^{\rm peak}_{A_{22}}}$ are, respectively, the amplitude of $h_{\ell m}$, its first and second-time derivative and the frequency evaluated at $t^{\rm peak}_{A_{22}}$; $\alpha_1 + i\omega_1$ is the ℓ-fundamental QNM frequency. The coefficients $\left\{c^A_3, c^A_5, c^\phi_2, c^\phi_3, c^\phi_4\right\}$ are determined performing the primary fits of $A_{\bar{h}}$ and $\phi_{\bar{h}}$ starting from $t^{\rm peak}_{A_{22}}$. Finally, this fitted waveform is used to determine the NQC corrections at $t^{\rm peak}_{A_{22}}$ and then is matched to the inspiral wave, always at $t^{\rm peak}_{A_{22}}$. Concerning the structure of the NQC correction to amplitude and phase, there is an additional subtlety. We realized that the standard NQC basis we used so far is not efficient when the NQC corrections are determined at $t^{\rm peak}_{A_{22}}$ for $m \neq \ell$, and it is thus better to resort to the NQC basis used by `SEOBNRv5PHM` that reads

$$n_1 = \frac{p^2_{r_*}}{(r\Omega)^2}, \tag{5.14}$$

$$n_2 = \frac{n_1}{r}\ , \tag{5.15}$$

$$n_3 = n_1 r^{-3/2}, \tag{5.16}$$

$$n_4 = \frac{p_{r_*}}{r\Omega}, \tag{5.17}$$

$$n_5 = n_4 p^2_{r_*}. \tag{5.18}$$

The real part, amplitude, and frequency of the final result for the $(2,1)$ and $(4,1)$ modes are shown in Fig. 5.13. It is remarkable how the different NQC approach can visibly improve the EOB/RWZ agreement. The only visible remaining differences between the two curves (mostly around the waveform peak) are related to the fact that the mode mixing only includes the fundamental mode and not the overtones.

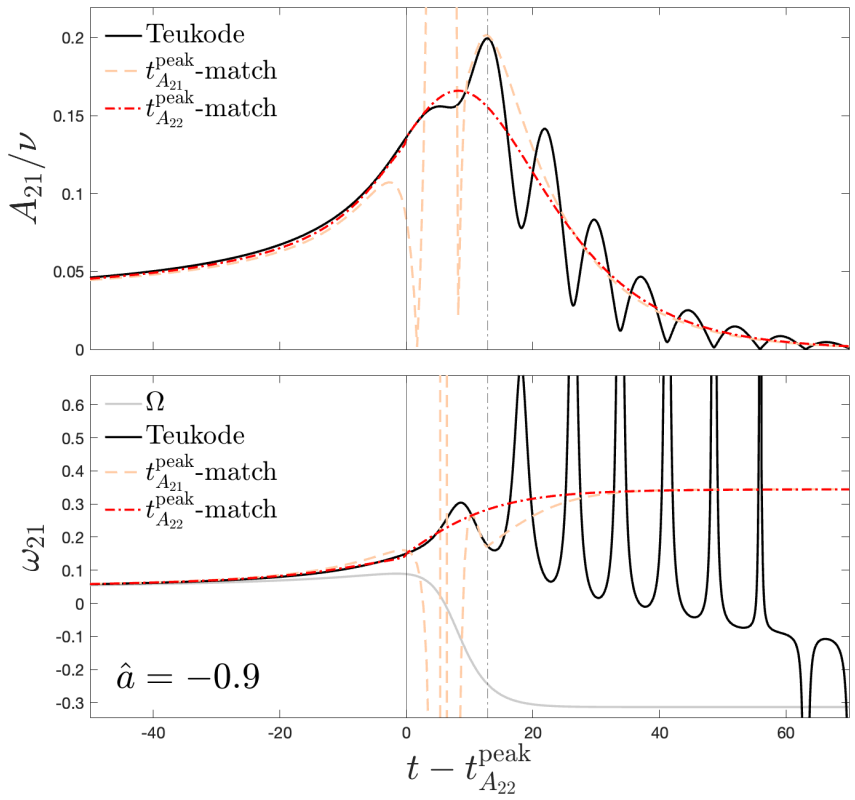

Figure 5.14: Spinning case with Kerr parameter $\hat{a} = -0.9$. The NQC and ringdown determined from $t^{\rm peak}_{A_{22}}$ instead of $t^{\rm peak}_{A_{\ell m}}$ allow for an excellent EOB/Teukode agreement. Note that the mode mixing in this case is not implemented in the EOB waveform.

Although the improvement discussed in the nonspinning case may be considered relatively marginal, it becomes essential when the central black hole is spinning and the spin is large and anti-aligned with the orbital angular momentum. In this case, the orbital frequency has a zero and thus the NQC basis becomes meaningless. This is clarified in Fig. 5.14, which refers to the $(2,1)$ mode for a particle inspiralling and plunging on a Kerr black hole with dimensionless spin $\hat{a} = -0.9$, where the numerical waveform (black) has been obtained with the time-domain code `Teukode` [126]. As the orbital frequency (gray online) passes through zero, the NQC corrected waveform determined using the standard approach oscillates unphysically. By contrast, the NQC correction determined at $t^{\rm peak}_{A_{22}}$, using the basis of Eqs. (5.14)-(5.18) allows one to smoothly and reliably connect the inspiral waveform to the ringdown one. In this preliminary study, we are evidently not considering the mode mixing during the Kerr ringdown [118], so the EOB frequency and amplitude do not present any modulation.

This method has been applied to the (2,1) mode in the latest version of `TEOBResumS` [11], showing that it helps to improve the accuracy of the EOB waveform in the spinning case. This is particularly evident in Fig. 28 and 29 of Ref. [11].

5.4 Phenomenology of quasi-normal-modes excitation

In the previous section, we have provided an accurate and complete EOB waveform where the ringdown model was based on a phenomenological description. In doing so, we assumed that the fundamental QNM was excited, but we did not attempt any qualitative (nor quantitative) investigation to understand the origin of this excitation. In this section we attempt to do this, still in a somehow phenomenological and heuristic way. Our main aim is to correlate the QNMs excitation with the behavior of the source of the RWZ equations that is driven by the dynamics. The material presented here is inspired by and extends the (qualitative) discussion of Sec. IIIB of Ref. [232] (see also Fig. 4 therein).

5.4.1 The RWZ source term during ringdown

We start by analyzing the source terms of the RWZ equations, Eq. (1.57). Their functional form is [55]

$$S^{(\rm o/e)}_{\ell m} = \bar{G}^{(\rm o/e)}_{\ell m}(\tilde{r},t)\delta(\tilde{r}_* - r_*(t)) + \bar{F}^{(\rm o/e)}_{\ell m}(\tilde{r},t)\partial_{\tilde{r}_*}\delta(\tilde{r}_* - r_*(t)), \tag{5.19}$$

where the tilde denotes the field tortoise coordinate, while $r_*(t)$ is the tortoise coordinate of the particle. To understand the relevance of the source terms during the ringdown, we evaluate it on the particle dynamics. More precisely, we neglect the term proportional to $\partial_{\tilde{r}_*}\delta(\tilde{r}_* - r_*(t))$ in Eq. (5.19) and just evaluate $\bar{G}^{(\rm o/e)}_{\ell m}$. This yields the expressions

$$\begin{aligned} F^{(\rm e)}_{\ell m}(t) =& \frac{16\pi\mu\, Y^*_{\ell m}(\Theta,\Phi)}{r\,\hat{H}\,\lambda[r(\lambda-2)+6]}\Bigg\{ 2im\,A\,p_{r_*}p_\varphi - A\Bigg[3\left(1+\frac{4\hat{H}^2 r}{r(\lambda-2)+6}\right) \\ & - \frac{r\,\lambda}{2} + \frac{p^2_\varphi}{r^2(\lambda-2)}\left(r(\lambda-2)(m^2-\lambda-1)+2(3m^2-\lambda-5)\right) \\ & + \frac{2}{r^2}\left(p^2_\varphi + r^2\right)\Bigg]\Bigg\}, \end{aligned} \tag{5.20a}$$

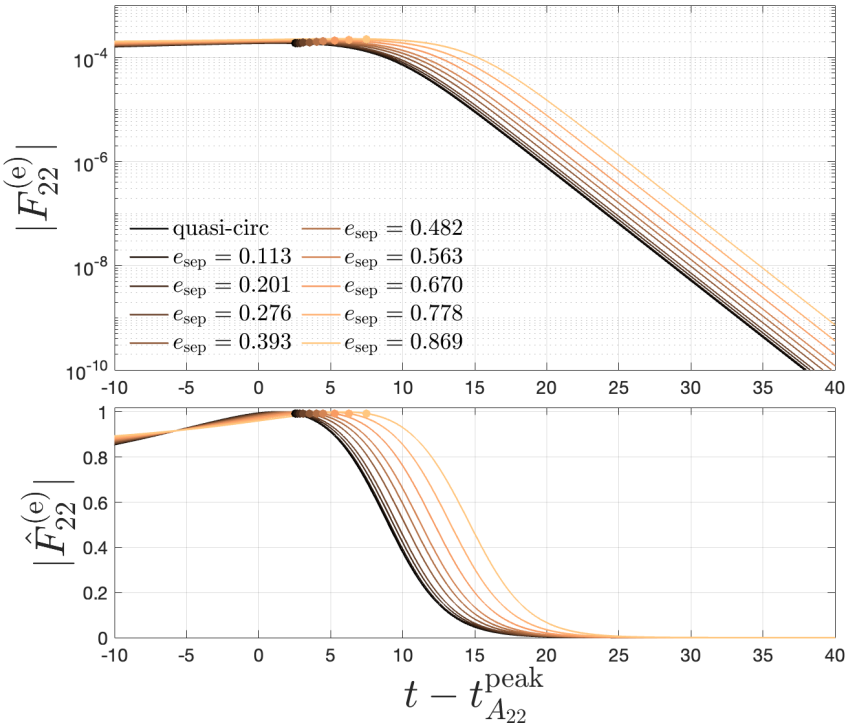

Figure 5.15: Upper panel: Zerilli source term evaluated along dynamics with different eccentricities for the (2,2) mode. Logarithmic vertical scale. Bottom panel: plot of $\hat{F}_{22}^{(e)} = |F_{22}^{(e)}|/\max(|F_{22}^{(e)}|)$. The retarded time is shifted using the peak time of the quadrupolar amplitude, $t^{peak}_{A_{22}}$. In both panels, the dots mark the light-ring crossing, t_{LR}.

$$F_{\ell m}^{(o)}(t) = \frac{16\pi\mu\,\partial_\Theta Y^*_{\ell m}(\Theta,\Phi)}{r\,\lambda(\lambda-2)}\left[\frac{d}{dt}\left(\frac{p_{r_*}p_\varphi}{\hat{H}}\right) - 2\frac{p_\varphi\,A}{r} - im\frac{A\,p_{r_*}p_\varphi^2}{r^2\hat{H}^2}\right], \tag{5.20b}$$

where $\lambda \equiv \ell(\ell+1)$. After having set $\Theta = \pi/2$, we show $|F_{\ell m}^{(o/e)}(t)|$ for the (2,2) mode in Fig. 5.15. Interestingly, $|F_{22}^{(e)}(t)|$ reaches its maximum after the peak of A_{22} and remains quite relevant also later on. For example, at $t = t^{peak}_{A_{22}} + 10$ we have $\hat{F}_{22}^{(e)} \equiv |F_{22}^{(e)}|/\max(|F_{22}^{(e)}|) \simeq 0.38$, and $\hat{F}_{22}^{(e)} < 10^{-2}$ only from $t = t^{peak}_{A_{22}} + 18.2$. For the odd modes we have that the maximum of the source is delayed with respect to the even ones. Since the source term is quite relevant during the ringdown, we do not expect *a priori* that a pure QNMs description (i.e. part of the solution of the homogeneous RWZ equations) can be used for the whole postpeak waveform. However, from a sufficient late time $t > t^{peak}_{A_{\ell m}}$, the (ℓ, m)-mode can be fully described in terms of QNMs using the ansatz of Eq. (1.63) since the source term becomes negligible.

5.4.2 Iterative time-domain fit of the postpeak frequency

We thus proceed to fit the late ringdown waveform assuming that is given by a linear superposition of QNMs with constant coefficients, see Eq. (1.63), using $\tau = t - t^{peak}_{A_{\ell m}}$. The

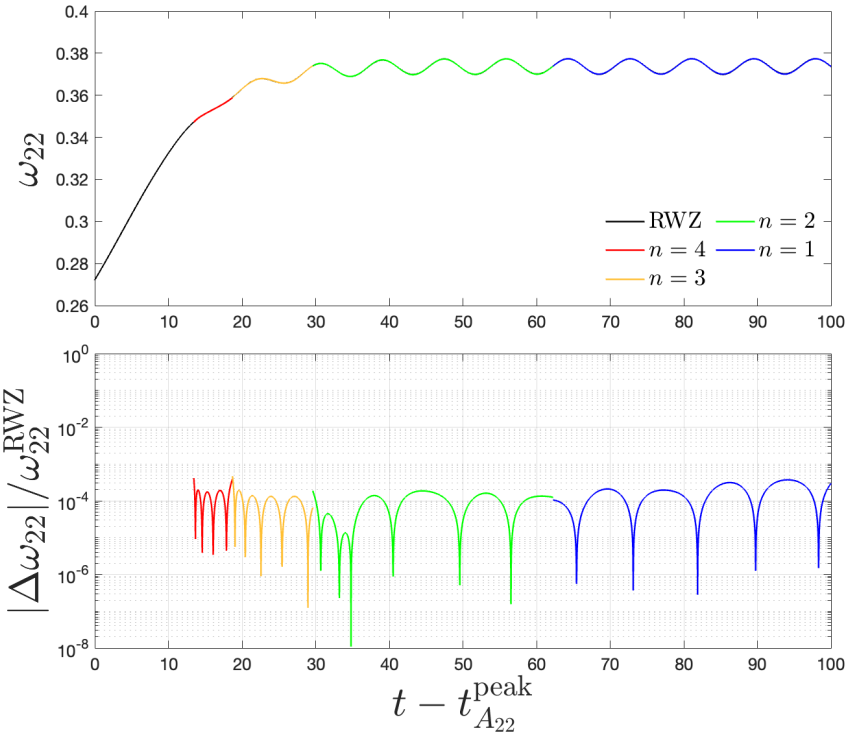

Figure 5.16: Iterative QNM-fit of the frequency considering the first 4 QNMs. In the upper panel we show the RWZ frequency (black) and the results obtained with the fits. Each color represents an iteration (and thus a QNM) of the fit. In the bottom panel we show the relative difference between the fit and the corresponding n-fit. See Sec. 5.4.2 for more details on the fitting procedure.

total QNM frequency of each multipole is obtained as

$$\omega_{\ell m}^{(\rm o/e)} = -\Im\left(\frac{\dot{\Psi}_{\ell m}^{(\rm o/e)}}{\Psi_{\ell m}^{(\rm o/e)}}\right) = -\Im\left[\frac{\sum_{n=1}^{\infty}\bar{b}_{\ell mn}\frac{\sigma^+_{\ell n}}{\sigma^+_{\ell 1}}e^{(\sigma^+_{\ell 1}-\sigma^+_{\ell n})\tau}\left(1+\hat{a}_{\ell mn}\frac{\sigma^-_{\ell n}}{\sigma^+_{\ell n}}e^{2i\omega_{\ell n}\tau}\right)}{\sum_{n=1}^{\infty}\bar{b}_{\ell mn}e^{(\sigma^+_{\ell 1}-\sigma^+_{\ell n})\tau}\left(1+\hat{a}_{\ell mn}e^{2i\omega_{\ell n}\tau}\right)}\right], \tag{5.21}$$

where $\hat{a}_{\ell mn} = C^-_{\ell mn}/C^+_{\ell mn}$ and $\bar{b}_{\ell mn} = C^+_{\ell mn}/C^+_{\ell m1}$. Since these are complex quantities, we define $\hat{a}_{\ell mn} \equiv \hat{A}_{\ell mn}e^{i\hat{\theta}_{\ell mn}}$ and $\bar{b}_{\ell mn} \equiv \bar{B}_{\ell mn}e^{i\bar{\phi}_{\ell mn}}$. Recalling the hierarchy of the inverse damping times $\alpha_{\ell n}$, the contributions in the frequency of the $n \geq 1$ overtones are exponentially damped with exponents $\alpha^+_{\ell 1} - \alpha^+_{\ell n}$. However, the contribution of the isolated fundamental frequencies is never damped and reads

$$\omega_{\ell m1}^{(\rm o/e)} = \frac{(1-\hat{A}^2_{\ell m1})\omega_{\ell 1}}{1+\ \hat{A}^2_{\ell m1}+2\hat{A}^2_{\ell m1}\cos(2\omega_{\ell 1}\tau+\hat{\theta}_{\ell m1})}. \tag{5.22}$$

The coefficients $\hat{A}_{\ell m1}$ and $\theta_{\ell m1}$ were already extracted from the late ringdown frequency in previous works [118, 122]. Here we extend this procedure to earlier times using Eq. (5.21).

Since the overtones have higher damping coefficients, we proceed to iteratively fit the late ringdown frequency on different time intervals considering only the relevant QNMs. To establish where a certain n mode becomes negligible, we set a small threshold, typically $\epsilon = 10^{-5}$, and we say that the nth-mode can be neglected if the condition $e^{(\alpha^+_{\ell 1}-\alpha^+_{\ell n})\tau} < \epsilon$ is satisfied. Applying this method to the (2,2) mode we can find $\left\{\hat{A}_{22n}, \hat{\theta}_{22n}, \bar{B}_{22n}, \bar{\phi}_{22n}\right\}$

Table 5.3: Coefficients $\hat{A}_{\ell m1} = |\hat{a}_{\ell m1}|$ describing the beating between positive and negative frequencies fundamental QNMs for all multipoles up to $\ell = 6$. See Table 5.4 for the eccentric fits of the $\hat{a}_{\ell m1}$ phase.

$\hat{A}_{\ell m1}$	$m=1$ $[\times 10^{-2}]$	$m=2$ $[\times 10^{-3}]$	$m=3$ $[\times 10^{-4}]$	$m=4$ $[\times 10^{-5}]$	$m=5$ $[\times 10^{-6}]$	$m=6$ $[\times 10^{-7}]$
$\ell=2$	7.30	4.89				
$\ell=3$	9.34	7.96	5.53			
$\ell=4$	9.14	9.11	8.90	6.28		
$\ell=5$	9.41	8.97	9.27	9.96	7.02	
$\ell=6$	9.46	9.12	9.11	9.67	11.15	8.33

Table 5.4: Global fits for the beating coefficients $\hat{a}_{\ell m1} = \hat{A}_{\ell m1} e^{i\theta_{\ell m1}}$. The template used for the phase is $\theta_{\ell m1} = \left(C^{\theta}_{\rm QC} + C^{\theta}_1 \hat{b}_{\Omega_{\rm pk}} + C^{\theta}_2 \hat{b}^2_{\Omega_{\rm pk}}\right) / \left(1 + D^{\theta}_1 \hat{b}_{\Omega_{\rm pk}}\right)$, while the modulus does not depend on the nature of the perturbation.

(ℓ, m)	$\hat{A}_{\ell m1}$	$C^{\theta}_{\rm QC}$	C^{θ}_1	C^{θ}_2	D^{θ}_1
(2,2)	$4.89 \cdot 10^{-3}$	5.369	−9.444	−37.992	...
(2,1)	$7.30 \cdot 10^{-2}$	2.893	−6.074	−15.134	−2.105
(3,3)	$5.53 \cdot 10^{-4}$	2.636	−11.635	−9.555	...
(3,2)	$7.96 \cdot 10^{-3}$	4.649	−3.890	−0.1176	...
(3,1)	$9.34 \cdot 10^{-2}$	3.810	0.3296	−0.03943	...
(4,4)	$6.28 \cdot 10^{-5}$	6.503	−13.096	−8.815	...
(4,3)	$8.90 \cdot 10^{-4}$	2.453	−6.041	−1.309	...
(4,2)	$9.11 \cdot 10^{-3}$	1.186	−2.772	−0.4334	...
(4,1)	$9.14 \cdot 10^{-2}$	3.714	0.3582	0.1166	...
(5,5)	$7.02 \cdot 10^{-6}$	4.509	−15.344	−4.330	...

up to $n = 4$. The results are shown in Fig. 5.16. It is interesting to note that for the (2,2) mode we are not able to go beyond $n = 4$ and thus at earlier times. This can be justified by the discussion on the source term above. Indeed, with $n = 4$ and $\epsilon = 10^{-5}$ we are able to fit from $t = 13.43$, but at that time we still have $|F_{22}^{(e)}|/\max(|F_{22}^{(e)}|) \simeq 0.097$ and thus the source term is not completely negligible. Also for this reason, the values of $\hat{a}_{22n}$ and $\bar{b}_{22n}$ found for the overtones are not robust and are in disagreement with the results found using different fitting procedures (see Appendix C.1). The procedure can be applied also to the higher modes, where the number of overtones that we are able to fit depends on the specific multipole considered. Generally, we have that for the modes with higher $\Delta t_{\ell m}$ (i.e. for the ones that are more delayed), we can fit more overtones, consistently with the fact that at later times the source terms become negligible. For example, for the (4,1) multipole we can fit up to $n = 7$ overtones (and thus from $t \simeq t_{41}^{\rm peak} + 5.94$) keeping the relative error of the frequency fit around 10^{-4}.

From a practical point of view, we are particularly interested in the values related to the fundamental frequencies, $\hat{a}_{\ell m1}$, since we can use them to improve the phenomenological ringdown description as discussed in Sec. 5.2, see in particular Eq. (5.2). The values found in this work are in agreement with previous work [122] and their modulus is reported in Table 5.3. Note that the order of magnitude of $\hat{A}_{\ell m1}$ is strictly linked to the number m and does not strongly depend on the eccentricity (see e.g. the right panel of Fig. 5.3). Therefore, we need to perform the global fits only on the phases $\theta_{\ell m1}$, that we report in Table 5.4 for all the multipoles considered in this work. The relevance of these fits can be particularly appreciated by looking at the analytical/numerical comparisons of the late-ringdown waveform frequencies shown in Figs. 5.6, 5.10, and 5.13.

Finally, we mention that since the iterative fit of the frequency did not provide satisfactory results for the whole quadrupolar postpeak waveform, we also attempted the same fit *without* the iterative procedure, focusing only on the (2,2) multipole. However, also this procedure did not lead to robust results for the whole postpeak waveform, as detailed in Appendix C.1.

5.4.3 EOB ringdown as superposition of QNMs

In the previous sections we have accumulated results that indicate that the ringdown description as a linear superposition of QNMs with constant coefficients, Eq. (1.63) cannot be consistently used for the whole postpeak waveform. However, in seminal EOB works [229, 232] the ringdown was modeled precisely in this way, although it was matched with the inspiral part of the waveform on an extended interval centered around the peak of the orbital frequency. We will now revisit this procedure, often referred to as "matching comb" [232]. The basic idea of this procedure is that the match is performed on a set of points rather than at only one point. To determine the complex coefficients $C^{\pm}_{\ell mn}$, we solve the linear system $h_{\ell m}(t_i) = \sum C^{\pm}_{\ell mn} e^{-\sigma^{\pm}_{\ell n} t_i}$, where t_i are the points of the time array used for the match, and $h_{\ell m} = h^{\rm inspl}\hat{h}^{\rm NQC}_{\ell m}$ is the NQC-corrected inspiral waveform. If we consider N QNMs (distinguished between positive and negative frequency), we then need N points. Note that this ringdown model does not require any tuned numerical parameters, it only needs the QNMs frequencies since the coefficients of the ringdown are determined using the analytical waveform. Similarly to what was discussed in Sec. 5.3 for the (2,2) waveform multipole, we use $\left\{A_{22}^{\rm NQC}, \dot{A}_{22}^{\rm NQC}, \ddot{A}_{22}^{\rm NQC}, \omega_{22}^{\rm NQC}, \dot{\omega}_{22}^{\rm NQC}, \ddot{\omega}_{22}^{\rm NQC}\right\}$, but here we directly extract them from the Zerilli waveform at $t_{22}^{\rm NQC} = t_{A_{22}}^{\rm peak} + 2$. We chose

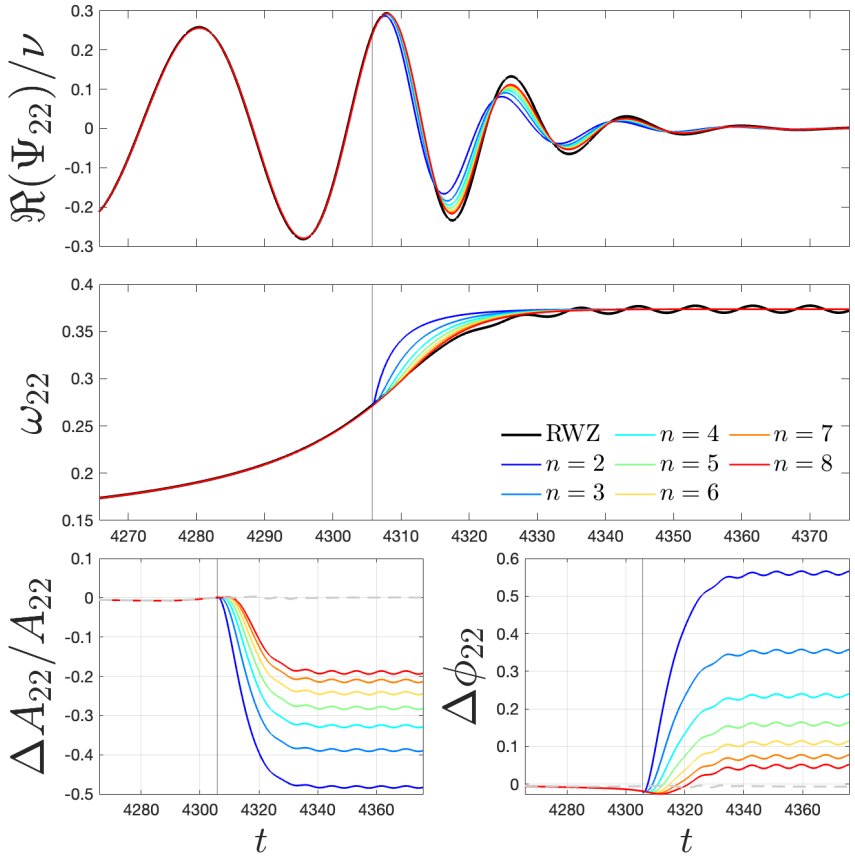

Figure 5.17: EOB waveform where the ringdown has been modeled with the matching comb procedure. In the bigger panels above we show the real part of the waveform and its frequency, black for the RWZ results and online colors for the analytical results. In the two small bottom panels we show the relative amplitude difference and the phase difference with the same color scheme of the upper panels. We also show the relative amplitude difference and the phase difference obtained with the waveform model discussed in Sec. 5.3 (dashed gray).

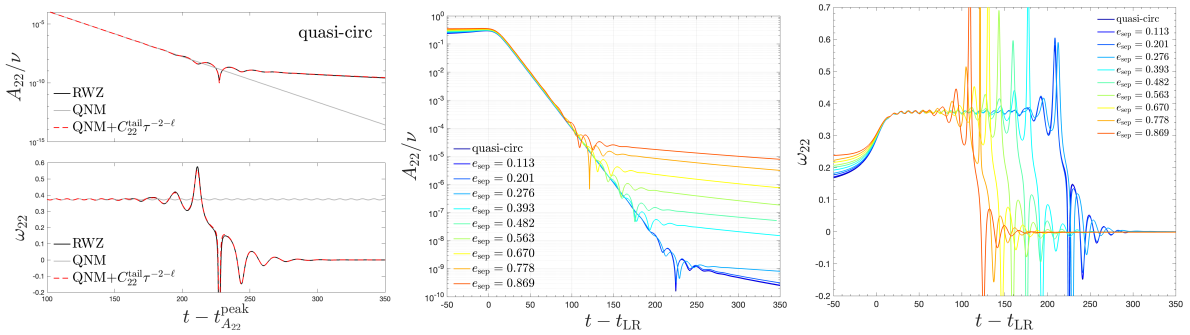

Figure 5.18: Leftmost panel: Amplitude and frequency of the Zerilli (2,2) of the quasi-circular waveform (black) compared with the results obtained considering only the QNMs contribution (gray) and the QNMs plus tail (dashed red). Middle and rightmost: RWZ amplitudes and frequencies for different eccentricities, aligned with respect to the light-ring crossing.

as matching points the adjacent points to $t_{A_{22}}^{\rm peak}$ in the time grid used to solve numerically the Hamilton's equations (2.56). The results of this procedure are shown from $n=2$ up to $n=8$ in Fig. 5.17. The configuration that reproduces the numerical waveform with the highest accuracy is the one with $n=8$ positive-frequency modes. For this configuration, in the late ringdown we have an 18% relative amplitude difference and a phase difference that oscillates around the 0.04 radians. We also show the relative amplitude difference and the phase difference obtained with the state-of-the-art waveform discussed in Sec. 5.3 (dashed gray). While the waveform obtained with the latter model is clearly more accurate (see also Fig. 5.6 for comparison), the results obtained in this section are still qualitatively good for the amplitude and quite accurate for the phase.

5.4.4 Tail contribution

Having considered only the first part of the waveform, we have so far neglected the power-tail effects in the waveform [233, 234]. However, since the QNMs are exponentially damped, there is a time when the tail effects become dominant. As can be seen from the frequency of the Zerilli (2,2) quasi-circular waveform shown in black in the left panel of Fig. 5.18, the effect of the tail starts to be visible at $t\sim t_{A_{22}}^{\rm peak}+170$, and becomes dominant shortly afterward. In order to reproduce the numerical waveform, we have to include a term of the form $C_{22}^{\rm tail}\tau^{-2-\ell}$, where the complex coefficient $C_{22}^{\rm tail}$ is determined with a fit and $-2-\ell$ is the asymptotic behavior of the tail term at future null infinity [235]. Using the (fundamental) QNMs and the power-law tail we can fully catch the behavior of the numerical amplitude and frequency, as shown in the left panel of Fig. 5.18. When eccentricity is taken into account, the tail contribution becomes more significant and starts to dominate over the QNM decay earlier, as shown in the middle and right panels of Fig. 5.18. Moreover, the tail cannot be described as before using the ansatz $C_{22}^{\rm tail}\tau^{-2-\ell}$ since the tail has not reached yet the asymptotic behavior. For example, for the configuration with $e_0=0.5$ the decay rate is roughly -1.3 instead of $-2-\ell$. Similar numbers are obtained for the other eccentric configurations with $e\gtrsim 0.3$.

Inspired by the results shown in Fig. 5.18, a recent work [236] has searched and found power-law tail effects in the ringdown generated by eccentric binary black holes with comparable masses. For this search, the authors of Ref. [236] have used the fourth RIT waveform catalog [87].

5.4.5 Heuristic modeling of QNMs excitation

Let us now introduce a toy model to grasp some insights into how the excitation of QNMs is driven by the dynamics and the related presence of a source term in the right-hand side of the RWZ equations. Following Ref. [232], and in particular Sec. III B, we base our analysis on the understanding that a Schwarzschild black hole can be seen as a resonating object. We start by generalizing Eq. (1.63), assuming that the constant coefficients $C^{\pm}_{\ell mn}$ are instead time-dependent functions, $C^{\pm}_{\ell mn}(t)$. The ringdown waveform reads then

$$\Psi^{(\mathrm{o/e})}_{\ell m} = \sum_n \Psi^{(\mathrm{o/e})}_{\ell mn}, \tag{5.23}$$

$$\Psi^{(\mathrm{o/e})}_{\ell mn}(t) \equiv C^{+}_{\ell mn}(t) e^{-\sigma^{+}_{\ell n} t} + C^{-}_{\ell mn}(t) e^{-\sigma^{-}_{\ell n} t}. \tag{5.24}$$

Here the origin of time, $t = 0$, is assumed to be the light-ring crossing, t_{LR}. The final goal of our investigation is to determine an approximate semi-analytical expression for the coefficients $C^{\pm}_{\ell mn}(t)$ so to understand when the associated QNMs are excited. Since we know that the solution of the homogeneous RWZ equations is a superposition of QNMs with constant coefficients $C^{\pm}_{\ell mn}$, each spherical mode is thought as the solution of the homogeneous second-order differential equation

$$\ddot{\Psi}^{(\mathrm{o/e})}_{\ell mn} + 2\alpha_{\ell n}\, \dot{\Psi}^{(\mathrm{o/e})}_{\ell mn} + (\alpha^2_{\ell n} + \omega^2_{\ell n})\, \Psi^{(\mathrm{o/e})}_{\ell mn} = 0, \tag{5.25}$$

under the ansatz $\Psi_{\ell mn}(t) \propto e^{-\sigma^{\pm}_{\ell n} t}$, with $\sigma^{\pm}_{\ell n} = \alpha_{\ell n} \pm i\omega_{\ell n}$. This is indeed the equation of an underdamped oscillator with damping coefficient $\alpha_{\ell n}$ and undamped angular frequency $\pm\omega_{\ell n}$. An external force $F(t)$ in the right-hand side of Eq. (5.25) yields an inhomogeneous differential equation corresponding to a driven harmonic oscillator. Our model is thus defined by *assuming* that the forcing term is given by Eq. (5.20), that is $F(t) \equiv F^{(\mathrm{e/o})}_{\ell m}(t)$. The solution of this inhomogeneous equation can be obtained starting from the one of the homogeneous problem by promoting the numerical coefficients therein to time-dependent functions. This is referred to as the *method of variation of parameters* (or *method of osculating elements*) [237–239]. With this approach we know *a priori* that the differential equation

$$\ddot{\Psi}^{(\mathrm{o/e})}_{\ell mn} + 2\alpha_{\ell n}\, \dot{\Psi}^{(\mathrm{o/e})}_{\ell mn} + (\alpha^2_{\ell n} + \omega^2_{\ell n})\, \Psi^{(\mathrm{o/e})}_{\ell mn} = F^{(\mathrm{e/o})}_{\ell m}(t) \tag{5.26}$$

admits a solution with the precise QNM structure of Eq. (5.24). We start by writing the time derivative of our particular solution *as if* the coefficients $C^{\pm}_{\ell mn}(t)$ were not time-dependent. This is equivalent to impose

$$\dot{\Psi}^{(\mathrm{o/e})}_{\ell mn}(t) = -\sigma^{+}_{\ell n} C^{+}_{\ell mn}(t) e^{-\sigma^{+}_{\ell n} t} - \sigma^{-}_{\ell n} C^{-}_{\ell mn}(t) e^{-\sigma^{-}_{\ell n} t}, \tag{5.27}$$

which is true only if the time dependence of $C^{\pm}_{\ell mn}(t)$ gives no contribution to the time derivative, namely if the condition

$$\dot{C}^{+}_{\ell mn}(t) e^{-\sigma^{+}_{\ell n} t} + \dot{C}^{-}_{\ell mn}(t) e^{-\sigma^{-}_{\ell n} t} = 0 \tag{5.28}$$

is satisfied. We can then take another time derivative on Eq. (5.27) in order to obtain $\ddot{\Psi}^{(\mathrm{o/e})}_{\ell m}$. We then insert $\dot{\Psi}^{(\mathrm{o/e})}_{\ell m}$ and $\ddot{\Psi}^{(\mathrm{o/e})}_{\ell m}$ in Eq. (5.26) and, considering that the sum of all the terms without the time derivatives $\dot{C}^{\pm}_{\ell mn}(t)$ separately solves the associated homogeneous equation (5.25), we get the second condition

$$-\sigma^{+}_{\ell n} \dot{C}^{+}_{\ell mn}(t) e^{-\sigma^{+}_{\ell n} t} - \sigma^{-}_{\ell n} \dot{C}^{-}_{\ell mn}(t) e^{-\sigma^{-}_{\ell n} t} = F^{(\mathrm{e/o})}_{\ell m}(t), \tag{5.29}$$

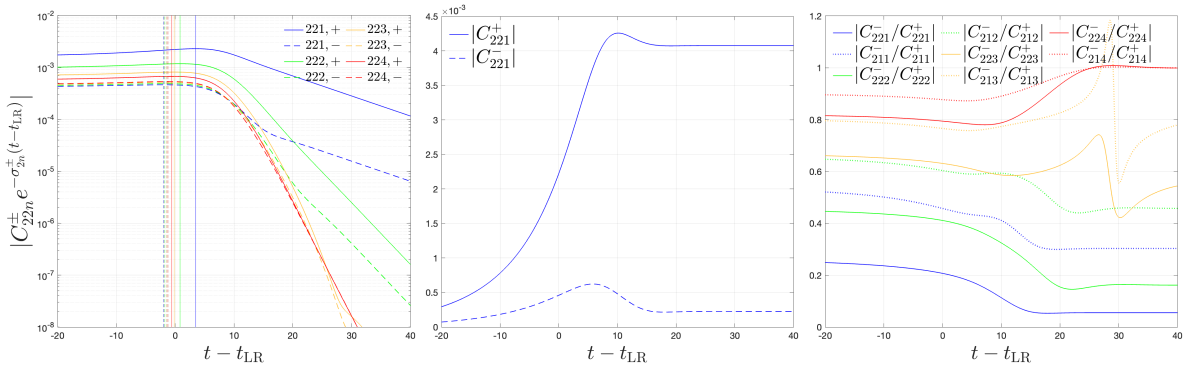

Figure 5.19: Time-dependent QNM-excitation coefficients $C^{\pm}_{\ell mn}(t)$ for the quasi-circular case, see Eq. (5.31). The positive-frequency modes are more relevant and are excited later than the negative ones, as shown by the location of the amplitude maxima (vertical lines in the leftmost plot). In the middle panel we plot the activation-like excitation coefficients for the fundamental frequency. The rightmost panel highlights the hierarchy of the ratios $|C^{-}_{\ell mn}/C^{+}_{\ell mn}|$ for the overtones of the (2,2) and (2,1) multipoles. Note that the beating is more relevant for the (2,1) mode (dotted line) than for the quadrupole (solid lines).

which together with Eq. (5.28) builds up a system of two equations that can be solved for $\dot{C}^{\pm}_{\ell mn}(t)$. A straightforward computation yields

$$\dot{C}^{\pm}_{\ell mn}(t) = \pm i \frac{e^{\sigma^{\pm}_{\ell n} t} F^{(\rm e/o)}_{\ell m}(t)}{2\omega_{\ell n}}, \tag{5.30}$$

and an ensuing time integral gives us the final expressions

$$C^{\pm}_{\ell mn}(t) = C^{\pm}_{\ell mn}(t_0) \pm \frac{i}{2\omega_{\ell n}} \int_{t_0}^{t} dt'\, F^{(\rm e/o)}_{\ell m}(t') e^{\sigma^{\pm}_{\ell n} t'}, \tag{5.31}$$

where t_0 is an arbitrary initial time. Considering that $F^{(\rm e/o)}_{\ell m}(t')$ does not diverge during the inspiral and that in the integrand we have $e^{\sigma^{\pm}_{\ell n} t'}$, we have that the computation of $C^{\pm}_{\ell mn}(t)$ is not influenced by the choice of t_0 as long as t_0 is not too close to $t_{\rm LR}$. In practice, we start to integrate from the beginning of our simulation.

Results

Some results for the (2,2) and (2,1) multipoles are shown in Fig. 5.19. In the leftmost panel we show the absolute value of the positive and negative parts of the solution, $|C^{\pm}_{\ell mn}(t) e^{-\sigma^{\pm}_{\ell n}(t-t_{\rm LR})}|$, for $n \leq 4$. We see that the negative-frequency contributions are smaller than the corresponding positive ones. The model thus predicts the negative-frequency modes to be less excited than the positive ones. The same feature can be seen in the third plot of the same figure, where we show the absolute value of the ratios of negative and positive solutions. In addition (see the rightmost panel of the figure) the negative-frequency modes become more and more relevant as n grows. This behavior is consistent with the qualitative discussion of Ref. [232], see in particular Fig. 4. In that case, the authors argued that the positive QNMs are excited during the plunge since the Newtonian frequency of the waveform $m\Omega$ gets "closer" to the positive QNM frequencies. Note in addition that what is found here is consistent with the structure of the actual solution of the RWZ equation. The second interesting finding, illustrated by the middle

panel of Fig. 5.19, is that $|C^{\pm}_{\ell m1}(t)|$ is reminiscent of an activation function and becomes constant after $t \sim t_{\rm LR}+15$, showing that from that time onward the $n=1$ solution can be written as a superposition of QNMs with constant coefficients. For the first overtone, we have that $C^{\pm}_{\ell m2}(t)$ has a similar behavior. However, for the $n \geq 3$ overtones, the behavior of $C^{\pm}_{\ell mn}(t)$ is less reminiscent of an activation function. In particular, for $n=3$ we see some oscillations in the solution, as can be seen e.g. from the third panel of Fig. 5.19. We are prone to exclude that these are physical features that can be found also in the full-RWZ case, and we rather interpret them as expressions of the limitation of our toy model. The third consideration regards the values of the $|C^{-}_{\ell mn}(t)/C^{+}_{\ell mn}(t)|$ ratios for different multipoles. We show these ratios for the (2,2) and (2,1) multipoles in the third panel of Fig. 5.19 with solid and dotted lines, respectively. As can be seen, the ratios of the (2,1) multipole are higher than the ones of the (2,2) multipole for the same n. This means that, according to our toy model, the mode mixing in the (2,1) multipole should be more evident than in the (2,2). This is precisely what happens in the numerical solutions of the full RWZ equations, as shown in Table 5.3. The driven harmonic oscillator correctly predicts also the qualitative relevance of the mode-mixing in the $(3,3)$ multipole, since the predicted ratio $|C^{-}_{331}(t)/C^{+}_{331}(t)|$ is smaller than the one of the (2,2) mode and, as can be seen from the numerical data, the mode-mixing is more relevant in the (2,2) multipole rather than in the (3,3). The final interesting feature that we discuss is that the positive and negative solutions reach their peaks at different times. This is shown for the (2,2) multipole in the first plot, where we mark the peak-times with vertical lines (solid for positive-frequency modes and dashed for negative ones). As can be seen, the negative modes with the same n are excited before the corresponding positive modes, and the overtones are excited before the fundamental QNMs.

To conclude, with this toy model we have reproduced some features that are observed when solving the actual RWZ equations and we have also argued that the overtones are excited before the fundamental frequency. However, since these results are only qualitative, we cannot exploit them to improve the description of the postpeak waveform.

5.5 Summary

In this chapter we have studied the transition from eccentric inspiral to plunge, merger, and ringdown of a binary black hole coalescence in the large mass ratio limit and its gravitational wave emission. We have also introduced and tested an EOB waveform that accurately described the GWs emitted by these systems.

More precisely, in Sec. 5.1 we have studied systematically the phenomenology of eccentric nonspinning binaries in the test particle limit, focusing in particular on the transition from inspiral to plunge and its corresponding waveform. In Sec. 5.2 we introduced a new ringdown waveform. The global fits on the parameter space are performed using as fitting parameter the gauge-invariant quantity $\hat{b}_{\Omega_{\rm pk}}$ (Eq. (5.3)), which is defined as the ratio between the angular momentum and energy at the peak of the orbital frequency (i.e., at the light-ring crossing). Notably, the ringdown waveform includes the mode-mixing between co-rotating and counter-rotating fundamental QNMs. We have then matched this ringdown model to the EOB inspiral waveform using NQC corrections. We have explored different configurations, both regarding the analytical information included in the waveform and the matching point between the inspiral and ringdown waveforms. The resulting waveform, which includes also 2PN noncircular corrections in the quadrupole,

has been extensively tested in Sec. 5.3, showing its accuracy over all the configurations considered. In Sec. 5.3.3 we have also tested an alternative way of modeling the ringdown waveform for the higher modes, as originally proposed in Ref. [58]. Finally, in Sec. 5.4 we have discussed the build-up of QNM excitations for the same configurations previously studied. We also discussed how the power-law tail contribution present at the end of the ringdown changes in the presence of eccentricity.

Chapter 6

Hyperbolic black hole binaries

In the previous chapters we have extensively discussed bound configurations with elliptic-like orbits, mainly in the test particle limit. In Sec. 4.2.1 we have also briefly discussed a few unbound cases, see Fig. 4.14. These hyperbolic-like orbits can be obtained by considering configuration with μ-normalized energy $\hat{E}$ above one and enough angular momentum such that the effective potential has a peak $V_{\rm max}$ greater than unity, i.e. $1 < \hat{E} \leq V_{\rm max}$. The configurations depicted in Fig. 4.14 involved geodesic motion; however, in realistic astrophysical scenarios, the gravitational wave burst emitted during the close passage can decrease the system's energy, transforming it into a bound configuration and leading the test particle to plunge toward the central black hole. This latter scenario is known as *dynamical capture*, since the system is initially unbound but then becomes bound due to dissipative effects. On the other hand, if the emission is not strong enough to make the system bound (i.e. if the energy remains above the rest mass of the system), then we have a scattering [176].

While the above discussion was restricted to the test mass limit, similar scenarios can take place for comparable mass binaries. In these cases, the effect of the radiation reaction is even more relevant. In particular, the event GW190521 [96] might have been generated by a black hole binary of this kind [2] (see in particular Fig. 1 and Fig. 3 therein). Due to the astrophysical relevance of these systems, we will discuss them in this chapter. We focus on the results shown in the Supplemental Material of Ref. [2] and on the `GR-Athena++` [14, 85] simulations presented in Ref. [7]. We also comment on some results that have not been made public yet, but that will be (hopefully) published in the near future. Note that, with an abuse of notation, we use the expression "hyperbolic systems" to encompass both scatterings and dynamical captures.

6.1 Test particle limit

As usual, we start by studying the test particle limit. In Sec. 6.1.1 we discuss the unbound dynamics, while in Sec. 6.1.2 we focus on the EOB modeling.

6.1.1 From scattering to dynamical captures

In this section we want to illustrate how the effects of the radiation reaction can lead to the capture of the particle for configurations that, from the geodesic point of view, would be unbound. To this end, we focus on test particles in Schwarzschild spacetime. Since in the previous chapter we have considered eccentric orbits and in the rest of this chapter

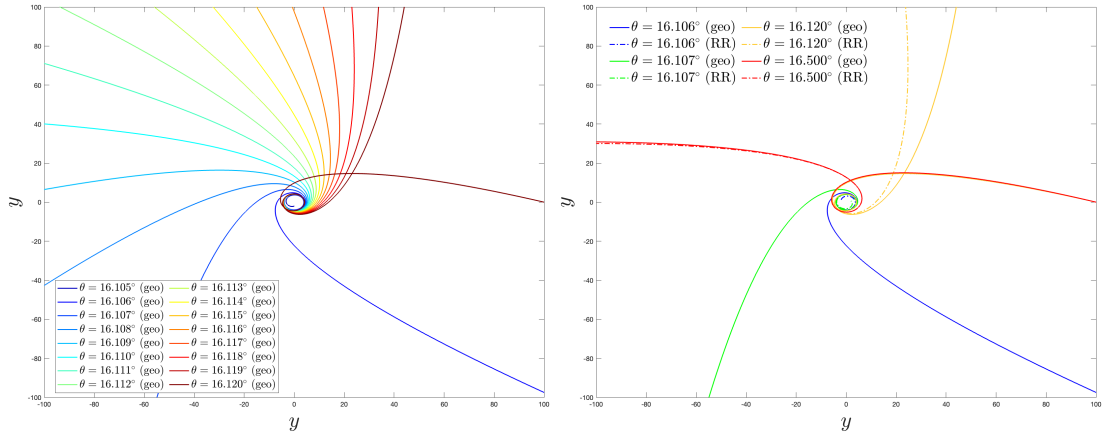

Figure 6.1: test particles in Schwarzschild with $\hat{E}_0 = 1$, $r_0 = 100$ and different shooting angles. They all start from $(x, y) = (100, 0)$. Left panel: geodesic configurations. Right panels: comparisons between some geodesic (solid) and non-geodesic (dot-dashed) configurations. For the latter, we consider $\nu = 10^{-3}$. Note that the two non-conservative configurations with $\theta = (16.106°, 16.107°)$ plunge, while the corresponding geodesic configurations scatter.

we will mainly consider hyperbolic-like orbits, here we will consider parabolic orbits for completeness. We will thus consider systems with initial energy $\hat{E}_0 = 1$.

While we could just specify the energy $\hat{E}$, the angular momentum p_φ, and the initial radius r_0, we prefer to use the shooting angle θ, defined as the angle between the Cartesian momenta p_x and p_y, instead of the angular momentum p_φ because the angle has a more clear geometrical meaning. This variable has been also used, for example, in Refs. [7, 240]. In Fig. 6.1 we show some configurations with $\hat{E} = 1$, $r_0 = 100$ and shooting angles around $\theta \sim 16.1°$. In the left panel, we consider only geodesic configurations and, as can be seen, for $\theta \lesssim 16.105°$ we have that the particle plunges in the Schwarzschild black hole, while for larger angles we have a scattering. When we introduce the effects of the radiation reaction (considering $\nu = 10^{-3}$), the transition from plunge to scattering is slightly shifted and occurs for $\theta \sim 16.108°$. However, the radiation reaction has an evident effect also on the scattering angle for angles close to the transition value. For larger angles (indicatively, for $\theta \gtrsim 18°$), the dissipative effects on the scattering angle are practically negligible.

Globally, the effect of the non-conservative part is quite small and we had to perform a fine-tuning on the shooting angle θ in order to see some relevant effects. However, this happens only because we are considering binaries with very high-mass ratio. For comparable mass binaries, the dissipative effect is far from being negligible, as we will see in Sec. 6.2.

6.1.2 Numerical and EOB waveforms

In Ref. [1, 3] we also presented some analytical/numerical comparisons for dynamical captures in the test particle limit. The numerical waveforms were obtained with `Teukode` [126]. The EOB dynamics and waveforms of this section are obtained with the EOB model discussed in Ref. [1], using the angular radiation reaction of Eq. (3.6), which is also the one used for the analysis of GW190521 in Ref. [2]. We choose the initial data of the dynamics directly by picking the energy $\hat{E}_0$ and the angular momentum p^0_φ. Practically, we choose p^0_φ and then pick $1 < \hat{E}_0 < V_{0,\max}$, where $V_{0,\max}$ is the peak of the effective potential (3.1). We choose this region of the parameter space because it is the

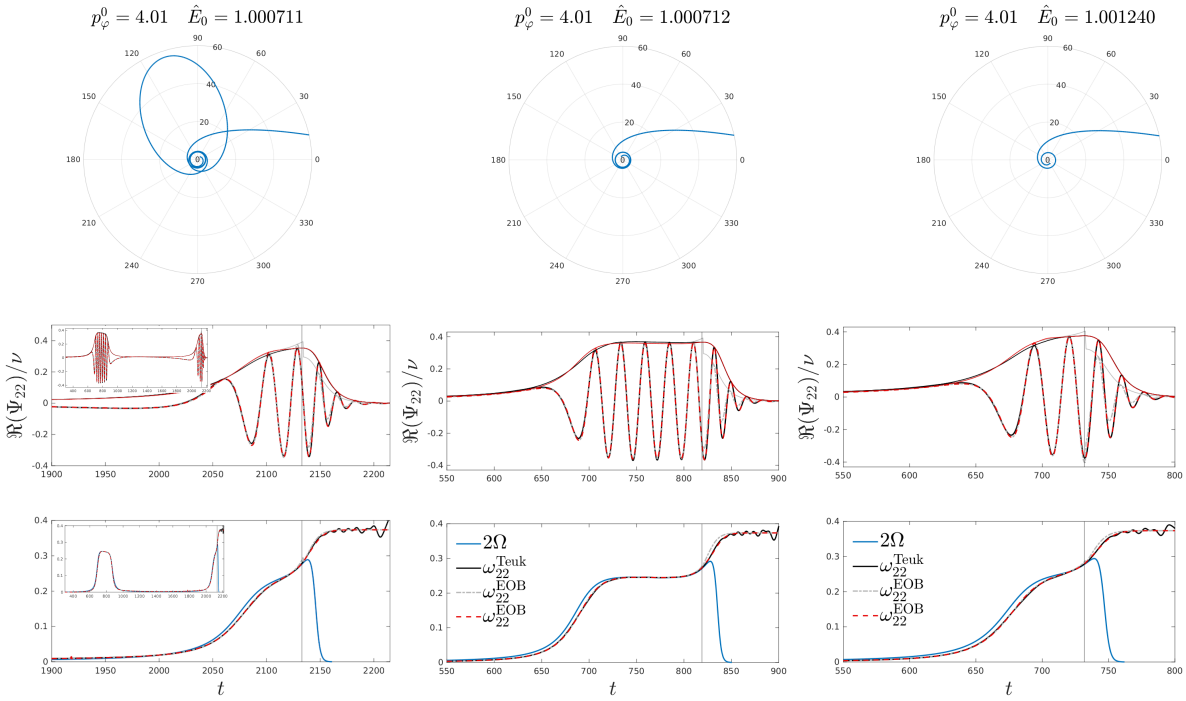

Figure 6.2: Upper panels: trajectories for nonspinning dynamical captures, with $\nu = 10^{-2}$, $p^0_\varphi = 4.01$, and $\hat{E}_0 = (1.000711, 1.000712, 1.001240)$. The trajectories start from $r_0 = 120$, but we show them from $r = 60$ in order to highlight the last part. Middle panels: corresponding quadrupolar waveforms. The black line is the numerical result from `Teukode`, while the red and grey lines are obtained with the EOB model using different prescriptions for the modelization of the ringdown. See text for more details. Bottom panels: frequency comparisons. The vertical lines mark the merger time (i.e. the peak of the $\ell = m = 2$ waveform amplitude), that in the hyperbolic case is extracted directly from numerical data.

one that yields the most interesting phenomenologies. In fact, for $\hat{E}_0 > V_{0,\rm max}$ there is always a direct plunge, while in the other case it is possible to have many close passages before merger. For example, choosing $\nu = 10^{-2}$ and starting the dynamics at $r_0 = 120$ with $p^0_\varphi = 4.08$ and $\hat{E}_0 = 1.00002$ leads to 11 close passages before merger.

It is not our aim here to carry out a systematic analysis of the parameter space as done for bound orbits in Ref. [146], so we will only focus our discussion on a few, illustrative, cases. Moreover, while in the previous section (and also in the other chapters) we have considered $\nu = 10^{-3}$, here we use $\nu = 10^{-2}$. This makes the dynamics with multiple encounters shorter and the corresponding numerical waveforms require less computational time. This is not a big deal at the moment, since we want to specifically focus on the ringdown part. We consider three $\nu = 10^{-2}$ configurations, with $r_0 = 120$, $p^0_\varphi = 4.01$ ($V_{0,\rm max} \simeq 1.00125$), and different values of energy: $\hat{E}_0 = (1.000711, 1.000712, 1.001240)$. The first one is a double encounter, while the others are single encounters. The trajectories, the quadrupolar waveforms, and the corresponding frequencies are shown in Fig. 6.2. The black waveform is as usual the numerical result, while on the analytical side we consider two different EOB waveforms colored in grey and red. The former is obtained by attaching the *circular* ringdown to the analytical waveform, similar to what is done for hyperbolic encounters in Refs. [146, 147], but *without* using NQC corrections as in Ref. [2]. The primary templates for the phase and the amplitude used in Fig. 6.2 are the ones described in Sec. 3.3.1. For the red waveform we consider the same templates, but we extract the fit parameters and the numerical quantities discussed in Sec. 3.3.1 directly from the numerical waveforms. A similar use of the numerical data is also done to

determine the NQC coefficients (a_i, b_i) of Eq. (2.53). Finally, also the merger time $t_{\rm mrg}$ is taken to be precisely the numerical one, since the simple prescription $t_{\rm mrg} = t^{\rm peak}_{\Omega_{\rm orb}} - 3$ used in Ref. [1] for bound orbits is found to be inaccurate in the hyperbolic case. A candidate variable to use in the global fits for the merger time in the dynamical capture scenario is $\hat{b}_{\Omega_{\rm pk}}$, defined in Eq. (5.3). Indeed, Ref. [12] has proven that a similar impact parameter b can be used to fit ringdown parameters also for dynamical captures in the comparable mass case. In any case, as a proof of principle, the improvement introduced in the red waveforms by the use of more precise parameters is clearly visible in Fig. 6.2, either before and after the merger. These comparisons show that including numerical information in the model from hyperbolic simulations could greatly enhance the analytical descriptions of waveforms emitted by the dynamical capture of two black holes. In particular, a systematic coverage of black hole binaries undergoing dynamical encounters using NR simulations can improve the waveform model `TEOBResumS` for these configurations [146], as shown in the recent work [7].

We conclude our brief discussion on dynamical captures in the test mass limit by mentioning that the 2PN noncircular corrections discussed in Chapter 4 can improve the phase accuracy of the analytical EOB waveform, as shown in Fig. 11 of Ref. [3], where we considered the same configurations of Fig. 6.2.

6.2 Dynamical captures for comparable mass binaries

We now turn our attention to hyperbolic configurations in the comparable mass case. Since in this scenario the effect of the radiation reaction is much more relevant, it is clear that we have more interesting phenomenologies. To introduce these physical systems, we follow a similar discussion to the one proposed in Ref. [146].

We thus consider the semi-analytical model `TEOBResumS-Dalì` [146–148] and we study how the phenomenology changes by fixing the initial separation at a very large value (typically $r_0 = 1000$ in this thesis) and varying the initial energy and angular momentum. Since the EOB maps the two-body dynamics in the dynamics of one-body in a ν-deformed black hole geometry, it is clear that the EOB orbits can be understood in the same way as we discussed in Sec. 3.1 for test particles in Kerr. In particular, now the effective potential is defined as $V(r; p_\varphi) \equiv H_{\rm EOB}|_{p_{r_*}=0}$, where the EOB Hamiltonian that we consider is linked to the effective one $\hat{H}_{\rm eff}$ of Eq. (2.15) by the map (2.5). If we consider configurations with initial energy $E_0 = H^0_{\rm EOB} > V^{\rm max}_0$, where $V^{\rm max}_0$ is the local maximum of the effective potential at $t = 0$, then the two black holes of the binary will inevitably merge. The region of the parameter space where $E_0 \leq V^{\rm max}_0$ and $V^{\rm max}_0 \geq 1$ is instead more interesting, since it has a richer phenomenology. In Fig. 6.3 we consider precisely this region for nonspinning configurations with four different mass ratios $q = (1, 4, 8, 16)$. The lowest initial angular momentum p^0_φ considered is the one for which $V^0_{\rm max} = 1$. For each mass ratio, we show a colormap of N, the number of peaks of the orbital frequency Ω. The case with $N = 2$ is highlighted in magenta, since it defines the transition region between scatterings and direct plunges, both characterized by $N = 1$. Note, however, that these last two cases have quite different phenomenologies: in the case of scatterings the Ω peak corresponds to the close passage and there is no merger (and thus no ringdown), while in the direct plunges the Ω peak corresponds to the (ν-deformed) light-ring crossing, and thus marks the merger of the two black holes. More vibrant colors indicate configurations in which

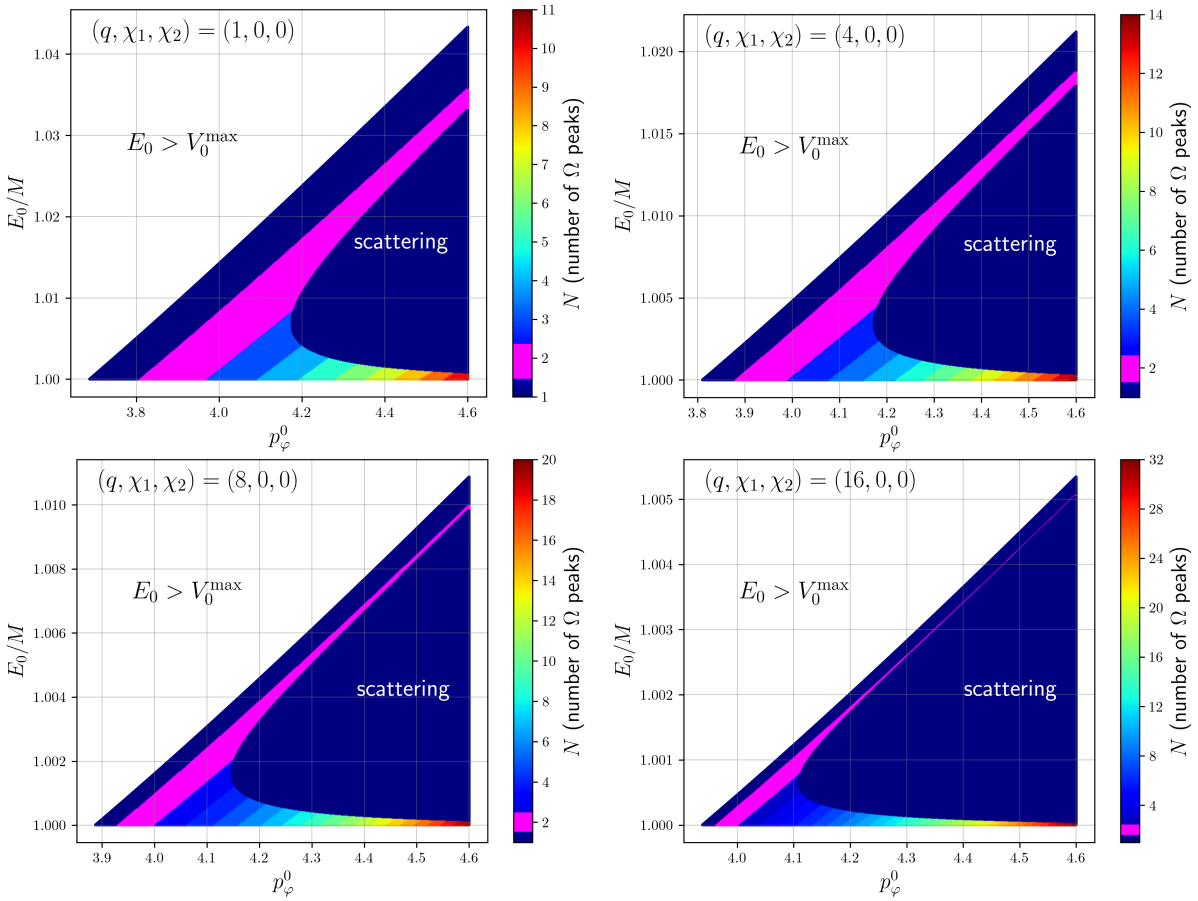

Figure 6.3: Number of peaks in the orbital frequency Ω on the (E_0, p_φ^0) plane as predicted by `TEOBResumS-Dali` for nonspinning binaries with different mass ratios. We plot N only where $E_0 \leq V_0^{\max}$, since for $E_0 > V_0^{\max}$ we always have direct captures (and therefore $N = 1$). Note the different vertical scales. In all the cases the initial EOB radius is $r_0 = 1000$. Plots analogous to Fig. 2 of Ref. [146].

the system undergoes many close encounters before merging. These cases are clearly accumulated near the threshold $E_0/M = 1$, since the many encounters are a consequence of the fact that a sufficient amount of energy to make the system bound is radiated during the first encounter. As one might expect, this region becomes narrower and narrower as the mass ratio increases, since the radiation reaction becomes less efficient. A similar fate befalls to the scattering-plunge transition region highlighted in magenta.

However, the analysis of the parameter space shown in Fig. 6.3 is obtained using a semi-analytical model that is PN-approximate. Moreover, while noncircular effects are included in the non-conservative dynamics as detailed in the previous chapters, the calibration of the Hamiltonian is performed only on quasi-circular NR simulations. We thus want to understand if this EOB prediction is reliable, and if it is to which extent. For this reason, in the next section we will start to consider NR simulations of hyperbolic scatterings and dynamical captures.

6.2.1 Preliminary `GR-Athena++` simulations

The NR simulations of hyperbolic black hole binaries that we are going to discuss have been obtained with the code `GR-Athena++` [85]. Some simulations have been presented in Ref. [7] and have been used to test the reliability of `TEOBResumS` in Ref. [2]. However, these numerical data were preliminary and present some minor problems that have been

now solved. We will first discuss these preliminary runs, and we will present the newer and more accurate simulations in Sec. 6.2.2. We thus start by reporting here the discussion on the `GR-Athena++` simulations of Ref. [7].

The initial data of these simulations are computed with a stand-alone version of the thorn `TwoPunctures` [182, 241]. The time evolution is then performed by `GR-Athena++` using the Z4c formulation [201]. Moving puncture gauge conditions with the same parameters of Ref. [85] are adopted. We use 6th-order finite-difference methods for the spatial derivatives and we perform the time-integration using a 4th-order Runge-Kutta algorithm. We apply a high-order Kreiss-Oliger dissipation doing the replacement $\partial_t[u] \leftarrow \partial_t[u] + \epsilon\mathcal{D}[u]$ with $\mathcal{D}[\cdot]$ proportional to a 8th-order spatial derivative and $\epsilon = 0.02$. The computational domain that we consider is a box with edge $L = 3072M$, so that in the coarsest level the cartesian coordinates range from $-1536M$ to $1536M$. The adaptive mesh refinement (AMR) in `GR-Athena++` is oct-tree based, with the grid organized as an initial Mesh divided into Meshblocks which have all the same number of grid points but (possibly) different physical sizes. For a cubic initial Mesh and cubic Meshblocks, the grid setup in `GR-Athena++` is regulated by three parameters: the number of grid points in the edges of the unrefined initial mesh N_M, the number of grid points in the edges of Meshblocks N_B, and the number of physical refinement levels N_L. The grid structure is ultimately determined by an AMR criterion, which, when satisfied, (de)refines a given MeshBlock, resulting in a (larger) smaller block with (half) double the resolution. For BBH simulations the AMR criterion used mimics the box-in-box strategy mentioned above. In our simulations we consider $N_B = 16$, $N_L = 11$, and $N_M = \{128, 192, 256\}$, that correspond to the resolutions $\delta x_p = (3.2438, 1.5625, 1.1719) \cdot 10^{-2}$ in the most refined level (i.e. at punctures' locations). For all the runs we consider a CFL number of 0.5. The Weyl scalar is then extracted at $R = \{80, 90, 100, 110, 120, 130, 140\}\, M$ using approximate geodesic spheres built using 9002 vertices. For the three grids considered, the resolutions in the extraction zones at the merger time are $\delta x_R = \{3, 2, 1.5\}\, M$ for $R > 96M$, while they are $\delta x_R = \{1.5, 1, 0.75\}\, M$ for $48M < R < 96M$. Note that at the beginning of the simulation the extraction zone for $R > 96M$ does not have a uniform resolution since the positions of the two punctures make some portions of the zone more refined. We observed that $R\psi_4$ remains approximately constant at all the extraction radii, showing that ψ_4 scales as $1/R$, as expected. More technical details on the structure of the grid and of the geodesic sphere can be found in Ref. [85]. Note that for this set of runs no grid symmetries are employed. Moreover, the apparent horizon finder (AHF) was not implemented in `GR-Athena++` at the time of these runs, so that we do not have horizon data.

In the NR simulations, we extract the Weyl scalar $\psi_4^{\ell m}$ at finite radius R, which is in turn related to $h_{\ell m}$ by the asymptotic relation (1.73) (modulo constant normalizations). Therefore, as a first step, we extrapolate $\psi_4^{\ell m}$ using the procedure proposed in Refs. [85, 242–244],

$$\lim_{r\to\infty} r\psi_4^{\ell m} \simeq A\left(r\psi_4^{\ell m} - \frac{(\ell-1)(\ell+2)}{2r}\int dt\, r\psi_4^{\ell m}\right), \tag{6.1}$$

where $A = 1 - 2M/r$ and $r = R(1 + M/(2R))^2$. At this point, obtaining $h_{\ell m}$ is theoretically straightforward, since we just need to perform a numerical double time-integration. However, it is well-known that performing this double time-integration is subtle due to the presence of numerical noise which induces drifts in the signal [245]. Note, moreover, that Eq. (6.1) requires an additional integral, so the extraction of the extrapolated strain modes takes three integrals in total. If one considers quasi-circular configurations, the

most reliable way to obtain $h_{\ell m}$ is to perform a fixed-frequency integration (FFI), where, as the name suggests, the integration is performed in the frequency-domain considering only the frequencies above a certain threshold f_0. If we consider quasi-circular configurations, the frequency increases monotonically in time, and therefore choosing the value of f_0 is quite straightforward. In the case of hyperbolic binaries, this choice is less obvious since these configurations have an infinite frequency spectrum. As discussed in Ref. [7], we observe that for choices of cut-offs that are large enough to remove the drift in the ringdown, FFI integration makes the amplitude of the precursor unphysically small. For these reasons, we start by using a time-domain integration and then remove the drift in the resulting signals. For the leading $(2,2)$ modes, after each time integration (including the one in Eq. (6.1)) we remove a complex constant by fitting a constant in a $100M$ time interval after the maximum of ψ_4. We also mention that in Ref. [7] we discussed the convergence of the extrapolated strain for `GR-Athena++` and `EinsteinToolkit`, both considering time-domain comparisons and frequency-domain mismatches. For `GR-Athena++` we found a 4th-order convergence before merger, but the convergence of the phase gets slightly worse after merger; see discussion in Sec. G.1 of Ref. [7] for more details.

`GR-Athena++` and `EinsteinToolkit` comparisons

Some configurations from the preliminary set discussed above have been used in Ref. [7] to compare the NR codes `GR-Athena++` and `EinsteinToolkit` [183, 184]. The initial data for these comparisons have been chosen as follows. We considered two nonspinning black holes of ADM masses M_1 and M_2 separated by a coordinate distance D. The total mass of the binary is computed as $M = M_1 + M_2$. We take their ADM linear momenta to be $\mathbf{P_1} = -\mathbf{P_2}$, with $\mathbf{P_1} = P_{\rm qc}(\cos\theta, \sin\theta, 0)$, where $P_{\rm qc}$ corresponds to the quasi-circular value. We take $D = 20M$, which in turn implies $P_{\rm qc} = 0.06175M$. Here we consider three configurations with $P = P_{\rm qc}$ and different shooting angles, $\theta = (42°, 48°, 50°)$. Note that these configurations were also considered in Ref. [246]. In terms of initial energy and angular momentum, these configurations correspond to $E^0_{\rm ADM} = 0.994M$ and $J^0_{\rm ADM} = (0.82634, 0.91774, 0.94602)M^2$.

Two subtleties should be discussed before proceeding. The first one is that we compute the total rest mass of the system as the sum of the two ADM masses of the punctures, i.e. $M = M_1 + M_2$. However, M_1 and M_2 do not have a precise physical meaning, they are just quantities that are practically useful to consider during the computation of the initial data. A better estimate of M could be obtained considering the sum of the two initial horizon masses (or better, their values after relaxation). However, as already mentioned, we do not have horizon data for these configurations, so that we stick with the computation of M discussed above. In practice, M_1 and M_2 are a good proxy of the physical masses, so this choice does to strongly affects our analysis. The second aspect is that in Ref. [7] we refer to these configurations as "dynamical captures". However, the initial ADM energy is below the rest mass M, so that the system is already bounded at the beginning of our numerical simulations. However, in Ref. [7] we still refer to them using this terminology since they could be considered final stages of evolutions whose energy was above M when the binary was dynamically formed. In other words, they could be considered the final orbits of systems that were originally in the colorful region of Fig. 6.3. In the next sections we will also consider configurations with $E^0_{\rm ADM} > M$ whose final fate is a merger. These latter systems can be unambiguously referred to as dynamical captures.

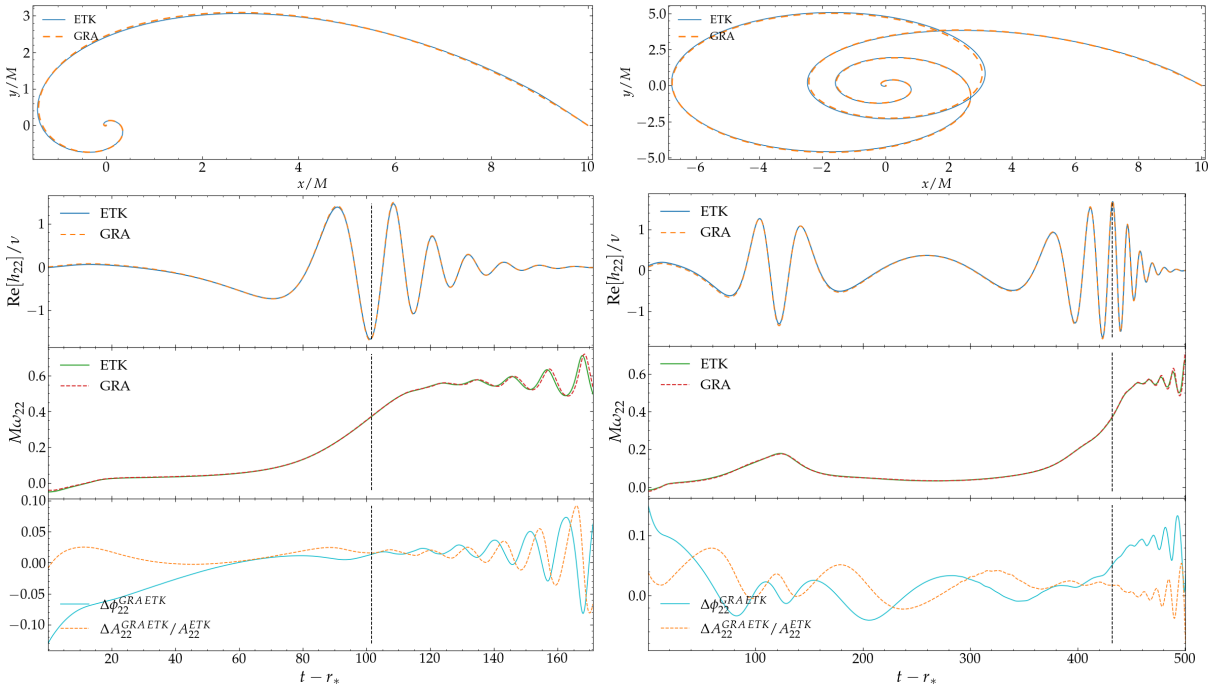

Figure 6.4: Example orbit, waveforms, frequency, and amplitude and phase difference, for the two configurations with $\theta = (42°, 50°)$. Note that there is no alignment applied to the waveforms. From Ref. [7].

In Fig. 6.4 we report the comparisons for the tracks and the quadrupolar strain for the $\theta = (42°, 50°)$ cases. The first configuration is a direct plunge, so that the gravitational signal is dominated by the ringdown, while the second one is a double encounter. We recall that the velocity of the punctures is strictly related to the shift vector β^i by Eq. (2.75), and that the evolution equation of β^i is a gauge choice (see e.g. Eq. (2.74)). However, `GR-Athena++` and `EinsteinToolkit` employ similar gauge conditions and therefore in the upper panels of Fig. 6.4 we also report the comparisons between tracks, that look indeed quite similar, even if some differences are visible by eye. However, the more meaningful comparisons are the ones of the gauge invariant strains and frequency, which are shown in the middle and bottom panels. While there is a good agreement between the two codes and the phase difference seems to converge away when increasing the resolution, the amplitude of the `GR-Athena++` waveform has an amplitude that is about 2% higher at merger than the `EinsteinToolkit` waveform. A similar result has been obtained in Ref. [85], which found a 2% difference at merger with the `BAM` code [195] for the quasi-circular case. This was indeed a consequence of a bug in the `GR-Athena++` code related to non-biased derivatives used in the ghost zones. This issue has been now solved, and therefore the waveform amplitudes of Sec. 6.2.2 are not affected by this. In Ref. [7] we also considered the frequency-domain mismatches for the quadrupolar waveforms, showing that at medium resolution ($N_M = 192$ for `GR-Athena++`) the unfaithfulness is of the order 10^{-5} (see Table IV of Ref. [7]). Since the comparisons discussed above are affected by the integration procedure to extrapolate the strain $h_{\ell m}$, in Appendix B of Ref. [7] we also compared directly the Weyl scalars from the two codes.

Globally, the waveforms of both codes are self-consistent, as shown by convergence tests, and they maintain this consistency with each other, except the previously discussed amplitude issue in the `GR-Athena++` waveforms, which has now been fixed. However, as discussed above, the computation of the strain from ψ_4 is one of the main technical chal-

lenging aspects of these simulations, and gets even worse for higher modes (that we have not discussed here). Possible solutions would be to directly extract the strain at infinity from NR simulations using techniques based on Regge-Wheeler-Zerilli perturbation theory [114, 247–249], or the Cauchy Characteristic Extraction (CCE) [250–252].

We conclude this discussion by remarking that Ref. [7] also considered EOB/NR comparisons using `TEOBResumS-Dalì` and the `EinsteinToolkit` simulations. We do not discuss these comparisons here, but we mention that it has been shown that `TEOBResumS-Dalì` can be consistently improved by incorporating NR information from dynamical captures, both in the ringdown model and in the NQC corrections.

Comparisons with `TEOBResumS`

Before moving to the newest `GR-Athena++` simulations, we briefly discuss the EOB/NR comparisons carried out in the Supplemental Material of Ref. [2]. We consider six configurations: the ones previously discussed in the preceding subsection, along with three additional configurations. The initial data for the latter are chosen by using the `TEOBResumS-Dalì` prediction shown in Fig. 6.3. After having chosen a (E_0, p^0_φ) pair that corresponds to a phenomenology of interest, we can use the EOB initial separation and EOB momenta to obtain the ADM cartesian momenta and the ADM separation using a 2PN-accurate EOB/ADM coordinate transformation [51]. Note that the energy and angular momentum of the system are the same in EOB and ADM charts. Moreover, for the cases where we consider an EOB radius of $r_{\rm EOB} = 100$, the corresponding ADM separation is, in practice, quite similar to $r_{\rm EOB}$, with differences of the few percent. Since the GW contribution at these separations is quite small, the precise value of the initial separation is not really relevant, in the sense that different but similar initial radii approximately produce the same waveforms, but only shifted in time. We still use the separation used from the 2PN EOB/ADM coordinate transformation, just for internal consistency. The three additional equal mass nonspinning configurations that we consider here have angular momentum $J_0/\nu = 3.97M^2$ and energies $E_0 = (1.003, 1.008, 1.007)M$. We label them as `Hq1_a5`, `Hq1_b5`, and `Hq1_c5`. The number 5 in the names indicates the resolution used, that is the one corresponding to $N_M = 256$. The evolution is performed as discussed in the previous subsection.

We now turn our attention to the EOB/NR comparisons. Given the previous discussion, it would be tempting to just take the energy and the angular momentum of the NR configuration under study, compute the initial separation from the 2PN EOB/ADM coordinate transformation, and compute the EOB waveform with these initial data. However, one has to take into account that at the beginning of the NR simulations there is spurious junk radiation, which is related to the fact that the initial data used are conformally flat. This radiation affects the evolution of the NR simulation, in the sense that the evolved system is not exactly the one that corresponds to the initial values of energy and angular momentum given in input. While for the configurations under examination this contribution is quite small[1], it is clear from Fig. 6.3 that even a small variation in the initial data can lead to completely different phenomenologies. For this reason, when considering EOB/NR comparisons, we search for the optimal values of energy and angular momentum using a dual-annealing optimization procedure from `scipy` [253], where the quantity on which we optimize is the unfaithfulness from Eq. (4.53) computed for a cer-

[1]See for example the discussion in Ref. [176], where scattering configurations with an ADM initial separation of $100M$ were considered.

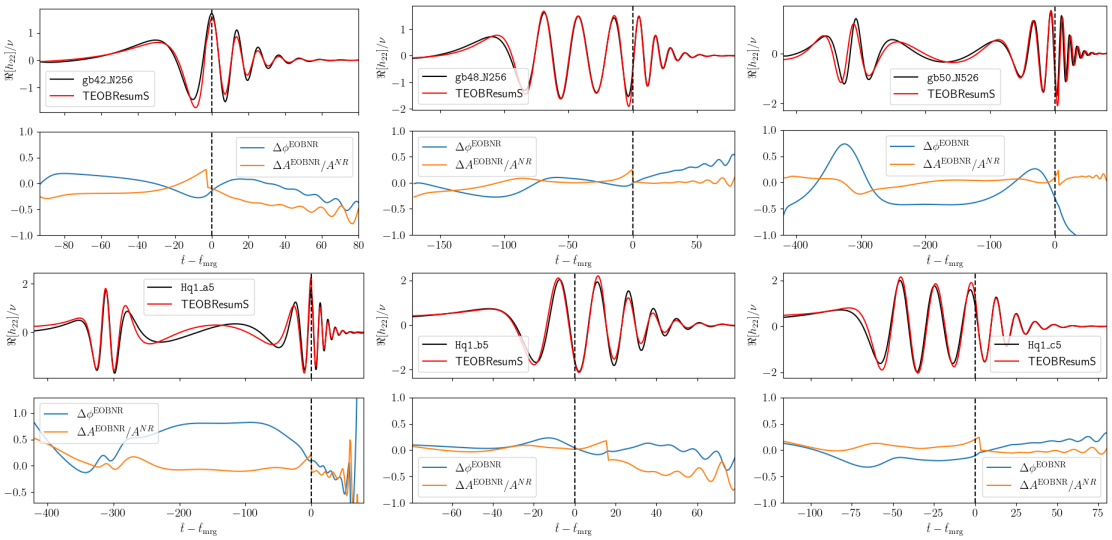

Figure 6.5: Comparisons between the `GR-Athena++` NR waveforms discussed in Sec. 6.2.1 to the analytical ones obtained using `TEOBResumS-Dalì` with optimized initial energy and angular momentum. For each configuration, the top panel displays the amplitude and the real part of the dominant multipole h_{22}, while the bottom panel shows the phase difference $\Delta\phi^{\rm EOBNR} = \phi^{\rm EOB} - \phi^{\rm NR}$ and the relative amplitude difference $\Delta A^{\rm EOBNR}/A^{\rm NR} = (A^{\rm EOB} - A^{\rm NR})/A^{\rm NR}$. Despite the lack of NQC corrections or of an hyperbolic-NR-informed ringdown, `TEOBResumS-Dalì` quantitatively captures the NR waveform for any configuration. From the Supplemental Material of Ref. [2].

tain reference mass $M_{\rm ref}$. In Ref. [2] we considered $M_{\rm ref} = 250 M_\odot$, that was the detector frame mass of GW190521, and frequencies between 11 and 512 Hz. The power spectral density $S_n(f)$ considered in the product of Eq. (4.54) is the GW190521 Hanford's PSD. The unfaithfulness is computed using the function `optimized_match` from `pyCBC` [254]. Following this procedure, we find mismatches between 0.2% and 3% (see also Fig. 2 of the Supplemental Material of Ref. [2]).

The EOB waveforms obtained using the optimized energies and angular momenta are compared to the NR waveforms in Fig. 6.5. The corresponding optimized initial values of energy and angular momentum are listed in Table I of the Supplemental Material of Ref. [2]. Moreover, in Fig. 6.5 we align the EOB and NR waveforms in order to maximize the cross-correlations between the two signals. This alignment procedure could be seen as an optimization on the initial distance D, since the radiation reaction is negligible at large separation, but consider that this alignment is also typically performed in EOB/NR comparisons for quasi-circular and eccentric binaries. The agreement obtained in Fig. 6.5 is quite remarkable considering that the EOB model used does not contain any NR information from non-circularized binaries, nor in the Hamiltonian or in the ringdown model. Moreover, note that in the optimization procedure, and thus in Fig. 6.5, we are not considering NQC corrections. As a consequence, the EOB amplitude at merger always overestimates the numerical one. On the other hand, the phase (and thus frequency) agreement of the waveforms is quite good for the whole evolution. This can be qualitatively understood by recalling the results obtained for eccentric test mass waveforms shown in Fig. 5.3. Indeed, in that case we have seen that the non-circularity of the dynamics strongly changes the value of the amplitude at merger, but has a less relevant effect on the waveform frequency.

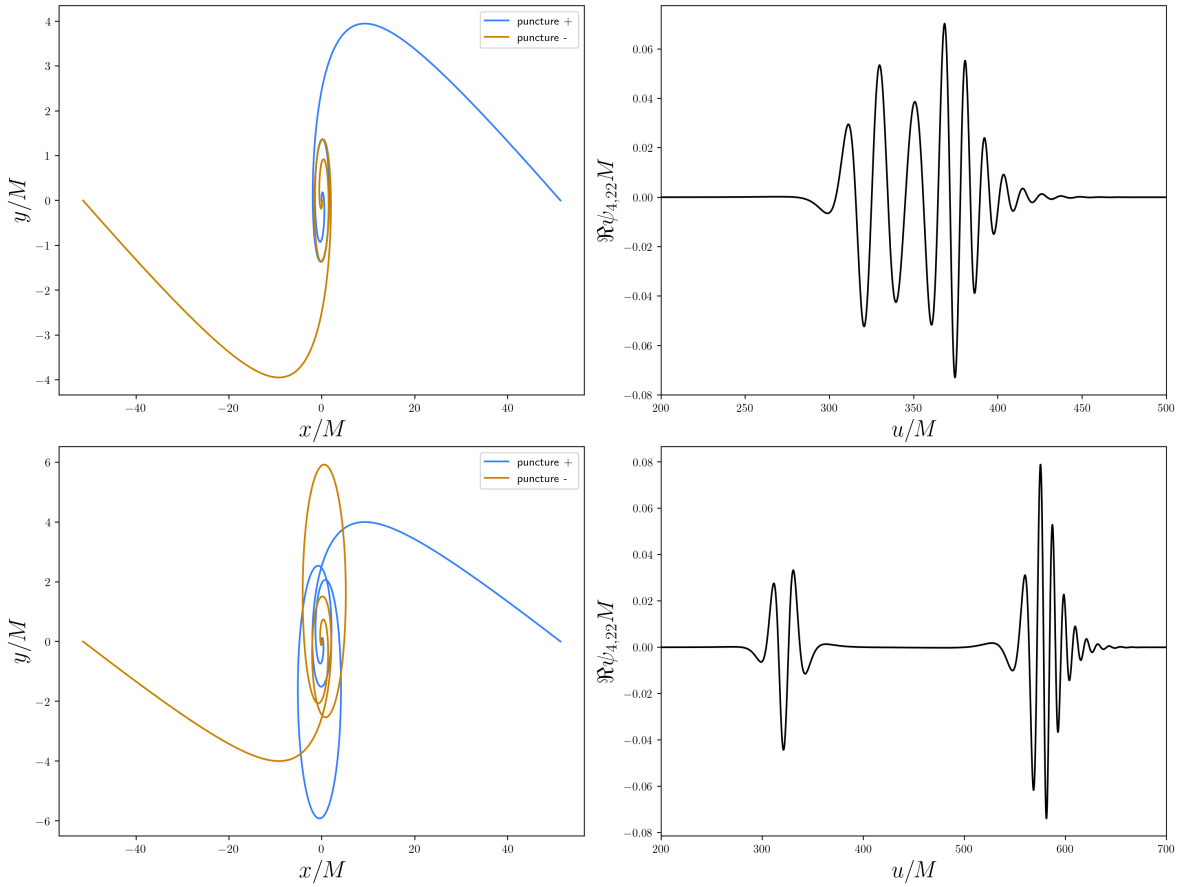

Figure 6.6: Tracks of the punctures and (2,2) mode of the Weyl scalar for the two configurations described in Sec. 6.2.2. We show the real part of ψ_4^{22} plotted against the retarded time $u = t - r_*$.

6.2.2 Up-to-date `GR-Athena++` simulations

We now briefly discuss two simulations of hyperbolic black hole binaries that are taken from the last `GR-Athena++` dataset. This dataset is currently under development, and therefore it has not been made public yet. These configurations are obtained similarly to what was discussed in Sec. 6.2.1, with a few but relevant changes that we discussed in the following. First of all, we numerically evolve only the $z \geq 0$ portion of the space and we obtain the lower half by exploiting bitant symmetry. Moreover, as discussed before, the 2% error on the amplitude has been now fixed. We also search for apparent horizons during the evolution of the binary using an apparent horizon finder (AHF) based on Ref. [255]. We do not discuss horizon data here, but the AHF has been used in Ref. [14], see in particular Fig. 14 therein. For the AMR used in these new runs, we considered the L_2-norm criterion, as discussed in Ref. [256], while in the runs of Sec. 6.2.1 we used the L_∞-norm. Finally, we use a CFL factor of 0.25, as opposed to the value 0.5 used for the previous runs.

In this section we focus only on two significative equal mass nonspinning configurations with initial energy $E_0^{\rm NR} = 1.01103\,M$ and angular momentum $J_0^{\rm NR}/M^2 = (1.00499, 1.01749)$. The tracks of the punctures and the quadrupolar Weyl scalars are shown in Fig. 6.6. The configuration with higher angular momentum is a double encounter, a phenomenology similar to one of the `gb50_N256` and `Hq1_a5` cases considered in the previous section and shown in Fig. 6.5. The other configuration with angular

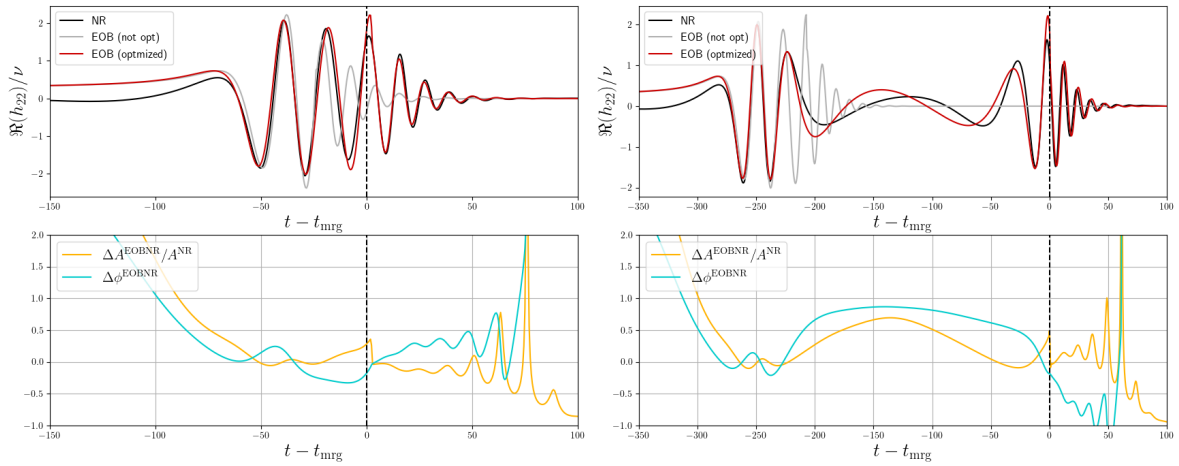

Figure 6.7: EOB/NR comparisons for the configurations discussed in Sec. 6.2.2. The NR strains (black) are obtained by applying an FFI to ψ_4 with $f_0 = 0.01/M$. The gray EOB waveforms are obtained without tuning the initial conditions, while the red EOB waveforms are obtained with the optimization procedure discussed in the text. The EOB/NR phase and amplitude differences in the bottom panels refer to the EOB optimized wave.

momentum $J_0^{\rm NR} = 1.01749\,M^2$ is an example of transition from a single to a double encounter, phenomenologically similar to the `gb48_N256` configuration shown in the middle upper panel of Fig. 6.5. In this case, the black holes perform a circular whirl before plunging, as shown by the tracks of the black holes in the upper left panel of Fig. 6.6. Phenomenologies of this kind correspond to the left edge of the magenta region in Fig. 6.3.

To complement the discussion of the previous section, we now compute the strain by performing an FFI, even though, as we will see in a moment, this choice leads to an unphysically small amplitude for the precursor (i.e. the part of the signal preceding the first encounter). We show in Fig. 6.7 the comparisons of these NR waveforms with the analytical ones obtained with `TEOBResumS-Dalì`. We consider two different EOB waveforms: the first ones, shown in grey in Fig. 6.7, are obtained using the initial energy and angular momentum of the NR simulation, while the red EOB waveforms are obtained by following the same optimization procedure discussed in the previous section, with the difference that we now consider the zero-detuned, high-power noise spectral density of Advanced LIGO [226]. The optimized unfaithfulness for the configuration with lowest angular momentum is $\bar{F} = 2.8\%$ and the optimized initial conditions are $(E_0^{\rm opt}, J_0^{\rm opt}) = (1.01107\,M, 1.01774\,M^2)$. For the other configuration we get, after optimization, $\bar{F} = 1.6\%$ and $(E_0^{\rm opt}, J_0^{\rm opt}) = (1.01112\,M, 1.02540\,M^2)$. While the EOB waveforms generated with optimized initial data are in good visual agreement with the NR data, some aspects need to be discussed. First of all, the NR amplitude of the precursor is close to zero, while the EOB amplitude is not. This is an artifact of the NR data that is a direct consequence of the FFI applied to the Weyl scalar ψ_4. Indeed, since we use a cut-off frequency of $f_0 = 0.01/M$, the part of the signal with lower frequencies (that is, the precursors) is simply removed by the integration procedure. However, lower frequencies would introduce artificial drifts in the waveform that would make the *whole* waveform unreliable. The second aspect that we highlight is that the not-optimized EOB waveforms are shorter than the corresponding NR waveform in both cases. Since this seems to be a general feature that occurs also for many other hyperbolic configurations, it may be an indication that the EOB fluxes overestimate the real ones in the hyperbolic

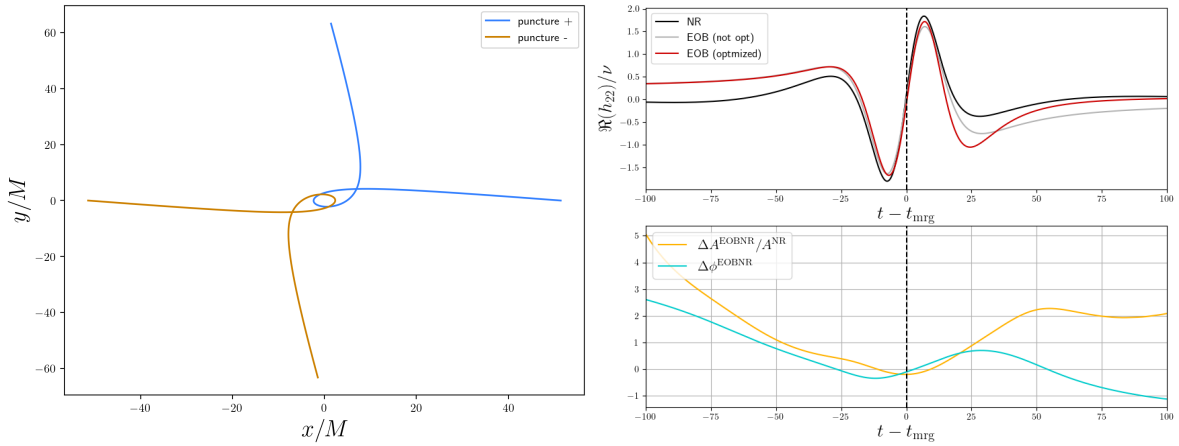

Figure 6.8: Scattering configuration discussed in Sec. 6.3. Left panel: tracks of the punctures; initial positions on the x-axis. Right panel: EOB/NR comparison, analogous to the ones shown in Fig. 6.7. The NR waveform is obtained using an FFI with a cut-off frequency $f_0 = 0.01/M$.

comparable mass scenario. When we studied hyperbolic geodesics in Schwarzschild, we already saw that the `TEOBResumS` energy fluxes overestimate the numerical results for the two hyperbolic geodesic configurations without zoom-whirl behavior shown in Fig. 4.14 (`TEOBResumS` fluxes in red). However, this effect may be linked also to the NR-tuning of the effective Hamiltonian, that is performed considering only quasi-circular binaries. As a consequence, a larger set of dynamical captures could be used to further improve EOB models, not only for the ringdown waveform as discussed in Ref. [7], but also to improve the calibration of the dynamical sector, as mentioned in Sec. 2.3.1.

6.3 Hyperbolic scatterings

Since in the previous sections we have mainly discussed dynamical captures, we now discuss an unbound configuration that is part of the new `GR-Athena++` dataset mentioned in Sec. 6.2.2. NR scattering configurations have received much attention in recent years [176, 257, 258], also because they can be used to test Post-Minkowskian predictions [177, 178].

The initial NR energy and angular momentum of the scattering configuration considered are $(E_0^{\rm NR}, J_0^{\rm NR}) = (1.01103\,M, 1.06249\,M^2)$. The corresponding tracks and the waveform are reported in Fig. 6.8. Also in this case, to obtain the strain we apply an FFI to ψ_4 with cut-off frequency $f_0 = 0.01/M$. For this configuration the mismatch (or unfaithfulness) between the NR (2,2) waveform and the not-optimized EOB waveform is already quite low: $\bar{F} = 1.4\%$. The optimization on the initial leads to a slight improvement, yielding $\bar{F} = 1.0\%$. The optimized initial conditions are $(E_0^{\rm opt}, J_0^{\rm opt}) = (1.01093\,M, 1.05059\,M^2)$. Note that in this case, the optimization procedure leads to an angular momentum that is slightly smaller than $J_0^{\rm NR}$, as opposed to the cases analyzed in Sec. 6.2.2. The EOB/NR comparison reported in the right panel of Fig. 6.8 clearly shows that the FFI leads to a strong underestimate of the precursor amplitude also in this case. Moreover, since here we do not have a high-frequency ringdown signal, the FFI also decreases the accuracy of the NR strain after the close passage.

Hyperbolic scattering configurations can be also used to test the dynamical sector of EOB models. This can be achieved by comparing the gauge-invariant scattering angles

χ obtained from the numerical simulation and the EOB model [176–178, 258]. The standard procedure used to extract the scattering angle χ from numerical simulations is to consider the relative motion of the two punctures in polar coordinates (r, θ), consider the incoming and outgoing parts, $\theta_{\rm in}(r)$ and $\theta_{\rm out}(r)$, and extrapolate them to infinity using $1/r$ polynomials. Note that there are some arbitrary choices in this procedure: i) the radial intervals of $\theta_{\rm in}(r)$ and $\theta_{\rm out}(r)$ considered in the fits, ii) the polynomial order N_P. The minimum value of the relative separation r has to be chosen in order to avoid the strong field regime. A typical choice, that we also adopt in this thesis, is to consider a cutoff at $r_{\rm min} = 25\,M$, both for $\theta_{\rm in}(r)$ and $\theta_{\rm out}(r)$. A more subtle detail is that one should choose an upper cut-off for the incoming trajectory $\theta_{\rm in}(r)$. This is a consequence of the gauge choices typically adopted in NR simulations with the moving punctures approach. Indeed, the shift vector β^i is initially set to zero, and thus Eq. (2.75) implies that the punctures are initially at rest. Then, when the system is evolved in time, the punctures acquire a certain velocity, and their trajectories become reasonably hyperbolic-like up to the strong-field regime. Therefore, it is a good practice to consider an upper cut-off for $\theta_{\rm in}(r)$. In this thesis we choose this cut-off as $r_{\rm max} = r_0 - 5\,M$. The outgoing part of the relative trajectory is clearly not affected by this problem, so we can consider the highest separation available. To wrap up, we fit $\theta_{\rm in}(r)$ over $r \in [r_0 - 5\,M, 25\,M]$ and $\theta_{\rm out}(r)$ over $r \in [25\,M, r_{\rm end}]$, where $r_{\rm end}$ is the relative separation at the end of the simulation. Regarding the polynomial order, we consider $N_P \in [2, 4]$. We then pick the value that corresponds to $N_P = 3$ and we compute the error associated with the fit as the difference between the minimum and maximum χ obtained.

Following this procedure, for the highest resolution ($N_M = 256$) of the configuration here discussed, we find $\chi_{\rm NR} = 287.28°$, with an error associated with the fit of $\Delta\chi_{\rm fit} = 1.05°$. To evaluate the error associated with the finite resolution of the NR simulations, we consider the same physical configuration but at a lower resolution, $N_M = 128$. By taking the difference between the angles obtained for the two different resolutions, we get an NR error $\Delta\chi_{\rm NR} = 0.33°$. We thus conclude that the error associated with the physical configuration here considered is $\chi_{\rm NR} = 287.3 \pm 1.1\,°$, where the error has been obtained as a quadrature sum of $\Delta\chi_{\rm fit}$ and $\Delta\chi_{\rm NR}$. Note that $\Delta\chi_{\rm NR}$ is practically negligible and the main contribution to the error is given by the fitting procedure.

If we now apply the same procedure to the EOB configuration with not-optimized initial data, we get $\chi_{\rm EOB} = 291.8 \pm 0.8\,°$. If we also remove the contribution of the junk radiation from the initial values of energy and angular momentum, the EOB model yields[2] $\chi_{\rm EOB}^{\rm after-junk} = 293.8 \pm 0.2\,°$. These results are not in perfect agreement with the NR results, but they are still remarkable considering that we are considering a configuration with large χ, and therefore a strong-field regime. This level of accuracy is compatible with the results reported in Ref. [258], see in particular Table II therein. Finally, if we consider the scattering angle obtained with the optimized EOB initial conditions, we get $\chi_{\rm EOB}^{\rm opt} \simeq 334°$. This shows that while the optimization procedure minimizes the unfaithfulness, by construction, it is not guaranteed that it improves also the scattering angle. This issue may be also linked to the artifacts introduced in the NR waveform by the integration of the Weyl scalar.

We briefly mention that if we apply the same procedure to a scattering configuration of

[2]When dealing with after junk values of E and J, we use $r_{\rm EOB} \to \infty$ ($r_{\rm EOB} = 10^4$ in practice) since those are the asymptotic values of energy and angular momentum. We verified this by computing these two quantities extrapolating $E(r)$ and $J(r)$ to $r \to \infty$ using $1/r$-polynomials.

the old dataset with $(E_0^{\rm NR}, J_0^{\rm NR}) = (1.00395\,M, 1.06613\,M^2)$, we get[3] $\chi_{\rm NR} = 267.8 \pm 2.3\,^\circ$ and $\chi_{\rm EOB}^{\rm after-junk} = 270.9 \pm 0.7\,^\circ$. The better EOB/NR agreement is a direct consequence of the fact that we are considering a configuration with a lower scattering angle, and therefore a weaker field regime than the configuration discussed above.

We conclude the discussion on the scattering angles by underlying that while χ is in principle a gauge invariant quantity, it is extracted from the NR data using the tracks of the punctures, which are strictly linked to the gauge quantity β^i. While this might seem, a priori, an unreliable procedure, the high level of accuracy achieved for $\chi \lesssim 250^\circ$ suggests that this way of computing $\chi_{\rm NR}$ is indeed reliable, at least in the low-energy regime considered in this thesis and Refs. [176–178, 258]. A test on the impact of different gauge choices on the NR scattering angle has been performed in Ref. [178], where the authors considered `EinsteinToolkit` simulations and showed that changing the initial value of the lapse function α does not have a great impact on the scattering angle $\chi_{\rm NR}$. However, it would be interesting to perform similar tests on the parameters (μ_S, η) used in the Gamma-driver (2.74). Indeed, Eq. (2.74) determines the evolution of the shift vector β^i, and thus, through Eq. (2.75), the motion of the punctures. However, it is not a priori guaranteed that this procedure will remain reliable also in the high-energy regime.

6.4 Summary

In this last chapter we have discussed hyperbolic configurations following Refs. [2, 7] and presenting some new results that have been not made public yet. We focused in particular on the dynamical capture scenario. In Sec. 6.1 we started to study the dynamics of these systems in the test mass limit case, but in Sec. 6.2 we rapidly moved to the comparable mass case, where dynamical captures are more likely to occur due to the greater relevance of the radiation reaction. We discussed the transition from scattering to plunge by analyzing the prediction of the EOB model `TEOBResumS-Dalì`. In Sec. 6.2.1 and 6.2.2 we tackled this problem using the NR code `GR-Athena++` to simulate dynamical captures of equal mass nonspinning black holes. The integration used to derive the extrapolated strain from the Weyl scalar of these configurations is complicated, and both the FFI and TDI methods present their own set of problematics. For this reason, CCE or waveform extraction à la Regge-Wheeler-Zerilli might be necessary to achieve accurate NR waveforms for hyperbolic binaries. Nonetheless, we presented EOB/NR waveform comparisons, highlighting that a larger set of NR dynamical captures could be used to inform and improve the `TEOBResumS-Dalì` model. We concluded this chapter by discussing in Sec. 6.3 a scattering configuration and how scattering angles can be computed from NR simulations.

[3] The higher NR error on χ is linked to the fact that this simulation has shorter outgoing tracks.

Chapter 7

Conclusions

In this Ph.D. thesis we have discussed in detail different approaches for non-circularized binaries, focusing in particular on the synergies between numerical and analytical methods. We started with a brief introduction to gravitational waves and test particle dynamics in black hole geometries in Chapter 1, and continued the introductory material in Chapter 2 by discussing EOB models and NR methods for black hole binaries with comparable masses.

We started to present original material from Chapter 3. We extensively discussed the test particle limit, both considering planar geodesics in Kerr and non-conservative dynamics. The latter were obtained by plugging an EOB radiation reaction in the Hamilton EOM. We computed the numerical gravitational waveforms and fluxes by solving the Regge-Wheeler and Zerilli equations [109, 110] with the time-domain code `RWZHyp` [122–125], or by solving the Teukolsky equation [116] with the 2+1 time-domain code `Teukode` [126]. We focus in particular on the linear perturbations produced by test masses on eccentric bounded orbits, whose corresponding gravitational signals have been fundamental in order to test and improve the non-circular analytical prescriptions employed in the EOB model `TEOBResumS-Dalì` [145–148]. In particular, Ref. [1] has extensively tested the *generic* (rather than circular) Newtonian prefactor introduced in Ref. [145], showing the reliability of the associated waveform and radiation reaction for a large range of planar orbits in Kerr spacetime. The accuracy of the generic Newtonian prefactor finds its roots in the fact that the time-derivatives of r and Ω are kept explicit, rather than PN-expanded. We concluded the discussion on test particle eccentric configurations in Chapter 3 by discussing the plunge, merger, and ringdown of such systems. We also proposed a simple ringdown model and related NQC corrections to complete the EOB analytical waveform for the inspiral. We thus obtained an accurate EOB waveform for the whole evolution of eccentric planar inspirals in the extreme-mass ratio regime.

In Chapter 4, we considered 2PN noncircular corrections to the inspiral waveform and to radiation reactions, which were crucially obtained by first factorizing the generic Newtonian prefactor discussed above. We start by introducing in Sec. 4.1 the instantaneous and hereditary 2PN noncircular contributions computed and tested in Ref. [3]. The numerical results obtained in the test particle limit have been once again crucial to test the reliability of the analytical expressions employed in the EOB model. After proper factorization and resummation, the 2PN corrections of Ref. [3] led to a more accurate phase for the multipolar EOB waveform. In Chapter 4 we also discussed higher-modes, $m = 0$ modes included. In Sec. 4.2 we then focused on the radiation reaction, showing that the prescriptions that factorize the generic Newtonian prefactor yield a better analyti-

cal/numerical agreement [4]. Finally, in Sec. 4.3 we introduced an alternative approach to computing the instantaneous 2PN noncircular contribution [5], which has been proven to be more accurate and reliable than the one previously discussed in Sec. 4.1. Through Chapter 4 we also discussed the impact of these 2PN noncircular corrections on the accuracy of `TEOBResumS-Dalì`, finding that they may indeed lead to some small improvements in the EOB waveforms. However, consider that 2PN-informed `TEOBResumS-Dalì` has been only tested against SXS simulations with maximum eccentricity $e_{\rm NR} \sim 0.3$, and is thus possible, and actually probable, that the 2PN noncircular corrections would become more relevant for more eccentric configurations.

While in Chapter 4 we mainly discussed the EOB inspiral waveform, in Chapter 5 we shifted our attention to the plunge, merger, and ringdown of eccentric nonspinning binaries, mainly following Ref. [6]. We studied in detail the phenomenology of the transition from inspiral to plunge, and all the pieces that enter the construction of the ringdown waveform and the NQC corrections. We thus presented a complete EOB waveform, that we proved to be extremely accurate in the quasi-circular case, and that still yields reliable results for all the eccentricities considered (up to $e \sim 0.9$), even if the performance slightly degrades as the eccentricity increases. A crucial aspect has been the introduction in Eq. (5.3) of an "impact parameter" $\hat{b}_{\Omega_{\rm pk}}$, that has been used to find order-relations between merger and ringdown quantities. Ref. [12] recently showed that a generalization of $\hat{b}_{\Omega_{\rm pk}}$ can be used with similar purposes also in the comparable mass case, notably even for spinning binaries. We also discussed the modelization of the postpeak (ringdown) waveforms for the higher-modes, showing that matching the ringdown waveform of the higher modes to the inspiral waveform at $t^{\rm peak}_{A_{22}}$ rather than at $t^{\rm peak}_{A_{\ell m}}$, as originally proposed in Ref. [58], leads to a more accurate analytical waveform. This latter modelization is particularly relevant for binaries with anti-aligned spins.

We concluded this thesis by discussing in Chapter 6 hyperbolic scatterings and dynamical captures. We opened, as usual, by discussing the test particle limit, but we then rapidly moved to the comparable mass case, where dynamical captures are more likely to occur. In Sec. 6.2 we studied the phenomenologies of (initially) unbounded configurations prediction using `TEOBResumS-Dalì`, as done in Ref. [146]. We then discussed NR simulations of hyperbolic systems performed with the code `GR-Athena++`. In particular, we reported the `GR-Athena++`/`EinsteinToolkit` comparisons discussed in Ref. [7] and the EOB/NR comparisons shown in the Supplemental Material of Ref. [2]. We argued that there are practical difficulties in computing the multipolar strain by integrating the Weyl scalar ψ_4 using standard techniques (both in the time and frequency domains). We continued by presenting a few examples of a new dataset that is currently under development. While the main focus of Chapter 6 has been on dynamical captures, in Sec. 6.3 we also considered a scattering configuration, showing the EOB/NR comparisons both for the waveform and for the scattering angle.

Appendix A

Test mass fluxes from eccentric configurations

In this appendix we report the explicit analytical expressions of the noncircular Newtonian prefactors of the $(\ell, m) = (2,2), (2,1), (3,3), (3,2), (4,4)$ multipoles [1], both for the waveform and the angular radiation reaction. We also list in Table A.1 all the numerical geodesics simulations analyzed in Chapter 3. We also report the corresponding numerical averaged fluxes in the same table, together with their analytical counterparts. The latter have been computed using the energy balance equations (2.37) and the radiation reaction from Eqs. (2.46) and (3.7). A visual representation of the analytical/numerical relative differences for these fluxes is reported in Fig. 3.6.

A.1 Noncircular Newtonian prefactors for waveforms and fluxes

$$\hat{h}^{(N,0)_{\rm nc}}_{22} = 1 - \frac{\dot{r}^2}{2r^2\Omega^2} - \frac{\ddot{r}}{2r\Omega^2} + i\left(\frac{2\dot{r}}{r\Omega} + \frac{\dot{\Omega}}{2\Omega^2}\right), \tag{A.1}$$

$$\hat{h}^{(N,1)_{\rm nc}}_{21} = 1 - \frac{6\dot{r}^2}{r^2\Omega^2} - \frac{3\ddot{r}}{r\Omega^2} - \frac{6\dot{r}\dot{\Omega}}{r\Omega^3} - \frac{\ddot{\Omega}}{\Omega^3} + i\left(\frac{6\dot{r}}{r\Omega} + \frac{3\dot{\Omega}}{\Omega^2}\right), \tag{A.2}$$

$$\hat{h}^{(N,0)_{\rm nc}}_{33} = 1 - \frac{2\dot{r}^2}{r^2\Omega^2} - \frac{\ddot{r}}{r\Omega^2} - \frac{\dot{r}\dot{\Omega}}{r\Omega^3} - \frac{\ddot{\Omega}}{9\Omega^3} + i\left(-\frac{2\dot{r}^3}{9r^3\Omega^3} - \frac{2\ddot{r}\dot{r}}{3r^2\Omega^3} - \frac{r^{(3)}}{9r\Omega^3} + \frac{3\dot{r}}{r\Omega} + \frac{\dot{\Omega}}{\Omega^2}\right), \tag{A.3}$$

$$\hat{h}^{(N,1)_{\rm nc}}_{32} = 1 - \frac{9\dot{r}^2}{r^2\Omega^2} - \frac{3\ddot{r}}{r\Omega^2} - \frac{9\dot{r}\dot{\Omega}}{r\Omega^3} - \frac{3\dot{\Omega}^2}{4\Omega^4} - \frac{\ddot{\Omega}}{\Omega^3} + i\left(-\frac{3\dot{r}^3}{r^3\Omega^3} - \frac{9\ddot{r}\dot{r}}{2r^2\Omega^3} - \frac{9\dot{r}^2\dot{\Omega}}{2r^2\Omega^4} - \frac{3\ddot{r}\dot{\Omega}}{2r\Omega^4} - \frac{r^{(3)}}{2r\Omega^3} - \frac{3\dot{r}\ddot{\Omega}}{2r\Omega^4} + \frac{6\dot{r}}{r\Omega} - \frac{\Omega^{(3)}}{8\Omega^4} + \frac{3\dot{\Omega}}{\Omega^2}\right), \tag{A.4}$$

$$\hat{h}^{(N,0)_{\rm nc}}_{44} = 1 + \frac{3\dot{r}^4}{32r^4\Omega^4} + \frac{9\ddot{r}\dot{r}^2}{16r^3\Omega^4} + \frac{9\ddot{r}^2}{64r^2\Omega^4} + \frac{3r^{(3)}\dot{r}}{16r^2\Omega^4} - \frac{9\dot{r}^2}{2r^2\Omega^2} - \frac{3\ddot{r}}{2r\Omega^2}$$

$$+\frac{r^{(4)}}{64r\Omega^4}-\frac{3\dot{r}\dot{\Omega}}{r\Omega^3}-\frac{3\dot{\Omega}^2}{16\Omega^4}-\frac{\ddot{\Omega}}{4\Omega^3}+i\left(-\frac{3\dot{r}^3}{2r^3\Omega^3}-\frac{9\ddot{r}\dot{r}}{4r^2\Omega^3}\right.$$
$$\left.-\frac{9\dot{r}^2\dot{\Omega}}{8r^2\Omega^4}-\frac{3\ddot{r}\dot{\Omega}}{8r\Omega^4}-\frac{r^{(3)}}{4r\Omega^3}-\frac{\dot{r}\ddot{\Omega}}{4r\Omega^4}+\frac{4\dot{r}}{r\Omega}-\frac{\Omega^{(3)}}{64\Omega^4}+\frac{3\dot{\Omega}}{2\Omega^2}\right), \tag{A.5}$$

$$\hat{f}^{\mathrm{N_{nc}}}_{\varphi,22}=1+\frac{3\dot{r}^4}{4r^4\Omega^4}+\frac{3\dot{r}^3\dot{\Omega}}{4r^3\Omega^5}+\frac{3\ddot{r}^2}{4r^2\Omega^4}+\frac{3\ddot{r}\dot{r}\dot{\Omega}}{8r^2\Omega^5}-\frac{r^{(3)}\dot{r}}{2r^2\Omega^4}+\frac{\dot{r}^2\ddot{\Omega}}{8r^2\Omega^5}+\frac{4\dot{r}^2}{r^2\Omega^2}$$
$$+\frac{\ddot{r}\ddot{\Omega}}{8r\Omega^5}-\frac{2\ddot{r}}{r\Omega^2}-\frac{r^{(3)}\dot{\Omega}}{8r\Omega^5}+\frac{3\dot{r}\dot{\Omega}}{r\Omega^3}+\frac{3\dot{\Omega}^2}{4\Omega^4}-\frac{\ddot{\Omega}}{4\Omega^3}, \tag{A.6}$$

$$\hat{f}^{\mathrm{N_{nc}}}_{\varphi,21}=1+\frac{72\dot{r}^4}{r^4\Omega^4}+\frac{144\dot{r}^3\dot{\Omega}}{r^3\Omega^5}+\frac{27\ddot{r}^2}{r^2\Omega^4}+\frac{27\ddot{r}\dot{r}\dot{\Omega}}{r^2\Omega^5}-\frac{18r^{(3)}\dot{r}}{r^2\Omega^4}+\frac{126\dot{r}^2\dot{\Omega}^2}{r^2\Omega^6}-\frac{12\dot{r}^2\ddot{\Omega}}{r^2\Omega^5}$$
$$+\frac{30\dot{r}^2}{r^2\Omega^2}-\frac{18\ddot{r}\dot{\Omega}^2}{r\Omega^6}+\frac{21\ddot{r}\ddot{\Omega}}{r\Omega^5}-\frac{12\ddot{r}}{r\Omega^2}-\frac{9r^{(3)}\dot{\Omega}}{r\Omega^5}+\frac{18\dot{r}\dot{\Omega}^3}{r\Omega^7}+\frac{24\dot{r}\ddot{\Omega}\dot{\Omega}}{r\Omega^6}$$
$$-\frac{6\dot{r}\Omega^{(3)}}{r\Omega^5}+\frac{30\dot{r}\dot{\Omega}}{r\Omega^3}+\frac{3\ddot{\Omega}\dot{\Omega}^2}{\Omega^7}+\frac{4\ddot{\Omega}^2}{\Omega^6}-\frac{3\Omega^{(3)}\dot{\Omega}}{\Omega^6}+\frac{15\dot{\Omega}^2}{\Omega^4}-\frac{5\ddot{\Omega}}{\Omega^3}, \tag{A.7}$$

$$\hat{f}^{\mathrm{N_{nc}}}_{\varphi,33}=1+\frac{16\dot{r}^6}{81r^6\Omega^6}+\frac{8\ddot{r}\dot{r}^4}{27r^5\Omega^6}+\frac{8\dot{r}^5\dot{\Omega}}{27r^5\Omega^7}+\frac{8\ddot{r}^2\dot{r}^2}{9r^4\Omega^6}+\frac{16\ddot{r}\dot{r}^3\dot{\Omega}}{27r^4\Omega^7}-\frac{32r^{(3)}\dot{r}^3}{81r^4\Omega^6}$$
$$+\frac{8\dot{r}^4\ddot{\Omega}}{81r^4\Omega^7}+\frac{40\dot{r}^4}{9r^4\Omega^4}-\frac{2\ddot{r}^3}{9r^3\Omega^6}+\frac{2\ddot{r}^2\dot{r}\dot{\Omega}}{9r^3\Omega^7}+\frac{8\ddot{r}r^{(3)}\dot{r}}{27r^3\Omega^6}+\frac{20\ddot{r}\dot{r}^2\ddot{\Omega}}{81r^3\Omega^7}$$
$$-\frac{20\ddot{r}\dot{r}^2}{9r^3\Omega^4}-\frac{4r^{(3)}\dot{r}^2\dot{\Omega}}{27r^3\Omega^7}-\frac{2r^{(4)}\dot{r}^2}{27r^3\Omega^6}+\frac{2\dot{r}^3\Omega^{(3)}}{243r^3\Omega^7}+\frac{20\dot{r}^3\dot{\Omega}}{3r^3\Omega^5}-\frac{2\ddot{r}^2\ddot{\Omega}}{81r^2\Omega^7}$$
$$+\frac{20\ddot{r}^2}{9r^2\Omega^4}+\frac{2\ddot{r}r^{(3)}\dot{\Omega}}{27r^2\Omega^7}-\frac{\ddot{r}r^{(4)}}{27r^2\Omega^6}+\frac{2\ddot{r}\dot{r}\Omega^{(3)}}{81r^2\Omega^7}+\frac{4r^{(3)^2}}{81r^2\Omega^6}+\frac{4r^{(3)}\dot{r}\ddot{\Omega}}{243r^2\Omega^7}$$
$$-\frac{40r^{(3)}\dot{r}}{27r^2\Omega^4}-\frac{r^{(4)}\dot{r}\dot{\Omega}}{27r^2\Omega^7}+\frac{10\dot{r}^2\dot{\Omega}^2}{3r^2\Omega^6}+\frac{6\dot{r}^2}{r^2\Omega^2}-\frac{\ddot{r}\dot{\Omega}^2}{3r\Omega^6}+\frac{2\ddot{r}\ddot{\Omega}}{3r\Omega^5}-\frac{3\ddot{r}}{r\Omega^2}$$
$$+\frac{r^{(3)}\Omega^{(3)}}{243r\Omega^7}-\frac{2r^{(3)}\dot{\Omega}}{3r\Omega^5}-\frac{r^{(4)}\ddot{\Omega}}{243r\Omega^7}+\frac{r^{(4)}}{27r\Omega^4}+\frac{\dot{r}\dot{\Omega}^3}{3r\Omega^7}+\frac{4\dot{r}\ddot{\Omega}\dot{\Omega}}{9r\Omega^6}-\frac{\dot{r}\Omega^{(3)}}{9r\Omega^5}$$
$$+\frac{5\dot{r}\dot{\Omega}}{r\Omega^3}+\frac{\ddot{\Omega}\dot{\Omega}^2}{27\Omega^7}+\frac{4\ddot{\Omega}^2}{81\Omega^6}-\frac{\Omega^{(3)}\dot{\Omega}}{27\Omega^6}+\frac{5\dot{\Omega}^2}{3\Omega^4}-\frac{5\ddot{\Omega}}{9\Omega^3}, \tag{A.8}$$

$$\hat{f}^{\mathrm{N_{nc}}}_{\varphi,32}=1+\frac{45\dot{r}^6}{2r^6\Omega^6}+\frac{135\dot{\Omega}\dot{r}^5}{2r^5\Omega^7}+\frac{675\dot{\Omega}^2\dot{r}^4}{8r^4\Omega^8}+\frac{135\dot{r}^4}{2r^4\Omega^4}+\frac{45\ddot{r}\dot{r}^4}{2r^5\Omega^6}+\frac{45\dot{\Omega}^3\dot{r}^3}{2r^3\Omega^9}-\frac{45\Omega^{(3)}\dot{r}^3}{8r^3\Omega^7}$$
$$+\frac{135\ddot{\Omega}\dot{\Omega}\dot{r}^3}{4r^3\Omega^8}+\frac{135\dot{\Omega}\dot{r}^3}{r^3\Omega^5}+\frac{135\ddot{r}\dot{\Omega}\dot{r}^3}{2r^4\Omega^7}-\frac{15r^{(3)}\dot{r}^3}{r^4\Omega^6}+\frac{15\ddot{\Omega}^2\dot{r}^2}{2r^2\Omega^8}+\frac{45\ddot{\Omega}\dot{\Omega}^2\dot{r}^2}{4r^2\Omega^9}$$
$$+\frac{495\dot{\Omega}^2\dot{r}^2}{4r^2\Omega^6}+\frac{81\ddot{r}\dot{\Omega}^2\dot{r}^2}{4r^3\Omega^8}-\frac{15\ddot{\Omega}\dot{r}^2}{r^2\Omega^5}+\frac{27\ddot{r}\ddot{\Omega}\dot{r}^2}{r^3\Omega^7}-\frac{9\Omega^{(4)}\dot{r}^2}{16r^2\Omega^7}-\frac{45\Omega^{(3)}\dot{\Omega}\dot{r}^2}{16r^2\Omega^8}$$
$$-\frac{27r^{(3)}\dot{\Omega}\dot{r}^2}{2r^3\Omega^7}+\frac{21\dot{r}^2}{r^2\Omega^2}-\frac{27\ddot{r}\dot{r}^2}{r^3\Omega^4}+\frac{135\ddot{r}^2\dot{r}^2}{4r^4\Omega^6}-\frac{9r^{(4)}\dot{r}^2}{4r^3\Omega^6}+\frac{135\dot{\Omega}^3\dot{r}}{4r\Omega^7}+\frac{9\ddot{r}\dot{\Omega}^3\dot{r}}{4r^2\Omega^9}$$
$$-\frac{33r^{(3)}\dot{\Omega}^2\dot{r}}{4r^2\Omega^8}+\frac{4r^{(3)}\ddot{\Omega}\dot{r}}{r^2\Omega^7}+\frac{15\ddot{\Omega}\Omega^{(3)}\dot{r}}{16r\Omega^8}-\frac{15\Omega^{(3)}\dot{r}}{4r\Omega^5}+\frac{33\ddot{r}\Omega^{(3)}\dot{r}}{16r^2\Omega^7}+\frac{15\ddot{\Omega}^2\dot{\Omega}\dot{r}}{8r\Omega^9}$$
$$+\frac{15\ddot{\Omega}\dot{\Omega}\dot{r}}{2r\Omega^6}+\frac{69\ddot{r}\ddot{\Omega}\dot{\Omega}\dot{r}}{8r^2\Omega^8}-\frac{9\Omega^{(4)}\dot{\Omega}\dot{r}}{16r\Omega^8}+\frac{21\dot{\Omega}\dot{r}}{r\Omega^3}-\frac{15\ddot{r}\dot{\Omega}\dot{r}}{2r^2\Omega^5}+\frac{81\ddot{r}^2\dot{\Omega}\dot{r}}{4r^3\Omega^7}-\frac{9r^{(4)}\dot{\Omega}\dot{r}}{4r^2\Omega^7}$$
$$-\frac{13r^{(3)}\dot{r}}{r^2\Omega^4}+\frac{9\ddot{r}r^{(3)}\dot{r}}{r^3\Omega^6}+\frac{45\dot{\Omega}^4}{16\Omega^8}-\frac{3r^{(3)}\dot{\Omega}^3}{4r\Omega^9}+\frac{5\ddot{\Omega}^2}{2\Omega^6}-\frac{3\ddot{r}\ddot{\Omega}^2}{2r\Omega^8}+\frac{5\Omega^{(3)^2}}{64\Omega^8}$$

$$
\begin{aligned}
&+\frac{15\ddot{\Omega}\dot{\Omega}^2}{8\Omega^7}+\frac{3\ddot{r}\ddot{\Omega}\dot{\Omega}^2}{4r\Omega^9}-\frac{3\Omega^{(4)}\dot{\Omega}^2}{64\Omega^9}+\frac{21\dot{\Omega}^2}{2\Omega^4}-\frac{75\ddot{r}\dot{\Omega}^2}{4r\Omega^6}+\frac{189\ddot{r}^2\dot{\Omega}^2}{16r^2\Omega^8}-\frac{3r^{(4)}\dot{\Omega}^2}{16r\Omega^8}\\
&-\frac{7\ddot{\Omega}}{2\Omega^3}+\frac{15\ddot{r}\ddot{\Omega}}{r\Omega^5}-\frac{27\ddot{r}^2\ddot{\Omega}}{4r^2\Omega^7}-\frac{r^{(4)}\ddot{\Omega}}{4r\Omega^7}+\frac{9r^{(3)}\Omega^{(3)}}{16r\Omega^7}-\frac{\ddot{\Omega}\Omega^{(4)}}{16\Omega^8}+\frac{\Omega^{(4)}}{16\Omega^5}-\frac{3\ddot{r}\Omega^{(4)}}{16r\Omega^7}\\
&-\frac{3r^{(3)}\ddot{\Omega}\dot{\Omega}}{8r\Omega^8}+\frac{5\ddot{\Omega}\Omega^{(3)}\dot{\Omega}}{32\Omega^9}-\frac{5\Omega^{(3)}\dot{\Omega}}{2\Omega^6}+\frac{33\ddot{r}\Omega^{(3)}\dot{\Omega}}{16r\Omega^8}-\frac{15r^{(3)}\dot{\Omega}}{2r\Omega^5}+\frac{9\ddot{r}r^{(3)}\dot{\Omega}}{2r^2\Omega^7}-\frac{9\ddot{r}}{r\Omega^2}\\
&+\frac{81\ddot{r}^2}{4r^2\Omega^4}+\frac{r^{(4)}}{4r\Omega^4}-\frac{27\ddot{r}^3}{4r^3\Omega^6}+\frac{{r^{(3)}}^2}{r^2\Omega^6}-\frac{3\ddot{r}r^{(4)}}{4r^2\Omega^6},
\end{aligned}
\tag{A.9}
$$

$$
\begin{aligned}
\hat{f}^{\mathrm{N_{nc}}}_{\varphi,44}=1&+\frac{45\dot{r}^8}{1024r^8\Omega^8}+\frac{45\dot{\Omega}\dot{r}^7}{512r^7\Omega^9}+\frac{45\ddot{\Omega}\dot{r}^6}{1024r^6\Omega^9}+\frac{45\dot{r}^6}{16r^6\Omega^6}+\frac{45\ddot{r}\dot{r}^6}{256r^7\Omega^8}+\frac{15\Omega^{(3)}\dot{r}^5}{2048r^5\Omega^9}\\
&+\frac{405\dot{\Omega}\dot{r}^5}{64r^5\Omega^7}+\frac{405\ddot{r}\dot{\Omega}\dot{r}^5}{1024r^6\Omega^9}-\frac{45r^{(3)}\dot{r}^5}{256r^6\Omega^8}+\frac{1215\dot{\Omega}^2\dot{r}^4}{256r^4\Omega^8}+\frac{135\ddot{\Omega}\dot{r}^4}{256r^4\Omega^7}+\frac{225\ddot{r}\ddot{\Omega}\dot{r}^4}{1024r^5\Omega^9}+\\
&\frac{3\Omega^{(4)}\dot{r}^4}{8192r^4\Omega^9}-\frac{75r^{(3)}\dot{\Omega}\dot{r}^4}{1024r^5\Omega^9}+\frac{189\dot{r}^4}{16r^4\Omega^4}+\frac{675\ddot{r}^2\dot{r}^4}{1024r^6\Omega^8}-\frac{75r^{(4)}\dot{r}^4}{1024r^5\Omega^8}+\frac{225\dot{\Omega}^3\dot{r}^3}{256r^3\Omega^9}\\
&+\frac{15r^{(3)}\ddot{\Omega}\dot{r}^3}{512r^4\Omega^9}-\frac{45\Omega^{(3)}\dot{r}^3}{256r^3\Omega^7}+\frac{165\ddot{r}\Omega^{(3)}\dot{r}^3}{4096r^4\Omega^9}+\frac{45\ddot{\Omega}\dot{\Omega}\dot{r}^3}{32r^3\Omega^8}+\frac{315\dot{\Omega}\dot{r}^3}{16r^3\Omega^5}+\frac{405\ddot{r}\dot{\Omega}\dot{r}^3}{128r^4\Omega^7}\\
&+\frac{225\ddot{r}^2\dot{\Omega}\dot{r}^3}{512r^5\Omega^9}-\frac{105r^{(4)}\dot{\Omega}\dot{r}^3}{2048r^4\Omega^9}-\frac{45r^{(3)}\dot{r}^3}{16r^4\Omega^6}+\frac{75\ddot{r}r^{(3)}\dot{r}^3}{256r^5\Omega^8}-\frac{3r^{(5)}\dot{r}^3}{512r^4\Omega^8}+\frac{25\ddot{\Omega}^2\dot{r}^2}{128r^2\Omega^8}\\
&+\frac{165\ddot{\Omega}\dot{\Omega}^2\dot{r}^2}{512r^2\Omega^9}+\frac{105\dot{\Omega}^2\dot{r}^2}{8r^2\Omega^6}+\frac{135\ddot{r}\dot{\Omega}^2\dot{r}^2}{128r^3\Omega^8}-\frac{35\ddot{\Omega}\dot{r}^2}{32r^2\Omega^5}+\frac{225\ddot{r}\ddot{\Omega}\dot{r}^2}{128r^3\Omega^7}+\frac{135\ddot{r}^2\ddot{\Omega}\dot{r}^2}{2048r^4\Omega^9}\\
&-\frac{15r^{(4)}\ddot{\Omega}\dot{r}^2}{2048r^3\Omega^9}+\frac{45r^{(3)}\Omega^{(3)}\dot{r}^2}{4096r^3\Omega^9}-\frac{9\Omega^{(4)}\dot{r}^2}{512r^2\Omega^7}+\frac{9\ddot{r}\Omega^{(4)}\dot{r}^2}{4096r^3\Omega^9}-\frac{15\Omega^{(3)}\dot{\Omega}\dot{r}^2}{256r^2\Omega^8}-\frac{315r^{(3)}\dot{\Omega}\dot{r}^2}{128r^3\Omega^7}\\
&+\frac{135\ddot{r}r^{(3)}\dot{\Omega}\dot{r}^2}{1024r^4\Omega^9}-\frac{9r^{(5)}\dot{\Omega}\dot{r}^2}{2048r^3\Omega^9}+\frac{8\dot{r}^2}{r^2\Omega^2}-\frac{63\ddot{r}\dot{r}^2}{8r^3\Omega^4}+\frac{135\ddot{r}^2\dot{r}^2}{32r^4\Omega^6}-\frac{15r^{(4)}\dot{r}^2}{64r^3\Omega^6}+\frac{15{r^{(3)}}^2\dot{r}^2}{128r^4\Omega^8}\\
&-\frac{45\ddot{r}r^{(4)}\dot{r}^2}{1024r^4\Omega^8}+\frac{45\dot{\Omega}^3\dot{r}}{16r\Omega^7}+\frac{45\ddot{r}\dot{\Omega}^3\dot{r}}{512r^2\Omega^9}-\frac{75r^{(3)}\dot{\Omega}^2\dot{r}}{128r^2\Omega^8}+\frac{15r^{(3)}\ddot{\Omega}\dot{r}}{128r^2\Omega^7}-\frac{r^{(5)}\ddot{\Omega}\dot{r}}{1024r^2\Omega^9}\\
&+\frac{5\ddot{\Omega}\Omega^{(3)}\dot{r}}{256r\Omega^8}-\frac{5\Omega^{(3)}\dot{r}}{16r\Omega^5}+\frac{75\ddot{r}\Omega^{(3)}\dot{r}}{512r^2\Omega^7}+\frac{45\ddot{r}^2\Omega^{(3)}\dot{r}}{8192r^3\Omega^9}+\frac{5r^{(4)}\Omega^{(3)}\dot{r}}{16384r^2\Omega^9}+\frac{3r^{(3)}\Omega^{(4)}\dot{r}}{4096r^2\Omega^9}\\
&+\frac{5\ddot{\Omega}^2\dot{\Omega}\dot{r}}{128r\Omega^9}+\frac{5\ddot{\Omega}\dot{\Omega}\dot{r}}{8r\Omega^6}+\frac{15\ddot{r}\ddot{\Omega}\dot{\Omega}\dot{r}}{32r^2\Omega^8}-\frac{3\Omega^{(4)}\dot{\Omega}\dot{r}}{256r\Omega^8}+\frac{7\dot{\Omega}\dot{r}}{r\Omega^3}-\frac{105\ddot{r}\dot{\Omega}\dot{r}}{32r^2\Omega^5}+\frac{405\ddot{r}^2\dot{\Omega}\dot{r}}{256r^3\Omega^7}\\
&-\frac{135r^{(4)}\dot{\Omega}\dot{r}}{512r^2\Omega^7}+\frac{135\ddot{r}^3\dot{\Omega}\dot{r}}{2048r^4\Omega^9}+\frac{15{r^{(3)}}^2\dot{\Omega}\dot{r}}{512r^3\Omega^9}-\frac{21r^{(3)}\dot{r}}{8r^2\Omega^4}+\frac{45\ddot{r}r^{(3)}\dot{r}}{32r^3\Omega^6}+\frac{r^{(5)}\dot{r}}{64r^2\Omega^6}\\
&-\frac{45\ddot{r}^2r^{(3)}\dot{r}}{512r^4\Omega^8}+\frac{15r^{(3)}r^{(4)}\dot{r}}{1024r^3\Omega^8}-\frac{9\ddot{r}r^{(5)}\dot{r}}{1024r^3\Omega^8}+\frac{45\dot{\Omega}^4}{256\Omega^8}-\frac{15r^{(3)}\dot{\Omega}^3}{512r\Omega^9}+\frac{5\ddot{\Omega}^2}{32\Omega^6}\\
&-\frac{5\ddot{r}\ddot{\Omega}^2}{128r\Omega^8}+\frac{5{\Omega^{(3)}}^2}{4096\Omega^8}+\frac{15\ddot{\Omega}\dot{\Omega}^2}{128\Omega^7}+\frac{15\ddot{r}\ddot{\Omega}\dot{\Omega}^2}{512r\Omega^9}-\frac{3\Omega^{(4)}\dot{\Omega}^2}{4096\Omega^9}+\frac{21\dot{\Omega}^2}{8\Omega^4}-\frac{15\ddot{r}\dot{\Omega}^2}{8r\Omega^6}\\
&+\frac{225\ddot{r}^2\dot{\Omega}^2}{512r^2\Omega^8}-\frac{15r^{(4)}\dot{\Omega}^2}{512r\Omega^8}-\frac{7\ddot{\Omega}}{8\Omega^3}+\frac{55\ddot{r}\ddot{\Omega}}{32r\Omega^5}-\frac{255\ddot{r}^2\ddot{\Omega}}{512r^2\Omega^7}-\frac{15r^{(4)}\ddot{\Omega}}{512r\Omega^7}+\frac{45\ddot{r}^3\ddot{\Omega}}{2048r^3\Omega^9}\\
&+\frac{5\ddot{r}r^{(4)}\ddot{\Omega}}{2048r^2\Omega^9}+\frac{15r^{(3)}\Omega^{(3)}}{512r\Omega^7}-\frac{15\ddot{r}r^{(3)}\Omega^{(3)}}{8192r^2\Omega^9}-\frac{r^{(5)}\Omega^{(3)}}{16384r\Omega^9}-\frac{\dot{\Omega}\Omega^{(4)}}{1024\Omega^8}+\frac{\Omega^{(4)}}{256\Omega^5}\\
&-\frac{3\ddot{r}\Omega^{(4)}}{512r\Omega^7}+\frac{9\ddot{r}^2\Omega^{(4)}}{16384r^2\Omega^9}+\frac{r^{(4)}\Omega^{(4)}}{16384r\Omega^9}+\frac{5\ddot{\Omega}\Omega^{(3)}\dot{\Omega}}{2048\Omega^9}-\frac{5\Omega^{(3)}\dot{\Omega}}{32\Omega^6}+\frac{15\ddot{r}\Omega^{(3)}\dot{\Omega}}{256r\Omega^8}\\
&-\frac{45r^{(3)}\dot{\Omega}}{32r\Omega^5}+\frac{165\ddot{r}r^{(3)}\dot{\Omega}}{256r^2\Omega^7}+\frac{3r^{(5)}\dot{\Omega}}{512r\Omega^7}-\frac{45\ddot{r}^2r^{(3)}\dot{\Omega}}{2048r^3\Omega^9}+\frac{5r^{(3)}r^{(4)}\dot{\Omega}}{2048r^2\Omega^9}-\frac{3\ddot{r}r^{(5)}\dot{\Omega}}{2048r^2\Omega^9}
\end{aligned}
$$

$$
\begin{aligned}
&- \frac{4\ddot{r}}{r\Omega^2} + \frac{147\ddot{r}^2}{32r^2\Omega^4} + \frac{3r^{(4)}}{32r\Omega^4} - \frac{45\ddot{r}^3}{32r^3\Omega^6} + \frac{5{r^{(3)}}^2}{32r^2\Omega^6} - \frac{5\ddot{r}r^{(4)}}{32r^2\Omega^6} + \frac{405\ddot{r}^4}{4096r^4\Omega^8} \\
&- \frac{15\ddot{r}{r^{(3)}}^2}{512r^3\Omega^8} + \frac{5{r^{(4)}}^2}{4096r^2\Omega^8} + \frac{45\ddot{r}^2r^{(4)}}{2048r^3\Omega^8} - \frac{r^{(3)}r^{(5)}}{1024r^2\Omega^8}.
\end{aligned} \tag{A.10}
$$

A.2 Geodesic eccentric configurations

Table A.1: List of geodesic eccentric configurations considered in Chapter 3, together with the corresponding numerical and analytical averaged fluxes and relative differences. For each eccentricity, there are three blocks of simulations, one for each class of semilatera recta: near, intermediate and distant; see discussion in Sec. 3.1. The relative differences for the fluxes are visualized in Fig. 3.6. From Ref. [1].

e	$\hat{a}$	p	p_s	$\langle \dot{E}_{\rm teuk} \rangle$	$\langle \dot{E}_{\rm NP} \rangle$	$\Delta E_{\rm NP}/E$	$\langle \dot{J}_{\rm teuk} \rangle$	$\langle \dot{J}_{\rm NP} \rangle$	$\Delta J_{\rm NP}/J$
0.0	−0.9	8.727	8.717	$1.732 \cdot 10^{-4}$	$1.731 \cdot 10^{-4}$	$4.9 \cdot 10^{-4}$	$4.309 \cdot 10^{-3}$	$4.307 \cdot 10^{-3}$	$4.9 \cdot 10^{-4}$
0.0	−0.8	8.442	8.432	$2.017 \cdot 10^{-4}$	$2.016 \cdot 10^{-4}$	$5.7 \cdot 10^{-4}$	$4.786 \cdot 10^{-3}$	$4.783 \cdot 10^{-3}$	$5.7 \cdot 10^{-4}$
0.0	−0.7	8.153	8.143	$2.365 \cdot 10^{-4}$	$2.364 \cdot 10^{-4}$	$6.7 \cdot 10^{-4}$	$5.341 \cdot 10^{-3}$	$5.337 \cdot 10^{-3}$	$6.7 \cdot 10^{-4}$
0.0	−0.6	7.861	7.851	$2.794 \cdot 10^{-4}$	$2.792 \cdot 10^{-4}$	$7.9 \cdot 10^{-4}$	$5.991 \cdot 10^{-3}$	$5.986 \cdot 10^{-3}$	$7.9 \cdot 10^{-4}$
0.0	−0.5	7.565	7.555	$3.326 \cdot 10^{-4}$	$3.323 \cdot 10^{-4}$	$9.4 \cdot 10^{-4}$	$6.754 \cdot 10^{-3}$	$6.748 \cdot 10^{-3}$	$9.4 \cdot 10^{-4}$
0.0	−0.4	7.264	7.254	$3.995 \cdot 10^{-4}$	$3.990 \cdot 10^{-4}$	$1.1 \cdot 10^{-3}$	$7.661 \cdot 10^{-3}$	$7.653 \cdot 10^{-3}$	$1.1 \cdot 10^{-3}$
0.0	−0.3	6.959	6.949	$4.843 \cdot 10^{-4}$	$4.836 \cdot 10^{-4}$	$1.4 \cdot 10^{-3}$	$8.745 \cdot 10^{-3}$	$8.734 \cdot 10^{-3}$	$1.4 \cdot 10^{-3}$
0.0	−0.2	6.649	6.639	$5.938 \cdot 10^{-4}$	$5.928 \cdot 10^{-4}$	$1.7 \cdot 10^{-3}$	$1.006 \cdot 10^{-2}$	$1.004 \cdot 10^{-2}$	$1.7 \cdot 10^{-3}$
0.0	−0.1	6.333	6.323	$7.374 \cdot 10^{-4}$	$7.359 \cdot 10^{-4}$	$2.0 \cdot 10^{-3}$	$1.168 \cdot 10^{-2}$	$1.165 \cdot 10^{-2}$	$2.0 \cdot 10^{-3}$
0.0	0.0	6.010	6.000	$9.287 \cdot 10^{-4}$	$9.264 \cdot 10^{-4}$	$2.5 \cdot 10^{-3}$	$1.368 \cdot 10^{-2}$	$1.365 \cdot 10^{-2}$	$2.5 \cdot 10^{-3}$
0.0	0.1	5.679	5.669	$1.189 \cdot 10^{-3}$	$1.185 \cdot 10^{-3}$	$3.2 \cdot 10^{-3}$	$1.621 \cdot 10^{-2}$	$1.616 \cdot 10^{-2}$	$3.2 \cdot 10^{-3}$
0.0	0.2	5.339	5.329	$1.553 \cdot 10^{-3}$	$1.547 \cdot 10^{-3}$	$4.0 \cdot 10^{-3}$	$1.947 \cdot 10^{-2}$	$1.939 \cdot 10^{-2}$	$4.0 \cdot 10^{-3}$
0.0	0.3	4.989	4.979	$2.075 \cdot 10^{-3}$	$2.064 \cdot 10^{-3}$	$5.2 \cdot 10^{-3}$	$2.375 \cdot 10^{-2}$	$2.362 \cdot 10^{-2}$	$5.2 \cdot 10^{-3}$
0.0	0.4	4.624	4.614	$2.857 \cdot 10^{-3}$	$2.837 \cdot 10^{-3}$	$6.9 \cdot 10^{-3}$	$2.955 \cdot 10^{-2}$	$2.935 \cdot 10^{-2}$	$6.9 \cdot 10^{-3}$
0.0	0.5	4.243	4.233	$4.072 \cdot 10^{-3}$	$4.034 \cdot 10^{-3}$	$9.4 \cdot 10^{-3}$	$3.763 \cdot 10^{-2}$	$3.728 \cdot 10^{-2}$	$9.4 \cdot 10^{-3}$
0.0	0.6	3.839	3.829	$6.089 \cdot 10^{-3}$	$6.008 \cdot 10^{-3}$	$1.3 \cdot 10^{-2}$	$4.945 \cdot 10^{-2}$	$4.880 \cdot 10^{-2}$	$1.3 \cdot 10^{-2}$
0.0	0.7	3.403	3.393	$9.715 \cdot 10^{-3}$	$9.520 \cdot 10^{-3}$	$2.0 \cdot 10^{-2}$	$6.779 \cdot 10^{-2}$	$6.643 \cdot 10^{-2}$	$2.0 \cdot 10^{-2}$
0.0	0.8	2.917	2.907	$1.709 \cdot 10^{-2}$	$1.652 \cdot 10^{-2}$	$3.3 \cdot 10^{-2}$	$9.882 \cdot 10^{-2}$	$9.551 \cdot 10^{-2}$	$3.3 \cdot 10^{-2}$
0.0	0.9	2.331	2.321	$3.552 \cdot 10^{-2}$	$3.312 \cdot 10^{-2}$	$6.7 \cdot 10^{-2}$	$1.583 \cdot 10^{-1}$	$1.477 \cdot 10^{-1}$	$6.7 \cdot 10^{-2}$
0.0	−0.9	13.076	8.717	$1.837 \cdot 10^{-5}$	$1.837 \cdot 10^{-5}$	$9.1 \cdot 10^{-5}$	$8.520 \cdot 10^{-4}$	$8.519 \cdot 10^{-4}$	$9.2 \cdot 10^{-5}$
0.0	−0.6	11.776	7.851	$3.015 \cdot 10^{-5}$	$3.015 \cdot 10^{-5}$	$8.8 \cdot 10^{-5}$	$1.200 \cdot 10^{-3}$	$1.200 \cdot 10^{-3}$	$8.9 \cdot 10^{-5}$
0.0	−0.2	9.959	6.639	$6.618 \cdot 10^{-5}$	$6.617 \cdot 10^{-5}$	$1.3 \cdot 10^{-4}$	$2.066 \cdot 10^{-3}$	$2.066 \cdot 10^{-3}$	$1.3 \cdot 10^{-4}$
0.0	0.0	9.000	6.000	$1.059 \cdot 10^{-4}$	$1.059 \cdot 10^{-4}$	$1.8 \cdot 10^{-4}$	$2.859 \cdot 10^{-3}$	$2.859 \cdot 10^{-3}$	$1.8 \cdot 10^{-4}$
0.0	0.2	7.994	5.329	$1.827 \cdot 10^{-4}$	$1.827 \cdot 10^{-4}$	$2.8 \cdot 10^{-4}$	$4.167 \cdot 10^{-3}$	$4.166 \cdot 10^{-3}$	$2.8 \cdot 10^{-4}$
0.0	0.6	5.744	3.829	$8.083 \cdot 10^{-4}$	$8.074 \cdot 10^{-4}$	$1.1 \cdot 10^{-3}$	$1.161 \cdot 10^{-2}$	$1.160 \cdot 10^{-2}$	$1.1 \cdot 10^{-3}$
0.0	0.9	3.481	2.321	$6.623 \cdot 10^{-3}$	$6.552 \cdot 10^{-3}$	$1.1 \cdot 10^{-2}$	$4.898 \cdot 10^{-2}$	$4.846 \cdot 10^{-2}$	$1.1 \cdot 10^{-2}$
0.0	−0.9	18.888	8.717	$2.702 \cdot 10^{-6}$	$2.702 \cdot 10^{-6}$	$1.3 \cdot 10^{-4}$	$2.194 \cdot 10^{-4}$	$2.194 \cdot 10^{-4}$	$1.4 \cdot 10^{-4}$
0.0	−0.6	17.010	7.851	$4.477 \cdot 10^{-6}$	$4.476 \cdot 10^{-6}$	$9.9 \cdot 10^{-5}$	$3.114 \cdot 10^{-4}$	$3.114 \cdot 10^{-4}$	$1.1 \cdot 10^{-4}$
0.0	−0.2	14.385	6.639	$1.000 \cdot 10^{-5}$	$1.000 \cdot 10^{-5}$	$7.6 \cdot 10^{-5}$	$5.438 \cdot 10^{-4}$	$5.438 \cdot 10^{-4}$	$7.6 \cdot 10^{-5}$
0.0	0.0	13.000	6.000	$1.621 \cdot 10^{-5}$	$1.621 \cdot 10^{-5}$	$6.5 \cdot 10^{-5}$	$7.598 \cdot 10^{-4}$	$7.597 \cdot 10^{-4}$	$6.2 \cdot 10^{-5}$
0.0	0.2	11.547	5.329	$2.843 \cdot 10^{-5}$	$2.843 \cdot 10^{-5}$	$5.8 \cdot 10^{-5}$	$1.121 \cdot 10^{-3}$	$1.121 \cdot 10^{-3}$	$5.8 \cdot 10^{-5}$
0.0	0.6	8.296	3.829	$1.336 \cdot 10^{-4}$	$1.335 \cdot 10^{-4}$	$1.1 \cdot 10^{-4}$	$3.272 \cdot 10^{-3}$	$3.271 \cdot 10^{-3}$	$1.1 \cdot 10^{-4}$
0.0	0.9	5.029	2.321	$1.280 \cdot 10^{-3}$	$1.278 \cdot 10^{-3}$	$1.4 \cdot 10^{-3}$	$1.558 \cdot 10^{-2}$	$1.556 \cdot 10^{-2}$	$1.4 \cdot 10^{-3}$
0.1	−0.9	9.014	9.004	$1.870 \cdot 10^{-4}$	$1.869 \cdot 10^{-4}$	$3.8 \cdot 10^{-4}$	$4.505 \cdot 10^{-3}$	$4.503 \cdot 10^{-3}$	$4.3 \cdot 10^{-4}$
0.1	−0.6	8.119	8.109	$3.002 \cdot 10^{-4}$	$3.000 \cdot 10^{-4}$	$7.8 \cdot 10^{-4}$	$6.241 \cdot 10^{-3}$	$6.236 \cdot 10^{-3}$	$8.2 \cdot 10^{-4}$
0.1	−0.2	6.869	6.859	$6.329 \cdot 10^{-4}$	$6.317 \cdot 10^{-4}$	$1.9 \cdot 10^{-3}$	$1.042 \cdot 10^{-2}$	$1.040 \cdot 10^{-2}$	$1.9 \cdot 10^{-3}$
0.1	0.0	6.210	6.200	$9.845 \cdot 10^{-4}$	$9.814 \cdot 10^{-4}$	$3.1 \cdot 10^{-3}$	$1.412 \cdot 10^{-2}$	$1.408 \cdot 10^{-2}$	$3.0 \cdot 10^{-3}$
0.1	0.2	5.518	5.508	$1.636 \cdot 10^{-3}$	$1.628 \cdot 10^{-3}$	$5.0 \cdot 10^{-3}$	$2.001 \cdot 10^{-2}$	$1.991 \cdot 10^{-2}$	$4.9 \cdot 10^{-3}$
0.1	0.6	3.970	3.960	$6.300 \cdot 10^{-3}$	$6.200 \cdot 10^{-3}$	$1.6 \cdot 10^{-2}$	$5.022 \cdot 10^{-2}$	$4.945 \cdot 10^{-2}$	$1.6 \cdot 10^{-2}$
0.1	0.9	2.415	2.405	$3.566 \cdot 10^{-2}$	$3.308 \cdot 10^{-2}$	$7.2 \cdot 10^{-2}$	$1.578 \cdot 10^{-1}$	$1.466 \cdot 10^{-1}$	$7.1 \cdot 10^{-2}$
0.1	−0.9	13.070	9.004	$1.897 \cdot 10^{-5}$	$1.901 \cdot 10^{-5}$	$-2.1 \cdot 10^{-3}$	$8.583 \cdot 10^{-4}$	$8.593 \cdot 10^{-4}$	$-1.2 \cdot 10^{-3}$
0.1	−0.6	11.772	8.109	$3.112 \cdot 10^{-5}$	$3.117 \cdot 10^{-5}$	$-1.7 \cdot 10^{-3}$	$1.209 \cdot 10^{-3}$	$1.210 \cdot 10^{-3}$	$-8.1 \cdot 10^{-4}$
0.1	−0.2	9.957	6.859	$6.825 \cdot 10^{-5}$	$6.830 \cdot 10^{-5}$	$-8.3 \cdot 10^{-4}$	$2.081 \cdot 10^{-3}$	$2.081 \cdot 10^{-3}$	$-6.0 \cdot 10^{-5}$
0.1	0.0	9.000	6.200	$1.091 \cdot 10^{-4}$	$1.092 \cdot 10^{-4}$	$-1.8 \cdot 10^{-4}$	$2.878 \cdot 10^{-3}$	$2.877 \cdot 10^{-3}$	$4.9 \cdot 10^{-4}$
0.1	0.2	7.996	5.508	$1.882 \cdot 10^{-4}$	$1.880 \cdot 10^{-4}$	$7.2 \cdot 10^{-4}$	$4.194 \cdot 10^{-3}$	$4.188 \cdot 10^{-3}$	$1.2 \cdot 10^{-3}$
0.1	0.6	5.749	3.960	$8.299 \cdot 10^{-4}$	$8.262 \cdot 10^{-4}$	$4.5 \cdot 10^{-3}$	$1.167 \cdot 10^{-2}$	$1.162 \cdot 10^{-2}$	$4.4 \cdot 10^{-3}$
0.1	0.9	3.491	2.405	$6.735 \cdot 10^{-3}$	$6.596 \cdot 10^{-3}$	$2.1 \cdot 10^{-2}$	$4.903 \cdot 10^{-2}$	$4.811 \cdot 10^{-2}$	$1.9 \cdot 10^{-2}$
0.1	−0.9	18.879	9.004	$2.768 \cdot 10^{-6}$	$2.773 \cdot 10^{-6}$	$-1.8 \cdot 10^{-3}$	$2.196 \cdot 10^{-4}$	$2.198 \cdot 10^{-4}$	$-8.6 \cdot 10^{-4}$
0.1	−0.6	17.004	8.109	$4.584 \cdot 10^{-6}$	$4.590 \cdot 10^{-6}$	$-1.5 \cdot 10^{-3}$	$3.117 \cdot 10^{-4}$	$3.118 \cdot 10^{-4}$	$-6.0 \cdot 10^{-4}$
0.1	−0.2	14.382	6.859	$1.023 \cdot 10^{-5}$	$1.024 \cdot 10^{-5}$	$-9.1 \cdot 10^{-4}$	$5.440 \cdot 10^{-4}$	$5.441 \cdot 10^{-4}$	$-6.7 \cdot 10^{-5}$
0.1	0.0	13.000	6.200	$1.657 \cdot 10^{-5}$	$1.658 \cdot 10^{-5}$	$-4.7 \cdot 10^{-4}$	$7.598 \cdot 10^{-4}$	$7.596 \cdot 10^{-4}$	$3.2 \cdot 10^{-4}$

Continued on next page

Table A.1 – continued from previous page

e	$\hat{a}$	p	p_s	$\langle \dot{E}_{\rm teuk} \rangle$	$\langle \dot{E}_{\rm NP} \rangle$	$\Delta E_{\rm NP}/E$	$\langle \dot{J}_{\rm teuk} \rangle$	$\langle \dot{J}_{\rm NP} \rangle$	$\Delta J_{\rm NP}/J$
0.1	0.2	11.549	5.508	$2.904 \cdot 10^{-5}$	$2.904 \cdot 10^{-5}$	$1.2 \cdot 10^{-4}$	$1.121 \cdot 10^{-3}$	$1.120 \cdot 10^{-3}$	$8.4 \cdot 10^{-4}$
0.1	0.6	8.304	3.960	$1.360 \cdot 10^{-4}$	$1.357 \cdot 10^{-4}$	$2.4 \cdot 10^{-3}$	$3.266 \cdot 10^{-3}$	$3.257 \cdot 10^{-3}$	$2.7 \cdot 10^{-3}$
0.1	0.9	5.043	2.405	$1.293 \cdot 10^{-3}$	$1.281 \cdot 10^{-3}$	$8.8 \cdot 10^{-3}$	$1.549 \cdot 10^{-2}$	$1.537 \cdot 10^{-2}$	$7.9 \cdot 10^{-3}$
0.3	−0.9	9.564	9.554	$2.546 \cdot 10^{-4}$	$2.550 \cdot 10^{-4}$	$-1.4 \cdot 10^{-3}$	$5.324 \cdot 10^{-3}$	$5.330 \cdot 10^{-3}$	$-1.1 \cdot 10^{-3}$
0.3	−0.6	8.622	8.612	$4.055 \cdot 10^{-4}$	$4.056 \cdot 10^{-4}$	$-2.0 \cdot 10^{-4}$	$7.339 \cdot 10^{-3}$	$7.337 \cdot 10^{-3}$	$1.9 \cdot 10^{-4}$
0.3	−0.2	7.305	7.295	$8.426 \cdot 10^{-4}$	$8.400 \cdot 10^{-4}$	$3.0 \cdot 10^{-3}$	$1.215 \cdot 10^{-2}$	$1.211 \cdot 10^{-2}$	$3.3 \cdot 10^{-3}$
0.3	0.0	6.610	6.600	$1.298 \cdot 10^{-3}$	$1.291 \cdot 10^{-3}$	$5.9 \cdot 10^{-3}$	$1.637 \cdot 10^{-2}$	$1.627 \cdot 10^{-2}$	$6.2 \cdot 10^{-3}$
0.3	0.1	6.250	6.240	$1.648 \cdot 10^{-3}$	$1.635 \cdot 10^{-3}$	$7.9 \cdot 10^{-3}$	$1.929 \cdot 10^{-2}$	$1.913 \cdot 10^{-2}$	$8.1 \cdot 10^{-3}$
0.3	0.2	5.881	5.871	$2.131 \cdot 10^{-3}$	$2.109 \cdot 10^{-3}$	$1.1 \cdot 10^{-2}$	$2.302 \cdot 10^{-2}$	$2.278 \cdot 10^{-2}$	$1.1 \cdot 10^{-2}$
0.3	0.3	5.500	5.490	$2.817 \cdot 10^{-3}$	$2.777 \cdot 10^{-3}$	$1.4 \cdot 10^{-2}$	$2.789 \cdot 10^{-2}$	$2.750 \cdot 10^{-2}$	$1.4 \cdot 10^{-2}$
0.3	0.4	5.104	5.094	$3.824 \cdot 10^{-3}$	$3.754 \cdot 10^{-3}$	$1.8 \cdot 10^{-2}$	$3.440 \cdot 10^{-2}$	$3.378 \cdot 10^{-2}$	$1.8 \cdot 10^{-2}$
0.3	0.5	4.689	4.679	$5.366 \cdot 10^{-3}$	$5.235 \cdot 10^{-3}$	$2.4 \cdot 10^{-2}$	$4.339 \cdot 10^{-2}$	$4.236 \cdot 10^{-2}$	$2.4 \cdot 10^{-2}$
0.3	0.6	4.250	4.240	$7.862 \cdot 10^{-3}$	$7.602 \cdot 10^{-3}$	$3.3 \cdot 10^{-2}$	$5.630 \cdot 10^{-2}$	$5.451 \cdot 10^{-2}$	$3.2 \cdot 10^{-2}$
0.3	0.7	3.777	3.767	$1.221 \cdot 10^{-2}$	$1.165 \cdot 10^{-2}$	$4.6 \cdot 10^{-2}$	$7.590 \cdot 10^{-2}$	$7.256 \cdot 10^{-2}$	$4.4 \cdot 10^{-2}$
0.3	0.8	3.249	3.239	$2.065 \cdot 10^{-2}$	$1.926 \cdot 10^{-2}$	$6.7 \cdot 10^{-2}$	$1.078 \cdot 10^{-1}$	$1.009 \cdot 10^{-1}$	$6.4 \cdot 10^{-2}$
0.3	0.9	2.615	2.605	$4.030 \cdot 10^{-2}$	$3.602 \cdot 10^{-2}$	$1.1 \cdot 10^{-1}$	$1.662 \cdot 10^{-1}$	$1.495 \cdot 10^{-1}$	$1.0 \cdot 10^{-1}$
0.3	−0.9	13.028	9.554	$2.350 \cdot 10^{-5}$	$2.392 \cdot 10^{-5}$	$-1.8 \cdot 10^{-2}$	$8.995 \cdot 10^{-4}$	$9.095 \cdot 10^{-4}$	$-1.1 \cdot 10^{-2}$
0.3	−0.6	11.743	8.612	$3.843 \cdot 10^{-5}$	$3.898 \cdot 10^{-5}$	$-1.4 \cdot 10^{-2}$	$1.265 \cdot 10^{-3}$	$1.275 \cdot 10^{-3}$	$-7.9 \cdot 10^{-3}$
0.3	−0.2	9.947	7.295	$8.381 \cdot 10^{-5}$	$8.443 \cdot 10^{-5}$	$-7.4 \cdot 10^{-3}$	$2.174 \cdot 10^{-3}$	$2.178 \cdot 10^{-3}$	$-1.7 \cdot 10^{-3}$
0.3	0.0	9.000	6.600	$1.335 \cdot 10^{-4}$	$1.338 \cdot 10^{-4}$	$-2.5 \cdot 10^{-3}$	$3.004 \cdot 10^{-3}$	$2.996 \cdot 10^{-3}$	$2.6 \cdot 10^{-3}$
0.3	0.2	8.006	5.871	$2.289 \cdot 10^{-4}$	$2.280 \cdot 10^{-4}$	$4.1 \cdot 10^{-3}$	$4.369 \cdot 10^{-3}$	$4.333 \cdot 10^{-3}$	$8.2 \cdot 10^{-3}$
0.3	0.6	5.782	4.240	$9.889 \cdot 10^{-4}$	$9.612 \cdot 10^{-4}$	$2.8 \cdot 10^{-2}$	$1.207 \cdot 10^{-2}$	$1.173 \cdot 10^{-2}$	$2.8 \cdot 10^{-2}$
0.3	0.9	3.553	2.605	$7.574 \cdot 10^{-3}$	$6.922 \cdot 10^{-3}$	$8.6 \cdot 10^{-2}$	$4.941 \cdot 10^{-2}$	$4.575 \cdot 10^{-2}$	$7.4 \cdot 10^{-2}$
0.3	−0.9	18.818	9.554	$3.231 \cdot 10^{-6}$	$3.284 \cdot 10^{-6}$	$-1.6 \cdot 10^{-2}$	$2.191 \cdot 10^{-4}$	$2.211 \cdot 10^{-4}$	$-9.0 \cdot 10^{-3}$
0.3	−0.6	16.962	8.612	$5.333 \cdot 10^{-6}$	$5.405 \cdot 10^{-6}$	$-1.3 \cdot 10^{-2}$	$3.105 \cdot 10^{-4}$	$3.124 \cdot 10^{-4}$	$-6.3 \cdot 10^{-3}$
0.3	−0.2	14.368	7.295	$1.184 \cdot 10^{-5}$	$1.193 \cdot 10^{-5}$	$-7.8 \cdot 10^{-3}$	$5.407 \cdot 10^{-4}$	$5.413 \cdot 10^{-4}$	$-1.2 \cdot 10^{-3}$
0.3	0.0	13.000	6.600	$1.910 \cdot 10^{-5}$	$1.918 \cdot 10^{-5}$	$-3.9 \cdot 10^{-3}$	$7.540 \cdot 10^{-4}$	$7.522 \cdot 10^{-4}$	$2.3 \cdot 10^{-3}$
0.3	0.2	11.564	5.871	$3.331 \cdot 10^{-5}$	$3.327 \cdot 10^{-5}$	$1.4 \cdot 10^{-3}$	$1.110 \cdot 10^{-3}$	$1.102 \cdot 10^{-3}$	$7.0 \cdot 10^{-3}$
0.3	0.6	8.352	4.240	$1.533 \cdot 10^{-4}$	$1.503 \cdot 10^{-4}$	$2.0 \cdot 10^{-2}$	$3.211 \cdot 10^{-3}$	$3.137 \cdot 10^{-3}$	$2.3 \cdot 10^{-2}$
0.3	0.9	5.132	2.605	$1.389 \cdot 10^{-3}$	$1.305 \cdot 10^{-3}$	$6.1 \cdot 10^{-2}$	$1.489 \cdot 10^{-2}$	$1.407 \cdot 10^{-2}$	$5.5 \cdot 10^{-2}$
0.5	−0.9	10.089	10.079	$3.287 \cdot 10^{-4}$	$3.302 \cdot 10^{-4}$	$-4.6 \cdot 10^{-3}$	$5.933 \cdot 10^{-3}$	$5.958 \cdot 10^{-3}$	$-4.2 \cdot 10^{-3}$
0.5	−0.6	9.107	9.097	$5.198 \cdot 10^{-4}$	$5.208 \cdot 10^{-4}$	$-2.0 \cdot 10^{-3}$	$8.149 \cdot 10^{-3}$	$8.160 \cdot 10^{-3}$	$-1.4 \cdot 10^{-3}$
0.5	−0.2	7.734	7.724	$1.067 \cdot 10^{-3}$	$1.062 \cdot 10^{-3}$	$4.7 \cdot 10^{-3}$	$1.341 \cdot 10^{-2}$	$1.334 \cdot 10^{-2}$	$5.5 \cdot 10^{-3}$
0.5	0.0	7.010	7.000	$1.630 \cdot 10^{-3}$	$1.613 \cdot 10^{-3}$	$1.1 \cdot 10^{-2}$	$1.799 \cdot 10^{-2}$	$1.779 \cdot 10^{-2}$	$1.1 \cdot 10^{-2}$
0.5	0.2	6.250	6.240	$2.647 \cdot 10^{-3}$	$2.595 \cdot 10^{-3}$	$2.0 \cdot 10^{-2}$	$2.517 \cdot 10^{-2}$	$2.466 \cdot 10^{-2}$	$2.0 \cdot 10^{-2}$
0.5	0.6	4.548	4.538	$9.403 \cdot 10^{-3}$	$8.859 \cdot 10^{-3}$	$5.8 \cdot 10^{-2}$	$6.039 \cdot 10^{-2}$	$5.693 \cdot 10^{-2}$	$5.7 \cdot 10^{-2}$
0.5	0.9	2.843	2.833	$4.424 \cdot 10^{-2}$	$3.792 \cdot 10^{-2}$	$1.4 \cdot 10^{-1}$	$1.696 \cdot 10^{-1}$	$1.463 \cdot 10^{-1}$	$1.4 \cdot 10^{-1}$
0.5	−0.9	12.959	10.079	$3.078 \cdot 10^{-5}$	$3.211 \cdot 10^{-5}$	$-4.3 \cdot 10^{-2}$	$9.314 \cdot 10^{-4}$	$9.592 \cdot 10^{-4}$	$-3.0 \cdot 10^{-2}$
0.5	−0.6	11.697	9.097	$5.009 \cdot 10^{-5}$	$5.182 \cdot 10^{-5}$	$-3.5 \cdot 10^{-2}$	$1.309 \cdot 10^{-3}$	$1.337 \cdot 10^{-3}$	$-2.1 \cdot 10^{-2}$
0.5	−0.2	9.931	7.724	$1.082 \cdot 10^{-4}$	$1.102 \cdot 10^{-4}$	$-1.8 \cdot 10^{-2}$	$2.243 \cdot 10^{-3}$	$2.256 \cdot 10^{-3}$	$-5.9 \cdot 10^{-3}$
0.5	0.0	9.000	7.000	$1.713 \cdot 10^{-4}$	$1.723 \cdot 10^{-4}$	$-5.8 \cdot 10^{-3}$	$3.093 \cdot 10^{-3}$	$3.078 \cdot 10^{-3}$	$4.9 \cdot 10^{-3}$
0.5	0.2	8.022	6.240	$2.914 \cdot 10^{-4}$	$2.885 \cdot 10^{-4}$	$1.0 \cdot 10^{-2}$	$4.488 \cdot 10^{-3}$	$4.403 \cdot 10^{-3}$	$1.9 \cdot 10^{-2}$
0.5	0.6	5.834	4.538	$1.222 \cdot 10^{-3}$	$1.143 \cdot 10^{-3}$	$6.4 \cdot 10^{-2}$	$1.228 \cdot 10^{-2}$	$1.147 \cdot 10^{-2}$	$6.6 \cdot 10^{-2}$
0.5	0.9	3.643	2.833	$8.674 \cdot 10^{-3}$	$7.191 \cdot 10^{-3}$	$1.7 \cdot 10^{-1}$	$4.867 \cdot 10^{-2}$	$4.117 \cdot 10^{-2}$	$1.5 \cdot 10^{-1}$
0.5	−0.9	18.718	10.079	$3.808 \cdot 10^{-6}$	$3.973 \cdot 10^{-6}$	$-4.3 \cdot 10^{-2}$	$2.062 \cdot 10^{-4}$	$2.115 \cdot 10^{-4}$	$-2.6 \cdot 10^{-2}$
0.5	−0.6	16.895	9.097	$6.255 \cdot 10^{-6}$	$6.473 \cdot 10^{-6}$	$-3.5 \cdot 10^{-2}$	$2.915 \cdot 10^{-4}$	$2.968 \cdot 10^{-4}$	$-1.8 \cdot 10^{-2}$
0.5	−0.2	14.345	7.724	$1.377 \cdot 10^{-5}$	$1.403 \cdot 10^{-5}$	$-1.9 \cdot 10^{-2}$	$5.058 \cdot 10^{-4}$	$5.077 \cdot 10^{-4}$	$-3.7 \cdot 10^{-3}$
0.5	0.0	13.000	7.000	$2.208 \cdot 10^{-5}$	$2.226 \cdot 10^{-5}$	$-8.1 \cdot 10^{-3}$	$7.038 \cdot 10^{-4}$	$6.995 \cdot 10^{-4}$	$6.0 \cdot 10^{-3}$
0.5	0.2	11.588	6.240	$3.822 \cdot 10^{-5}$	$3.799 \cdot 10^{-5}$	$6.1 \cdot 10^{-3}$	$1.033 \cdot 10^{-3}$	$1.014 \cdot 10^{-3}$	$1.9 \cdot 10^{-2}$
0.5	0.6	8.427	4.538	$1.715 \cdot 10^{-4}$	$1.624 \cdot 10^{-4}$	$5.3 \cdot 10^{-2}$	$2.960 \cdot 10^{-3}$	$2.785 \cdot 10^{-3}$	$5.9 \cdot 10^{-2}$
0.5	0.9	5.262	2.833	$1.467 \cdot 10^{-3}$	$1.259 \cdot 10^{-3}$	$1.4 \cdot 10^{-1}$	$1.343 \cdot 10^{-2}$	$1.165 \cdot 10^{-2}$	$1.3 \cdot 10^{-1}$
0.7	−0.9	10.595	10.585	$3.364 \cdot 10^{-4}$	$3.394 \cdot 10^{-4}$	$-8.9 \cdot 10^{-3}$	$5.335 \cdot 10^{-3}$	$5.381 \cdot 10^{-3}$	$-8.8 \cdot 10^{-3}$
0.7	−0.6	9.580	9.570	$5.294 \cdot 10^{-4}$	$5.316 \cdot 10^{-4}$	$-4.2 \cdot 10^{-3}$	$7.320 \cdot 10^{-3}$	$7.346 \cdot 10^{-3}$	$-3.6 \cdot 10^{-3}$
0.7	−0.2	8.160	8.150	$1.077 \cdot 10^{-3}$	$1.070 \cdot 10^{-3}$	$7.4 \cdot 10^{-3}$	$1.203 \cdot 10^{-2}$	$1.193 \cdot 10^{-2}$	$8.6 \cdot 10^{-3}$
0.7	0.0	7.410	7.400	$1.637 \cdot 10^{-3}$	$1.609 \cdot 10^{-3}$	$1.7 \cdot 10^{-2}$	$1.613 \cdot 10^{-2}$	$1.583 \cdot 10^{-2}$	$1.9 \cdot 10^{-2}$
0.7	0.2	6.622	6.612	$2.641 \cdot 10^{-3}$	$2.558 \cdot 10^{-3}$	$3.2 \cdot 10^{-2}$	$2.255 \cdot 10^{-2}$	$2.181 \cdot 10^{-2}$	$3.3 \cdot 10^{-2}$
0.7	0.6	4.858	4.848	$9.173 \cdot 10^{-3}$	$8.375 \cdot 10^{-3}$	$8.7 \cdot 10^{-2}$	$5.390 \cdot 10^{-2}$	$4.916 \cdot 10^{-2}$	$8.8 \cdot 10^{-2}$
0.7	0.9	3.088	3.078	$4.151 \cdot 10^{-2}$	$3.437 \cdot 10^{-2}$	$1.7 \cdot 10^{-1}$	$1.504 \cdot 10^{-1}$	$1.249 \cdot 10^{-1}$	$1.7 \cdot 10^{-1}$
0.7	−0.9	12.873	10.585	$3.427 \cdot 10^{-5}$	$3.680 \cdot 10^{-5}$	$-7.4 \cdot 10^{-2}$	$8.231 \cdot 10^{-4}$	$8.685 \cdot 10^{-4}$	$-5.5 \cdot 10^{-2}$
0.7	−0.6	11.639	9.570	$5.545 \cdot 10^{-5}$	$5.871 \cdot 10^{-5}$	$-5.9 \cdot 10^{-2}$	$1.155 \cdot 10^{-3}$	$1.201 \cdot 10^{-3}$	$-4.1 \cdot 10^{-2}$
0.7	−0.2	9.912	8.150	$1.186 \cdot 10^{-4}$	$1.222 \cdot 10^{-4}$	$-3.0 \cdot 10^{-2}$	$1.974 \cdot 10^{-3}$	$2.000 \cdot 10^{-3}$	$-1.3 \cdot 10^{-2}$
0.7	0.0	9.000	7.400	$1.865 \cdot 10^{-4}$	$1.882 \cdot 10^{-4}$	$-9.2 \cdot 10^{-3}$	$2.719 \cdot 10^{-3}$	$2.702 \cdot 10^{-3}$	$5.9 \cdot 10^{-3}$
0.7	0.2	8.042	6.612	$3.144 \cdot 10^{-4}$	$3.089 \cdot 10^{-4}$	$1.8 \cdot 10^{-2}$	$3.937 \cdot 10^{-3}$	$3.817 \cdot 10^{-3}$	$3.0 \cdot 10^{-2}$
0.7	0.6	5.896	4.848	$1.278 \cdot 10^{-3}$	$1.143 \cdot 10^{-3}$	$1.1 \cdot 10^{-1}$	$1.068 \cdot 10^{-2}$	$9.517 \cdot 10^{-3}$	$1.1 \cdot 10^{-1}$
0.7	0.9	3.744	3.078	$8.476 \cdot 10^{-3}$	$6.396 \cdot 10^{-3}$	$2.5 \cdot 10^{-1}$	$4.133 \cdot 10^{-2}$	$3.186 \cdot 10^{-2}$	$2.3 \cdot 10^{-1}$
0.7	−0.9	18.595	10.585	$3.648 \cdot 10^{-6}$	$3.952 \cdot 10^{-6}$	$-8.3 \cdot 10^{-2}$	$1.578 \cdot 10^{-4}$	$1.660 \cdot 10^{-4}$	$-5.2 \cdot 10^{-2}$
0.7	−0.6	16.812	9.570	$5.957 \cdot 10^{-6}$	$6.349 \cdot 10^{-6}$	$-6.6 \cdot 10^{-2}$	$2.225 \cdot 10^{-4}$	$2.307 \cdot 10^{-4}$	$-3.7 \cdot 10^{-2}$
0.7	−0.2	14.317	8.150	$1.298 \cdot 10^{-5}$	$1.341 \cdot 10^{-5}$	$-3.4 \cdot 10^{-2}$	$3.846 \cdot 10^{-4}$	$3.879 \cdot 10^{-4}$	$-8.5 \cdot 10^{-3}$

Continued on next page

Table A.1 – continued from previous page

e	$\hat{a}$	p	p_s	$\langle \dot{E}_{\rm teuk} \rangle$	$\langle \dot{E}_{\rm NP} \rangle$	$\Delta E_{\rm NP}/E$	$\langle \dot{J}_{\rm teuk} \rangle$	$\langle \dot{J}_{\rm NP} \rangle$	$\Delta J_{\rm NP}/J$
0.7	0.0	13.000	7.400	$2.067 \cdot 10^{-5}$	$2.093 \cdot 10^{-5}$	$-1.2 \cdot 10^{-2}$	$5.338 \cdot 10^{-4}$	$5.283 \cdot 10^{-4}$	$1.0 \cdot 10^{-2}$
0.7	0.2	11.616	6.612	$3.548 \cdot 10^{-5}$	$3.497 \cdot 10^{-5}$	$1.5 \cdot 10^{-2}$	$7.815 \cdot 10^{-4}$	$7.550 \cdot 10^{-4}$	$3.4 \cdot 10^{-2}$
0.7	0.6	8.517	4.848	$1.550 \cdot 10^{-4}$	$1.397 \cdot 10^{-4}$	$9.9 \cdot 10^{-2}$	$2.219 \cdot 10^{-3}$	$1.982 \cdot 10^{-3}$	$1.1 \cdot 10^{-1}$
0.7	0.9	5.408	3.078	$1.257 \cdot 10^{-3}$	$9.635 \cdot 10^{-4}$	$2.3 \cdot 10^{-1}$	$9.906 \cdot 10^{-3}$	$7.716 \cdot 10^{-3}$	$2.2 \cdot 10^{-1}$
0.9	−0.9	11.084	11.074	$1.439 \cdot 10^{-4}$	$1.460 \cdot 10^{-4}$	$-1.5 \cdot 10^{-2}$	$2.040 \cdot 10^{-3}$	$2.071 \cdot 10^{-3}$	$-1.5 \cdot 10^{-2}$
0.9	−0.6	10.042	10.032	$2.261 \cdot 10^{-4}$	$2.277 \cdot 10^{-4}$	$-7.2 \cdot 10^{-3}$	$2.807 \cdot 10^{-3}$	$2.826 \cdot 10^{-3}$	$-6.7 \cdot 10^{-3}$
0.9	−0.2	8.582	8.572	$4.594 \cdot 10^{-4}$	$4.544 \cdot 10^{-4}$	$1.1 \cdot 10^{-2}$	$4.643 \cdot 10^{-3}$	$4.585 \cdot 10^{-3}$	$1.2 \cdot 10^{-2}$
0.9	0.0	7.810	7.800	$6.979 \cdot 10^{-4}$	$6.799 \cdot 10^{-4}$	$2.6 \cdot 10^{-2}$	$6.253 \cdot 10^{-3}$	$6.080 \cdot 10^{-3}$	$2.8 \cdot 10^{-2}$
0.9	0.2	6.999	6.989	$1.126 \cdot 10^{-3}$	$1.073 \cdot 10^{-3}$	$4.7 \cdot 10^{-2}$	$8.798 \cdot 10^{-3}$	$8.368 \cdot 10^{-3}$	$4.9 \cdot 10^{-2}$
0.9	0.6	5.177	5.167	$3.935 \cdot 10^{-3}$	$3.467 \cdot 10^{-3}$	$1.2 \cdot 10^{-1}$	$2.155 \cdot 10^{-2}$	$1.894 \cdot 10^{-2}$	$1.2 \cdot 10^{-1}$
0.9	0.9	3.344	3.334	$1.877 \cdot 10^{-2}$	$1.516 \cdot 10^{-2}$	$1.9 \cdot 10^{-1}$	$6.525 \cdot 10^{-2}$	$5.270 \cdot 10^{-2}$	$1.9 \cdot 10^{-1}$
0.9	−0.9	12.778	11.074	$1.704 \cdot 10^{-5}$	$1.883 \cdot 10^{-5}$	$-1.0 \cdot 10^{-1}$	$3.320 \cdot 10^{-4}$	$3.598 \cdot 10^{-4}$	$-8.4 \cdot 10^{-2}$
0.9	−0.6	11.576	10.032	$2.741 \cdot 10^{-5}$	$2.969 \cdot 10^{-5}$	$-8.3 \cdot 10^{-2}$	$4.654 \cdot 10^{-4}$	$4.944 \cdot 10^{-4}$	$-6.2 \cdot 10^{-2}$
0.9	−0.2	9.891	8.572	$5.806 \cdot 10^{-5}$	$6.043 \cdot 10^{-5}$	$-4.1 \cdot 10^{-2}$	$7.946 \cdot 10^{-4}$	$8.120 \cdot 10^{-4}$	$-2.2 \cdot 10^{-2}$
0.9	0.0	9.000	7.800	$9.068 \cdot 10^{-5}$	$9.169 \cdot 10^{-5}$	$-1.1 \cdot 10^{-2}$	$1.093 \cdot 10^{-3}$	$1.087 \cdot 10^{-3}$	$6.1 \cdot 10^{-3}$
0.9	0.2	8.064	6.989	$1.516 \cdot 10^{-4}$	$1.475 \cdot 10^{-4}$	$2.7 \cdot 10^{-2}$	$1.582 \cdot 10^{-3}$	$1.515 \cdot 10^{-3}$	$4.2 \cdot 10^{-2}$
0.9	0.6	5.962	5.167	$5.996 \cdot 10^{-4}$	$5.120 \cdot 10^{-4}$	$1.5 \cdot 10^{-1}$	$4.278 \cdot 10^{-3}$	$3.633 \cdot 10^{-3}$	$1.5 \cdot 10^{-1}$
0.9	0.9	3.847	3.334	$3.818 \cdot 10^{-3}$	$2.678 \cdot 10^{-3}$	$3.0 \cdot 10^{-1}$	$1.656 \cdot 10^{-2}$	$1.184 \cdot 10^{-2}$	$2.8 \cdot 10^{-1}$
0.9	−0.9	18.457	11.074	$1.474 \cdot 10^{-6}$	$1.679 \cdot 10^{-6}$	$-1.4 \cdot 10^{-1}$	$5.209 \cdot 10^{-5}$	$5.684 \cdot 10^{-5}$	$-9.1 \cdot 10^{-2}$
0.9	−0.6	16.720	10.032	$2.391 \cdot 10^{-6}$	$2.651 \cdot 10^{-6}$	$-1.1 \cdot 10^{-1}$	$7.330 \cdot 10^{-5}$	$7.803 \cdot 10^{-5}$	$-6.5 \cdot 10^{-2}$
0.9	−0.2	14.287	8.572	$5.151 \cdot 10^{-6}$	$5.430 \cdot 10^{-6}$	$-5.4 \cdot 10^{-2}$	$1.262 \cdot 10^{-4}$	$1.284 \cdot 10^{-4}$	$-1.7 \cdot 10^{-2}$
0.9	0.0	13.000	7.800	$8.148 \cdot 10^{-6}$	$8.299 \cdot 10^{-6}$	$-1.8 \cdot 10^{-2}$	$1.747 \cdot 10^{-4}$	$1.724 \cdot 10^{-4}$	$1.3 \cdot 10^{-2}$
0.9	0.2	11.648	6.989	$1.387 \cdot 10^{-5}$	$1.352 \cdot 10^{-5}$	$2.5 \cdot 10^{-2}$	$2.550 \cdot 10^{-4}$	$2.421 \cdot 10^{-4}$	$5.1 \cdot 10^{-2}$
0.9	0.6	8.612	5.167	$5.904 \cdot 10^{-5}$	$5.003 \cdot 10^{-5}$	$1.5 \cdot 10^{-1}$	$7.194 \cdot 10^{-4}$	$6.041 \cdot 10^{-4}$	$1.6 \cdot 10^{-1}$
0.9	0.9	5.557	3.334	$4.602 \cdot 10^{-4}$	$3.105 \cdot 10^{-4}$	$3.3 \cdot 10^{-1}$	$3.196 \cdot 10^{-3}$	$2.211 \cdot 10^{-3}$	$3.1 \cdot 10^{-1}$

Appendix B

Noncircular 2PN corrections

B.1 Corrections for $m \neq 0$ higher modes

In this appendix we present the 2PN noncircular relativistic factors of Sec. 4.1.6 for all the subdominant $m \neq 0$ modes relevant at 2PN (global) order. The contributions $\hat{h}^{\text{tail-nc}}_{32}$, $\hat{h}^{\text{tail-nc}}_{41}$, $\hat{h}^{\text{tail-nc}}_{42}$, $\hat{h}^{\text{tail-nc}}_{43}$, and $\hat{h}^{\text{tail-nc}}_{44}$ are not written below since they are all equal to 1.

Tail noncircular factors

$$\begin{aligned}\hat{h}^{\text{tail-nc}}_{21} = 1 - \frac{\pi}{11520c^3}\Bigg[&6ip_{r_*}u\Big(3029 + 6035p_\varphi^2 u - 10870p_\varphi^4 u^2 + 8350p_\varphi^6 u^3 \\ &- 3215p_\varphi^8 u^4 + 511p_\varphi^{10}u^5\Big) - \frac{15p_{r_*}^2}{p_\varphi}\Big(635 - 1388p_\varphi^2 u + 666p_\varphi^4 u^2 - 92p_\varphi^6 u^3 - \\ &13p_\varphi^8 u^4\Big) + 20ip_{r_*}^3\Big(619 - 981p_\varphi^2 u + 573p_\varphi^4 u^2 - 115p_\varphi^6 u^3\Big) \\ &+ \frac{15p_{r_*}^4}{p_\varphi u}\Big(183 - 82p_\varphi^2 u - 17p_\varphi^4 u^2\Big)\Bigg]. \end{aligned} \tag{B.1}$$

$$\begin{aligned}\hat{h}^{\text{tail-nc}}_{31} = 1 - \frac{\pi}{1920c^3 p_\varphi^2\left(7 - 6p_\varphi^2 u\right)^2}\Bigg[&ip_{r_*}\Big(88130 - 107366p_\varphi^2 u + 89843p_\varphi^4 u^2 \\ &- 388835p_\varphi^6 u^3 + 588840p_\varphi^8 u^4 - 397460p_\varphi^{10}u^5 + 139731p_\varphi^{12}u^6 - 20563p_\varphi^{14}u^7\Big) \\ &+ \frac{p_{r_*}^2}{2p_\varphi u\left(7 - 6p_\varphi^2 u\right)}\Big(2115120 - 3821769p_\varphi^2 u + 915328p_\varphi^4 u^2 - 2431548\mathrm{p}\phi^6 u^3 \\ &+ 9399380p_\varphi^8 u^4 - 10528645p_\varphi^{10}u^5 + 5655444p_\varphi^{12}u^6 - 1592318p_\varphi^{14}u^7 \\ &+ 186288\mathrm{p}\phi^{16}u^8\Big) - \frac{ip_{r_*}^3}{3p_\varphi^2 u^2\left(7 - 6p_\varphi^2 u\right)^2}\Big(38072160 - 92454747p_\varphi^2 u \\ &+ 79749569p_\varphi^4 u^2 - 137703015p_\varphi^6 u^3 + 356358768p_\varphi^8 u^4 - 482607515p_\varphi^{10}u^5 \\ &+ 363100527p_\varphi^{12}u^6 - 161234979p_\varphi^{14}u^7 + 40408200p_\varphi^{16}u^8 - 4441608p_\varphi^{18}u^9\Big)\end{aligned}$$

$$
\begin{aligned}
&- \frac{p_{r_*}^4}{2p_\varphi^3 u^3 \left(7-6p_\varphi^2 u\right)^3}\Bigg(304577280 - 928941216 p_\varphi^2 u + 1082387695 p_\varphi^4 u^2 \\
&- 1365588354 p_\varphi^6 u^3 + 3139841017 p_\varphi^8 u^4 - 4991336104 p_\varphi^{10} u^5 \\
&+ 4638849326 p_\varphi^{12} u^6 - 2632737900 p_\varphi^{14} u^7 + 916090404 p_\varphi^{16} u^8 \\
&- 181221912 p_\varphi^{18} u^9 + 15589584 p_\varphi^{20} u^{10}\Bigg)\Bigg]. \qquad \text{(B.2)}
\end{aligned}
$$

$$
\begin{aligned}
\hat{h}_{33}^{\text{tail-nc}} &= 1 - \frac{\pi}{3840 c^3 p_\varphi^2 \left(2p_\varphi^2 u+7\right)^2}\Bigg[ip_{r_*}\Bigg(47630 + 134366 p_\varphi^2 u + 721737 p_\varphi^4 u^2 \\
&- 429865 \mathrm{p}\phi^6 u^3 + 308120 p_\varphi^8 u^4 - 107220 p_\varphi^{10} u^5 + 16769 p_\varphi^{12} u^6 - 337 p_\varphi^{14} u^7\Bigg) \\
&+ \frac{p_{r_*}^2}{2p_\varphi u \left(2p_\varphi^2 u+7\right)}\Bigg(381040 + 1407963 p_\varphi^2 u - 2751544 p_\varphi^4 u^2 \\
&+ 8146332 p_\varphi^6 u^3 - 5435500 p_\varphi^8 u^4 + 3011095 p_\varphi^{10} u^5 - 1073428 p_\varphi^{12} u^6 \\
&+ 170074 p_\varphi^{14} u^7 + 14688 p_\varphi^{16} u^8\Bigg) - \frac{i p_{r_*}^3}{p_\varphi^2 u^2 \left(2p_\varphi^2 u+7\right)^2}\Bigg(762080 + 3125521 p_\varphi^2 u \\
&+ 5675333 p_\varphi^4 u^2 - 28858731 p_\varphi^6 u^3 + 28110216 p_\varphi^8 u^4 - 14716055 p_\varphi^{10} u^5 \\
&+ 7128059 p_\varphi^{12} u^6 - 2725303 p_\varphi^{14} u^7 + 281976 p_\varphi^{16} u^8 + 41864 p_\varphi^{18} u^9\Bigg) \\
&- \frac{p_{r_*}^4}{2p_\varphi^3 u^3 \left(2p_\varphi^2 u+7\right)^3}\Bigg(6096640 + 27480928 p_\varphi^2 u + 92901791 p_\varphi^4 u^2 \\
&+ 57821954 p_\varphi^6 u^3 - 472378615 p_\varphi^8 u^4 + 376035640 p_\varphi^{10} u^5 - 164962538 p_\varphi^{12} u^6 \\
&+ 71523844 p_\varphi^{14} u^7 - 24385644 p_\varphi^{16} u^8 + 1291400 p_\varphi^{18} u^9 + 320720 p_\varphi^{20} u^{10}\Bigg)\Bigg]. \qquad \text{(B.3)}
\end{aligned}
$$

Instantaneous noncircular factors

$$
f_{21}^{\text{inst-nc}} = 1 + \frac{1}{c^2} p_{r_*}^2 \left(\frac{9}{14} + \frac{5\nu}{7}\right), \qquad \text{(B.4)}
$$

$$
\delta_{21}^{\text{inst-nc}} = \frac{1}{c^2} p_{r_*} p_\varphi \left(\frac{1}{14} + \frac{6\nu}{7}\right). \qquad \text{(B.5)}
$$

$$
\begin{aligned}
f_{31}^{\text{inst-nc}} &= 1 + \frac{1}{c^2}\Bigg\{\frac{p_{r_*}^2}{p_\varphi^2 u \left(-7+6p_\varphi^2 u\right)^3}\Bigg[(-1076+1168\nu) + p_\varphi^2 u\left(\frac{4783}{2} - 4242\nu\right) \\
&+ p_\varphi^4 u^2(-1520+4834\nu) + p_\varphi^6 u^3(6-2136\nu) + p_\varphi^8 u^4(180+288\nu)\Bigg] \\
&+ \frac{p_{r_*}^4}{p_\varphi^4 u^3 \left(-7+6p_\varphi^2 u\right)^5}\Bigg[(154944-168192\nu) + p_\varphi^2 u(-569222+740344\nu)
\end{aligned}
$$

$$+ p_\varphi^4 u^2(840044 - 1241680\nu) + p_\varphi^6 u^3(-622914 + 1014636\nu)$$
$$+ p_\varphi^8 u^4(232812 - 408168\nu) + p_\varphi^{10} u^5(-35208 + 65232\nu)\Bigg]\Bigg\}, \tag{B.6}$$

$$\delta_{31}^{\text{inst-nc}} = \frac{1}{c^2}\Bigg\{\frac{p_{r_*}}{p_\varphi\left(7 - 6p_\varphi^2 u\right)^2}\Bigg[\left(\frac{269}{3} - \frac{292\nu}{3}\right) + p_\varphi^2 u(-146 + 222\nu)$$
$$+ p_\varphi^4 u^2(61 - 110\nu)\Bigg] + \frac{p_{r_*}^3}{p_\varphi^3 u^2\left(7 - 6p_\varphi^2 u\right)^4}\Bigg[(-12912 + 14016\nu)$$
$$+ p_\varphi^2 u(39410 - 52984\nu) + p_\varphi^4 u^2(-45043 + 69758\nu) + p_\varphi^6 u^3(22704$$
$$- 39288\nu) + p_\varphi^8 u^4(-4248 + 8064\nu)\Bigg]\Bigg\}. \tag{B.7}$$

$$f_{32}^{\text{inst-nc}} = 1 + \frac{1}{c^2}\Bigg\{\frac{p_{r_*}^2}{p_\varphi^2 u(-1 + 3\nu)}\Bigg[\left(-\frac{187}{2880} + \frac{223\nu}{576} - \frac{265\nu^2}{576}\right) + p_\varphi^2 u\left(-\frac{221}{192}$$
$$+ \frac{547\nu}{192} + \frac{227\nu^2}{192}\right)\Bigg] + \frac{p_{r_*}^4}{p_\varphi^4 u^3(-1 + 3\nu)}\Bigg[\left(\frac{187}{46080} - \frac{223\nu}{9216} + \frac{265\nu^2}{9216}\right)$$
$$+ p_\varphi^2 u\left(\frac{61}{3072} - \frac{323\nu}{3072} + \frac{317\nu^2}{3072}\right)\Bigg]\Bigg\}, \tag{B.8}$$

$$\delta_{32}^{\text{inst-nc}} = \frac{1}{c^2}\Bigg\{\frac{p_{r_*}}{p_\varphi(-1 + 3\nu)}\Bigg[\left(-\frac{187}{720} + \frac{223\nu}{144} - \frac{265\nu^2}{144}\right) + p_\varphi^2 u\left(-\frac{433}{240}$$
$$+ \frac{355\nu}{48} - \frac{157\nu^2}{48}\right)\Bigg] + \frac{p_{r_*}^3}{p_\varphi^3 u^2(-1 + 3\nu)}\Bigg[\left(\frac{187}{11520} - \frac{223\nu}{2304} + \frac{265\nu^2}{2304}\right)$$
$$+ p_\varphi^2 u\left(\frac{61}{768} - \frac{323\nu}{768} + \frac{317\nu^2}{768}\right)\Bigg]\Bigg\}. \tag{B.9}$$

$$f_{33}^{\text{inst-nc}} = 1 + \frac{1}{c^2}\Bigg\{\frac{p_{r_*}^2}{p_\varphi^2 u\left(7 + 2p_\varphi^2 u\right)^3}\Bigg[\left(\frac{1076}{9} - \frac{1168\nu}{9}\right) + p_\varphi^2 u\left(\frac{9161}{18} + \frac{2626\nu}{9}\right)$$
$$+ p_\varphi^4 u^2\left(\frac{1292}{3} - \frac{214\nu}{3}\right) + p_\varphi^6 u^3\left(\frac{1430}{3} - \frac{424\nu}{3}\right) + p_\varphi^8 u^4\left(\frac{20}{3} + \frac{32\nu}{3}\right)\Bigg]$$
$$+ \frac{p_{r_*}^4}{p_\varphi^4 u^3\left(7 + 2p_\varphi^2 u\right)^5}\Bigg[\left(-\frac{17216}{9} + \frac{18688\nu}{9}\right) + p_\varphi^2 u\left(-\frac{55034}{9} + \frac{52744\nu}{9}\right)$$
$$+ p_\varphi^4 u^2\left(-\frac{23140}{3} + \frac{23984\nu}{3}\right) + p_\varphi^6 u^3\left(\frac{11510}{3} - \frac{44260\nu}{3}\right) + p_\varphi^8 u^4\left(\frac{163540}{9}\right.$$
$$\left.- \frac{57560\nu}{9}\right) + p_\varphi^{10} u^5\left(-\frac{11912}{3} + \frac{7888\nu}{3}\right)\Bigg]\Bigg\}, \tag{B.10}$$

$$\delta_{33}^{\text{inst-nc}} = \frac{1}{c^2}\Bigg\{\frac{p_{r_*}}{p_\varphi\left(7 + 2p_\varphi^2 u\right)^2}\Bigg[\left(\frac{269}{9} - \frac{292\nu}{9}\right) + p_\varphi^2 u\left(\frac{970}{9} - \frac{1142\nu}{9}\right)$$

$$+ p_\varphi^4 u^2 \left(\frac{313}{3} - \frac{182\nu}{3}\right)\Bigg] + \frac{p_{r_*}^3}{p_\varphi^3 u^2 \left(7 + 2p_\varphi^2 u\right)^4}\Bigg[\left(-\frac{4304}{9} + \frac{4672\nu}{9}\right)$$
$$+ p_\varphi^2 u \left(-\frac{12010}{9} + \frac{11288\nu}{9}\right) + p_\varphi^4 u^2 (431 - 1318\nu) + p_\varphi^6 u^3 \left(\frac{5456}{3} + \frac{968\nu}{3}\right)$$
$$+ p_\varphi^8 u^4 (-1336 + 864\nu)\Bigg]\Bigg\}. \tag{B.11}$$

$$f_{41}^{\text{inst-nc}} = 1, \tag{B.12}$$
$$\delta_{42}^{\text{inst-nc}} = 0. \tag{B.13}$$

$$f_{42}^{\text{inst-nc}} = 1 + \frac{1}{c^2}\Bigg\{\frac{p_{r_*}^2}{\left(-7 - 3p_\varphi^2 u + 6p_\varphi^4 u^2\right)^3 (-1 + 3\nu)}\Bigg[\left(-\frac{5495}{11} + \frac{78435\nu}{22}\right.$$
$$\left. - \frac{123711\nu^2}{22}\right) + p_\varphi^2 u \left(\frac{22794}{55} - \frac{95055\nu}{22} + \frac{237351\nu^2}{22}\right) + p_\varphi^4 u^2 \left(\frac{2308683}{220}\right.$$
$$\left. - \frac{778917\nu}{22} + \frac{83871\nu^2}{22}\right) + p_\varphi^6 u^3 \left(-\frac{4346379}{220} + \frac{1713879\nu}{22} - \frac{991377\nu^2}{22}\right)$$
$$+ p_\varphi^8 u^4 \left(\frac{692577}{55} - \frac{603477\nu}{11} + \frac{491211\nu^2}{11}\right) + p_\varphi^{10} u^5 \left(-\frac{127386}{55} + \frac{136890\nu}{11}\right.$$
$$\left. - \frac{160650\nu^2}{11}\right) + p_\varphi^{12} u^6 \left(-\frac{2484}{11} + \frac{2916\nu}{11} + \frac{11340\nu^2}{11}\right)\Bigg]$$
$$+ \frac{p_{r_*}^4}{u\left(-7 - 3p_\varphi^2 u + 6p_\varphi^4 u^2\right)^5 (-1 + 3\nu)}\Bigg[\left(-\frac{997983}{11} + \frac{4635792\nu}{11}\right.$$
$$\left. - \frac{4635792\nu^2}{11}\right) + p_\varphi^2 u \left(\frac{43866123}{55} - \frac{47651520\nu}{11} + \frac{63443142\nu^2}{11}\right)$$
$$+ p_\varphi^4 u^2 \left(\frac{35844849}{22} - \frac{16122492\nu}{11} - \frac{135164952\nu^2}{11}\right) + p_\varphi^6 u^3 \left(-\frac{525077109}{44}\right.$$
$$\left. + \frac{441545616\nu}{11} - \frac{53867457\nu^2}{11}\right) + p_\varphi^8 u^4 \left(\frac{4684992993}{220} - \frac{914171508\nu}{11}\right.$$
$$\left. + \frac{489089961\nu^2}{11}\right) + p_\varphi^{10} u^5 \left(-\frac{2041998687}{110} + \frac{865358424\nu}{11} - \frac{634963050\nu^2}{11}\right)$$
$$+ p_\varphi^{12} u^6 \left(\frac{96254487}{11} - \frac{433938060\nu}{11} + \frac{377733780\nu^2}{11}\right) + p_\varphi^{14} u^7 \left(-\frac{23603562}{11}\right.$$
$$\left. + \frac{112003560\nu}{11} - \frac{109437480\nu^2}{11}\right) + p_\varphi^{16} u^8 \left(\frac{1077948}{5} - 1069200\nu\right.$$
$$\left. + 1139184\nu^2\right)\Bigg]\Bigg\}, \tag{B.14}$$

$$\delta_{42}^{\text{inst-nc}} = \frac{1}{c^2}\Bigg\{\frac{p_{r_*}p_\varphi u}{\left(7+3p_\varphi^2 u-6p_\varphi^4u^2\right)^2(-1+3\nu)}\Bigg[\left(-\frac{5513}{55}+\frac{5854\nu}{11}-\frac{7548\nu^2}{11}\right)$$
$$+p_\varphi^2 u\left(-\frac{86061}{220}+\frac{13686\nu}{11}+\frac{273\nu^2}{11}\right)+p_\varphi^4u^2\left(\frac{139401}{220}-\frac{29826\nu}{11}+\frac{22599\nu^2}{11}\right)$$
$$+p_\varphi^6u^3\left(-\frac{2556}{11}+\frac{12186\nu}{11}-\frac{11988\nu^2}{11}\right)\Bigg]$$
$$+\frac{p_{r_*}^3p_\varphi}{\left(7+3p_\varphi^2 u-6p_\varphi^4u^2\right)^4(-1+3\nu)}\Bigg[\left(-\frac{3434319}{110}+\frac{1677774\nu}{11}\right.$$
$$\left.-\frac{1868580\nu^2}{11}\right)+p_\varphi^2u\left(-\frac{1623252}{55}-\frac{321240\nu}{11}+\frac{4439970\nu^2}{11}\right)$$
$$+p_\varphi^4u^2\left(\frac{80592003}{220}-\frac{13474980\nu}{11}+\frac{1467963\nu^2}{11}\right)+p_\varphi^6u^3\left(-\frac{138830193}{220}\right.$$
$$\left.+\frac{27487404\nu}{11}-\frac{15732441\nu^2}{11}\right)+p_\varphi^8u^4\left(\frac{26404461}{55}-\frac{22944114\nu}{11}+\frac{18134496\nu^2}{11}\right)$$
$$+p_\varphi^{10}u^5\left(-\frac{9559404}{55}+\frac{8902440\nu}{11}-\frac{8355960\nu^2}{11}\right)+p_\varphi^{12}u^6\left(\frac{1342332}{55}\right.$$
$$\left.-\frac{1324512\nu}{11}+\frac{1395792\nu^2}{11}\right)\Bigg]\Bigg\}. \tag{B.15}$$

$$f_{43}^{\text{inst-nc}} = 1, \tag{B.16}$$
$$\delta_{43}^{\text{inst-nc}} = 0. \tag{B.17}$$

$$f_{44}^{\text{inst-nc}} = 1+\frac{1}{c^2}\Bigg\{\frac{p_{r_*}^2}{\left(7+51p_\varphi^2 u+6p_\varphi^4u^2\right)^3(-1+3\nu)}\Bigg[\left(\frac{5495}{11}-\frac{78435\nu}{22}+\frac{123711\nu^2}{22}\right)$$
$$+p_\varphi^2u\left(\frac{210159}{55}-\frac{667917\nu}{22}+\frac{914625\nu^2}{22}\right)+p_\varphi^4u^2\left(-\frac{9429801}{55}+\frac{12229341\nu}{22}\right.$$
$$\left.-\frac{2912121\nu^2}{22}\right)+p_\varphi^6u^3\left(-\frac{19606626}{55}+\frac{22336029\nu}{22}+\frac{2602071\nu^2}{22}\right)$$
$$+p_\varphi^8u^4\left(-\frac{7261839}{55}+\frac{4772385\nu}{11}-\frac{1459053\nu^2}{11}\right)+p_\varphi^{10}u^5\left(-\frac{564948}{11}\right.$$
$$\left.+\frac{1931958\nu}{11}-\frac{475470\nu^2}{11}\right)+p_\varphi^{12}u^6\left(-\frac{2484}{11}+\frac{2916\nu}{11}+\frac{11340\nu^2}{11}\right)\Bigg]$$
$$+\frac{p_{r_*}^4}{u\left(7+51p_\varphi^2 u+6p_\varphi^4u^2\right)^5(-1+3\nu)}\Bigg[\left(\frac{997983}{11}-\frac{4635792\nu}{11}+\frac{4635792\nu^2}{11}\right)$$

$$
\begin{aligned}
&+ p_\varphi^2 u \left(-\frac{144030369}{110} + \frac{92715672\nu}{11} - \frac{152428248\nu^2}{11} \right) \\
&+ p_\varphi^4 u^2 \left(-\frac{737730837}{11} + \frac{3011803560\nu}{11} - \frac{2051555040\nu^2}{11} \right) \\
&+ p_\varphi^6 u^3 \left(-\frac{2431571553}{55} + \frac{1633697784\nu}{11} - \frac{187083648\nu^2}{11} \right) \\
&+ p_\varphi^8 u^4 \left(\frac{486563193}{5} - 405446040\nu + 297670464\nu^2 \right) \\
&+ p_\varphi^{10} u^5 \left(\frac{3125458143}{110} - \frac{956714976\nu}{11} - \frac{188690472\nu^2}{11} \right) \\
&+ p_\varphi^{12} u^6 \left(-\frac{3895064577}{55} + \frac{3530464704\nu}{11} - \frac{3326475600\nu^2}{11} \right) \\
&+ p_\varphi^{14} u^7 \left(-\frac{673781166}{11} + \frac{2335443840\nu}{11} - \frac{497702880\nu^2}{11} \right) \\
&+ p_\varphi^{16} u^8 \left(\frac{305560836}{55} - \frac{229080960\nu}{11} + \frac{102316608\nu^2}{11} \right) \Bigg] \Bigg\}, \qquad \text{(B.18)}
\end{aligned}
$$

$$
\begin{aligned}
\delta_{44}^{\text{inst-nc}} = &-\frac{1}{c^2} \Bigg\{ \frac{p_{r_*} p_\varphi u}{\left(7 + 51 p_\varphi^2 u + 6 p_\varphi^4 u^2\right)^2 (-1+3\nu)} \Bigg[\left(\frac{11026}{55} - \frac{11708\nu}{11} + \frac{15096\nu^2}{11} \right) \\
&+ p_\varphi^2 u \left(\frac{555681}{110} - \frac{233274\nu}{11} + \frac{175788\nu^2}{11} \right) + p_\varphi^4 u^2 \left(\frac{939051}{110} - \frac{377406\nu}{11} \right. \\
&\left. + \frac{241380\nu^2}{11} \right) + p_\varphi^6 u^3 \left(\frac{172872}{55} - \frac{126540\nu}{11} + \frac{47736\nu^2}{11} \right) \Bigg] \\
&+ \frac{p_{r_*}^3 p_\varphi}{\left(7 + 51 p_\varphi^2 u + 6 p_\varphi^4 u^2\right)^4 (-1+3\nu)} \Bigg[\left(\frac{3434319}{55} - \frac{3355548\nu}{11} + \frac{3737160\nu^2}{11} \right) \\
&+ p_\varphi^2 u \left(\frac{68284914}{55} - \frac{53840352\nu}{11} + \frac{31634784\nu^2}{11} \right) + p_\varphi^4 u^2 \left(-\frac{69674769}{55} \right. \\
&\left. + \frac{66841884\nu}{11} - \frac{71727336\nu^2}{11} \right) + p_\varphi^6 u^3 \left(-\frac{221951034}{55} + \frac{179751888\nu}{11} \right. \\
&\left. - \frac{118566720\nu^2}{11} \right) + p_\varphi^8 u^4 \left(\frac{64377018}{55} - \frac{49429008\nu}{11} + \frac{25417152\nu^2}{11} \right) \\
&+ p_\varphi^{10} u^5 \left(\frac{74535768}{55} - \frac{42300576\nu}{11} - \frac{20036160\nu^2}{11} \right) \\
&+ p_\varphi^{12} u^6 \left(-\frac{29497608}{55} + \frac{22006080\nu}{11} - \frac{9517824\nu^2}{11} \right) \Bigg] \Bigg\}. \qquad \text{(B.19)}
\end{aligned}
$$

Appendix C

Ringdown of eccentric binaries with small-mass-ratio

C.1 Time-domain fits of the postpeak waveform using QNMs

In this appendix we attempt to fit the complete postpeak waveform using the pure QNMs ansatz of Eq. (1.63) on a time interval $\tau \equiv t - t^{\rm peak}_{A_{22}} \in [t_0^{\rm QNM}, 100]$. We start by performing the fit of the real and imaginary parts of the waveform using the fundamental QNMs and 7 overtones starting from the peak of the amplitude, i.e. considering $n = 8$ and $t_0^{\rm QNM} = 0$; the results of this procedure are shown in Fig. C.1 (dash-dotted green lines). The QNMs waveform overlaps quite well with the numerical RWZ waveform (black), and the corresponding residual is around 10^{-3} shortly after the amplitude peak. However, it is easy to see that: i) the beating between positive and negative frequency QNMs in the late ringdown is not well reproduced, as shown by the waveform frequency in the second panel, ii) the frequency of the fitted wave shows spurious oscillations in the early ringdown. In order to ensure the correct late-ringdown behavior, we refine this procedure by prefitting only the fundamental QNMs on $\tau \in [62, 100]$, so that we can easily find $C^{\pm}_{221}$ since the overtones are negligible in the late ringdown, and then performing the fit of Eq. (1.63) on the whole time interval $\tau \in [0, 100]$, so that we can find the remaining $C^{\pm}_{\ell mn}$ coefficients. The result of this procedure is shown with dashed red lines in Fig. C.1. While the beating in the late ringdown frequency is now well reproduced, the spurious oscillations in the early ringdown frequency are still present. Note that in this case the residual is a little bit higher in the early ringdown, but way lower in the late evolution. We thus concluded that, while the residual of the waveforms in quite low in both fits, the waveform frequency shows that there are some inaccuracies in the early ringdown.

In an attempt to solve the issue of the spurious frequency oscillations, we also explore the possibility to find the $C^{\pm}_{\ell mn}$ coefficients fitting directly the frequency using Eq. (5.21). Note that if we proceed this way, we cannot find C^{+}_{221} since the frequency is invariant under global normalizations and phase shifts of the waveform. We thus find C^{+}_{221} as done before, i.e. fitting Eq (1.63) with $n = 1$ in the late time interval $\tau \in [62, 100]$. In the left panel of Fig. C.2 we show this frequency-fit compared with the waveform-fit discussed above. To evaluate the goodness of the fits, we show in this case the relative differences of amplitude and frequency, that we consider more informative than the residual. As can be seen, while the frequency-fit solves the issue of the early spurious oscillations, produce

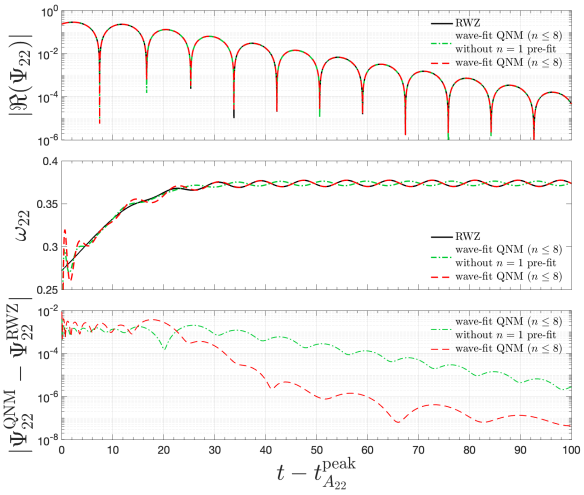

Figure C.1: Upper panels: RWZ waveform and frequency (black) compared with the results from the waveform fits performed (1) considering all the QNMs together (dash-dotted green), and (2) prefitting the fundamental QNMs (dashed red) and then fitting all the overtones. In the bottom panel we show the residuals with same color scheme. See discussion in Appendix C.1.

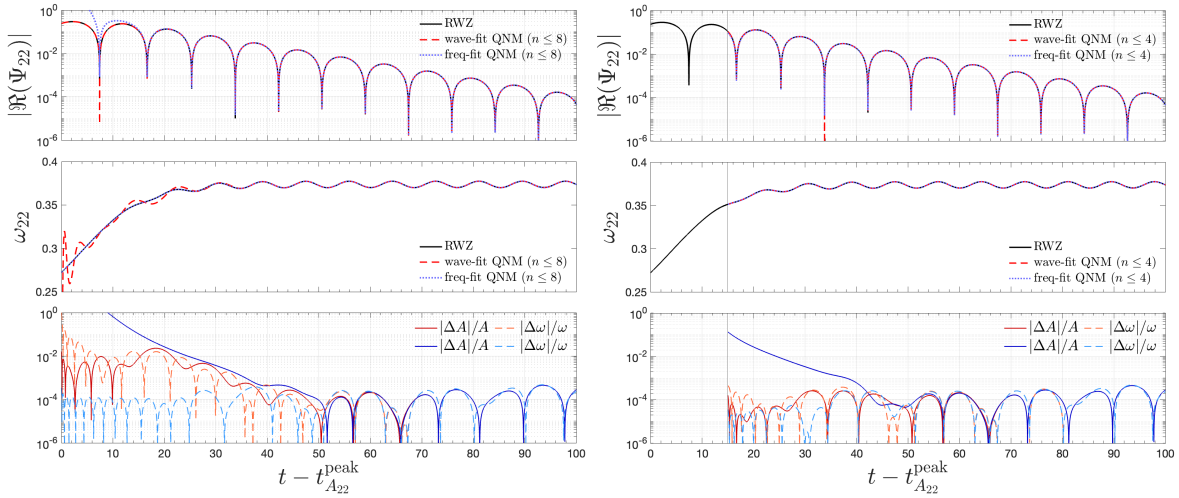

Figure C.2: Upper panels: RWZ waveform and frequency (black) compared with the results from the wave-fit (red) and frequency-fit (blue). In the bottom panels we show the relative differences of the amplitude and frequency (hot colors for the waveform-fit, cold colors for the frequency-fit). On the left, we fit the whole postpeak waveform using 8 QNMs, while on the right we fit from $t \geq 15 + t^{\rm peak}_{A_{22}}$ using 4 QNMs. See discussion in Appendix C.1.

a waveform that is way less accurate than the one found with the waveform-fit.

Finally, in the right panels of Fig. C.2 we show the comparison between the frequency and waveform fits performed considering $n = 4$ and $t_0^{\rm QNM} = 15$. In this case the waveform fit is accurate and the recovered frequency is consistent with the numerical result, leading to relative amplitude and frequency errors around 10^{-4}. However, the amplitude of the waveform recovered from the frequency-fit reaches a 10% error at $\tau \sim 15$, and thus the frequency-fit seems less robust than the waveform-fit, even if we do not fit the early ringdown.

We thus conclude that: i) it is a good practice to check the waveform frequency in order to evaluate the goodness of the QNMs fits of the ringdown waveform, ii) within our methods, the waveform can be consistently fitted only starting from later times. This is again consistent with the discussion of Sec. 5.4.1 on the RWZ source terms and with the iterative frequency-fit of Sec. 5.4.2.

C.2 Global fits for the eccentric Schwarzschild post-peak waveform

In this appendix we report all the global fits that we use in the ringdown model discussed in Sec. 5.2.3; see that section for more detail on how we perform the global fits. We start by reporting the global fits of the quantities needed to reconstruct the postpeak waveform for all the modes in Table C.1. We then proceed to show the global fits for $\left\{A_{22}^{\rm NQC}, \dot{A}_{22}^{\rm NQC}, \ddot{A}_{22}^{\rm NQC}, \omega_{22}^{\rm NQC}, \dot{\omega}_{22}^{\rm NQC}, \ddot{\omega}_{22}^{\rm NQC}\right\}$ evaluated at $t_{\ell m}^{\rm NQC} = t_{A_{\ell m}}^{\rm peak} - 2$ in Table C.2. Note that we report the fits also for $\ell = m = 2$, but for the quadrupolar waveform we do not use them since we use $t_{22}^{\rm NQC} = t_{A_{22}}^{\rm peak} + 2$, as discussed in Sec. 5.2.4. In all the cases we use a parabolic global template.

Table C.1: Global fits of the coefficients entering the ringdown template. For each quantity y, the fitting function is: $y = C_{\rm QC} + C_1 \hat{b}_{\Omega_{\rm pk}} + C_2 \hat{b}^2_{\Omega_{\rm pk}}$, where QC indicates the quasi-circular value. The amplitude considered in this table is the amplitude of the strain, $A_{\ell m} = |h_{\ell m}|$, rather than the amplitude of the RWZ-normalized waveform.

coeff	(ℓ, m)	$C_{\rm QC}$	C_1	C_2	(ℓ, m)	$C_{\rm QC}$	C_1	C_2
c_2^ϕ	(2,2)	1.561×10^{-1}	-5.067×10^{-2}	-5.493×10^{-2}	(4,4)	1.845×10^{-1}	-6.271×10^{-3}	-2.849×10^{-3}
c_3^ϕ		3.272	5.021	6.554		2.249	2.991	5.909
c_4^ϕ		2.592	8.305	1.108×10^2		1.025	2.617	12.471
c_2^A		2.161×10^{-1}	-1.999×10^{-2}	7.199×10^{-3}		2.178×10^{-1}	-1.276×10^{-2}	2.823×10^{-2}
c_3^A		2.334	3.030	5.583		1.145	1.476	2.040
$A_{\rm peak}$		1.444	9.914×10^{-1}	9.177×10^{-1}		2.754×10^{-1}	2.374×10^{-1}	2.296×10^{-1}
$\ddot{A}_{\rm peak}$		-2.359×10^{-3}	6.830×10^{-3}	-3.238×10^{-3}		-1.258×10^{-3}	8.999×10^{-4}	8.471×10^{-4}
$\Delta\omega_{\rm peak}$		1.015×10^{-1}	-1.061×10^{-2}	4.131×10^{-3}		1.751×10^{-1}	-1.720×10^{-2}	1.743×10^{-2}
c_2^ϕ	(2,1)	$1.539 \cdot 10^{-1}$	$4.563 \cdot 10^{-2}$	$1.250 \cdot 10^{-1}$	(4,3)	$1.876 \cdot 10^{-1}$	$-2.091 \cdot 10^{-3}$	$2.781 \cdot 10^{-4}$
c_3^ϕ		1.185	1.721	10.167		1.320	1.129	$-7.914 \cdot 10^{-4}$
c_4^ϕ		3.866	7.989	80.460		$3.513 \cdot 10^{-1}$	$6.880 \cdot 10^{-1}$	$3.418 \cdot 10^{-1}$
c_2^A		$3.656 \cdot 10^{-1}$	$2.191 \cdot 10^{-1}$	-2.017		$2.252 \cdot 10^{-1}$	$4.376 \cdot 10^{-3}$	$-6.836 \cdot 10^{-2}$
c_3^A		$-1.535 \cdot 10^{-1}$	-3.204	31.896		$3.600 \cdot 10^{-1}$	1.192	-3.611
$A_{\rm peak}$		$5.238 \cdot 10^{-1}$	$2.332 \cdot 10^{-1}$	$2.119 \cdot 10^{-1}$		$9.418 \cdot 10^{-2}$	$7.365 \cdot 10^{-2}$	$6.538 \cdot 10^{-2}$
$\ddot{A}_{\rm peak}$		$-2.624 \cdot 10^{-3}$	$5.624 \cdot 10^{-3}$	$2.423 \cdot 10^{-2}$		$-7.851 \cdot 10^{-4}$	$-4.334 \cdot 10^{-5}$	$-1.645 \cdot 10^{-4}$
$\Delta\omega_{\rm peak}$		$8.302 \cdot 10^{-2}$	$-8.936 \cdot 10^{-2}$	$5.023 \cdot 10^{-1}$		$1.722 \cdot 10^{-1}$	$8.015 \cdot 10^{-3}$	$-2.205 \cdot 10^{-2}$
c_2^ϕ	(3,3)	$1.783 \cdot 10^{-1}$	$-1.361 \cdot 10^{-2}$	$-1.330 \cdot 10^{-3}$	(4,2)	$1.848 \cdot 10^{-1}$	$-1.045 \cdot 10^{-2}$	$2.014 \cdot 10^{-2}$
c_3^ϕ		2.818	4.107	9.523		1.316	$4.910 \cdot 10^{-1}$	$-3.244 \cdot 10^{-1}$
c_4^ϕ		1.536	4.592	28.099		$8.103 \cdot 10^{-1}$	1.244	-1.645
c_2^A		$2.192 \cdot 10^{-1}$	$-1.750 \cdot 10^{-2}$	$3.036 \cdot 10^{-2}$		$2.589 \cdot 10^{-1}$	$4.823 \cdot 10^{-2}$	$-1.436 \cdot 10^{-1}$
c_3^A		1.585	1.715	2.634		$-7.454 \cdot 10^{-1}$	1.157	-1.954
$A_{\rm peak}$		$5.635 \cdot 10^{-1}$	$4.299 \cdot 10^{-1}$	$3.883 \cdot 10^{-1}$		$3.138 \cdot 10^{-2}$	$1.544 \cdot 10^{-2}$	$1.181 \cdot 10^{-2}$
$\ddot{A}_{\rm peak}$		$-1.823 \cdot 10^{-3}$	$2.287 \cdot 10^{-3}$	$1.026 \cdot 10^{-3}$		$-2.743 \cdot 10^{-4}$	$1.623 \cdot 10^{-4}$	$-3.799 \cdot 10^{-4}$
$\Delta\omega_{\rm peak}$		$1.462 \cdot 10^{-1}$	$-1.916 \cdot 10^{-2}$	$1.800 \cdot 10^{-2}$		$1.836 \cdot 10^{-1}$	$-2.595 \cdot 10^{-2}$	$2.780 \cdot 10^{-2}$
c_2^ϕ	(3,2)	$1.851 \cdot 10^{-1}$	$-8.128 \cdot 10^{-3}$	$9.774 \cdot 10^{-3}$	(4,1)	$1.428 \cdot 10^{-1}$	$-1.797 \cdot 10^{-2}$	$3.577 \cdot 10^{-2}$
c_3^ϕ		1.308	$3.395 \cdot 10^{-1}$	$7.985 \cdot 10^{-1}$		$-7.583 \cdot 10^{-1}$	$-3.777 \cdot 10^{-1}$	$6.408 \cdot 10^{-1}$
c_4^ϕ		$2.172 \cdot 10^{-1}$	$1.135 \cdot 10^{-1}$	$2.334 \cdot 10^{-1}$		$1.155 \cdot 10^{-1}$	$1.294 \cdot 10^{-1}$	$-2.141 \cdot 10^{-1}$
c_2^A		$2.425 \cdot 10^{-1}$	$6.597 \cdot 10^{-4}$	$-7.605 \cdot 10^{-3}$		1.067	$-4.888 \cdot 10^{-1}$	$8.161 \cdot 10^{-1}$
c_3^A		$9.188 \cdot 10^{-1}$	$8.761 \cdot 10^{-1}$	$-4.018 \cdot 10^{-1}$		10.890	-4.684	8.425
$A_{\rm peak}$		$1.991 \cdot 10^{-1}$	$1.289 \cdot 10^{-1}$	$1.017 \cdot 10^{-1}$		$9.263 \cdot 10^{-3}$	$3.514 \cdot 10^{-3}$	$2.333 \cdot 10^{-3}$
$\ddot{A}_{\rm peak}$		$-1.561 \cdot 10^{-3}$	$-5.955 \cdot 10^{-4}$	$6.250 \cdot 10^{-4}$		$-7.568 \cdot 10^{-4}$	$-4.506 \cdot 10^{-4}$	$-3.366 \cdot 10^{-5}$
$\Delta\omega_{\rm peak}$		$1.476 \cdot 10^{-1}$	$1.704 \cdot 10^{-4}$	$9.627 \cdot 10^{-3}$		$2.572 \cdot 10^{-1}$	$-5.064 \cdot 10^{-2}$	$6.728 \cdot 10^{-2}$
c_2^ϕ	(3,1)	$1.483 \cdot 10^{-1}$	$-7.316 \cdot 10^{-3}$	$2.289 \cdot 10^{-2}$	(5,5)	$1.872 \cdot 10^{-1}$	$-3.773 \cdot 10^{-3}$	$-1.675 \cdot 10^{-3}$
c_3^ϕ		$1.406 \cdot 10^{-4}$	$-2.424 \cdot 10^{-4}$	$6.491 \cdot 10^{-4}$		1.844	2.360	3.290
c_4^ϕ		$6.005 \cdot 10^{-5}$	$-4.839 \cdot 10^{-5}$	$1.522 \cdot 10^{-4}$		$7.272 \cdot 10^{-1}$	1.786	5.737
c_2^A		$2.917 \cdot 10^{-1}$	$-1.330 \cdot 10^{-1}$	$2.315 \cdot 10^{-1}$		$2.157 \cdot 10^{-1}$	$-6.055 \cdot 10^{-3}$	$-7.261 \cdot 10^{-3}$
c_3^A		2.068	-1.589	2.079		$8.165 \cdot 10^{-1}$	1.536	$3.433 \cdot 10^{-1}$
$A_{\rm peak}$		$6.230 \cdot 10^{-2}$	$2.460 \cdot 10^{-2}$	$1.575 \cdot 10^{-2}$		$1.509 \cdot 10^{-1}$	$1.458 \cdot 10^{-1}$	$1.537 \cdot 10^{-1}$
$\ddot{A}_{\rm peak}$		$-2.678 \cdot 10^{-3}$	$-1.660 \cdot 10^{-3}$	$5.739 \cdot 10^{-4}$		$-8.648 \cdot 10^{-4}$	$3.099 \cdot 10^{-4}$	$4.012 \cdot 10^{-4}$
$\Delta\omega_{\rm peak}$		$1.881 \cdot 10^{-1}$	$-3.904 \cdot 10^{-2}$	$1.385 \cdot 10^{-2}$		$1.954 \cdot 10^{-1}$	$-1.188 \cdot 10^{-2}$	$-5.822 \cdot 10^{-3}$

Table C.2: Global fits of the coefficients for the quantities used to determine NQC corrections for $t^{\rm NQC}_{\ell m} = t^{\rm peak}_{A_{\ell m}} - 2$. The fitting template is a quadratic function: $y = C_{\rm QC} + C_1 \hat{b}_{\Omega_{\rm pk}} + C_2 \hat{b}^2_{\Omega_{\rm pk}}$. The amplitude considered in this table is RWZ-normalized as usual, i.e. $A_{\ell m} = |\Psi_{\ell m}| = |h_{\ell m}|/\sqrt{(\ell+2)(\ell+1)\ell(\ell-1)}$.

$X^{\rm NQC}_{\ell m}$	(ℓ, m)	$C_{\rm QC}$	C_1	C_2	(ℓ, m)	$C_{\rm QC}$	C_1	C_2
A	(2,2)	$2.938 \cdot 10^{-1}$	$2.049 \cdot 10^{-1}$	$1.860 \cdot 10^{-1}$	(4,4)	$1.440 \cdot 10^{-2}$	$1.261 \cdot 10^{-2}$	$1.215 \cdot 10^{-2}$
$\dot{A}$		$7.898 \cdot 10^{-4}$	$-2.420 \cdot 10^{-3}$	$1.338 \cdot 10^{-3}$		$1.124 \cdot 10^{-4}$	$-1.072 \cdot 10^{-4}$	$-3.334 \cdot 10^{-5}$
$\ddot{A}$		$-3.160 \cdot 10^{-4}$	$1.042 \cdot 10^{-3}$	$-7.056 \cdot 10^{-4}$		$-4.584 \cdot 10^{-5}$	$5.504 \cdot 10^{-5}$	$1.442 \cdot 10^{-6}$
ω		$2.609 \cdot 10^{-1}$	$3.121 \cdot 10^{-2}$	$-2.361 \cdot 10^{-3}$		$6.041 \cdot 10^{-1}$	$4.204 \cdot 10^{-2}$	$1.016 \cdot 10^{-3}$
$\dot{\omega}$		$5.367 \cdot 10^{-3}$	$-1.031 \cdot 10^{-2}$	$-5.196 \cdot 10^{-4}$		$1.476 \cdot 10^{-2}$	$-1.500 \cdot 10^{-2}$	$-1.774 \cdot 10^{-4}$
$\ddot{\omega}$		$2.649 \cdot 10^{-4}$	$1.256 \cdot 10^{-4}$	$-1.332 \cdot 10^{-3}$		$3.536 \cdot 10^{-4}$	$1.146 \cdot 10^{-3}$	$-1.417 \cdot 10^{-3}$
A	(2,1)	$1.063 \cdot 10^{-1}$	$5.236 \cdot 10^{-2}$	$2.594 \cdot 10^{-2}$	(4,3)	$4.887 \cdot 10^{-3}$	$3.881 \cdot 10^{-3}$	$3.445 \cdot 10^{-3}$
$\dot{A}$		$4.784 \cdot 10^{-4}$	$-1.940 \cdot 10^{-3}$	$1.196 \cdot 10^{-3}$		$7.313 \cdot 10^{-5}$	$-3.014 \cdot 10^{-6}$	$5.836 \cdot 10^{-6}$
$\ddot{A}$		$-1.140 \cdot 10^{-4}$	$4.152 \cdot 10^{-4}$	$-3.622 \cdot 10^{-3}$		$-3.104 \cdot 10^{-5}$	$5.333 \cdot 10^{-6}$	$-3.956 \cdot 10^{-6}$
ω		$2.809 \cdot 10^{-1}$	$2.037 \cdot 10^{-2}$	$-1.893 \cdot 10^{-1}$		$5.980 \cdot 10^{-1}$	$1.029 \cdot 10^{-2}$	$-1.114 \cdot 10^{-2}$
$\dot{\omega}$		$9.270 \cdot 10^{-3}$	$7.587 \cdot 10^{-3}$	$3.664 \cdot 10^{-2}$		$1.979 \cdot 10^{-2}$	$-7.181 \cdot 10^{-3}$	$-3.824 \cdot 10^{-4}$
$\ddot{\omega}$		$-3.868 \cdot 10^{-3}$	$9.083 \cdot 10^{-4}$	$3.541 \cdot 10^{-2}$		$-1.791 \cdot 10^{-4}$	$1.279 \cdot 10^{-3}$	$3.702 \cdot 10^{-4}$
A	(3,3)	$5.115 \cdot 10^{-2}$	$3.967 \cdot 10^{-2}$	$3.547 \cdot 10^{-2}$	(4,2)	$1.627 \cdot 10^{-3}$	$8.138 \cdot 10^{-4}$	$5.752 \cdot 10^{-4}$
$\dot{A}$		$2.767 \cdot 10^{-4}$	$-4.255 \cdot 10^{-4}$	$1.457 \cdot 10^{-5}$		$2.687 \cdot 10^{-5}$	$7.489 \cdot 10^{-6}$	$4.104 \cdot 10^{-5}$
$\ddot{A}$		$-1.109 \cdot 10^{-4}$	$1.999 \cdot 10^{-4}$	$-5.411 \cdot 10^{-5}$		$-1.470 \cdot 10^{-5}$	$-1.090 \cdot 10^{-5}$	$-7.254 \cdot 10^{-6}$
ω		$4.322 \cdot 10^{-1}$	$4.023 \cdot 10^{-2}$	$-2.155 \cdot 10^{-3}$		$5.784 \cdot 10^{-1}$	$2.331 \cdot 10^{-2}$	$-2.894 \cdot 10^{-2}$
$\dot{\omega}$		$1.026 \cdot 10^{-2}$	$-1.279 \cdot 10^{-2}$	$3.809 \cdot 10^{-4}$		$2.622 \cdot 10^{-2}$	$-4.593 \cdot 10^{-3}$	$-3.936 \cdot 10^{-3}$
$\ddot{\omega}$		$3.777 \cdot 10^{-4}$	$5.998 \cdot 10^{-4}$	$-1.296 \cdot 10^{-3}$		$-4.671 \cdot 10^{-4}$	$6.784 \cdot 10^{-3}$	$-4.209 \cdot 10^{-3}$
A	(3,2)	$1.790 \cdot 10^{-2}$	$1.174 \cdot 10^{-2}$	$9.344 \cdot 10^{-3}$	(4,1)	$4.311 \cdot 10^{-4}$	$1.636 \cdot 10^{-4}$	$1.081 \cdot 10^{-4}$
$\dot{A}$		$2.582 \cdot 10^{-4}$	$-3.442 \cdot 10^{-7}$	$-3.865 \cdot 10^{-5}$		$4.004 \cdot 10^{-5}$	$7.867 \cdot 10^{-6}$	$1.042 \cdot 10^{-5}$
$\ddot{A}$		$-1.076 \cdot 10^{-4}$	$4.345 \cdot 10^{-5}$	$-2.468 \cdot 10^{-5}$		$5.997 \cdot 10^{-6}$	$1.533 \cdot 10^{-5}$	$9.482 \cdot 10^{-8}$
ω		$4.205 \cdot 10^{-1}$	$1.124 \cdot 10^{-2}$	$2.154 \cdot 10^{-3}$		$5.673 \cdot 10^{-1}$	$9.191 \cdot 10^{-2}$	$-3.606 \cdot 10^{-2}$
$\dot{\omega}$		$1.534 \cdot 10^{-2}$	$-6.496 \cdot 10^{-3}$	$2.843 \cdot 10^{-3}$		$-1.560 \cdot 10^{-2}$	$-1.071 \cdot 10^{-2}$	$8.617 \cdot 10^{-3}$
$\ddot{\omega}$		$2.792 \cdot 10^{-4}$	$-3.190 \cdot 10^{-4}$	$-8.332 \cdot 10^{-5}$		$-3.018 \cdot 10^{-2}$	$-3.355 \cdot 10^{-2}$	$5.444 \cdot 10^{-3}$
A	(3,1)	$5.358 \cdot 10^{-3}$	$2.113 \cdot 10^{-3}$	$1.367 \cdot 10^{-3}$	(5,5)	$5.151 \cdot 10^{-3}$	$5.057 \cdot 10^{-3}$	$5.331 \cdot 10^{-3}$
$\dot{A}$		$2.413 \cdot 10^{-4}$	$5.772 \cdot 10^{-5}$	$5.734 \cdot 10^{-5}$		$5.170 \cdot 10^{-5}$	$-2.949 \cdot 10^{-5}$	$-2.260 \cdot 10^{-5}$
$\ddot{A}$		$4.851 \cdot 10^{-6}$	$7.180 \cdot 10^{-5}$	$6.059 \cdot 10^{-6}$		$-2.150 \cdot 10^{-5}$	$1.723 \cdot 10^{-5}$	$6.342 \cdot 10^{-6}$
ω		$4.189 \cdot 10^{-1}$	$7.247 \cdot 10^{-2}$	$-2.821 \cdot 10^{-2}$		$7.789 \cdot 10^{-1}$	$4.215 \cdot 10^{-2}$	$6.786 \cdot 10^{-4}$
$\dot{\omega}$		$-2.106 \cdot 10^{-3}$	$-1.196 \cdot 10^{-2}$	$7.362 \cdot 10^{-3}$		$1.894 \cdot 10^{-2}$	$-1.663 \cdot 10^{-2}$	$-1.112 \cdot 10^{-3}$
$\ddot{\omega}$		$-1.256 \cdot 10^{-2}$	$-1.138 \cdot 10^{-2}$	$1.408 \cdot 10^{-3}$		$2.169 \cdot 10^{-4}$	$1.746 \cdot 10^{-3}$	$-1.577 \cdot 10^{-3}$

Bibliography

[1] S. Albanesi, A. Nagar, and S. Bernuzzi, "Effective one-body model for extreme-mass-ratio spinning binaries on eccentric equatorial orbits: Testing radiation reaction and waveform," *Phys. Rev. D*, vol. 104, no. 2, p. 024067, 2021.

[2] R. Gamba, M. Breschi, G. Carullo, S. Albanesi, P. Rettegno, S. Bernuzzi, and A. Nagar, "GW190521 as a dynamical capture of two nonspinning black holes," *Nature Astron.*, vol. 7, no. 1, pp. 11–17, 2023.

[3] A. Placidi, S. Albanesi, A. Nagar, M. Orselli, S. Bernuzzi, and G. Grignani, "Exploiting Newton-factorized, 2PN-accurate waveform multipoles in effective-one-body models for spin-aligned non-circularized binaries," *Phys. Rev. D*, vol. 105, no. 10, p. 104030, 2022.

[4] S. Albanesi, A. Nagar, S. Bernuzzi, A. Placidi, and M. Orselli, "Assessment of effective-one-body radiation reactions for generic planar orbits," *Phys. Rev. D*, vol. 105, no. 10, p. 104031, 2022.

[5] S. Albanesi, A. Placidi, A. Nagar, M. Orselli, and S. Bernuzzi, "New avenue for accurate analytical waveforms and fluxes for eccentric compact binaries," *Phys. Rev. D*, vol. 105, no. 12, p. L121503, 2022.

[6] S. Albanesi, S. Bernuzzi, T. Damour, A. Nagar, and A. Placidi, "Faithful effective-one-body waveform of small-mass-ratio coalescing black hole binaries: The eccentric, nonspinning case," *Phys. Rev. D*, vol. 108, no. 8, p. 084037, 2023.

[7] T. Andrade *et al.*, "Towards numerical-relativity informed effective-one-body waveforms for dynamical capture black hole binaries," 7 2023.

[8] A. Albertini, A. Nagar, P. Rettegno, S. Albanesi, and R. Gamba, "Waveforms and fluxes: Towards a self-consistent effective one body waveform model for nonprecessing, coalescing black-hole binaries for third generation detectors," 11 2021.

[9] F. Di Giovanni, D. Guerra, S. Albanesi, M. Miravet-Tenés, and D. Tseneklidou, "Fermion-axion stars: Static solutions and dynamical stability," *Phys. Rev. D*, vol. 106, no. 8, p. 084013, 2022.

[10] A. Nagar and S. Albanesi, "Toward a gravitational self-force-informed effective-one-body waveform model for nonprecessing, eccentric, large-mass-ratio inspirals," *Phys. Rev. D*, vol. 106, no. 6, p. 064049, 2022.

[11] A. Nagar, P. Rettegno, R. Gamba, A. Albertini, and S. Bernuzzi, "TEOBResumS: Analytic systematics in next-generation of effective-one-body gravitational waveform models for future observations," 4 2023.

[12] G. Carullo, S. Albanesi, A. Nagar, R. Gamba, S. Bernuzzi, T. Andrade, and J. Trenado, "Unveiling the merger structure of black hole binaries in generic planar orbits," 9 2023.

[13] M. Berbel, M. Miravet-Tenés, S. S. Chaudhary, S. Albanesi, M. Cavaglià, L. M. n. Zertuche, D. Tseneklidou, Y. Zheng, M. W. Coughlin, and A. Toivonen, "Bayesian real-time classification of multi-messenger electromagnetic and gravitational-wave observations," 10 2023.

[14] W. Cook, B. Daszuta, J. Fields, P. Hammond, S. Albanesi, F. Zappa, S. Bernuzzi, and D. Radice, "GR-Athena++: General-relativistic magnetohydrodynamics simulations of neutron star spacetimes," 11 2023.

[15] B. P. Abbott *et al.*, "Observation of Gravitational Waves from a Binary Black Hole Merger," *Phys. Rev. Lett.*, vol. 116, no. 6, p. 061102, 2016.

[16] B. P. Abbott *et al.*, "GWTC-1: A Gravitational-Wave Transient Catalog of Compact Binary Mergers Observed by LIGO and Virgo during the First and Second Observing Runs," *Phys. Rev.*, vol. X9, no. 3, p. 031040, 2019.

[17] R. Abbott *et al.*, "GWTC-2: Compact Binary Coalescences Observed by LIGO and Virgo During the First Half of the Third Observing Run," *Phys. Rev. X*, vol. 11, p. 021053, 2021.

[18] R. Abbott *et al.*, "GWTC-3: Compact Binary Coalescences Observed by LIGO and Virgo During the Second Part of the Third Observing Run," 11 2021.

[19] B. P. Abbott *et al.*, "GW170817: Observation of Gravitational Waves from a Binary Neutron Star Inspiral," *Phys. Rev. Lett.*, vol. 119, no. 16, p. 161101, 2017.

[20] B. P. Abbott *et al.*, "Gravitational Waves and Gamma-rays from a Binary Neutron Star Merger: GW170817 and GRB 170817A," *Astrophys. J. Lett.*, vol. 848, no. 2, p. L13, 2017.

[21] B. P. Abbott *et al.*, "Multi-messenger Observations of a Binary Neutron Star Merger," *Astrophys. J. Lett.*, vol. 848, no. 2, p. L12, 2017.

[22] C. Unnikrishnan, "IndIGO and LIGO-India: Scope and plans for gravitational wave research and precision metrology in India," *Int.J.Mod.Phys.*, vol. D22, p. 1341010, 2013.

[23] M. Saleem *et al.*, "The science case for LIGO-India," *Class. Quant. Grav.*, vol. 39, no. 2, p. 025004, 2022.

[24] M. Punturo, M. Abernathy, F. Acernese, B. Allen, N. Andersson, *et al.*, "The Einstein Telescope: A third-generation gravitational wave observatory," *Class.Quant.Grav.*, vol. 27, p. 194002, 2010.

[25] M. Maggiore *et al.*, "Science Case for the Einstein Telescope," *JCAP*, vol. 03, p. 050, 2020.

[26] D. Reitze *et al.*, "Cosmic Explorer: The U.S. Contribution to Gravitational-Wave Astronomy beyond LIGO," *Bull. Am. Astron. Soc.*, vol. 51, p. 035, 7 2019.

[27] P. Amaro-Seoane *et al.*, "Laser Interferometer Space Antenna," 2 2017.

[28] J. Luo *et al.*, "TianQin: a space-borne gravitational wave detector," *Class. Quant. Grav.*, vol. 33, no. 3, p. 035010, 2016.

[29] S. Kawamura *et al.*, "Current status of space gravitational wave antenna DECIGO and B-DECIGO," *PTEP*, vol. 2021, no. 5, p. 05A105, 2021.

[30] G. Hobbs *et al.*, "The international pulsar timing array project: using pulsars as a gravitational wave detector," *Class. Quant. Grav.*, vol. 27, p. 084013, 2010.

[31] N. Yunes and X. Siemens, "Gravitational-Wave Tests of General Relativity with Ground-Based Detectors and Pulsar Timing-Arrays," *Living Rev. Rel.*, vol. 16, p. 9, 2013.

[32] J. Antoniadis *et al.*, "The second data release from the European Pulsar Timing Array - I. The dataset and timing analysis," *Astron. Astrophys.*, vol. 678, p. A48, 2023.

[33] J. Antoniadis *et al.*, "The second data release from the European Pulsar Timing Array - II. Customised pulsar noise models for spatially correlated gravitational waves," *Astron. Astrophys.*, vol. 678, p. A49, 2023.

[34] J. Antoniadis *et al.*, "The second data release from the European Pulsar Timing Array - III. Search for gravitational wave signals," *Astron. Astrophys.*, vol. 678, p. A50, 2023.

[35] J. Antoniadis *et al.*, "The second data release from the European Pulsar Timing Array IV. Search for continuous gravitational wave signals," 6 2023.

[36] J. Antoniadis *et al.*, "The second data release from the European Pulsar Timing Array: V. Implications for massive black holes, dark matter and the early Universe," 6 2023.

[37] A. Einstein, L. Infeld, and B. Hoffmann, "The Gravitational equations and the problem of motion," *Annals Math.*, vol. 39, pp. 65–100, 1938.

[38] A. Einstein and L. Infeld, "The Gravitational equations and the problem of motion. 2.," *Annals Math.*, vol. 41, pp. 455–464, 1940.

[39] L. Blanchet and T. Damour, "Postnewtonian Generation of Gravitational Waves," *Ann. Inst. H. Poincaré Phys. Theor.*, vol. 50, pp. 377–408, 1989.

[40] T. Damour, P. Jaranowski, and G. Schäfer, "Nonlocal-in-time action for the fourth post-Newtonian conservative dynamics of two-body systems," *Phys. Rev. D*, vol. 89, no. 6, p. 064058, 2014.

[41] G. Schaefer and P. Jaranowski, "Hamiltonian formulation of general relativity and post-Newtonian dynamics of compact binaries," *Living Rev. Rel.*, vol. 21, no. 1, p. 7, 2018.

[42] L. Bel, T. Damour, N. Deruelle, J. Ibanez, and J. Martin, "Poincaré-invariant gravitational field and equations of motion of two pointlike objects: The postlinear approximation of general relativity," *Gen. Rel. Grav.*, vol. 13, pp. 963–1004, 1981.

[43] T. Damour, "Gravitational scattering, post-Minkowskian approximation and Effective One-Body theory," *Phys. Rev.*, vol. D94, no. 10, p. 104015, 2016.

[44] Z. Bern, C. Cheung, R. Roiban, C.-H. Shen, M. P. Solon, and M. Zeng, "Scattering Amplitudes and the Conservative Hamiltonian for Binary Systems at Third Post-Minkowskian Order," *Phys. Rev. Lett.*, vol. 122, no. 20, p. 201603, 2019.

[45] T. Damour, "Radiative contribution to classical gravitational scattering at the third order in G," *Phys. Rev. D*, vol. 102, no. 12, p. 124008, 2020.

[46] C. Dlapa, G. Kälin, Z. Liu, J. Neef, and R. A. Porto, "Radiation Reaction and Gravitational Waves at Fourth Post-Minkowskian Order," *Phys. Rev. Lett.*, vol. 130, no. 10, p. 101401, 2023.

[47] L. Blanchet, T. Damour, B. R. Iyer, C. M. Will, and A. Wiseman, "Gravitational radiation damping of compact binary systems to second postNewtonian order," *Phys.Rev.Lett.*, vol. 74, pp. 3515–3518, 1995.

[48] L. Blanchet, T. Damour, G. Esposito-Farese, and B. R. Iyer, "Gravitational radiation from inspiralling compact binaries completed at the third post-Newtonian order," *Phys.Rev.Lett.*, vol. 93, p. 091101, 2004.

[49] L. Blanchet, "Gravitational Radiation from Post-Newtonian Sources and Inspiralling Compact Binaries," *Living Rev. Relativity*, vol. 17, p. 2, 2014.

[50] L. Blanchet, G. Faye, Q. Henry, F. Larrouturou, and D. Trestini, "Gravitational-wave flux and quadrupole modes from quasicircular nonspinning compact binaries to the fourth post-Newtonian order," *Phys. Rev. D*, vol. 108, no. 6, p. 064041, 2023.

[51] A. Buonanno and T. Damour, "Effective one-body approach to general relativistic two-body dynamics," *Phys. Rev.*, vol. D59, p. 084006, 1999.

[52] A. Buonanno and T. Damour, "Transition from inspiral to plunge in binary black hole coalescences," *Phys. Rev.*, vol. D62, p. 064015, 2000.

[53] T. Damour, P. Jaranowski, and G. Schaefer, "On the determination of the last stable orbit for circular general relativistic binaries at the third postNewtonian approximation," *Phys. Rev.*, vol. D62, p. 084011, 2000.

[54] A. Buonanno, G. B. Cook, and F. Pretorius, "Inspiral, merger and ring-down of equal-mass black-hole binaries," *Phys. Rev. D*, vol. 75, p. 124018, 2007.

[55] A. Nagar, T. Damour, and A. Tartaglia, "Binary black hole merger in the extreme mass ratio limit," *Class. Quant. Grav.*, vol. 24, pp. S109–S124, 2007.

[56] T. Damour, A. Nagar, and S. Bernuzzi, "Improved effective-one-body description of coalescing nonspinning black-hole binaries and its numerical-relativity completion," *Phys.Rev.*, vol. D87, p. 084035, 2013.

[57] A. Nagar *et al.*, "Time-domain effective-one-body gravitational waveforms for coalescing compact binaries with nonprecessing spins, tides and self-spin effects," *Phys. Rev.*, vol. D98, no. 10, p. 104052, 2018.

[58] R. Cotesta, A. Buonanno, A. Bohé, A. Taracchini, I. Hinder, and S. Ossokine, "Enriching the Symphony of Gravitational Waves from Binary Black Holes by Tuning Higher Harmonics," *Phys. Rev.*, vol. D98, no. 8, p. 084028, 2018.

[59] M. Khalil, A. Buonanno, H. Estelles, D. P. Mihaylov, S. Ossokine, L. Pompili, and A. Ramos-Buades, "Theoretical groundwork supporting the precessing-spin two-body dynamics of the effective-one-body waveform models SEOBNRv5," 3 2023.

[60] L. Pompili *et al.*, "Laying the foundation of the effective-one-body waveform models SEOBNRv5: improved accuracy and efficiency for spinning non-precessing binary black holes," 3 2023.

[61] P. Ajith, M. Hannam, S. Husa, Y. Chen, B. Brügmann, *et al.*, "Inspiral-merger-ringdown waveforms for black-hole binaries with non-precessing spins," *Phys.Rev.Lett.*, vol. 106, p. 241101, 2011.

[62] L. Santamaria, F. Ohme, P. Ajith, B. Brügmann, N. Dorband, *et al.*, "Matching post-Newtonian and numerical relativity waveforms: systematic errors and a new phenomenological model for non-precessing black hole binaries," *Phys.Rev.*, vol. D82, p. 064016, 2010.

[63] S. Khan, F. Ohme, K. Chatziioannou, and M. Hannam, "Including higher order multipoles in gravitational-wave models for precessing binary black holes," *Phys. Rev. D*, vol. 101, no. 2, p. 024056, 2020.

[64] G. Pratten, S. Husa, C. Garcia-Quiros, M. Colleoni, A. Ramos-Buades, H. Estelles, and R. Jaume, "Setting the cornerstone for a family of models for gravitational waves from compact binaries: The dominant harmonic for nonprecessing quasicircular black holes," *Phys. Rev. D*, vol. 102, no. 6, p. 064001, 2020.

[65] G. Pratten *et al.*, "Computationally efficient models for the dominant and subdominant harmonic modes of precessing binary black holes," *Phys. Rev. D*, vol. 103, no. 10, p. 104056, 2021.

[66] C. García-Quirós, M. Colleoni, S. Husa, H. Estellés, G. Pratten, A. Ramos-Buades, M. Mateu-Lucena, and R. Jaume, "Multimode frequency-domain model for the gravitational wave signal from nonprecessing black-hole binaries," *Phys. Rev. D*, vol. 102, no. 6, p. 064002, 2020.

[67] H. Estellés, A. Ramos-Buades, S. Husa, C. García-Quirós, M. Colleoni, L. Haegel, and R. Jaume, "Phenomenological time domain model for dominant quadrupole gravitational wave signal of coalescing binary black holes," *Phys. Rev. D*, vol. 103, no. 12, p. 124060, 2021.

[68] H. Estellés, S. Husa, M. Colleoni, D. Keitel, M. Mateu-Lucena, C. García-Quirós, A. Ramos-Buades, and A. Borchers, "Time domain phenomenological model of gravitational wave subdominant harmonics for quasi-circular non-precessing binary black hole coalescences," 12 2020.

[69] T. Tanaka, Y. Mino, M. Sasaki, and M. Shibata, "Gravitational waves from a spinning particle in circular orbits around a rotating black hole," *Phys.Rev.*, vol. D54, pp. 3762–3777, 1996.

[70] Y. Mino, M. Sasaki, and T. Tanaka, "Gravitational radiation reaction to a particle motion," *Phys.Rev.*, vol. D55, pp. 3457–3476, 1997.

[71] E. Poisson, A. Pound, and I. Vega, "The Motion of point particles in curved spacetime," *Living Rev.Rel.*, vol. 14, p. 7, 2011.

[72] L. Barack and A. Pound, "Self-force and radiation reaction in general relativity," *Rept. Prog. Phys.*, vol. 82, no. 1, p. 016904, 2019.

[73] A. Pound, B. Wardell, N. Warburton, and J. Miller, "Second-Order Self-Force Calculation of Gravitational Binding Energy in Compact Binaries," *Phys. Rev. Lett.*, vol. 124, no. 2, p. 021101, 2020.

[74] A. Antonelli, C. Kavanagh, M. Khalil, J. Steinhoff, and J. Vines, "Gravitational spin-orbit coupling through third-subleading post-Newtonian order: from first-order self-force to arbitrary mass ratios," *Phys. Rev. Lett.*, vol. 125, no. 1, p. 011103, 2020.

[75] L. V. Drummond, P. Lynch, A. G. Hanselman, D. R. Becker, and S. A. Hughes, "Extreme mass-ratio inspiral and waveforms for a spinning body into a Kerr black hole via osculating geodesics and near-identity transformations," 10 2023.

[76] F. Pretorius, "Evolution of binary black hole spacetimes," *Phys. Rev. Lett.*, vol. 95, p. 121101, 2005.

[77] M. Campanelli, C. O. Lousto, P. Marronetti, and Y. Zlochower, "Accurate Evolutions of Orbiting Black-Hole Binaries Without Excision," *Phys. Rev. Lett.*, vol. 96, p. 111101, 2006.

[78] A. H. Mroue, M. A. Scheel, B. Szilagyi, H. P. Pfeiffer, M. Boyle, *et al.*, "A catalog of 174 binary black-hole simulations for gravitational-wave astronomy," *Phys.Rev.Lett.*, vol. 111, p. 241104, 2013.

[79] S. Husa, S. Khan, M. Hannam, M. Pürrer, F. Ohme, X. Jiménez Forteza, and A. Bohé, "Frequency-domain gravitational waves from nonprecessing black-hole binaries. I. New numerical waveforms and anatomy of the signal," *Phys. Rev.*, vol. D93, no. 4, p. 044006, 2016.

[80] B. Szilágyi, J. Blackman, A. Buonanno, A. Taracchini, H. P. Pfeiffer, M. A. Scheel, T. Chu, L. E. Kidder, and Y. Pan, "Approaching the Post-Newtonian Regime with Numerical Relativity: A Compact-Object Binary Simulation Spanning 350 Gravitational-Wave Cycles," *Phys. Rev. Lett.*, vol. 115, no. 3, p. 031102, 2015.

[81] K. Jani, J. Healy, J. A. Clark, L. London, P. Laguna, and D. Shoemaker, "Georgia Tech Catalog of Gravitational Waveforms," *Class. Quant. Grav.*, vol. 33, no. 20, p. 204001, 2016.

[82] I. Hinder, L. E. Kidder, and H. P. Pfeiffer, "An eccentric binary black hole inspiral-merger-ringdown gravitational waveform model from numerical relativity and post-Newtonian theory," 2017.

[83] M. Boyle *et al.*, "The SXS Collaboration catalog of binary black hole simulations," *Class. Quant. Grav.*, vol. 36, no. 19, p. 195006, 2019.

[84] E. A. Huerta *et al.*, "Physics of eccentric binary black hole mergers: A numerical relativity perspective," *Phys. Rev.*, vol. D100, no. 6, p. 064003, 2019.

[85] B. Daszuta, F. Zappa, W. Cook, D. Radice, S. Bernuzzi, and V. Morozova, "GR-Athena++: Puncture Evolutions on Vertex-centered Oct-tree Adaptive Mesh Refinement," *Astrophys. J. Supp.*, vol. 257, no. 2, p. 25, 2021.

[86] A. Ciarfella, J. Healy, C. O. Lousto, and H. Nakano, "Eccentricity estimation from initial data for numerical relativity simulations," *Phys. Rev. D*, vol. 106, no. 10, p. 104035, 2022.

[87] J. Healy and C. O. Lousto, "Fourth RIT binary black hole simulations catalog: Extension to eccentric orbits," *Phys. Rev. D*, vol. 105, no. 12, p. 124010, 2022.

[88] D. Ferguson *et al.*, "Second MAYA Catalog of Binary Black Hole Numerical Relativity Waveforms," 9 2023.

[89] J. Samsing, M. MacLeod, and E. Ramirez-Ruiz, "The Formation of Eccentric Compact Binary Inspirals and the Role of Gravitational Wave Emission in Binary-Single Stellar Encounters," *Astrophys. J.*, vol. 784, p. 71, 2014.

[90] C. L. Rodriguez, S. Chatterjee, and F. A. Rasio, "Binary Black Hole Mergers from Globular Clusters: Masses, Merger Rates, and the Impact of Stellar Evolution," *Phys. Rev.*, vol. D93, no. 8, p. 084029, 2016.

[91] K. Belczynski, D. E. Holz, T. Bulik, and R. O'Shaughnessy, "The first gravitational-wave source from the isolated evolution of two 40-100 Msun stars," *Nature*, vol. 534, p. 512, 2016.

[92] J. Samsing, "Eccentric Black Hole Mergers Forming in Globular Clusters," *Phys. Rev.*, vol. D97, no. 10, p. 103014, 2018.

[93] C. L. Rodriguez, P. Amaro-Seoane, S. Chatterjee, K. Kremer, F. A. Rasio, J. Samsing, C. S. Ye, and M. Zevin, "Post-Newtonian Dynamics in Dense Star Clusters: Formation, Masses, and Merger Rates of Highly-Eccentric Black Hole Binaries," *Phys. Rev. D*, vol. 98, no. 12, p. 123005, 2018.

[94] S. Mukherjee, S. Mitra, and S. Chatterjee, "Detectability of hyperbolic encounters of compact stars with ground-based gravitational waves detectors," 10 2020.

[95] S. Naoz, G. Li, M. Zanardi, G. C. de Elía, and R. P. Di Sisto, "The eccentric kozai–lidov mechanism for outer test particle," *The Astronomical Journal*, vol. 154, p. 18, June 2017.

[96] R. Abbott *et al.*, "GW190521: A Binary Black Hole Merger with a Total Mass of $150M_{\odot}$," *Phys. Rev. Lett.*, vol. 125, no. 10, p. 101102, 2020.

[97] I. M. Romero-Shaw, P. D. Lasky, E. Thrane, and J. C. Bustillo, "GW190521: orbital eccentricity and signatures of dynamical formation in a binary black hole merger signal," *Astrophys. J. Lett.*, vol. 903, no. 1, p. L5, 2020.

[98] V. Gayathri, J. Healy, J. Lange, B. O'Brien, M. Szczepanczyk, I. Bartos, M. Campanelli, S. Klimenko, C. O. Lousto, and R. O'Shaughnessy, "Eccentricity estimate for black hole mergers with numerical relativity simulations," *Nature Astron.*, vol. 6, no. 3, pp. 344–349, 2022.

[99] J. Calderón Bustillo, N. Sanchis-Gual, A. Torres-Forné, J. A. Font, A. Vajpeyi, R. Smith, C. Herdeiro, E. Radu, and S. H. W. Leong, "GW190521 as a Merger of Proca Stars: A Potential New Vector Boson of 8.7×10^{-13} eV," *Phys. Rev. Lett.*, vol. 126, no. 8, p. 081101, 2021.

[100] V. De Luca, V. Desjacques, G. Franciolini, P. Pani, and A. Riotto, "GW190521 Mass Gap Event and the Primordial Black Hole Scenario," *Phys. Rev. Lett.*, vol. 126, no. 5, p. 051101, 2021.

[101] A. H. Nitz and C. D. Capano, "GW190521 may be an intermediate mass ratio inspiral," *Astrophys. J. Lett.*, vol. 907, no. 1, p. L9, 2021.

[102] S. Babak, J. Gair, A. Sesana, E. Barausse, C. F. Sopuerta, C. P. L. Berry, E. Berti, P. Amaro-Seoane, A. Petiteau, and A. Klein, "Science with the space-based interferometer LISA. V: Extreme mass-ratio inspirals," *Phys. Rev. D*, vol. 95, no. 10, p. 103012, 2017.

[103] E. Rosenthal, "Second-order gravitational self-force," *Phys. Rev. D*, vol. 74, p. 084018, 2006.

[104] J. M. Stewart and M. Walker, "Perturbations of spacetimes in general relativity," *Proc. Roy. Soc. Lond. A*, vol. 341, pp. 49–74, 1974.

[105] M. Maggiore, *Gravitational Waves. Vol. 1: Theory and Experiments.* Oxford University Press, 2007.

[106] K. S. Thorne, "Gravitational Wave Research: Current Status and Future Prospects," *Rev. Mod. Phys.*, vol. 52, pp. 285–297, 1980.

[107] L. E. Kidder, "Using Full Information When Computing Modes of Post- Newtonian Waveforms From Inspiralling Compact Binaries in Circular Orbit," *Phys. Rev.*, vol. D77, p. 044016, 2008.

[108] A. Albertini, R. Gamba, A. Nagar, and S. Bernuzzi, "Tailoring an effective-one-body waveform model to extreme-mass-ratio inspirals: achieving full consistency with second-order gravitational self-force results and beyond," 10 2023.

[109] T. Regge and J. A. Wheeler, "Stability of a Schwarzschild singularity," *Phys. Rev.*, vol. 108, pp. 1063–1069, 1957.

[110] F. J. Zerilli, "Effective potential for even parity Regge-Wheeler gravitational perturbation equations," *Phys. Rev. Lett.*, vol. 24, pp. 737–738, 1970.

[111] V. Moncrief, "Gravitational perturbations of spherically symmetric systems. I. The exterior problem," *Ann. Phys.*, vol. 88, pp. 323–342, 1974.

[112] K. Martel and E. Poisson, "Gravitational perturbations of the schwarzschild spacetime: A practical covariant and gauge-invariant formalism," *Physical Review D (Particles, Fields, Gravitation, and Cosmology)*, vol. 71, no. 10, p. 104003, 2005.

[113] O. Sarbach and M. Tiglio, "Gauge invariant perturbations of Schwarzschild black holes in horizon-penetrating coordinates," *Phys. Rev.*, vol. D64, p. 084016, 2001.

[114] A. Nagar and L. Rezzolla, "Gauge-invariant non-spherical metric perturbations of Schwarzschild black-hole spacetimes," *Class. Quant. Grav.*, vol. 22, p. R167, 2005.

[115] R. P. Kerr, "Gravitational field of a spinning mass as an example of algebraically special metrics," *Phys. Rev. Lett.*, vol. 11, pp. 237–238, 1963.

[116] S. A. Teukolsky, "Perturbations of a rotating black hole. 1. Fundamental equations for gravitational electromagnetic and neutrino field perturbations," *Astrophys. J.*, vol. 185, pp. 635–647, 1973.

[117] B. J. Kelly and J. G. Baker, "Decoding mode mixing in black-hole merger ringdown," *Phys. Rev. D*, vol. 87, no. 8, p. 084004, 2013.

[118] A. Taracchini, A. Buonanno, G. Khanna, and S. A. Hughes, "Small mass plunging into a Kerr black hole: Anatomy of the inspiral-merger-ringdown waveforms," *Phys.Rev.*, vol. D90, p. 084025, 2014.

[119] E. W. Leaver, "An Analytic representation for the quasi normal modes of Kerr black holes," *Proc. Roy. Soc. Lond.*, vol. A402, pp. 285–298, 1985.

[120] K. D. Kokkotas and B. G. Schmidt, "Quasi-normal modes of stars and black holes," *Living Rev. Rel.*, vol. 2, p. 2, 1999.

[121] E. Harms, S. Bernuzzi, and B. Brügmann, "Numerical solution of the 2+1 Teukolsky equation on a hyperboloidal and horizon penetrating foliation of Kerr and application to late-time decays," *Class.Quant.Grav.*, vol. 30, p. 115013, 2013.

[122] S. Bernuzzi and A. Nagar, "Binary black hole merger in the extreme-mass-ratio limit: a multipolar analysis," *Phys. Rev.*, vol. D81, p. 084056, 2010.

[123] S. Bernuzzi, A. Nagar, and A. Zenginoglu, "Binary black hole coalescence in the large-mass-ratio limit: the hyperboloidal layer method and waveforms at null infinity," *Phys.Rev.*, vol. D84, p. 084026, 2011.

[124] S. Bernuzzi, A. Nagar, and A. Zenginoglu, "Horizon-absorption effects in coalescing black-hole binaries: An effective-one-body study of the non-spinning case," *Phys.Rev.*, vol. D86, p. 104038, 2012.

[125] S. Bernuzzi, A. Nagar, and A. Zenginoglu, "Binary black hole coalescence in the extreme-mass-ratio limit: testing and improving the effective-one-body multipolar waveform," *Phys.Rev.*, vol. D83, p. 064010, 2011.

[126] E. Harms, S. Bernuzzi, A. Nagar, and A. Zenginoglu, "A new gravitational wave generation algorithm for particle perturbations of the Kerr spacetime," *Class.Quant.Grav.*, vol. 31, p. 245004, 2014.

[127] C. O. Lousto and R. H. Price, "Headon collisions of black holes: The Particle limit," *Phys.Rev.*, vol. D55, pp. 2124–2138, 1997.

[128] C. O. Lousto and R. H. Price, "Understanding initial data for black hole collisions," *Phys. Rev.*, vol. D56, pp. 6439–6457, 1997.

[129] C. O. Lousto, "A time-domain fourth-order-convergent numerical algorithm to integrate black hole perturbations in the extreme-mass-ratio limit," *Class.Quant.Grav.*, vol. 22, pp. S543–S568, 2005.

[130] A. Zenginoğlu, "Hyperboloidal layers for hyperbolic equations on unbounded domains," *J.Comput.Phys.*, vol. 230, pp. 2286–2302, 2011.

[131] G. Calabrese and C. Gundlach, "Discrete boundary treatment for the shifted wave equation," *Class. Quant. Grav.*, vol. 23, pp. S343–S368, 2006.

[132] E. Pazos-Avalos and C. O. Lousto, "Numerical integration of the Teukolsky equation in the time domain," *Phys. Rev. D*, vol. 72, p. 084022, 2005.

[133] B. Carter, "Global structure of the kerr family of gravitational fields," *Phys. Rev.*, vol. 174, pp. 1559–1571, Oct 1968.

[134] T. Damour and A. Nagar, "New effective-one-body description of coalescing nonprecessing spinning black-hole binaries," *Phys.Rev.*, vol. D90, no. 4, p. 044018, 2014.

[135] J. A. Font, "Numerical Hydrodynamics and Magnetohydrodynamics in General Relativity," *Living Rev. Rel.*, vol. 11, p. 7, 2008.

[136] T. Dietrich, D. Radice, S. Bernuzzi, F. Zappa, A. Perego, B. Brügmann, S. V. Chaurasia, R. Dudi, W. Tichy, and M. Ujevic, "CoRe database of binary neutron star merger waveforms," *Class. Quant. Grav.*, vol. 35, no. 24, p. 24LT01, 2018.

[137] C. O. Lousto and J. Healy, "Study of the intermediate mass ratio black hole binary merger up to 1000:1 with numerical relativity," *Class. Quant. Grav.*, vol. 40, no. 9, p. 09LT01, 2023.

[138] A. Taracchini, Y. Pan, A. Buonanno, E. Barausse, M. Boyle, *et al.*, "Prototype effective-one-body model for nonprecessing spinning inspiral-merger-ringdown waveforms," *Phys.Rev.*, vol. D86, p. 024011, 2012.

[139] A. Taracchini, A. Buonanno, Y. Pan, T. Hinderer, M. Boyle, *et al.*, "Effective-one-body model for black-hole binaries with generic mass ratios and spins," *Phys.Rev.*, vol. D89, no. 6, p. 061502, 2014.

[140] T. Damour, B. R. Iyer, and A. Nagar, "Improved resummation of post-Newtonian multipolar waveforms from circularized compact binaries," *Phys. Rev.*, vol. D79, p. 064004, 2009.

[141] S. Ossokine *et al.*, "Multipolar Effective-One-Body Waveforms for Precessing Binary Black Holes: Construction and Validation," *Phys. Rev. D*, vol. 102, no. 4, p. 044055, 2020.

[142] S. Akcay, R. Gamba, and S. Bernuzzi, "A hybrid post-Newtonian – effective-one-body scheme for spin-precessing compact-binary waveforms," *Phys. Rev. D*, vol. 103, no. 2, p. 024014, 2021.

[143] R. Gamba, S. Akçay, S. Bernuzzi, and J. Williams, "Effective-one-body waveforms for precessing coalescing compact binaries with post-Newtonian twist," *Phys. Rev. D*, vol. 106, no. 2, p. 024020, 2022.

[144] A. Ramos-Buades, A. Buonanno, H. Estellés, M. Khalil, D. P. Mihaylov, S. Ossokine, L. Pompili, and M. Shiferaw, "SEOBNRv5PHM: Next generation of accurate and efficient multipolar precessing-spin effective-one-body waveforms for binary black holes," 3 2023.

[145] D. Chiaramello and A. Nagar, "Faithful analytical effective-one-body waveform model for spin-aligned, moderately eccentric, coalescing black hole binaries," *Phys. Rev. D*, vol. 101, no. 10, p. 101501, 2020.

[146] A. Nagar, P. Rettegno, R. Gamba, and S. Bernuzzi, "Effective-one-body waveforms from dynamical captures in black hole binaries," *Phys. Rev. D*, vol. 103, no. 6, p. 064013, 2021.

[147] A. Nagar, A. Bonino, and P. Rettegno, "Effective one-body multipolar waveform model for spin-aligned, quasicircular, eccentric, hyperbolic black hole binaries," *Phys. Rev. D*, vol. 103, no. 10, p. 104021, 2021.

[148] A. Nagar and P. Rettegno, "Next generation: Impact of high-order analytical information on effective one body waveform models for noncircularized, spin-aligned black hole binaries," *Phys. Rev. D*, vol. 104, no. 10, p. 104004, 2021.

[149] A. Ramos-Buades, A. Buonanno, M. Khalil, and S. Ossokine, "Effective-one-body multipolar waveforms for eccentric binary black holes with nonprecessing spins," *Phys. Rev. D*, vol. 105, no. 4, p. 044035, 2022.

[150] M. Khalil, A. Buonanno, J. Steinhoff, and J. Vines, "Radiation-reaction force and multipolar waveforms for eccentric, spin-aligned binaries in the effective-one-body formalism," *Phys. Rev. D*, vol. 104, no. 2, p. 024046, 2021.

[151] A. Placidi, G. Grignani, T. Harmark, M. Orselli, S. Gliorio, and A. Nagar, "2.5PN accurate waveform information for generic-planar-orbit binaries in effective one-body models," *Phys. Rev. D*, vol. 108, no. 2, p. 024068, 2023.

[152] C. P. L. Berry, S. A. Hughes, C. F. Sopuerta, A. J. K. Chua, A. Heffernan, K. Holley-Bockelmann, D. P. Mihaylov, M. C. Miller, and A. Sesana, "The unique potential of extreme mass-ratio inspirals for gravitational-wave astronomy," 2019.

[153] M. van de Meent, A. Buonanno, D. P. Mihaylov, S. Ossokine, L. Pompili, N. Warburton, A. Pound, B. Wardell, L. Durkan, and J. Miller, "Enhancing the SEOBNRv5 effective-one-body waveform model with second-order gravitational self-force fluxes," 3 2023.

[154] D. Bini, T. Damour, and A. Geralico, "Binary dynamics at the fifth and fifth-and-a-half post-Newtonian orders," *Phys. Rev. D*, vol. 102, no. 2, p. 024062, 2020.

[155] A. Nagar, F. Messina, P. Rettegno, D. Bini, T. Damour, A. Geralico, S. Akcay, and S. Bernuzzi, "Nonlinear-in-spin effects in effective-one-body waveform models of spin-aligned, inspiralling, neutron star binaries," *Phys. Rev.*, vol. D99, p. 044007, 2019.

[156] T. Damour, P. Jaranowski, and G. Schäfer, "Effective one body approach to the dynamics of two spinning black holes with next-to-leading order spin-orbit coupling," *Phys.Rev.*, vol. D78, p. 024009, 2008.

[157] J. M. Bardeen, W. H. Press, and S. A. Teukolsky, "Rotating black holes: Locally nonrotating frames, energy extraction, and scalar synchrotron radiation," *Astrophys. J.*, vol. 178, p. 347, 1972.

[158] A. Nagar and A. Shah, "Factorization and resummation: A new paradigm to improve gravitational wave amplitudes," *Phys. Rev.*, vol. D94, no. 10, p. 104017, 2016.

[159] F. Messina, A. Maldarella, and A. Nagar, "Factorization and resummation: A new paradigm to improve gravitational wave amplitudes. II: the higher multipolar modes," *Phys. Rev.*, vol. D97, no. 8, p. 084016, 2018.

[160] D. Bini and T. Damour, "Gravitational radiation reaction along general orbits in the effective one-body formalism," *Phys.Rev.*, vol. D86, p. 124012, 2012.

[161] M. Isi and W. M. Farr, "Analyzing black-hole ringdowns," 7 2021.

[162] M. Giesler, M. Isi, M. A. Scheel, and S. Teukolsky, "Black Hole Ringdown: The Importance of Overtones," *Phys. Rev. X*, vol. 9, no. 4, p. 041060, 2019.

[163] L. Magaña Zertuche *et al.*, "High precision ringdown modeling: Multimode fits and BMS frames," *Phys. Rev. D*, vol. 105, no. 10, p. 104015, 2022.

[164] Y. Zlochower, R. Gomez, S. Husa, L. Lehner, and J. Winicour, "Mode coupling in the nonlinear response of black holes," *Phys. Rev. D*, vol. 68, p. 084014, 2003.

[165] L. London, D. Shoemaker, and J. Healy, "Modeling ringdown: Beyond the fundamental quasinormal modes," *Phys. Rev.*, vol. D90, no. 12, p. 124032, 2014. [Erratum: Phys. Rev.D94,no.6,069902(2016)].

[166] K. Mitman *et al.*, "Nonlinearities in Black Hole Ringdowns," *Phys. Rev. Lett.*, vol. 130, no. 8, p. 081402, 2023.

[167] V. Baibhav, M. H.-Y. Cheung, E. Berti, V. Cardoso, G. Carullo, R. Cotesta, W. Del Pozzo, and F. Duque, "Agnostic black hole spectroscopy: Quasinormal mode content of numerical relativity waveforms and limits of validity of linear perturbation theory," *Phys. Rev. D*, vol. 108, no. 10, p. 104020, 2023.

[168] J. Redondo-Yuste, G. Carullo, J. L. Ripley, E. Berti, and V. Cardoso, "Spin dependence of black hole ringdown nonlinearities," 8 2023.

[169] T. Damour and A. Nagar, "A new analytic representation of the ringdown waveform of coalescing spinning black hole binaries," *Phys.Rev.*, vol. D90, p. 024054, 2014.

[170] E. Gourgoulhon, *3+1 formalism and bases of numerical relativity*. Lecture notes in physics, Berlin: Springer, 2012.

[171] R. L. Arnowitt, S. Deser, and C. W. Misner, "The Dynamics of general relativity," *Gen. Rel. Grav.*, vol. 40, pp. 1997–2027, 2008.

[172] J. W. York, Jr., "Kinematics and Dynamics of General Relativity," in *Workshop on Sources of Gravitational Radiation*, pp. 83–126, 1978.

[173] J. York, James W., "Gravitational degrees of freedom and the initial-value problem," *Phys.Rev.Lett.*, vol. 26, pp. 1656–1658, 1971.

[174] J. York, James W., "Role of conformal three geometry in the dynamics of gravitation," *Phys.Rev.Lett.*, vol. 28, pp. 1082–1085, 1972.

[175] A. Lichnerowicz, "L'integration des equations de la gravitation relativiste et le probleme des n corps," *J. Math. Pures Appl.*, vol. 23, p. 37, 1944.

[176] T. Damour, F. Guercilena, I. Hinder, S. Hopper, A. Nagar, and L. Rezzolla, "Strong-Field Scattering of Two Black Holes: Numerics Versus Analytics," *Phys. Rev. D*, vol. 89, no. 8, p. 081503, 2014.

[177] T. Damour and P. Rettegno, "Strong-field scattering of two black holes: Numerical relativity meets post-Minkowskian gravity," *Phys. Rev. D*, vol. 107, no. 6, p. 064051, 2023.

[178] P. Rettegno, G. Pratten, L. Thomas, P. Schmidt, and T. Damour, "Strong-field scattering of two spinning black holes: Numerical Relativity versus post-Minkowskian gravity," 7 2023.

[179] T. Damour, A. Nagar, D. Pollney, and C. Reisswig, "Energy versus Angular Momentum in Black Hole Binaries," *Phys.Rev.Lett.*, vol. 108, p. 131101, 2012.

[180] J. W. York, Jr., "Conformatlly invariant orthogonal decomposition of symmetric tensors on Riemannian manifolds and the initial value problem of general relativity," *J. Math. Phys.*, vol. 14, pp. 456–464, 1973.

[181] J. M. Bowen and J. W. York, Jr., "Time asymmetric initial data for black holes and black hole collisions," *Phys. Rev.*, vol. D21, pp. 2047–2056, 1980.

[182] M. Ansorg, B. Brügmann, and W. Tichy, "A single-domain spectral method for black hole puncture data," *Phys. Rev.*, vol. D70, p. 064011, 2004.

[183] F. Löffler *et al.*, "The Einstein Toolkit: A Community Computational Infrastructure for Relativistic Astrophysics," *Class. Quant. Grav.*, vol. 29, p. 115001, 2012.

[184] L. Werneck, S. Cupp, T. Assumpção, S. R. Brandt, C.-H. Cheng, P. Diener, J. Doherty, Z. Etienne, R. Haas, T. P. Jacques, B. Karakaş, K. Topolski, B.-J. Tsao, M. Alcubierre, D. Alic, G. Allen, M. Ansorg, M. Babiuc-Hamilton, L. Baiotti, W. Benger, E. Bentivegna, S. Bernuzzi, T. Bode, G. Bozzola, B. Brendal, B. Bruegmann, M. Campanelli, F. Cipolletta, G. Corvino, R. D. Pietri, A. Dima, H. Dimmelmeier, R. Dooley, N. Dorband, M. Elley, Y. E. Khamra, J. Faber, G. Ficarra, T. Font, J. Frieben, B. Giacomazzo, T. Goodale, C. Gundlach, I. Hawke, S. Hawley, I. Hinder, E. A. Huerta, S. Husa, T. Ikeda, S. Iyer, L. Ji, D. Johnson, A. V. Joshi, H. Kalyanaraman, A. Kankani, W. Kastaun, T. Kellermann, A. Knapp, M. Koppitz, N. Kuo, P. Laguna, G. Lanferman, P. Lasky, L. Leung, F. Löffler, H. Macpherson, J. Masso, L. Menger, A. Merzky, J. M. Miller, M. Miller, P. Moesta, P. Montero, B. Mundim, P. Nelson, A. Nerozzi, S. C. Noble, C. Ott, L. J. Papenfort, R. Paruchuri, D. Pollney, D. Price, D. Radice, T. Radke, C. Reisswig, L. Rezzolla, C. B. Richards, D. Rideout, M. Ripeanu, L. Sala, J. A. Schewtschenko, E. Schnetter, B. Schutz, E. Seidel, E. Seidel, J. Shalf, K. Sible, U. Sperhake, N. Stergioulas, W.-M. Suen, B. Szilagyi, R. Takahashi, M. Thomas, J. Thornburg, C. Tian, M. Tobias, A. Tonita, S. Tootle, P. Walker, M.-B. Wan, B. Wardell, A. Wen, H. Witek, M. Zilhão, B. Zink, and Y. Zlochower, "The einstein toolkit," May 2023. To find out more, visit http://einsteintoolkit.org.

[185] J. York, James W., "Conformal 'thin sandwich' data for the initial-value problem," *Phys.Rev.Lett.*, vol. 82, pp. 1350–1353, 1999.

[186] I. Ruchlin, J. Healy, C. O. Lousto, and Y. Zlochower, "Puncture Initial Data for Black-Hole Binaries with High Spins and High Boosts," *Phys. Rev. D*, vol. 95, no. 2, p. 024033, 2017.

[187] H. P. Pfeiffer and J. W. York, Jr., "Extrinsic curvature and the Einstein constraints," *Phys. Rev.*, vol. D67, p. 044022, 2003.

[188] E. Gourgoulhon, P. Grandclement, and S. Bonazzola, "Binary black holes in circular orbits. 1. A Global space-time approach," *Phys. Rev.*, vol. D65, p. 044020, 2002.

[189] P. Grandclement, E. Gourgoulhon, and S. Bonazzola, "Binary black holes in circular orbits. 2. Numerical methods and first results," *Phys. Rev. D*, vol. 65, p. 044021, 2002.

[190] B. Brügmann, "Adaptive mesh and geodesically sliced Schwarzschild spacetime in 3+1 dimensions," *Phys. Rev.*, vol. D54, pp. 7361–7372, 1996.

[191] C. Bona, J. Masso, E. Seidel, and J. Stela, "A New formalism for numerical relativity," *Phys. Rev. Lett.*, vol. 75, pp. 600–603, 1995.

[192] M. Alcubierre, B. Brügmann, P. Diener, M. Koppitz, D. Pollney, *et al.*, "Gauge conditions for long term numerical black hole evolutions without excision," *Phys.Rev.*, vol. D67, p. 084023, 2003.

[193] J. R. van Meter, J. G. Baker, M. Koppitz, and D.-I. Choi, "How to move a black hole without excision: gauge conditions for the numerical evolution of a moving puncture," *Phys. Rev.*, vol. D73, p. 124011, 2006.

[194] C. Gundlach and J. M. Martin-Garcia, "Well-posedness of formulations of the Einstein equations with dynamical lapse and shift conditions," *Phys.Rev.*, vol. D74, p. 024016, 2006.

[195] B. Brügmann, J. A. Gonzalez, M. Hannam, S. Husa, U. Sperhake, *et al.*, "Calibration of Moving Puncture Simulations," *Phys.Rev.*, vol. D77, p. 024027, 2008.

[196] H. Friedrich, "On the hyperbolicity of Einstein's and other gauge field equations," *Communications in Mathematical Physics*, vol. 100, pp. 525–543, Dec. 1985.

[197] D. Garfinkle, "Harmonic coordinate method for simulating generic singularities," *Phys.Rev.*, vol. D65, p. 044029, 2002.

[198] F. Pretorius, "Numerical relativity using a generalized harmonic decomposition," *Class.Quant.Grav.*, vol. 22, pp. 425–452, 2005.

[199] M. Shibata and T. Nakamura, "Evolution of three-dimensional gravitational waves: Harmonic slicing case," *Phys. Rev.*, vol. D52, pp. 5428–5444, 1995.

[200] T. W. Baumgarte and S. L. Shapiro, "On the numerical integration of Einstein's field equations," *Phys. Rev.*, vol. D59, p. 024007, 1999.

[201] C. Bona, T. Ledvinka, C. Palenzuela, and M. Zacek, "General-covariant evolution formalism for Numerical Relativity," *Phys. Rev.*, vol. D67, p. 104005, 2003.

[202] S. Bernuzzi and D. Hilditch, "Constraint violation in free evolution schemes: comparing BSSNOK with a conformal decomposition of Z4," *Phys. Rev.*, vol. D81, p. 084003, 2010.

[203] D. Hilditch, S. Bernuzzi, M. Thierfelder, Z. Cao, W. Tichy, and B. Bruegmann, "Compact binary evolutions with the Z4c formulation," *Phys. Rev.*, vol. D88, p. 084057, 2013.

[204] A. Ori and K. S. Thorne, "The Transition from inspiral to plunge for a compact body in a circular equatorial orbit around a massive, spinning black hole," *Phys.Rev.*, vol. D62, p. 124022, 2000.

[205] R. W. O'Shaughnessy, "Transition from inspiral to plunge for eccentric equatorial Kerr orbits," *Phys. Rev. D*, vol. 67, p. 044004, 2003.

[206] L. C. Stein and N. Warburton, "Location of the last stable orbit in Kerr spacetime," *Phys. Rev. D*, vol. 101, no. 6, p. 064007, 2020.

[207] P. C. Peters and J. Mathews, "Gravitational radiation from point masses in a Keplerian orbit," *Phys. Rev.*, vol. 131, pp. 435–439, 1963.

[208] T. Damour and N. Deruelle, "General relativistic celestial mechanics of binary systems. i. the post-newtonian motion," *Annales de l'I.H.P. Physique théorique*, vol. 43, no. 1, pp. 107–132, 1985.

[209] K. Martel, "Gravitational waveforms from a point particle orbiting a Schwarzschild black hole," *Phys. Rev.*, vol. D69, p. 044025, 2004.

[210] A. M. Knee, I. M. Romero-Shaw, P. D. Lasky, J. McIver, and E. Thrane, "A Rosetta Stone for Eccentric Gravitational Waveform Models," *Astrophys. J.*, vol. 936, no. 2, p. 172, 2022.

[211] L. Barack and N. Sago, "Gravitational self-force on a particle in eccentric orbit around a Schwarzschild black hole," *Phys. Rev.*, vol. D81, p. 084021, 2010.

[212] R. Fujita, W. Hikida, and H. Tagoshi, "An Efficient Numerical Method for Computing Gravitational Waves Induced by a Particle Moving on Eccentric Inclined Orbits around a Kerr Black Hole," *Prog.Theor.Phys.*, vol. 121, pp. 843–874, 2009.

[213] K. Glampedakis and D. Kennefick, "Zoom and whirl: Eccentric equatorial orbits around spinning black holes and their evolution under gravitational radiation reaction," *Phys.Rev.*, vol. D66, p. 044002, 2002.

[214] M. Shibata, "Gravitational waves by compact stars orbiting around rotating supermassive black holes," *Phys. Rev. D*, vol. 50, pp. 6297–6311, 1994.

[215] R. Fujita, "Gravitational Waves from a Particle in Circular Orbits around a Rotating Black Hole to the 11th Post-Newtonian Order," *PTEP*, vol. 2015, no. 3, p. 033E01, 2015.

[216] Y. Kojima and T. Nakamura, "Gravitational Radiation from a Particle Scattered by a Kerr Black Hole," *Progress of Theoretical Physics*, vol. 72, pp. 494–504, 09 1984.

[217] N. E. Rifat, G. Khanna, and L. M. Burko, "Repeated Ringing of the Black Hole's Bell: Quasi-Normal Bursts from Highly Eccentric, Extreme Mass-Ratio Binaries," *Phys. Rev. Research.*, vol. 1, p. 033150, 2019.

[218] J. Thornburg, B. Wardell, and M. van de Meent, "Excitation of Kerr quasinormal modes in extreme–mass-ratio inspirals," *Phys. Rev. Res.*, vol. 2, no. 1, p. 013365, 2020.

[219] C. Munna, C. R. Evans, S. Hopper, and E. Forseth, "Determination of new coefficients in the angular momentum and energy fluxes at infinity to 9PN order for eccentric Schwarzschild extreme-mass-ratio inspirals using mode-by-mode fitting," *Phys. Rev. D*, vol. 102, no. 2, p. 024047, 2020.

[220] C. Munna, "Analytic post-Newtonian expansion of the energy and angular momentum radiated to infinity by eccentric-orbit nonspinning extreme-mass-ratio inspirals to the 19th order," *Phys. Rev. D*, vol. 102, no. 12, p. 124001, 2020.

[221] C. K. Mishra, K. G. Arun, and B. R. Iyer, "Third post-Newtonian gravitational waveforms for compact binary systems in general orbits: Instantaneous terms," *Phys. Rev.*, vol. D91, no. 8, p. 084040, 2015.

[222] Y. Boetzel, C. K. Mishra, G. Faye, A. Gopakumar, and B. R. Iyer, "Gravitational-wave amplitudes for compact binaries in eccentric orbits at the third post-Newtonian order: Tail contributions and postadiabatic corrections," *Phys. Rev. D*, vol. 100, no. 4, p. 044018, 2019.

[223] T. Hinderer and S. Babak, "Foundations of an effective-one-body model for coalescing binaries on eccentric orbits," *Phys. Rev.*, vol. D96, no. 10, p. 104048, 2017.

[224] C. M. Will and A. G. Wiseman, "Gravitational radiation from compact binary systems: Gravitational wave forms and energy loss to second postNewtonian order," *Phys. Rev. D*, vol. 54, pp. 4813–4848, 1996.

[225] A. Gopakumar and B. R. Iyer, "Second postNewtonian gravitational wave polarizations for compact binaries in elliptical orbits," *Phys. Rev. D*, vol. 65, p. 084011, 2002.

[226] "Updated Advanced LIGO sensitivity design curve." https://dcc.ligo.org/LIGO-T1800044/public.

[227] A. Bohé *et al.*, "Improved effective-one-body model of spinning, nonprecessing binary black holes for the era of gravitational-wave astrophysics with advanced detectors," *Phys. Rev.*, vol. D95, no. 4, p. 044028, 2017.

[228] R. Ruffini and J. A. Wheeler, "Gravitational Radiation," in *Atti del convengno internazionale sul tema: The astrophysical aspects of weak interactions. Cortona, il Palazzone, 10-12 giugno 1970* (L. Radicati, ed.), vol. 157, p. 165, Accademia Nazionale dei Lincei, Rome, 1971.

[229] T. Damour and A. Nagar, "An improved analytical description of inspiralling and coalescing black-hole binaries," *Phys. Rev.*, vol. D79, p. 081503, 2009.

[230] "SXS Gravitational Waveform Database." https://data.black-holes.org/waveforms/index.html.

[231] G. Riemenschneider, P. Rettegno, M. Breschi, A. Albertini, R. Gamba, S. Bernuzzi, and A. Nagar, "Assessment of consistent next-to-quasicircular corrections and postadiabatic approximation in effective-one-body multipolar waveforms for binary black hole coalescences," *Phys. Rev. D*, vol. 104, no. 10, p. 104045, 2021.

[232] T. Damour and A. Nagar, "Faithful Effective-One-Body waveforms of small-mass-ratio coalescing black-hole binaries," *Phys. Rev.*, vol. D76, p. 064028, 2007.

[233] E. W. Leaver, "Spectral decomposition of the perturbation response of the Schwarzschild geometry," *Phys.Rev.*, vol. D34, pp. 384–408, 1986.

[234] N. Andersson, "Evolving test-fields in a black-hole geometry," *Phys. Rev.*, vol. D55, pp. 468–479, 1997.

[235] A. Zenginoglu, "Asymptotics of black hole perturbations," *Class. Quant. Grav.*, vol. 27, p. 045015, 2010.

[236] G. Carullo and M. De Amicis, "Late-time tails in nonlinear evolutions of merging black hole binaries," 10 2023.

[237] J. L. Lagrange, "Sur la théorie des variations des éléments des planètes et en particulier des variations des grands axes de leurs orbites," *Oeuvres de Lagrange*, vol. 6, pp. 713–768, 1808.

[238] J. L. Lagrange, "Sur la théorie générale de la variation des constantes arbitraires dans tous les problèmes de la méchanique," *Oeuvres de Lagrange*, vol. 6, pp. 771–805, 1809.

[239] J. L. Lagrange, "Sur la théorie générale de la variation des constantes arbitraires dans tous les problèmes de la méchanique," *Oeuvres de Lagrange*, vol. 6, pp. 809–816, 1810.

[240] R. Gold and B. Brügmann, "Radiation from low-momentum zoom-whirl orbits," *Class. Quant. Grav.*, vol. 27, p. 084035, 2010.

[241] S. Brandt and B. Brügmann, "A Simple construction of initial data for multiple black holes," *Phys. Rev. Lett.*, vol. 78, pp. 3606–3609, 1997.

[242] C. O. Lousto, H. Nakano, Y. Zlochower, and M. Campanelli, "Intermediate-mass-ratio black hole binaries: Intertwining numerical and perturbative techniques," *Phys.Rev.*, vol. D82, p. 104057, 2010.

[243] H. Nakano, J. Healy, C. O. Lousto, and Y. Zlochower, "Perturbative extraction of gravitational waveforms generated with Numerical Relativity," *Phys. Rev. D*, vol. 91, no. 10, p. 104022, 2015.

[244] H. Nakano, "A note on gravitational wave extraction from binary simulations," *Class. Quant. Grav.*, vol. 32, no. 17, p. 177002, 2015.

[245] C. Reisswig and D. Pollney, "Notes on the integration of numerical relativity waveforms," *Class.Quant.Grav.*, vol. 28, p. 195015, 2011.

[246] R. Gold and B. Brügmann, "Eccentric black hole mergers and zoom-whirl behavior from elliptic inspirals to hyperbolic encounters," *Phys. Rev.*, vol. D88, no. 6, p. 064051, 2013.

[247] A. M. Abrahams and R. H. Price, "Applying black hole perturbation theory to numerically generated space-times," *Phys. Rev.*, vol. D53, pp. 1963–1971, 1996.

[248] E. Pazos *et al.*, "How far away is far enough for extracting numerical waveforms, and how much do they depend on the extraction method?," *Class. Quant. Grav.*, vol. 24, pp. S341–S368, 2007.

[249] A. Buonanno, Y. Pan, H. P. Pfeiffer, M. A. Scheel, L. T. Buchman, and L. E. Kidder, "Effective-one-body waveforms calibrated to numerical relativity simulations: Coalescence of non-spinning, equal-mass black holes," *Phys. Rev. D*, vol. 79, p. 124028, 2009.

[250] N. T. Bishop, C. Reisswig, D. Pollney, and B. Szilagyi, "Determination of unambiguous binary black hole merger waveforms at SCRI," in *12th Marcel Grossmann Meeting on General Relativity*, pp. 816–819, 7 2009.

[251] C. Reisswig, N. Bishop, D. Pollney, and B. Szilagyi, "Unambiguous determination of gravitational waveforms from binary black hole mergers," *Phys.Rev.Lett.*, vol. 103, p. 221101, 2009.

[252] C. Reisswig, N. T. Bishop, D. Pollney, and B. Szilagyi, "Characteristic extraction in numerical relativity: binary black hole merger waveforms at null infinity," *Class. Quant. Grav.*, vol. 27, p. 075014, 2010.

[253] P. Virtanen, R. Gommers, T. E. Oliphant, M. Haberland, T. Reddy, D. Cournapeau, E. Burovski, P. Peterson, W. Weckesser, J. Bright, S. J. van der Walt, M. Brett, J. Wilson, K. J. Millman, N. Mayorov, A. R. J. Nelson, E. Jones, R. Kern, E. Larson, C. J. Carey, İ. Polat, Y. Feng, E. W. Moore, J. VanderPlas, D. Laxalde, J. Perktold, R. Cimrman, I. Henriksen, E. A. Quintero, C. R. Harris, A. M. Archibald, A. H. Ribeiro, F. Pedregosa, P. van Mulbregt, and SciPy 1.0 Contributors, "SciPy 1.0: Fundamental Algorithms for Scientific Computing in Python," *Nature Methods*, vol. 17, pp. 261–272, 2020.

[254] C. Biwer, C. D. Capano, S. De, M. Cabero, D. A. Brown, A. H. Nitz, and V. Raymond, "PyCBC Inference: A Python-based parameter estimation toolkit for compact binary coalescence signals," *Publ. Astron. Soc. Pac.*, vol. 131, no. 996, p. 024503, 2019.

[255] C. Gundlach, "Pseudospectral apparent horizon finders: An Efficient new algorithm," *Phys. Rev. D*, vol. 57, pp. 863–875, 1998.

[256] A. Rashti, M. Bhattacharyya, D. Radice, B. Daszuta, W. Cook, and S. Bernuzzi, "Adaptive mesh refinement in binary black holes simulations," 12 2023.

[257] G. Morrás, J. García-Bellido, and S. Nesseris, "Search for black hole hyperbolic encounters with gravitational wave detectors," *Phys. Dark Univ.*, vol. 35, p. 100932, 2022.

[258] S. Hopper, A. Nagar, and P. Rettegno, "Strong-field scattering of two spinning black holes: Numerics versus analytics," *Phys. Rev. D*, vol. 107, no. 12, p. 124034, 2023.